Project No. 13-5494

Molecular Dynamics-based Simulations of Bulk/Interfacial Structures and Diffusion Behaviors in Nuclear Waste Glasses

Fuel Cycle Research and Development

Jincheng Du
University of North Texas

Kimberly Gray, Federal POC
John Vienna, Technical POC

NEUP Nuclear Energy University Programs
U.S. Department of Energy

NEUP 13-5494 1 Annual Report 2016-2017
FINAL PROJECT REPORT
(October 2013 – December 2017)

Molecular dynamics-based simulations of bulk/interfacial structures and diffusion behaviors in nuclear waste glasses

Prepared by:
Dr. Jincheng Du (PI) (Jincheng.du@unt.edu)[1]

Jessica Rimsza[1]
Lu Deng[1]
Xiaonan Lu[1]
Mengguo Ren[1]
Wei Sun[1]

National Lab collaborators:
Louise Criscenti (Sandia National Laboratories)
Joe Ryan (Pacific Northwest National Laboratory)
Sebastien Kerisit (Pacific Northwest National Laboratory)

[1]Department of Materials Science and Engineering, University of North Texas
1155 Union Circle # 305310, Denton, Texas 76203-5017

Program Controls: Val Seeley
TPOC: John Vienna
National Technical Director: John Vienna
Federal Manager: Kim Gray
HQ Program Manager: Andrew Griffith

Rev. 0

March 15, 2018

DE-NE0000748 (NEUP 13-5494) Final Report

(This page intentionally left blank)
Molecular dynamics-based simulations of bulk/interfacial structures and diffusion behaviors in nuclear waste glasses

Table of Contents

1 Executive Summary

This NEUP Project aimed to generate accurate atomic structural models of nuclear waste glasses by using large-scale molecular dynamics-based computer simulations and to use these models to investigate self-diffusion behaviors, interfacial structures, and hydrated gel structures formed during dissolution of these glasses. The goal was to obtain realistic and accurate short and medium range structures of these complex oxide glasses, to provide a mechanistic understanding of the dissolution behaviors, and to generate reliable information with predictive power in designing nuclear waste glasses for long-term geological storage. Looking back of the research accomplishments of this project, most of the scientific goals initially proposed have been achieved through intensive research in the three and a half year period of the project. This project has also generated a wealth of scientific data and vibrant discussions with various groups through collaborations within and outside of this project. Throughout the project one book chapter and 14 peer reviewed journal publications have been generated (including one under review) and 16 presentations (including 8 invited talks) have been made to disseminate the results of this project in national and international conference. Furthermore, this project has trained several outstanding graduate students and young researchers for future workforce in nuclear related field, especially on nuclear waste immobilization. One postdoc and four PhD students have been fully or partially supported through the project with intensive training in the field material science and engineering with expertise on glass science and nuclear waste disposal.

2. List of publications and presentations of this project

With the support of this NEUP project, one book chapter, and 13 peer reviewed papers have been created (including one currently under revision). It also leads to 16 presentations in national and international conferences and workshops (including 8 invited talks). The papers and presentations are listed below:

2.1 Book chapter:

1. J. Du, “Challenges in molecular dynamics simulations of multicomponent oxide glasses”, in “Molecular Dynamics Simulations of Disordered Materials: from Network Glasses to Phase-Change Memory Alloys”, Springer Series in Material Science, Vol. 215, pp157-180, Springer, ISBN 978-3-319-15674-3 (2015).

2.2 Journal papers:

1. L. Deng and J. Du, "Development of effective empirical potentials for molecular dynamics simulations of the structures and properties of boroaluminosilicate glasses", *Journal of Non-Crystalline Solids*, **453** 177-194 (2016).
2. M. Ren, L. Deng, J. Du, "Surface structures of sodium borosilicate glasses from molecular dynamics simulations", *Journal of American Ceramic Society*, **100** 2516-2524 (2017).
3. J. Du and J. Rimsza, "Atomistic computer simulations of water interactions and dissolution of inorganic glasses", *Nature Partner Journal Materials Degradations*, 1 16 (pp1-12), (2017).
4. M. Ren and J. Du, "Structural origin of the therma11 and diffusion behaviors of lithium aluminosilicate crystal polymorphs and glasses", *Journal of American Ceramic Society*, **99** 2823-2833 (2016).
5. J. Rimsza, J. Du, "*ab initio* Molecular Dynamics Simulations of the Hydroxylation of Nanoporous Silica", *Journal of American Ceramic Society*, **98** [12] 3748-3757 (2015).
6. J. R. Rimsza, J. Du, "Structural and Mechanical Properties of Nano-porous Silica", *Journal of American Ceramic Society*, **97**, 2772-2781 (2014).
7. J. Rimsza, L. Deng, J. Du, "Molecular dynamics simulations of nanoporous silica and organosilicate glasses using reactive force field (ReaxFF)", *Journal of Non-Crystalline Solids*, **431** 103-111 (2016).
8. J. Rimsza, J. Du, "Nanoporous Silica Gel Structures and Evolution from Reactive Force Field Based Molecular Dynamics Simulations", *Nature Partner Journal Materials Degradations,* under revisions.
9. J. M. Rimsza, J. Yeon, A.C.T. van Duin, and J. Du, "Water-nanoporous silica interactions: comparison of ReaxFF and ab initio based molecular dynamics simulations", *Journal of Physical Chemistry C*, 140, 24803-24816 (2016).
10. J. Rimsza, J. Du, "Interfacial Structure and Evolution of the Water-Silica Gel System by Reactive Force Field Based Molecular Dynamics Simulations", *Journal of Physical Chemistry C*, **121** 11534-11543 (2017).
11. J. Rimsza, J. Du, "Surface reactions and structural evolution of organosilicate glass under Ar plasma bombardment", *Computational Material Science*, **110** 287-294 (2015).
12. X. Lu, J. J. Neeway, J. R. Ryan, J. Du, "Influence of low concentration V and Co oxide doping on the dissolution behaviors of simplified nuclear waste glasses", *Journal of Non-Crystalline Solids*, **452**, 161-168 (2016).
13. X. Lu, D. Schreiber, J. Neeway, J. Ryan, J. Du, "Effects of Optical Dopants and Laser Wavelength on Atom Probe Tomography Analyses of Borosilicate Glasses", *Journal of American Ceramic Society*, **100** 4801-4815 (2017).

2.3 Presentations:

1. J. Du, Invited talk, "Corrosion of glasses for nuclear waste disposal", Environmental Engineering Symposium, AIChE Dallas Section, Richardson TX (Oct. 27, 2017).

2. J. Du, Invited talk, "Atomistic computer simulations of nuclear waste materials", Symposium on Materials Issues in Nuclear Waste Management: Nuclear Waste Process Analysis and Modeling, MS&T 2017 Pittsburg, PA (Oct. 8-12, 2017).
3. J. Du, Invited talk, "Radiation induced structural and property changes of borosilicate nuclear waste glasses", International Workshop on Laser and Ion Beams Interactions with Materials (LIBIM 2017), Chengdu, China (June 18-21, 2017).
4. J. Du, Invited talk, "Structures and properties of multicomponent oxide glasses with mixed glass formers from molecular dynamics simulations", American Ceramic Society Glass and Optical Materials Division annual meeting (May 24, 2016).
5. J. Du, Invited talk, "Water/glass interactions from *ab initio* and ReaxFF based molecular dynamics simulations", The 3rd Glass Materials Atomistic Simulations International Symposium, Wuhan, China (April 5, 2016).
6. J. Du, Invited talk, "Challenges in molecular dynamics simulations of multicomponent oxide glasses with mixed glass formers", Sandia Glass Summit, Albuquerque, NM (Jan. 8, 2016).
7. J. Du, Invited talk, "Molecular dynamics simulations of multicomponent oxide glasses with mixed glass formers", Computational Design of Ceramics and Glasses Symposium, MS&T 2015, Columbus, OH (Oct. 7, 2015).
8. J. Du, Invited talk, "Atomistic Computer Simulations of Glasses and Melts: Experimental Validation and Structure Interpretation", NOMAD Aerodynamic Levitator Workshop 2015, Oak Ridge National Lab, Oak Ridge, TN (Feb. 10, 2015).
9. L. Deng*, J. Du, "Structures and properties of boroaluminosilicate glasses from molecular dynamics simulations", Materials Science and Technology (MS&T 2016), Salt Lake City UT (Oct. 26, 2016).
10. M. Ren*, J. Du, "Structure features of sodium borosilicate glasses from molecular dynamics simulations", Materials Science and Technology (MS&T 2016), Salt Lake City UT (Oct. 26, 2016).
11. X. Lu*, J. Neeway, J. Ryan, J. Du, "Influence of transition metal oxide on the properties and dissolution behaviors of simplified high-level nuclear waste glasses", American Ceramic Society Glass and Optical Materials Division annual meeting (May 24, 2016).
12. J. M. Rimsza*, J. Du, "Interfacial behavior and dissolution gel structures of silicate glasses from ReaxFF and *ab initio* based computer simulations", American Ceramic Society Glass and Optical Materials Division annual meeting (May 25, 2016).
13. J. M. Rimsza*, J. Du, "Diffusion and Interaction of Water in Nanoporous Silica from Ab Initio Simulation", Computational Design of Ceramics and Glasses Symposium, MS&T 2015, Columbus, OH (Oct. 8, 2015).
14. M. Ren*, J. Du, "Molecular dynamics simulations of structures and lithium diffusion in $LiAlSi_2O_6$ glass and crystals", XIV International Conference on Physics of Non-Crystalline Solids, Niagra Falls, NY (Sept. 20-25, 2015).
15. J. Du*, L. Deng, M. Ren, "Structure and diffusion properties of boroaluminosilicate nuclear waste glasses", 2015 ACerS GOMD – DGG joint meeting on Glass and Optical Materials, Miami, FL (May 17-21, 2015).
16. L. Deng* and J. Du, "Molecular dynamics simulations of borate and borosilicate glasses", 2015 ACerS GOMD – DGG joint meeting on Glass and Optical Materials, Miami, FL (May 17-21, 2015).

3. Summary of major accomplishments and findings of this project

Findings and progresses of this project have been reported in milestone and annual reports. Here we summarize the main scientific accomplishments of this project:

(1) In order to obtain realistic structure models of complex, multicomponent nuclear waste glasses, we have developed empirical potentials that enabled molecular dynamics (MD) simulations of borosilicate glasses. One of the key challenge is the parameters for boron containing systems where boron coordination changes with composition. The development work enable MD simulations of boroaluminosilicate multicomponent glasses. The work of potential development and discussion of challenges of MD simulations of multicomponent glasses. Detailed results and findings can be found in Paper 1-2 in the attachments.

(2) Generated realistic bulk and surface structure models of nuclear waste glasses by using large scale MD simualtions. Furthermore the structures and properties of these glass have been explored and compared with experimental data. Paper 3-4 in the attachment.

(3) Generated models of hydrated nanporous silica gel structure models that led to enhanced understanding of the gel layer as a result of glass dissolution and their impact on transport behaviors. In order to study water/glass interfaces, Reactive Force Field (ReaxFF) potentials were explored and validated by comparing with *ab initio* based MD simulations of water/silica reactions. The validated parameters were used to study the short range, microstructural and other characteristics of nanporous silica gel layers. Paper 5-8 in the attachment.

(4) Investigated the water/porous gel layer/glass interfacial layer structure and behaviors. Interracial models of dense bulk glass, porous silica gel, and bulk water were generated and their evolution at different temperature were investigated. Paper 9 in the attachment.

(5) To complement the simulation tasks, we have also performed experimental work on static corrosion of ISG glasses with various transition metal and rare earth ions. Furthermore, the effect of optical absorption as a result of these TM and RE ion doping on the atom probe tomography detection efficiency were investigated. These paved the way for future APT studies of nuclear glass and gel structures. Paper 10-11 in the attachment.

(6) Lastly, the research in this NEUP project leads to several new areas and on-going studies of simulations of nuclear waste glasses. These include Monte Carlo simulations of glass dissolution by using glass structure models from MD simulation instead of idealized lattices. By collaborating with Sebastien Kerisit of PNNL, we have made initial testing of this approach for sodium borosilicate glasses but more extensive work on code development and improvement (such as including the condensation reactions) will be needed. Furthermore, by utilizing large computational resources such as the one at Sandia National Lab (by collaborating with Louise Criscenti) we have performed some long simulations (up to a few nanoseconds) for larger water/silica gel systems (over 10,000 atoms) by using ReaxFF based MD simulations. These will lead to future work of gel structure evolutions.

The rest of the report include copies of the papers that are in the order presented in the summary.

4. Copies of papers that summarize the findings of this project

List of the papers with copies as major findings of this project corresponding the project summary in section **3**:

1) L. Deng and J. Du, "Development of effective empirical potentials for molecular dynamics simulations of the structures and properties of boroaluminosilicate glasses", *Journal of Non-Crystalline Solids*, **453** 177-194 (2016).
2) J. Du, "Challenges in molecular dynamics simulations of multicomponent oxide glasses", in "Molecular Dynamics Simulations of Disordered Materials: from Network Glasses to Phase-Change Memory Alloys", Springer Series in Material Science, Vol. 215, pp157-180, Springer, ISBN 978-3-319-15674-3 (2015).
3) M. Ren, L. Deng, J. Du, "Surface structures of sodium borosilicate glasses from molecular dynamics simulations", *Journal of American Ceramic Society*, **100** 2516-2524 (2017).
4) M. Ren and J. Du, "Structural origin of the therma1 and diffusion behaviors of lithium aluminosilicate crystal polymorphs and glasses", *Journal of American Ceramic Society*, **99** 2823-2833 (2016).
5) J. Rimsza, J. Du, "*ab initio* Molecular Dynamics Simulations of the Hydroxylation of Nanoporous Silica", *Journal of American Ceramic Society*, **98** [12] 3748-3757 (2015).
6) J. M. Rimsza, J. Yeon, A.C.T. van Duin, and J. Du, "Water-nanoporous silica interactions: comparison of ReaxFF and *ab initio* based molecular dynamics simulations", *Journal of Physical Chemistry C*, 140, 24803-24816 (2016).

7) J. Du and J. Rimsza, “Atomistic computer simulations of water interactions and dissolution of inorganic glasses”, *Nature Partner Journal Materials Degradations*, 1 16 (pp1-12), (2017).
8) J. Rimsza, J. Du, “Nanoporous Silica Gel Structures and Evolution from Reactive Force Field Based Molecular Dynamics Simulations”, *Nature Partner Journal Materials Degradations,* under revisions.
9) J. Rimsza, J. Du, “Interfacial Structure and Evolution of the Water-Silica Gel System by Reactive Force Field Based Molecular Dynamics Simulations”, *Journal of Physical Chemistry C*, **121** 11534-11543 (2017).
10) X. Lu, J. J. Neeway, J. R. Ryan, J. Du, “Influence of low concentration V and Co oxide doping on the dissolution behaviors of simplified nuclear waste glasses”, *Journal of Non-Crystalline Solids*, **452**, 161-168 (2016).
11) X. Lu, D. Schreiber, J. Neeway, J. Ryan, J. Du, “Effects of Optical Dopants and Laser Wavelength on Atom Probe Tomography Analyses of Borosilicate Glasses”, *Journal of American Ceramic Society*, **100** 4801-4815 (2017).

Journal of Non-Crystalline Solids 453 (2016) 177–194

Contents lists available at ScienceDirect

Journal of Non-Crystalline Solids

journal homepage: www.elsevier.com/locate/jnoncrysol

Development of effective empirical potentials for molecular dynamics simulations of the structures and properties of boroaluminosilicate glasses

Lu Deng, Jincheng Du *

Department of Materials Science and Engineering, University of North Texas, Denton, TX, USA

ARTICLE INFO

Article history:
Received 5 June 2016
Received in revised form 21 September 2016
Accepted 22 September 2016
Available online 21 October 2016

Keywords:
Empirical potential development
Molecular dynamics simulations
Boroaluminosilicate glass
Borosilicate glass
Glass structure
Mechanical property

ABSTRACT

A set of empirical potentials have been developed to enable molecular dynamics simulations of oxide glasses with the most common glass formers: silica, boron and aluminum oxides. Built upon the recent borosilicate potentials, this set of partial charge effective potentials features composition dependent variable atomic charges and pairwise short range interactions that ensure high computational efficiency. They can correctly reproduce the short range structure features of boroaluminosilicate glasses including [SiO_4] tetrahedral network, aluminum coordination, and, importantly, the coordination change of boron as a function of composition. By using the newly developed potentials, a series of sodium boroaluminosilicate glasses were simulated and the structures analyzed in terms of bond distance, bond angle, and coordination number, which were compared with available theoretical, simulation and experimental results. Structural analysis such as polyhedral connectivity analysis, Q^n analysis, and ring size distribution were obtained to investigate the medium range structure features of these glasses. Furthermore, mechanical properties such as Young's, shear and bulk moduli were calculated and were found to be in good agreement with experimental data. The vibrational density of states was also calculated and compared with previous MD and *ab initio* results. The results show $^{[3]}$B and $^{[4]}$B had distinctive spectra features and vibrational spectra were in good agreement with earlier *ab initio* studies.

1. Introduction

Boroaluminosilicate glasses find wide applications in industry and technological fields such as nuclear waste disposal, sealing materials for fuel cells, chemical and heat-resistant glass containers (such as the Pyrex® glasses), optical components, and insulating fiber glasses [1,2,3,4]. However, as compared to silicate glasses, the structures of these glasses are more complex due to interactions of multiple glass formers including SiO_2, B_2O_3 and Al_2O_3, as well as their interactions and competition for modifier cations and oxygen ions. These complex interactions lead to the known mixed glass former effect [5]. The lack of detailed structural information hinders the understanding the composition-structure-property relationship hence the rational design of these glasses for various applications. In this paper, we aim to develop a set of effective composition dependent partial charge potentials that enable molecular dynamics simulations of these glasses to account for the interaction of multi glass formers and accurately predict both the structures and properties of these glasses with many practical industrial and technological applications.

Addition of boron oxide and aluminum oxide to silicate glasses leads to complex competition of alkali cations and the intriguing mixed glass former effect. It is known that introduction of alkali oxide to silica results in breaking the Si-O-Si linkages and the three-dimensional network by the formation of non-bridging oxygen (NBO). When alkali oxide is added to borosilicate glasses, however, there is a competition between the formation of NBOs on [SiO_4] tetrahedrons and conversion of boron from 3- to 4-fold coordination state ($^{[3]}$B to $^{[4]}$B), which can be described by a two-state statistical model with difference in enthalpy of the two process [6]. In sodium aluminosilicate glasses, especially those peralkali compositions, aluminum ions mainly exist in 4-coordination state and sodium ions play a charge compensation role [7]. When the three glass formers coexist in boroaluminosilicate glasses, addition of alkali oxide modifiers can play multiple competing roles including charge compensation of $[AlO_4]^-$, conversion of $^{[3]}$B to $^{[4]}$B, and creating NBOs on [SiO_4] [4,8]. It is generally believed that the enthalpy of formation increases in the three competing processes [6,8]. As a result, the empirical potential for boroaluminosilicate glasses needs to properly describe the three competing processes.

Solids state NMR results have shown that the $^{[3]}$B to $^{[4]}$B conversion is the structural origin of the boron anomaly behaviors in a number of properties such as glass transition temperature, coefficient of thermal expansion and density of borate glasses [9], where the structure of

* Corresponding author.
E-mail address: du@unt.edu (J. Du).

http://dx.doi.org/10.1016/j.jnoncrysol.2016.09.021
0022-3093/

borate glasses is characterized by $R = [Na_2O]/[B_2O_3]$ and the fraction of $^{[4]}B$ and consequently the properties show a maximum at around R = 0.4. In borosilicate glasses, the trend is preserved but the maximum R value varies with $K = [SiO_2]/[B_2O_3]$; thus both R and K are important parameters to characterize the borosilicate glasses. Yun and Bray [10] proposed a model for sodium borosilicate glasses to calculate the four-fold coordinated boron percentage (N_4) with different R and K values based on NMR studies, and this model was later modified and improved by Dell and Bray [11]. In the boroaluminosilicate glasses, the addition of alumina creates competition of between boron and aluminum for oxygen and charge compensating alkali ions. For example, it is generally accepted that the addition of aluminum ions will reduce the excess sodium content which in turn changes the boron N_4 value [4]. NMR studies [12] showed that the experimental N_4 value in sodium boroaluminosilicate glasses is smaller than those in sodium borosilicate glasses that have the same $([Na_2O]-[Al_2O_3])/[B_2O_3]$ and K values. The reason of the lower N_4 value in sodium boroaluminosilicate glass was suggested to be that the sodium oxide is firstly used to convert aluminum from higher coordination states and Na^+ ions charge compensate $[AlO_4]^-$. Du and Stebbins [8] proposed a modification of the Yun, Dell and Bray model (YDB model) [10,11] where the R and K values in original YDB model are replaced by $R' = [Na_2O]/([B_2O_3]+[Al_2O_3])$ and $K' = [SiO_2]/([B_2O_3]+[Al_2O_3])$, since boron and aluminum have similar behavior of mixing. This new model is designed for sodium boroaluminosilicate glasses in which the sodium concentration is higher than that of aluminum. In this model, $[Na_2O]-[Al_2O_3]$ defines the practically available quantity of the sodium for $^{[3]}B$ to $^{[4]}B$ conversion and NBOs for SiO_4 tetrahedrons. Although this model works well for most compositions, it has limitations in compositions with $[Al_2O_3] \gg [B_2O_3]$, since the N_4 is incorrectly predicted to be 1 when the R′ value is larger than 1.

Molecular dynamic (MD) simulations have been an important method to study the structures of glass and amorphous materials since its first application about four decades ago [5]. Among other factors, the interatomic potential plays a key role in MD simulations. Although there are many suitable potentials for silicate glasses, potentials that are capable of simulating borate and aluminate glasses are limited. It is especially challenging for borate containing silicate and aluminate glasses due to the interaction of the glass formers, or, the mixed glass former effect. There are several attempted potentials for multicomponent glasses. Among these potentials, only a few of them contain boron oxide and none of them can fully study the structures of boroaluminosilicate compositions. For example, Delaye and Cormier [13,14] proposed a set of potential which can be applied to the systems containing Na, B, Al, Si, O, Zr and Ca using the combination of two- and three-body potential terms. However, this potential produces glasses with over-estimated four-fold coordinated boron, since the N_4 values in boroaluminosilicate glass should be less than the ones in sodium borosilicate glasses based on El Damrawi's work [12]; moreover, the BMH potential uses full ionic charge where partial covalency of the Si-O network was not properly described. Huang and Kieffer [15,16] proposed a coordination dependent potential set which includes the charge transfer effects. However, the potentials were developed for silica and boron oxide only, and, compared to other commonly used oxide glass potentials, the potential form is relatively complex. Du and Cormack [17,18] employed a set of partial charge potential to describe partial covalency of silicate systems and the potential set has parameters for Si, Na, O, P [19], rare earth ions [20], and Al [7]. However, boron is not included in this potential. Pedone and coworkers [21] proposed a potential set which can deal with alkali and alkali earth silicate and aluminate glasses but boron oxide is not included in this potential set either. There are several separate sets of potentials that were developed to describe borate or borosilicate glasses. These potentials have a general feature that is to take the local coordination environment into consideration for boron charge or B-O interactions, only through which the boron coordination change with composition can be described by the potentials. For example, Park and Cormack proposed a set of coordination dependent potential for borate and borosilicate glasses [22]. Depending on the coordination number, different parameters, were used for 3- and 4-coordinated boron atoms. Huang and Kieffer [16] proposed a set of charge transfer potential for boron oxide glass where the atomic charge is allowed redistribute depending on the local environment during the simulations. However, this potential was developed only for B_2O_3 and it has a complicated form and relatively high computational cost. Inoue et al. [23] developed a set of partial charge pairwise potential for sodium borosilicate glasses and it was shown to be able reproduce boron coordination change with composition. Kieu and coworkers [24] recently developed a set of composition dependent variable charge pair-wise potential for sodium borosilicate glasses which were shown to have high computational efficiency and can reproduce the structural information and mechanical properties of sodium borosilicate glasses. Boron coordination change with composition was addressed by the variation of atomic charge on boron and other ions, as well as the repulsion term of the short range B-O interactions. Alumina is not included in this potential set, however, which prevents us from the simulations of common glass composition of the boroaluminosilicate system.

In addition to classical MD simulations, several *ab initio* MD or first principles calculations were used to study boron oxide or borosilicate glasses. These results provide input from first principles and valuable comparison for empirical potential development. Ferlat et al. [25] studied boron oxide glasses using *ab initio* MD simulations, in which two numerical models containing boroxol ring units have been tested. Structural and vibrational properties have been investigated and compared with experimental data from static structure factor, NMR and Raman. More recently, Kob and co-workers [26,27] studied sodium borosilicate glasses for both liquid and glass states using *ab initio* MD. Static and dynamic properties of liquid state such as partial structure factor, boron coordination and diffusion behavior have been studied. Furthermore, radial distribution, sodium distribution around $^{[3]}B$ and $^{[4]}B$, total electronic density of states and vibrational density of states have been analyzed for the glass state. In addition, average boron charge on oxygen atoms, dielectric function and absorption spectra give insight into understanding the sodium borate glass system.

In this paper, we've developed a set of compatible and effective potential for simulating sodium boroaluminosilicate glass systems based on the framework for sodium borosilicate systems proposed by Kieu et al. [24]. After extensive testing and addressing some limitations of the original potential, aluminum related parameters were developed by empirical fitting and applied several series of boroaluminosilicate glasses. Detailed short and medium range structure characterization of the glasses and calculations of mechanical and vibrational properties are then presented.

2. Methodologies

2.1. Empirical potentials for borosilicate glasses

Kieu and coworkers [24] developed a set of potential for sodium borosilicate glasses based on earlier development of partial charge empirical potentials for silicate magma and minerals by Guillot et al. [28]. Similar to several of the potentials for silicates [18,29,30], this set of potential combines a long range coulomb term and a short range Buckingham term:

$$\Phi(r_{ij}) = \frac{q_i\, q_j}{r_{ij}} + A_{ij} e^{\frac{-r_{ij}}{\rho_{ij}}} - \frac{C_{ij}}{r_{ij}^6} \qquad 1$$

where, r_{ij} is the interatomic distance between atom i and j; q_i and q_j are the effective charge for atom i and j, respectively. A_{ij}, ρ_{ij} and C_{ij} are the parameters for the Buckingham term.

One essential component of the Kieu et al. potential [24] is the compositional dependent variable atomic charges. The charges of boron, and consequently all other elements, vary with two ratios are commonly employed in describing the structures of borosilicate glasses: $R = \frac{Na_2O}{B_2O_3}$ and $K = \frac{SiO_2}{B_2O_3}$. Two assumptions were made on the atomic charges: Firstly, the ratio of atomic charge between 3- and 4-coordinated boron, and those between the two boron species and oxygen remain constant: $\frac{q_{B_4}}{q_{B_3}} = 1.14$, $\frac{q_{B_4}}{q_O} = -1.71$, $\frac{q_{B_3}}{q_O} = -1.5$. This is based on the results of quantum mechanical calculations of lithium borate system [31] and molecular dynamics simulation result of B_2O_3 glass [16]. Secondly, the average boron charge is determined by $|\frac{q'_B}{q'_O}| = f_{B_3}|\frac{q_{B_3}}{q_O}| + f_{B_4}|\frac{q_{B_4}}{q_O}|$, where f_{B3} and f_{B4} are the fraction of 3- and 4-coordinated boron based on the YDB model [10,11] that was originated from solid state NMR studies. Based on these assumptions, the average boron to oxygen charge ratio as a function of R is fitted to those from YDB model. As a result, the charge of boron and other elements can be calculated by solving following two equation:

$$q'_B = -q'_O\left(C_6K^2 + \sum_{i=1}^{5} C_iR^i + C_0\right) \tag{2}$$

$$q'_i = q_i - N_B\frac{q'_B - q_B}{N_{Si} + N_O + N_{Na}} \quad where \quad i = Si, O, Na \tag{3}$$

where, $C_i (i = 0,1,2,\ldots,6)$ are empirical parameters, N_i $(i = B,Na,Si,O)$ are atom numbers of each element, and q_i $(i = B,Na,Si,O)$ are the initial charge values from Guillot-Sator's paper [28] with the values being −0.945, 1.89, 0.4725 for O, Si and Na, respectively.

In addition to compositional dependent charges, this potential set also has an adjustable "A" parameters for the B-O Buckingham potential, and the ratios R and K are also involved in "A" parameter determination for B-O pair obtained by Eq. (4):

$$A_{B-O} = \sum_{i=1}^{5} a_iR^{*i} + \ a_0 \tag{4}$$

where, $a_i (i = 0,1,2,\ldots,5)$ are empirical values and R* is defined by both R and K values through following equation:

$$R^* = \begin{cases} min\left(R, \frac{K}{16} + 0.5\right) & R < \frac{K}{4} + 0.5 \\ 0 & R \in \left(\frac{K}{4} + 0.5, K + 2\right) \end{cases} \tag{5}$$

It is worth mentioning that there exists a discontinuity of R* value when R equals to K/4 + 0.5, which will also affect boron N_4 values.

2.2. Addition of aluminum to the borosilicate potentials

2.2.1. Assumptions for adding Al_2O_3

Alumina is a common component that improves the chemical durability and mechanical strength of glasses. From structure point of view, addition of Al_2O_3 to borosilicate glasses introduces competition for oxygen and charge compensation alkali ions with boron. In order to include Al^{3+} related parameters to the sodium borosilicate potential [24], we added a new ratio $H = \frac{Al_2O_3}{B_2O_3}$ so that both charge and A value of B-O Buckingham pair can vary while Al composition changes. Moreover, based on the model proposed by Du and Stebbins [8], the YDB model [10,11] for borosilicate glasses can be applied to boroaluminosilicate glasses by modifying R and K values. Since the network forming behavior of 4-coordinated aluminum, which is the majority coordination species in these glasses, is quite similar to 4-coordinated boron, these two species are considered as one general type. As a result, the modified R value called R' is introduced and defined as shown below:

$$R' = \frac{Na_2O}{B_2O_3 + Al_2O_3} \tag{6}$$

The modified K value called K' is then defined as:

$$K' = \frac{SiO_2}{B_2O_3 + Al_2O_3} \tag{7}$$

The new ratio N'_4 that describes four-coordinated boron can be expressed in the following equation:

$$N'_4 = \frac{N_4 \times B_2O_3 + Al_2O_3}{B_2O_3 + Al_2O_3} \tag{8}$$

Additionally, we realize that the R* value plays the similar role comparing with the N_4 value of the systems in the original Kieu's potential in the low sodium content region $(R < \frac{K}{4} + 0.5)$. Furthermore, for those systems with K' larger than 8, YDB model of high silicon content (K > 8) [10] is employed to deal with the problem that N_4 is higher than 1. This will be useful while dealing with the systems which has high silicon together with low boron content. As a result, by modifying Eq. (5), the R*′ value is calculated from Eq. (9):

$$R^{*\prime} = \begin{cases} \min\left(R\prime, \frac{K\prime}{16} + 0.5\right), & R\prime \le \frac{K\prime}{4} + 0.5, \ K\prime \le 8 \\ 0, & R\prime \in \left(\frac{K\prime}{4} + 0.5, \ K\prime + 2\right), \ K\prime \le 8 \\ R\prime & R\prime \le 1, \ K\prime > 8 \\ 0 & R\prime > 1, \ K\prime > 8 \end{cases} \tag{9}$$

According to recent NMR studies of boroaluminosilicate glasses [12], it is shown that sodium ions first convert aluminum from 5-6 to 4-coordination, then the remaining sodium ions convert boron from 3 to 4-coordination. Therefore, those compositions with higher Al_2O_3 than Na_2O will give a N_4 value which equal to 0. In addition, the smallest value of R*′, which may obtain a non-negative N_4 value, is equal to H' ($H' = \frac{Al_2O_3}{B_2O_3 + Al_2O_3}$). As a result, the effective R* value, which is called R^*_e, will be applied to calculate the A parameter of B-O pair instead of R^* in Eq. (4). This variable is the N_4 value (*i.e.* the fraction of four-coordinated boron) based on the Du and Stebbins model [8] and can be calculated through Eq. (10):

$$R^*_e = \begin{cases} \frac{\left[R^{*\prime} \times (Al_2O_3 + B_2O_3) - Al_2O_3\right]}{B_2O_3} & R \ge H, R^{*\prime} \ge H' \\ 0 & R \ge H, R^{*\prime} < H' \\ & R < H \end{cases} \tag{10}$$

The charge determination equations were also modified based on the Du and Stebbins model [8]. Furthermore, since sodium ions preferentially bond to aluminum and then boron, the amount of sodium which will affect boron charge is more accurately defined as:

$$R'_e = R' - H' = \frac{Na_2O - Al_2O_3}{B_2O_3 + Al_2O_3} \tag{11}$$

Notice that if the aluminum concentration is higher than that of sodium, this value will become 0. Therefore, the charge values of each element can be obtained by solving following two equations:

$$q'_B = -q'_O\left(C_6K'^2 + \sum_{i=1}^{5} C_iR'^i_e + C_0\right) \tag{12}$$

$$q'_i = q_i - N_B\frac{q'_B - q_B}{N_{Na} + N_{Al} + N_{Si} + N_O} \tag{13}$$

where, C_i ($i = 0,1,2,\ldots,6$) are empirical parameters which also are given in Table 1, N_i ($i = B,Na,Al,Si,O$) are atom numbers of each element, and q_i ($i = B,Na,Al,Si,O$) are the initial charge values from Guillot-Sator's paper [28]: $q_B = 1.4175$; $q_{Na} = 0.4725$; $q_{Al} = 1.4175$; $q_{Si} = 1.89$; $q_O = -0.945$.

2.2.2. Parameters for Al related pairs

The Al related potential parameters were initially fitted to the experimental structure information of various crystals by using GULP [33]. The parameters were refined by systematically adjusting the parameters to reproduce boron coordination and B-O bond distances in a series of sodium boroaluminosilicate glasses. This process involved simulations of large number of glass structures generated through the melt-and-quench process by using MD simulations. A weighted cost function was used to search for the optimal parameters. The final parameters for the sodium boroaluminosilicate glasses are shown in Table 2.

2.2.3. Simulation procedures for glass generation

The initial configurations with around 3000 atoms are randomly generated and overlapping atoms are pushed away from each other. These systems are first energy minimized at 0 K and then relaxed at 300 K for 60 ps. After the relaxation, these systems are melted at 6000 K for 60 ps, relaxed at 5000 K for 100 ps, and then cooled down to 300 K at a cooling rate of 5 K/ps. NPT ensemble relaxation is applied in order to obtain density information. All the final structures are relaxed using NVT and NVE ensembles in order to remove inner stress. The whole melting-quench process is carried by DL_POLY simulation package [34]. This process is shown in Fig. 1.

2.3. Structural analysis methods

Various structure analysis methods have been used to study both short-range and intermediate-range order structural information. The typical analysis for the short-range structure of glass are pair distributions functions (PDF), bond angle distribution functions (BAD) and coordination number analysis. As long-range order structure units don't exist in amorphous materials due to the non-periodicity, the intermediate-range structural order is another important information to study the glass which focus on the range of 5–10 Å. The medium-range order is usually characterized by using Q_n distribution and ring size distribution analysis.

2.3.1. Pair distributions functions

The PDF is basically the probability to find an atom at certain distance from the center atom. And the first peak gives the distance between two nearest atoms; therefore, the center position of the peak is considered as the bond distance of these two elements. The distributions of the interatomic distances of certain particle pairs in a given volume can be described through following equation:

$$g(r) = \frac{1}{4\pi r^2 \rho \delta r} \frac{\sum_{t=1}^{T}\sum_{j=1}^{N} \Delta N(r \to r+\delta r)}{N \times T} \quad (14)$$

where, $g(r)$ is the ratio between the local density and the bulk density of the system, ρ is the number density of the system, N is the total number of the atoms, and T is the total time-step of the calculation, δr is the integration step, and ΔN is the number of atoms in the region between r and $r + \delta r$. The structure factor of the system can be developed directly from $g(r)$ through a Fourier transform; therefore, the PDF plot can be compared with the experimental data obtained from the X-ray or neutron diffraction [35,36].

Table 2
Empirical potential parameters newly fitted for Al-O, Al-Al, Al-Na, Al-Si and Al-B pairs, as well as the parameters for Si-O, Na-O, O-O, Si-Si, Si-B, B-B, B-O pairs from Kieu et al. [24].

Pair	A_{ij} (eV)	ρ_{ij} (Å)	C_{ij} ($eV \cdot Å^6$)
Al-O	28,287.00	0.172	34.7600
Al-Al	351.94	0.360	0.0000
Al-Na	175.21	0.130	0.0000
Al-Si	646.67	0.120	0.0000
Al-B	137.58	0.479	0.0000
Si-O[a]	45,296.72	0.161	46.1395
Na-O[a]	120,360.22	0.170	0.0000
O-O[a]	9027.03	0.265	85.0321
Si-Si[a]	834.40	0.290	0.0000
Si-B[a]	337.70	0.290	0.0000
B-B[a]	121.10	0.350	0.0000
B-O[a,b]	$A_{B\text{-}O}$ (from Eq. (4))[a]	0.124[b]	35.0019[b]

[a] Pair parameters are from Kieu et al. [24].
[b] Updated B-O parameters from Kwon et al. [32].

2.3.2. Bond angle distribution

BAD is a method to analyze the distribution of the angle formed by an atom together with two nearby atoms. The formula to calculate BAD is shown by following equation [37]:

$$a_{ijk}(\theta) = \frac{1}{N_a} \sum_{l=1}^{N_a} \delta\left(\theta - (\theta_{ijk})_l\right) \quad (15)$$

where, θ_{ijk} is the angle formed by atom j and two closest atoms i and k. N_a is the number of all angles formed by atoms i, j (center atom) and k. The cutoff value is the first minimum point after the first intense peak on the pair distribution function plot. The cutoff values we chose for the Si-O, B-O and Al-O pairs are 2.25 Å, 1.85 Å and 2.25 Å, respectively.

2.3.3. Coordination number

Coordination number (CN) is the number of first nearest neighbor of the center atom i which can be obtained through counting the atom number of type j within the sphere of radium r_0. The r_0 value is the cutoff distance and is the same to the one in BAD calculation.

2.3.4. Q_n distribution and ring size distribution

Q_n distribution is a method to count the number of each Q_n species which is originally defined in a "quaternary" (four-coordinated) units. The Q_n is formed by the glass network former atom and the nearest neighbor oxygen atoms, while "n" stands for the number of surrounding bridging oxygen atoms connected to each center glass-former atom. However, for Al and B polyhedrons, there exist "trinary" (three-coordinated) or "quinary" (five-coordinated) units. In this paper, we use Q_n for all these three polyhedral units in the multicomponent glass systems, although other coordinated units may exist.

Table 1
Empirical parameters in Eqs. (4) and (12) based on Kieu et al. [24].

	0	1	2	3	4	5	6
a_i	180,390.53	47,166.67	−43,827.65	210,268.55	−52,520.42	−139,041.69	–
C_i	1.49643	0.29504	−0.2565	0.08721	−0.01323	0.00073	0.0 ($R'_e \le 0.5 + K'/16$)[a] 0.00315 ($R'_e > 0.5 + K'/16$)[a]

[a] The original value 0.55 was modified to $0.5 + K'/16$ based on the Dell and Bray model.

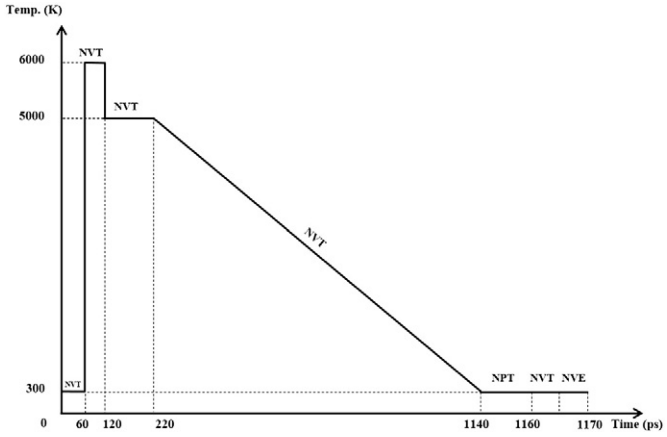

Fig. 1. Temperature profile of the MD simulation process of glass formation.

Another way to describe the intermediate-range structure is the ring size distribution analysis which gives the information of the glass network connectivity. Statistics of the ring size distributions represented by the number of polyhedrons that form the shortest path rings were calculated from the final configurations of the simulated glass structures.

2.4. Property calculations

2.4.1. Vibrational properties measurement

The total and partial vibrational density of states (VDOS) is a way to study the vibrational properties of glass systems [38]. To obtain the VDOS data, Fourier transformation is applied to velocity autocorrelation function through following equation:

$$g(\omega) = \frac{2}{\pi}\int_0^\infty C(t)\cos(\omega t)dt \tag{16}$$

where, ω is the frequency of vibration, C(t) is the velocity autocorrelation function, and t is the time. Partial VDOS is noted as $g_\alpha(\omega)$, where α is Al, B, Na, Si, O, $^{[3]}$B and $^{[4]}$B.Mechanical properties measurement

As a way to describe the stiffness of a material, the elastic constant matrix can be obtained by solving the relationship between stress and strain tensors through a deformation process. The notation can be expressed as:

$$S_{ij} = C_{ijkl} * \epsilon_{kl} \tag{17}$$

where, S_{ij} are symmetric stress tensor elements, C_{ijkl} are the fourth rank of the elastic constants, and ϵ_{kl} are the symmetric strain elements. The number of distinct constants reduced by symmetry is 21. Deformations of the stimulated configurations are applied from six directions (x, y, z, xy, yz, xz), and zero energy minimization method are employed to obtain the elastic constant matrix. The calculations were carried by using the LAMMPS [39] package. Elastic moduli are calculated using Hill's methods [40], in which the geometric average values of the Voigt and Reuss ones are used. The Voigt and Reuss bulk modulus values can be obtained through the Eqs. (18) and (19):

$$B_R = 1/(S_{11} + S_{22} + S_{33} + 2 \times (S_{31} + S_{21} + S_{32})) \tag{18}$$

$$B_V = \frac{1}{9} \times (C_{11} + C_{22} + C_{33} + 2 \times (C_{12} + C_{13} + C_{23}) \tag{19}$$

And the shear modulus ones are calculated by the following equations:

$$G_R = 15/(4 \times (S_{11} + S_{22} + S_{33}) - 4 \times (S_{12} + S_{23} + S_{31}) + 3 \times (S_{44} + S_{55} + S_{66})) \tag{20}$$

$$G_V = \frac{1}{15} \times ((C_{11} + C_{22} + C_{33}) - (C_{12} + C_{23} + C_{31}) + 3 \times (C_{44} + C_{55} + C_{66})) \tag{21}$$

The Young's modulus values were calculated based on the relationship between bulk modulus and shear modulus through Eq. (22):

$$E = \left(\frac{1}{3 \times G} + \frac{1}{9 \times K}\right)^{-1} \tag{22}$$

Six glasses from randomly generated initial structures were generated and used for the mechanical property calculations and structure analysis. Average values of the properties and standard deviations were obtained from these samples of each composition.

3. Results

3.1. Validation of the potential model and glass compositions for MD simulations

To validate the newly developed aluminum related parameters, two aluminum containing ternary crystal structures were calculated using the developed potentials and compared with experimental structure values (Table 3). The new potential parameters were able to reproduce both structure features such as bond lengths, the unit cell volume and densities of these crystals.

By using the developed potentials, a series of glass compositions of sodium boroaluminosilicate glasses have been studied in this work. These glasses have the same constant amount of sodium oxide but varying concentrations of the three glass formers with formula being $16Na_2O$-$4xAl_2O_3$-$4yB_2O_3$-4(21-x-y) SiO_2 (x = 1, 2, 3, 4 and y = 3, 4, 5, 6). These compositions (abbreviated as SBNA x-y glasses) are summarized in Table 4 and the atomic charges of the simulated glass compositions can be found in the Appendix (Table 1). This series of glass covers wide range of R_e^*: from 0.00 to 0.688; therefore, the applicability of the newly developed potential has been tested.

Snapshot of the simulated structures of SBNA 1-6 and SBNA 4-6 are shown in Fig. 2a and b, respectively. The structures are shown in ball-stick (atom and bonding) style (Fig. 2a and b, upper) and can be seen that the glass structures are made of silicon-oxygen tetrahedrons, aluminum-oxygen tetrahedrons, and boron-oxygen triangles and tetrahedrons, which is shown in the polyhedron representation (Fig. 2a and b, lower). With composition change, the percentage of these network

Table 3
Structural information of $NaAlSiO_4$ and $Na_2Al_2B_2O_7$ crystal structures.

Crystals	$NaAlSiO_4$		$Na_2Al_2B_2O_7$	
Source	Experiment [41]	Simulation	Experiment [42]	Simulation
a (Å)	9.995	9.892	4.811	5.097
b (Å)	9.995	9.892	4.811	5.097
c (Å)	24.797	25.081	15.278	15.128
α (°)	90.0	90.0	90.0	90.0
β (°)	90.0	90.0	90.0	90.0
γ (°)	120.0	120.0	120.0	120.0
$d_{Si\text{-}O}$ (Å)	1.618	1.601	–	–
$d_{Al\text{-}O}$ (Å)	1.741	1.735	1.693	1.746
$d_{Na\text{-}O}$ (Å)	2.562	2.651	2.668	2.761
$d_{B\text{-}O}$ (Å)	–	–	1.408	1.362
ρ (g/cm^3)	2.639	2.663	2.532	2.279

Table 4
Composition information of SBNA x-y glasses (16Na2O-4xAl2O3-4yB2O3-4(21-x-y) SiO2 (x = 1, 2, 3, 4 and y = 3, 4, 5, 6)) [43] with calculated N_4 and R_e^* values using our modified potential model.

SBNA x-y (in mol%)	Na_2O	Al_2O_3	B_2O_3	SiO_2	ρ (g/cm^3)	R_e	K_e	H_e	N_4^a	R_e^{*b}
SBNA 4-6	16	16	24	44	2.322	0.400	1.100	0.400	0.400	0.000
SBNA 3-6	16	12	24	48	2.342	0.444	1.333	0.333	0.444	0.167
SBNA 3-5	16	12	20	52	2.361	0.500	1.625	0.375	0.500	0.200
SBNA 3-4	16	12	16	56	2.395	0.571	2.000	0.429	0.571	0.250
SBNA 3-3	16	12	12	60	2.399	0.667	2.500	0.500	0.656	0.313
SBNA 2-6	16	8	24	52	2.375	0.500	1.625	0.250	0.500	0.333
SBNA 2-5	16	8	20	56	2.399	0.571	2.000	0.286	0.571	0.400
SBNA 2-4	16	8	16	60	2.429	0.667	2.500	0.333	0.656	0.484
SBNA 2-3	16	8	12	64	2.426	0.800	3.200	0.400	0.700	0.500
SBNA 1-6	16	4	24	56	2.419	0.571	2.000	0.143	0.571	0.500
SBNA 1-5	16	4	20	60	2.446	0.667	2.500	0.167	0.656	0.588
SBNA 1-4	16	4	16	64	2.471	0.800	3.200	0.200	0.700	0.625
SBNA 1-3	16	4	12	68	2.465	1.000	4.250	0.250	0.766	0.688

[a] The N_4 value is the theoretical percentage of four-coordinated boron and aluminum calculated by using Du and Stebbins's model [8].
[b] The R_e^* value calculated from Eq. (10), and is equal to the N_4 value in sodium boroaluminosilicate glasses based on Du and Stebbins's model [8].

building blocks and their connectivity changes, which will be further analyzed in the subsequent sections.

Structure information such as coordination number, Q_n species distributions, pair distribution functions and bond angle distribution functions of the simulated glasses have been analyzed. Additionally, medium range structures such as polyhedral connections and ring size distribution functions were also analyzed. Furthermore, the vibrational properties and mechanical properties of this series of glasses have been calculated and compared with previous simulation results and experimental data.

3.2. Short range structures

3.2.1. Pair distribution function analysis

In order to give an inside view of the structures, one common used distribution function, the total distribution function has a form of $4\pi\rho rg(r)$, has been studied. In order to keep it brief, the neutron broadened total distribution function and all the partial pair distributions are only plotted for the SBNA 3-3 glass as shown in Fig. 3.

As shown in Fig. 3, the first main peak of Si-O pair is located at around 1.61 Å which is typical for silicon oxygen tetrahedrons. The Si-O bond distance of 1.61 Å is in good agreement with previous MD simulation results for sodium aluminosilicate glasses [7,44] and experimental value from X-ray absorption spectra for silicate glasses [45].The first main peak of Al-O pair is centered at around 1.74 Å, which is in good agreement with previous MD simulation results for sodium aluminosilicate glasses [7], as well as the experimental data collected by XRD and EXAFS for both alumina and sodium aluminosilicate glasses [46–49]. Detailed comparison between our simulated results and experimental data for main bond distances of the SBNA3-3 glass is listed in Table 5. In general, the simulation results are in good agreement with the experimental values. No diffraction data for any of the compositions studied

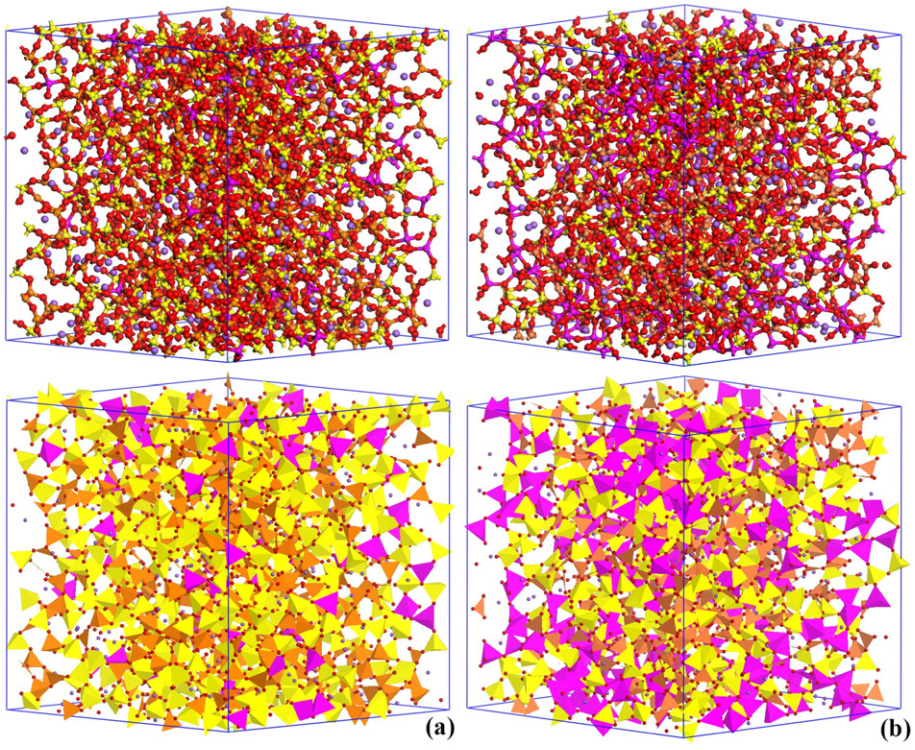

Fig. 2. Simulated structures in ball-stick (top) and polyhedron (bottom) styles for a) SBNA 1-6 and b) SBNA 4-6, respectively. Red balls are oxygen atoms and purple balls are sodium atoms. Magenta, yellow and orange polyhedrons are for Al, Si and B, respectively.

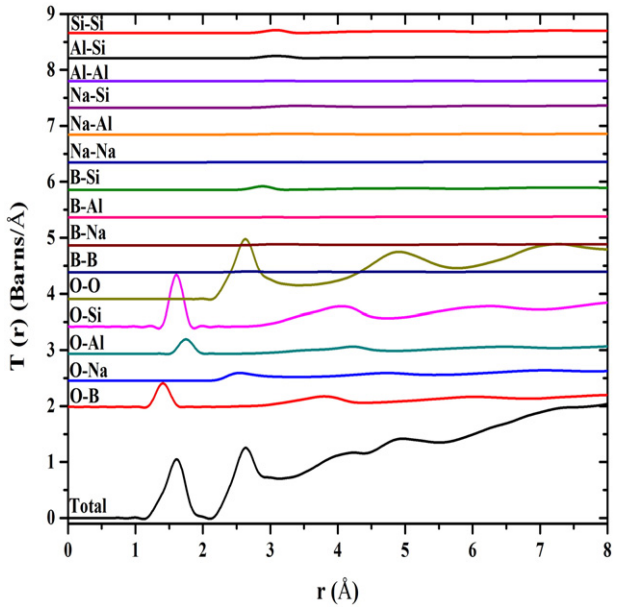

Fig. 3. Simulated neutron broadened total correlation and partial pair distribution function for the SBNA 3-3 structure.

in this work is available to further validate the potentials and this will be pursued in future work through collaboration with experimental groups.

The B-O pair distribution function plots (Fig. 4a) and b)) for two series of glasses have been obtained through Eq. (14). These two figures indicate that there are two main peaks in B-O PDF plot. For compositions with same alumina (Fig. 4a)), the first main peak locates at around 1.36 Å for the SBNA 3-6 composition, and it shifts to the right to around 1.37 Å for the SBNA 3-3 composition. The second main peak is centered at around 1.43 Å for SBNA 3-6 composition, and it shifts to higher r values of 1.44 Å for SBNA 3-3 composition. For those compositions with same boron oxide content (Fig. 4b)), the first main peak shifts from 1.36 for the SBNA 4-6 composition to 1.39 Å for the SBNA 1-6 composition, and the second one shifts from 1.43 for the SBNA 4-6 composition to 1.45 Å for the SBNA 1-6 composition. These two peaks are corresponding to three- and four-coordinated boron, respectively. The values of peak position are generally in good agreement with previous MD simulation results [23,24] and *ab initio* simulation results [27] for Na-B-Si ternary systems, as well as the experimental data [51] for vitreous boron oxide.

3.2.2. Glass former cation coordination numbers (CN)

The coordination number analysis of Al indicates that most of the aluminum ions are four-coordinated and form $[AlO_4]^-$ tetrahedral units (Fig. 5). This means most of the Al are converted from three/five coordinated to four coordinated, which is in good agreement with our presumption that modifier cation such as Na^+ first charge compensate $[AlO_4]^-$ units. The total percentage of the three and five coordinated aluminum is within 5%.

The Si coordination number is independent of R_e^* value change and stays at 4.0 in all the compositions. This result validates the silicon part of this potential that most of Si atoms are four coordinated in these glasses and form the tetrahedral units.

The average number of four coordinated boron as a function of effective R value is shown in Fig. 6. The values from simulations, together with those calculated from the Du and Stebbins for boroaluminosilicate glasses and the Yun, Dell and Bray model for borosilicate glasses, are compared in Fig. 6. It can be seen that simulation results follow well of the trend of the Du and Stebbins model, with the overall difference between the theoretical value (calculated by the D&B model and D&S model) and simulated results being <10%. We expected the presence of the irregular peak at $R_e^* = 0.5$, since there are two sets of data points which stand for two compositions with different R_e and K_e values as shown in Table 4. Coincidentally, the R_e^* values of these two compositions are calculated to be equal to each other by solving the Eqs. (9) and (10). As a result, two sets of the data points can be found at $R_e^* = 0.5$.

Further coordination analysis results are shown in Fig. 7. It is shown that the simulated value N_4' (percentage of four coordinated B and Al) follows the same trend of that calculated from the Du and Stebbins model. It is worth noting that the difference of N_4' between simulation and the model is larger for lower alumina content (small x value) (Fig. 7a–c)). And for the same amount of alumina, smaller y value or lower concentration of boron oxide also leads to larger differences of the N_4' values between simulation and the model. This is due to the presence of high N_4 differences of these compositions (shown in Fig. 6, R_e^* from 0.5 to 0.67). The general good agreement shows that the Du and Stebbins model of B and Al coordination change is well reproduced by the new developed potential parameters; therefore, together with other agreement with experiments, the developed potentials enable MD simulations of sodium boroaluminosilicate glass systems.

3.2.3. Q_n species distributions analysis

The Q_n (glass-former atoms connecting with *n* bridging oxygen, as discussed in Section 2) distribution provides information about how the network formers structural units connect with each other. Since SiO_2, B_2O_3 and Al_2O_3 are all considered as network formers, all the linkages connecting the structural units formed by these former cations are took into consideration. That is, the oxygen atoms in Si-O-Al, Si-O-B and B-O-Al are also counted as a bridging oxygen.

Q_n analysis of $[SiO_4]$ and $[AlO_n]$ polyhedrons are shown in Table 6 and Table 7, respectively. The results indicate that the preferred species for both Si and Al is Q_4, suggesting high connectivity of network formers. For those compositions with same Al content, the number of Q_4 specie increases while the B content is increasing; whereas, with same B content, this number increases while the Al content is decreasing. On the other hand, for those with same Si content, higher Al content gives lower Q_4 species of the $[SiO_4]$ units. Thus, additional B content increases the probability to form linkages between $[SiO_4]$ and other glass-former polyhedral units; whereas, Al decreases this probability. Similar results can be found in the polyhedral analysis section shown later. Additionally, with the same amount of alumina (x), when boron oxide (y) gradually replacing silica, the percentage of silicon Q_3 species decreases. In all compositions, Q_2 species is close to zero.

For $[AlO_n]$, there exists small amount of Q_3 and Q_5 with majority (over 95%) being Q_4. Increasing B content (at same Al content) generally increases the number of Q_4 units. That is, the B content increases the probability of forming linkages between $[AlO_n]$ and other glass-former polyhedral units. The existence of Q_5 units is caused by the presence of 5 coordinated Al in the glasses. It also suggests that most of aluminum ions are connected to the other network formers in the glass network.

The Q_n distribution of $[BO_3]$ and $[BO_4]$ units is shown in Table 8. The main species are Q_3 and Q_4 for $[BO_3]$ and $[BO_4]$ units, respectively. And the Q_1 and Q_2 species in $[BO_3]$ units and Q_3 species in $[BO_4]$ units are

Table 5
Comparisons of bond distance of different pairs between experimental data and simulation results. The simulated bond distances are obtained from the SBNA3-3 glasses (16% Na_2O, 12% Al_2O_3, 12%B_2O_3 and 60%SiO_2).

Bond length (Å)	This work	Previous simulation works	Experiment
Si-O	1.61	1.59–1.61 [44]	1.60–1.61 [45]
Al-O	1.74	1.74–1.75 [44], 1.74 [7], 1.78 [7]	1.81 [46], 1.83 [47], 1.91 [48], 1.77 [49]
Na-O	2.51	2.4–2.6 [44], 2.42 [7], 2.46 [7]	2.30–2.43 [45], 2.46–2.62 [50]

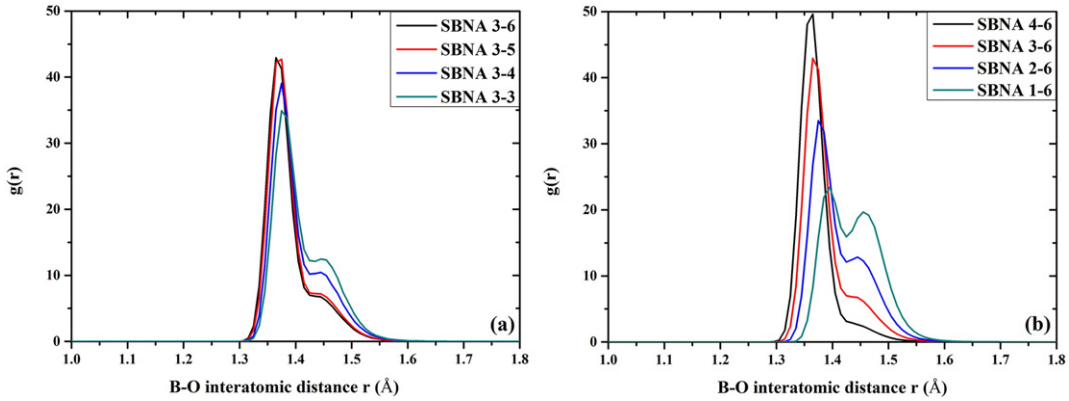

Fig. 4. Comparison of the main peak positions in B-O PDF plots for compositions with a) same Al_2O_3 content and b) same B_2O_3 content, respectively. The formula of these glasses is $16Na_2O$-$4xAl_2O_3$-$4yB_2O_3$-$4(21-x-y)$ SiO_2 (x = 1, 2, 3, 4 and y = 3, 4, 5, 6).

due to the association of non-bridging oxygen with boron polyhedral units. With the same soda and silica content (same x + y value), increasing B/Al ratio (x/y) leads to an increase of the amount of Q_3 specie of the three-coordinated boron, and the amount of Q_4 species of [BO_4] units gives similar trend.

With the same sodium and aluminum content (same x value), the increase of boron content (and decrease of silica content) results in an increase trend of the Q_3 species of three-coordinated boron (in Fig. 8a)) and Q_4 species of four-coordinated boron (in Fig. 8b)). These are due to the availability of more sodium ions to combine with [BO_3] and [BO_4] units, and less competition of aluminum/silicon for sodium and oxygen. In addition, with same sodium and boron content (same y value), decreasing aluminum content (and increasing silicon content) slightly increases the Q_3 species of three-coordinated boron, especially at high boron concentration ones. This indicates that silica has stronger network-forming ability than aluminum oxide in these glasses.

3.2.4. Bond angle distribution analysis (BAD)

The bond angle distributions have been analyzed for the angle inside a polyhedron, as well as the angle formed by two glass-former atoms in two different polyhedrons and an oxygen atom in the center (inter-polyhedron). Fig. 9a) shows the O-Si-O bond angle distribution and it indicates that the main peak of O-Si-O distribution is located at around 109.5°, which is close to the theoretical angle in a tetrahedral unit. The O-Al-O bond angle distribution gives a relatively broad peak, as compared to the main peak in O-Si-O distribution, and the main peak locates at around 107°. The results of O-Si-O and O-Al-O distributions are similar to previous simulation results in sodium aluminosilicate glasses [7]. The inter-polyhedron BAD as shown in Fig. 9b) gives general information about how the polyhedrons connect with each other, *e.g.*, the bond angle formed by two polyhedrons and center oxygen atoms. The main peak of the Al-O-Al bond angle centered at around 120°, and is in good agreement with previous simulation results for sodium aluminosilicate glasses[7]. The intensity of the peak for each bond angle also reflects the forming probability of the linkage between two polyhedrons. For example, the higher Al-O-Si peak intensity indicates the Al-O-Si linkage is the most favorable one in this glass.

The O-B-O bond angle distributions of two series of glass structures were analyzed and shown in Fig. 10 a) and b). Two main peaks in the BAD plots of O-B-O are observed: the first peak locates at around 109.5° which corresponds to the four coordinated boron and the second peak is centered at around 120.0° which corresponds to the three coordinated boron. While compositions varying, the positions of these two peaks stay the same; whereas, the intensity of the peaks changes since the number of three and four-coordinated boron changes in those compositions.

To give a detailed understanding about the contribution of each boron coordination to the PDF plot of B-O pair and BAD plot of O-B-O angle, both of the plots are decomposed into species of $^{[3]}$B and $^{[4]}$B

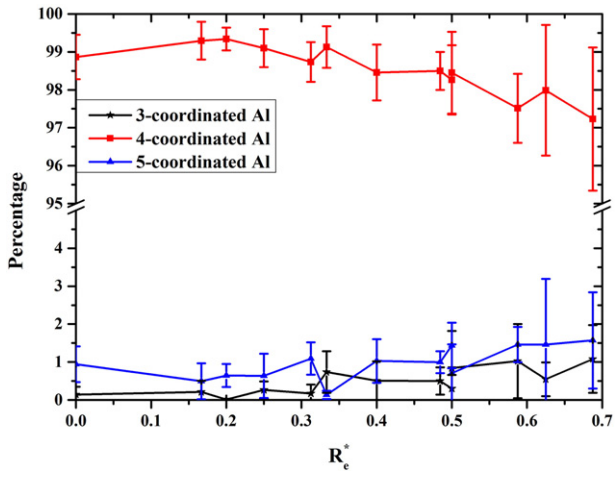

Fig. 5. Percentage of 3 to 5 coordinated aluminum as a function of R_e^* value. The R_e^* value is calculated by solving Eq. (10), and listed in Table 4. The formula of these glasses is $16Na_2O$-$4xAl_2O_3$-$4yB_2O_3$-$4(21-x-y)$ SiO_2 (x = 1, 2, 3, 4 and y = 3, 4, 5, 6).

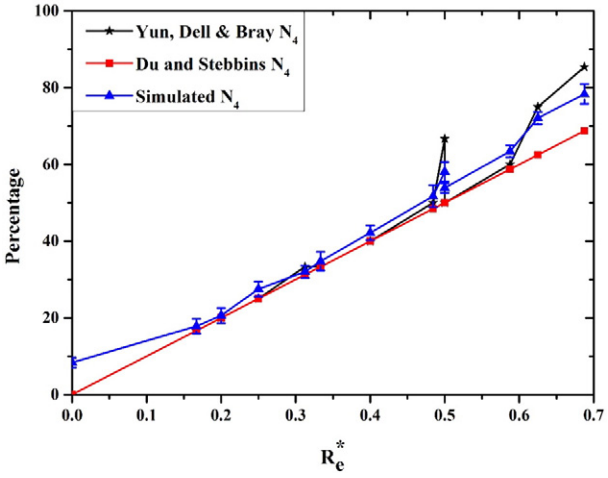

Fig. 6. Percentage of four-coordinated B as a function of R_e^* where N_4 is four coordinated B. The simulation results (in blue triangles) are compared with the ones from YDB model (in black stars, using $R_e^* = R' = (Na_2O - Al_2O_3)/B_2O_3$) and D&S model (in red squares). The R_e^* value is calculated by solving Eq. (10), and listed in Table 4.

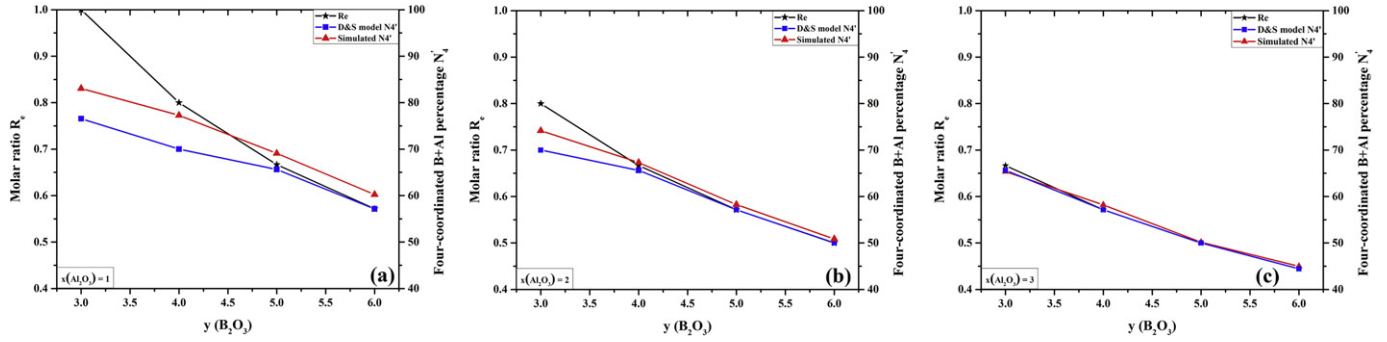

Fig. 7. Molar ratio R_e ($Na_2O/(B_2O_3+Al_2O_3)$), theoretical N'_4 (fraction of four –fold coordinated boron, calculated by Du and Stebbin model) and simulated N'_4 values as a function of y at different x value: x = 1, 2, 3 for a), b) and c), respectively. The N'_4 value is the total four-coordinated percentage of B and Al. The formula of these glasses is $16Na_2O$-$4xAl_2O_3$-$4yB_2O_3$-4(21-x-y) SiO_2 (x = 1, 2, 3, 4 and y = 3, 4, 5, 6).

ones (as shown in Fig. 11 a) and b), respectively). The PDF plot gives that the peak position of $^{[3]}$B-O is at 1.37 Å and the $^{[4]}$B-O one is at around 1.45 Å. The main peaks of O-$^{[3]}$B-O and O-$^{[4]}$B-O angle are centered at around 109.5° and 120.0°, respectively. The peak positions in the decomposed plots agrees well with previous simulation results and experimental data as we discussed above. Therefore, the existence of double main peaks in the B-O PDF and O-B-O PDF plots are results of three and four-coordinated boron.

3.2.5. Sodium local environments

The Na-O pair distribution function has been analyzed. The main peak in Na-O pair distribution function plot is located at the range from 2.50 Å to 2.52 Å. This is consistent with earlier simulations for Na_2O-B_2O_3-SiO_2 ternary systems with the same potentials [24]. It was shown that the Na-O distance increases from 2.29 Å to 2.62 Å when the role of the sodium atom changes from a network modifier to a charge compensator [24].

In order to monitor the structural role of sodium, the percentage of non-bridging oxygen and bridging oxygen as a function of $\frac{Na_2O-Al_2O_3}{B_2O_3}$ are shown in Fig. 12. For those oxygen around all the glass-former atoms (Fig. 12 a)), the majority species is bridging oxygen which is about 92–95%, while about 2–5% of non-bridging and tri-bridging oxygen exist. However, those values are quite steady while composition varies. Therefore, further analysis of the oxygen species around boron atoms is studied and plotted in Fig. 12 b). It can be seen that over 80% of oxygen ions play the role of bridging oxygen and only 5–20% of them are non-bridging oxygen. This explains why the average Na-O distance (around 2.5 Å) in the compositions studied in this work is toward the longer side (2.29 to 2.62 Å) [24] as majority of sodium ions play the role of charge compensators. The bridging oxygen percentage decreases while the excess sodium content (remaining amount after converting the Al from 5-6 to 4 coordinated) increases, when sodium ions began to play the role of breaking the network linkages by forming non-bridging oxygen ions. The percentage of non-bridging oxygen increases with $\frac{Na_2O-Al_2O_3}{B_2O_3}$ and shows the opposite trend of bridging oxygen. Furthermore, the percentage of non-bridging oxygen increases slightly faster with $\frac{Na_2O-Al_2O_3}{B_2O_3}$ at the low excess sodium content range than the high excess sodium one. This can be seen from the change of slope before and after 0.5 in Fig. 12b).

3.3. Network and medium range structures in the glasses

3.3.1. Polyhedral connection analysis

Polyhedral connectivity shows how the network former oxygen polyhedrons are connected hence provides additional information of the network structures. Experimentally, these can be revealed by analyzing multiple quantum ^{17}O NMR spectra [52]. For a glass with three glass formers, there would be six different linkages: [AO_n]-[AO_n], [AO_n]-[BO_m], [AO_n]-[CO_l], [BO_m]-[BO_m], [BO_m]-[CO_l] and [CO_l]-[CO_l], which we simplified as [A][A], [A][B], [A][C], [B][B], [B][C] and [C][C]). Important information on medium range structure, the preferences of these linkages, can impact glass properties. In order to characterize the connectivity, we defined P_{AB}, the probability of a polyhedral linkage [A][B], as the ratio between the normalized number of this linkage ([A][B]) and normalized number of the all possible linkages. The normalized value was calculated through dividing the number of the linkage by the number of each linking glass former cation. Hence, the probability of the linkage between glass former cation A and B, P_{AB}, is defined as,

$$P_{AB} = \frac{N_{[A][B]}/(N_A \times N_B)}{\sum_{i=A,B,C} \sum_{j=A,B,C} \left(\frac{n}{2} \times N_{[i][j]}/(N_i \times N_j)\right)} \quad (23)$$

where, i and j represent the glass-forming elements *A*, *B* or *C*. N_i and N_j

Table 6
Percentage of Q_n speciation of [SiO_4] units in SBNA x-y glasses ($16Na_2O$-$4xAl_2O_3$-$4yB_2O_3$-4(21-x-y) SiO_2 (x = 1, 2, 3, 4 and y = 3, 4, 5, 6)) with the standard deviation from six parallel tests.

Glass	x (Al_2O_3)	y (B_2O_3)	(21-x-y) SiO_2	Q_2	Q_3	Q_4
SBNA 4-6	4	6	11	0.1 ± 0.15	4.6 ± 0.69	95.3 ± 0.79
SBNA 3-6	3	6	12	0.0 ± 0.10	5.0 ± 1.11	95.0 ± 1.17
SBNA 3-5	3	5	13	0.2 ± 0.27	6.2 ± 1.09	93.6 ± 1.09
SBNA 3-4	3	4	14	0.2 ± 0.27	6.1 ± 0.64	93.7 ± 0.87
SBNA 3-3	3	3	15	0.0 ± 0.08	7.0 ± 0.47	93.0 ± 0.47
SBNA 2-6	2	6	13	0.0 ± 0.10	4.5 ± 1.30	95.5 ± 1.26
SBNA 2-5	2	5	14	0.1 ± 0.11	4.8 ± 0.98	95.1 ± 1.08
SBNA 2-4	2	4	15	0.1 ± 0.15	5.9 ± 1.13	94.0 ± 1.18
SBNA 2-3	2	3	16	0.2 ± 0.20	7.9 ± 0.52	91.9 ± 0.67
SBNA 1-6	1	6	14	0.1 ± 0.11	3.8 ± 0.69	96.1 ± 0.62
SBNA 1-5	1	5	15	0.2 ± 0.08	4.9 ± 0.33	94.9 ± 0.27
SBNA 1-4	1	4	16	0.0 ± 0.07	6.3 ± 0.35	93.7 ± 0.34
SBNA 1-3	1	3	17	0.3 ± 0.27	10.6 ± 0.70	89.1 ± 0.68

Table 7
Percentage of Q_n speciation of [AlO_n] units in SBNA x-y glasses ($16Na_2O$-$4xAl_2O_3$-$4yB_2O_3$-4(21-x-y) SiO_2 (x = 1, 2, 3, 4 and y = 3, 4, 5, 6)) with the standard deviation from six parallel tests.

Glass	x (Al_2O_3)	y (B_2O_3)	(21-x-y) SiO_2	Q_3	Q_4	Q_5
SBNA 4-6	4	6	11	1.8 ± 0.70	97.2 ± 0.76	1.0 ± 0.47
SBNA 3-6	3	6	12	2.0 ± 0.73	97.5 ± 0.80	0.5 ± 0.48
SBNA 3-5	3	5	13	1.7 ± 1.09	97.7 ± 1.06	0.6 ± 0.30
SBNA 3-4	3	4	14	2.2 ± 0.65	97.2 ± 0.81	0.6 ± 0.58
SBNA 3-3	3	3	15	2.1 ± 1.34	96.8 ± 1.63	1.1 ± 0.43
SBNA 2-6	2	6	13	1.9 ± 1.13	98.0 ± 1.18	0.1 ± 0.11
SBNA 2-5	2	5	14	2.3 ± 1.51	96.7 ± 1.84	1.0 ± 0.57
SBNA 2-4	2	4	15	1.2 ± 0.98	97.8 ± 1.05	1.0 ± 0.29
SBNA 2-3	2	3	16	1.9 ± 1.33	96.7 ± 1.65	1.4 ± 0.60
SBNA 1-6	1	6	14	1.6 ± 1.28	97.7 ± 1.12	0.7 ± 0.76
SBNA 1-5	1	5	15	3.0 ± 2.70	95.5 ± 2.41	1.5 ± 0.47
SBNA 1-4	1	4	16	2.7 ± 1.22	95.9 ± 1.22	1.4 ± 1.73
SBNA 1-3	1	3	17	2.7 ± 1.56	95.7 ± 2.75	1.6 ± 1.27

are number of each glass former cation, and $N_{[i][j]}$ is the number of the linkages of *i* and *j*. The parameter n equals to 2 if *i* is the same as *j*, or equals to 1 if *i* and *j* are different.

The preferences of each linkages in sodium boroaluminosilicate glasses, [SiO_4]-[SiO_4], [SiO_4]-[AlO_m], [SiO_4]-[BO_n], [BO_n][BO_n], [BO_n][AlO_m], and [AlO_m][AlO_m], have been calculated from the simulated glass configurations and plotted in Fig. 13a), b) and c) for compositions with x = 1, 2 and 3, respectively. As shown in all of these three figures, the P_{SiAl} value is the largest one and the P_{SiSi} value is the lowest one among the probabilities of three linkages which formed by silicon. This indicates that silicon prefer to form a [Si][Al] linkage rather than a [Si][B] linkage and the [Si][Si] linkage has the lowest probability. On the other hand, the probabilities of the three linkages formed by aluminum decreases in the order of [Si][Al], [Al][Al] and [B][Al]; this means that aluminum prefers forming linkage with silicon, than with itself, and the least with boron. Moreover, probabilities of the linkages formed by boron illustrate that the [Si][B] linkage is the most preferred one, [B][B] linkage is the second one and [B][Al] is the last one. Among all the linkages, [Si][Al] is the most probable one and [Al][B] is the least probable one. Furthermore, with the same sodium and aluminum contents (same x), increasing boron content gives lower P_{SiB} values; whereas, the P_{SiAl} value and P_{AlAl} one increase.

Moreover, the results show that the probabilities of the [Si][Al] linkages are around 0.33 for all the compositions. They are higher than the combination ones of the [Si][Si] and [Al][Al] linkages, which range from 0.1 to 0.2. This result suggests that [Si][Al] linkages are statistically more favorable as compared to the other two. This is in agreement with the "aluminum avoidance" or the Loewenstein's rule [53], and has been observed in both the previous theoretical calculations and NMR experiments [54,55].

Fig. 14 illustrates the probability of linkages for compositions with the same soda and silica contents: a) and b) are for x + y = 6 and x + y = 7, respectively. Again in these two series, [Si][Al] has the highest probability and [Al][B] has lowest probability. It is also shown that the probability of the [Si][Si], [Si][Al] and [B][B] linkages almost remain constant when alumina is increased and, at the same time, boron oxide is decreased. With decreasing boron oxide (and increasing alumina) concentrations, the probability of the [Si][B] linkages slightly increases while that of the [B][Al] linkages slightly decreases. Furthermore, increasing alumina (reducing boron oxide) leads to slight decrease of the probability of the [Al][Al] linkages.

3.3.2. Ring size distribution

Primitive ring size distributions of network forming glasses provide characteristic information of the medium range structures [17,56]. For silica, it has a symmetric distribution with a peak at around 6 membered rings. With the addition of modifiers such as sodium oxide, larger rings are created and, at the same time, the intensity of the major peak decreases [17]. The primitive ring size distributions of the sodium boroaluminosilicate glasses were analyzed and the results are shown in Fig. 15 a), b) and c). In these analyses, we considered the linkages of all the three glass formers. These were done through evaluating the Si-O, B-O and Al-O linkages with different cutoffs obtained from the first peak minimum from their corresponding pair distribution functions. The results show the ring size distributions of the mixed former glasses have generally symmetric distributions ranging from 3 to 13 membered rings, with a broad peak centered at around 7 membered rings. With the constant soda concentration (16 mol%) of the glasses studied, the change of the ring size distribution with composition is relatively small. There are, however, some noticeable trend exists. For glasses with same boron content (Fig. 15 a)), increasing alumina (decreasing silica) leads to a lower peak intensity and slightly broader peak, as well as small right shift of the peak position from 7 to 8–9. This indicates that silica is stronger glass-former comparing with

Table 8
Percentage of Q_n speciation of [BO_3] and [BO_4] units in SBNA x-y glasses ($16Na_2O$-$4xAl_2O_3$-$4yB_2O_3$-4(21-x-y) SiO_2 (x = 1, 2, 3, 4 and y = 3, 4, 5, 6)) with the standard deviation from six parallel tests.

Q_n of 3-coord. B	n = 1	n = 2	n = 3	Q_n of 4-coord. B	n = 3	n = 4
SBNA 4-6	0.1 ± 0.20	7.2 ± 1.61	92.7 ± 1.45	SBNA 4-6	1.5 ± 2.48	98.4 ± 2.55
SBNA 3-6	0.1 ± 0.13	6.7 ± 1.35	93.2 ± 1.45	SBNA 3-6	2.4 ± 1.87	97.4 ± 1.66
SBNA 3-5	0.1 ± 0.16	7.4 ± 1.39	92.5 ± 1.49	SBNA 3-5	1.0 ± 1.17	98.7 ± 1.13
SBNA 3-4	0.1 ± 0.21	8.6 ± 1.65	91.3 ± 1.79	SBNA 3-4	3.4 ± 1.32	96.6 ± 1.32
SBNA 3-3	0.2 ± 0.37	8.8 ± 1.52	91.0 ± 1.81	SBNA 3-3	5.0 ± 2.94	95.0 ± 2.94
SBNA 2-6	0.0 ± 0.00	5.4 ± 1.34	94.6 ± 1.34	SBNA 2-6	0.9 ± 1.01	99.0 ± 1.17
SBNA 2-5	0.2 ± 0.26	6.3 ± 1.47	93.5 ± 1.49	SBNA 2-5	2.6 ± 1.14	97.4 ± 1.13
SBNA 2-4	0.0 ± 0.00	6.1 ± 2.43	93.9 ± 2.43	SBNA 2-4	1.7 ± 1.76	98.3 ± 1.76
SBNA 2-3	0.0 ± 0.00	9.3 ± 1.69	90.7 ± 1.69	SBNA 2-3	5.2 ± 2.24	94.6 ± 2.39
SBNA 1-6	0.0 ± 0.00	3.6 ± 0.66	96.4 ± 0.66	SBNA 1-6	1.8 ± 1.03	98.1 ± 1.16
SBNA 1-5	0.0 ± 0.00	3.7 ± 0.68	96.3 ± 0.68	SBNA 1-5	2.7 ± 0.82	97.3 ± 0.82
SBNA 1-4	0.6 ± 0.71	5.7 ± 1.98	93.7 ± 2.05	SBNA 1-4	4.1 ± 1.11	95.7 ± 1.23
SBNA 1-3	0.0 ± 0.00	9.1 ± 4.48	90.9 ± 4.48	SBNA 1-3	3.3 ± 1.45	96.6 ± 1.47

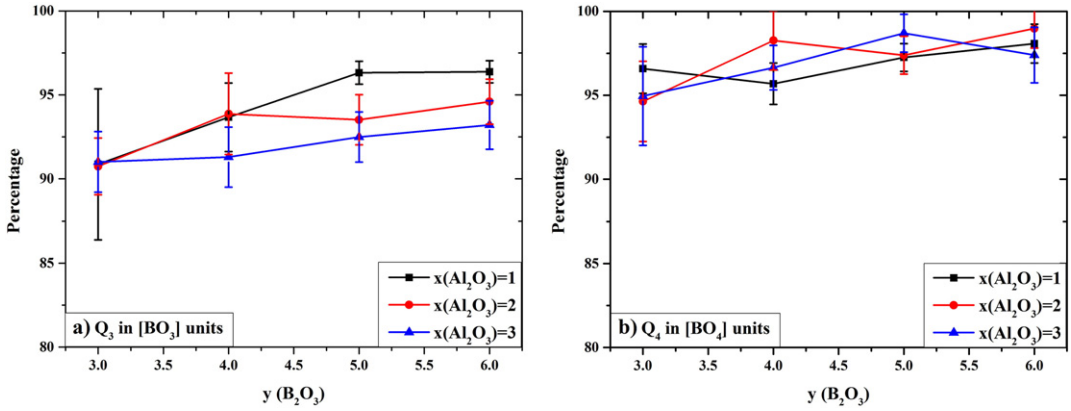

Fig. 8. Main Q_n species percentage *vs* boron concentration in a) [BO_3] and b) [BO_4] units at different x (Al_2O_3 content), respectively. The values in these plots are the averaged value of six parallel tests with the standard error bar, and the lines are the guide of eyes. The glass compositions are SBNA x-y: $16Na_2O$-$4xAl_2O_3$-$4yB_2O_3$-$4(21\text{-}x\text{-}y)$ SiO_2 (x = 1, 2, 3 and y = 3, 4, 5, 6).

alumina. For glasses with same silicon content (shown in Fig. 15 b)), the position and shape of the peak stay the same. For glasses with same alumina (shown in Fig. 15 c)), the peak intensity slightly decreases and the shape becomes border while increasing boron oxide content (decreasing silica); meanwhile, the peak position slightly shifts to the right. That is, the silica has the strongest network forming ability. In general, the ring size distribution show that all the three glass formers link together to form the three dimensional network similar to that of silica. This result agrees well with previous simulation results of sodium aluminosilicate glasses [7].

3.4. Physical properties of boroaluminosilicate glasses

3.4.1. Vibrational spectra

Vibrational density of states (VDOS) can be calculated from static or dynamic methods and present important information for infrared, Raman or inelastic neutron spectra interpretation. In this work, the VDOS was obtained from Fourier transformation of velocity autocorrelation function at 300 K. The VDOS plots for a series of glass compositions with the same sodium and silicon contents (*i.e.* the same x + y value) are shown in Fig. 16 (left side: a–f). The VDOS values are normalized to 1 for better comparison. The VDOS from classical MD simulations show similar total and partial spectra features as compared to *ab initio* simulations but the frequency from classical simulations systematically shifted to higher frequency. Similar results were found in earlier comparison of classical and *ab initio* vibrational spectra. In order to directly compare with previous *ab initio* results [27], the frequency from classical simulations is rescaled to 2/3 of the original values; moreover, the *ab initio* plots are also shown in Fig. 16 (right side: a) and b)) for better comparison. Four major peaks of the total VDOS are observed in the top plots (Fig. 16 left side: a), c) and e)): the first one is from 0 to 565 cm^{-1}, the second one is from 565 cm^{-1} to 948 cm^{-1}, the third one from 948 cm^{-1} to 1200 cm^{-1} and the forth one is from 1200 cm^{-1} to 1600 cm^{-1}. These peak regions are quite close to those values observe in sodium borosilicate system in previous simulation study[27] (as shown in Fig. 16 right side: a) and b)), which are 0–600 cm^{-1}, 600–820 cm^{-1}, 820–1200 cm^{-1} and 1200–1600 cm^{-1}, respectively. Detailed observation tells that the first peak is mainly contributed by sodium, oxygen, silicon and aluminum partial VDOS; whereas the boron one is relatively weak. The second peak mainly consists of the oxygen, silicon and boron partial VDOS, while the third and fourth peaks are mainly contributed by the oxygen and boron ones. This tells that the oxygen partial VDOS form the major frame of the total VDOS spectrum, while sodium one has no high frequency effect. The aluminum and silicon effects only exist in low and medium frequency regions; whereas, the boron one gives the effect during the whole range especially at medium and high frequency regions. These observations are generally in good agreement with previous simulation results for sodium borosilicate glass [27], 45S5 bioactive glass [57], and lithium silicate glass [38]. It's worth noting that the sodium partial VDOS peak is centered at 56 cm^{-1} which is lower than the value in previous *ab initio* and MD simulation results [27,57].

In order to understand the contributions of $^{[3]}$B and $^{[4]}$B units to the total boron VDOS, the decomposed boron partial VDOS plots for the same glasses are normalized to 1 and given in Fig. 16 left side: b), d) and f). The first main peak of $^{[3]}$B VDOS is from 0 to 581 cm^{-1}, and the second one is from 1200 to 1600 cm^{-1}. This indicates the low and high frequency effects of boron VDOS are mainly caused by the $^{[3]}$B units. On the other hand, the main peak of $^{[4]}$B VDOS is a boarder peak ranging from 500 cm^{-1} to 1600 cm^{-1}, and it corresponds to the peak

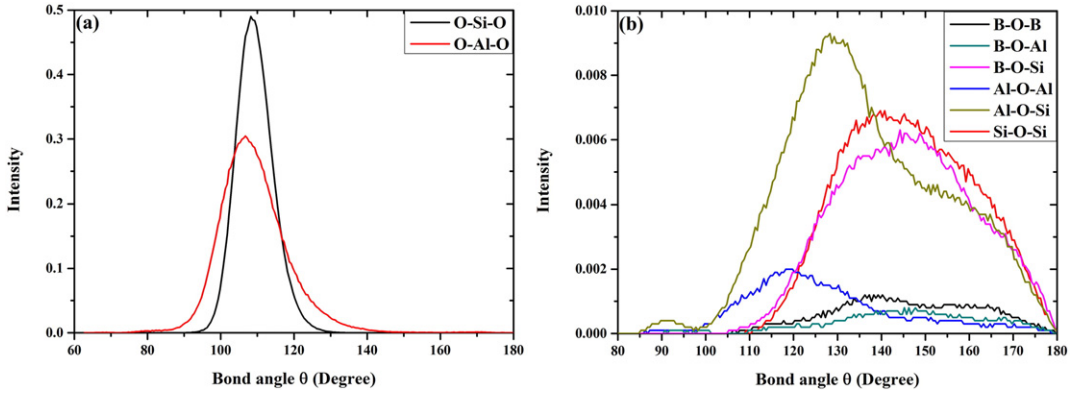

Fig. 9. a) Bond angle distributions and b) inter-polyhedron bond angle distributions plots for SBNA 3-3 structure. The glass compositions are SBNA x-y: $16Na_2O$-$4xAl_2O_3$-$4yB_2O_3$-$4(21\text{-}x\text{-}y)$ SiO_2 (x = 1, 2, 3 and y = 3, 4, 5, 6).

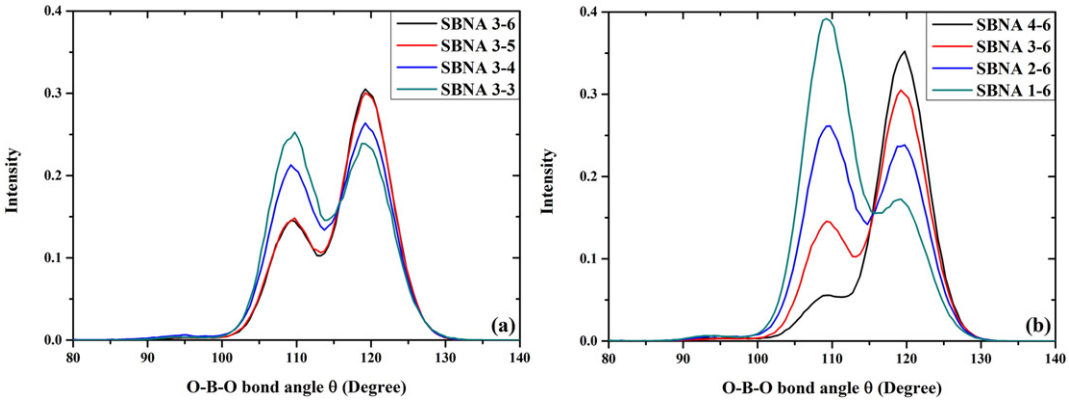

Fig. 10. O—B—O bond angle distribution of sodium boroaluminosilicate glasses with a) same Al_2O_3 content and b) same B_2O_3 content. The glass compositions are SBNA x-y: $16Na_2O$-$4xAl_2O_3$-$4yB_2O_3$-$4(21-x-y)$ SiO_2 (x = 1, 2, 3 and y = 3, 4, 5, 6).

in medium frequency range of the total boron VDOS. The increase of the fraction of four-coordinated boron enhances the intensity of the main peak of $^{[4]}$B VDOS and that of $^{[3]}$B VDOS follows the opposite trend. As a result, the VDOS plots we calculated have the trend generally in good agreement with previous simulation results [27,38,57], but some of the peak positions diverge from those in *ab initio* calculations [27] for ternary systems which may be caused by additional aluminum content.

3.4.2. Mechanical properties

Mechanical properties were calculated by applying strains in six different directions. By using the finite difference method, the elastic constants were first obtained and mechanical properties such as bulk modulus, shear modulus, Young's modulus were then calculated by using Hill's method [40] (Eqs. (18)–(22)). The comparison between the experimental values [43] and the calculated values are shown in Fig. 17. It is worth mentioning that there is an outlier of the bulk modulus values which can be due to input of Poisson's ratio in the calculation. The shear and Young's moduli were from experiments and bulk moduli were calculated with the two moduli together with the Poisson's ratio. As shown in the figure, the mechanical property values of our simulated glass structures reproduced well of the trend of the experimental values as a function of R_e^* for all four series with the different x (Al_2O_3 mol%) values, with the differences between the simulated and experimental values being within 10GPa for most compositions. The difference is larger for high R_e^* range with compositions of lower x values (*i.e.* lower alumina and hence higher boron oxide concentrations) which can be explained by the higher N_4 values of boron as shown in Fig. 6. Furthermore, with same sodium and silicon content (same x + y), decreasing alumina (increasing boron oxide content) increases all three moduli. Moreover, with the same sodium and boron content (same y), increasing aluminum (and hence decreasing silica content) also reduces the mechanical moduli of these glass systems. Based on the experimental data and most of our simulation results (mainly the series of x = 2 and x = 3), with the same sodium and aluminum content (same x), increasing boron content (and decreasing silica content) lowers the moduli. As a result, the order of contribution to mechanical properties among the three glass formers is: silica > boron oxide > alumina.

4. Discussions

4.1. Validation and testing of the borosilicate and boroaluminosilicate potentials

In order to validate the original potentials by Kieu et al. [23] for borosilicate glasses, we have simulated sodium borosilicate glasses in wide composition ranges using MD simulations. The limitation of the original potential set was also investigated by analyzing the composition dependent of the potential parameters.

One of the two characters of the potential for boron containing glasses is the composition dependent A parameters (Eq. (4)) for B-O interactions [24]. Careful examination of the potential parameters found that there are certain composition regions, mainly those with high silica concentration, that the original potential failed to provide reasonable boron coordination. This is mainly due to the unreasonable "A" parameter for the B-O pair interactions (denoted as $A_{B\text{-}O}$). This is shown in Fig. 18 where $A_{B\text{-}O}$ is plotted against R*. The $A_{B\text{-}O}$ value first increases slowly with R*, based on the concept that $A_{B\text{-}O}$ is composition dependent to correctly reproduce the coordination number change of B. When the R* value is larger than 0.78, the $A_{B\text{-}O}$ value begins to decrease which leads to slightly shorter B-O bond distance. This situation becomes severe when the R* value is larger than 0.9. When the R* value is larger

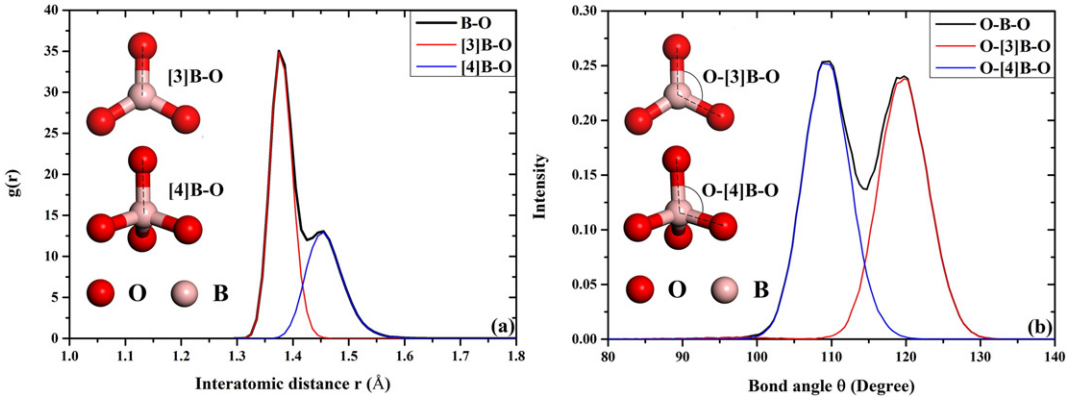

Fig. 11. Decomposed plots of a) PDF of B-O pair and b) BAD of O-B-O angle in SBNA 3-3 glasses, respectively.

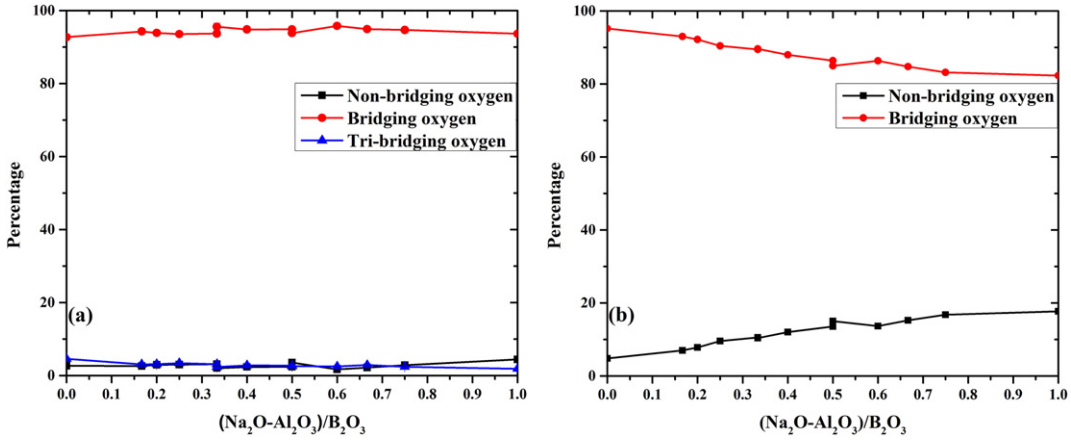

Fig. 12. Percentage of oxygen species around a) all the glass-former atoms and b) boron atoms as a function of $(Na_2O\text{-}Al_2O_3)/B_2O_3$, respectively. The two data points at same value of x axis correspond to two compositions with same excess sodium content ($Na_2O - Al_2O_3/B_2O_3$).

than 1.2, the $A_{B\text{-}O}$ becomes extremely small and even negative once the R* value is larger than 1.27. These led to unphysical B-O bonding and coordination in certain composition ranges. This limits MD simulations of certain compositions with high silica and high soda concentrations.

To describe the conversion of boron coordination between three-fold (N_3) and four-fold (N_4), we tested two series of compositions (for $[SiO_2]/[B_2O_3] = 1$ and 2, respectively) and marked them as the dots shown in the composition triangle. The details of the compositions can be found in the Appendix (Table 2). The glass structures were generated using the procedures described in Section 2. Each composition had around 3000 atoms. The simulated structures showed compositional dependence of boron coordination with distributions of 3 and 4 coordinated B. The values of averaged B coordination numbers and those from the Yun, Dell and Bray [10,11] model are also listed in the Appendix Table 2. The results show that most differences of boron coordination are within 4% with the model. Base on the YDB model, the R_{max}, which numerically equals to $\frac{K}{16} + 0.5$, is the R value at which N_4 reaches a plateau. For R below R_{max}, the simulation properly reproduced the linear relationship of $^{[4]}B$ with R. There is, however, a difference of the exact location of the R_{max} and existence of some discrepancy between the simulated one and the one from model for high R values.

Together with favorable comparison of mechanical properties and other structural features such as B-O and Si-O distances, it can be concluded that the Kieu et al. [23] potential set can generate reasonable glass structures of the borosilicate glasses in wide composition ranges. It is, however, worth noting that in some compositions, especially high silica compositions regions, the potential would not be able to correctly describe boron environment due to unphysical A values of B-O short range interactions. In addition, the difference of theoretical and simulated percentage of $^{[4]}B$ is found to be larger at high R (*i.e.* Na_2O/B_2O_3 ratio) values than lower R ones. Since the development of potentials for boroaluminosilicate glasses of this work is based on the borosilicate potentials by Kieu et al. [24], the newly developed potentials would inherit some of these limitations. As the boroaluminosilicate glass compositions studied in this paper are away from these regions so the validity of the results is not influenced. Nevertheless, these critical analyses also point out directions of improvement of the current potential system, which we are currently working on and will be reported in future publications.

4.2. Comparisons of theoretical models: Dell and Bray model, Du and Stebbins model and two state model

The structures of sodium boroaluminosilicate glasses are complicated due to the interaction of the structural units generated by the three glass network formers. One major difficulty for MD simulations to reproduce reasonable structures of this kind of glasses is lacking of parameters to describe the three to four coordination conversion of boron (N_4). For the ternary systems (alkali borosilicate glass), Yun, Dell and Bray [10,11] proposed a model to estimate the four-coordinated boron percentage based on NMR studies. Kieu et al. [24], therefore, developed a composition-dependent empirical potential to simulate the ternary systems by fitting parameters based on the YDB model. However, the situation becomes even more complicated when come to the quaternary systems, since increasing aluminum content induces the competition

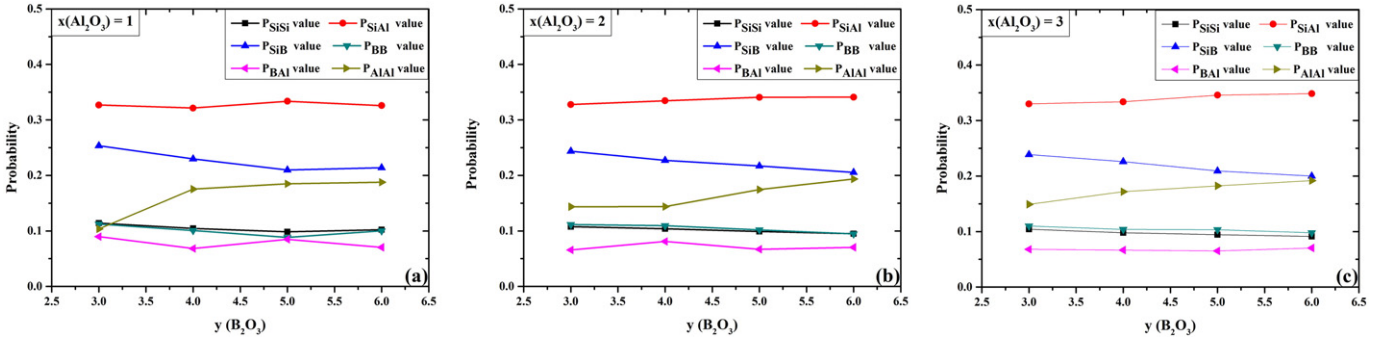

Fig. 13. Preferences of [Si][Si], [Si][Al], [Si][B], [B][B], [B][Al] and [Al][Al] linkages for a) x = 1, b) x = 2 and c) x = 3, respectively. The formula of these glasses is $16Na_2O\text{-}4xAl_2O_3\text{-}4yB_2O_3\text{-}4(21\text{-}x\text{-}y)\ SiO_2$ (x = 1, 2, 3, 4 and y = 3, 4, 5, 6).

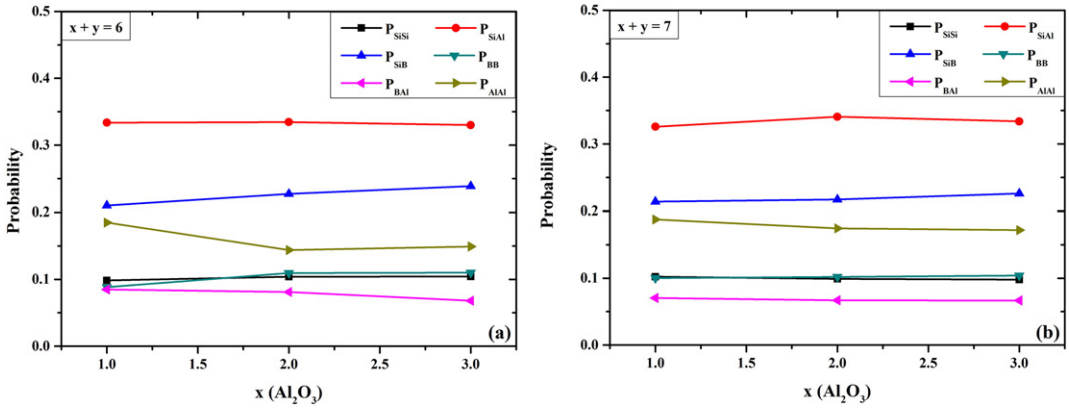

Fig. 14. Preferences of [Si][Si], [Si][Al], [Si][B], [B][B], [B][Al] and [Al][Al] linkages for compositions with two different values of Si content: a) for x + y = 6 ones and b) for x + y = 7 ones, respectively. The formula of the glasses is $16Na_2O$-$4xAl_2O_3$-$4yB_2O_3$-4(21-x-y) SiO_2 (x = 1, 2, 3, 4 and y = 3, 4, 5, 6).

between boron and aluminum for oxygen and charge compensating sodium ions. El Damrawi and Gohar's [12] replaced R in ternary system by $R' = (Na_2O - Al_2O_3)/B_2O_3$ in the quaternary systems, and noticed that the four-coordinated boron percentage in the quaternary systems at low sodium concentration is much lower than the one in the ternary systems. Du and Stebbins [8] then proposed a modified YDB model by treating aluminum as boron since they have similar network mixing behavior. Most recently, Smedskjaer et al. [6] proposed a temperature-dependent constraint model, two-state model, to calculate the four-coordinated boron percentage of sodium borosilicate glasses. In order to handle the competition between boron coordination conversion and non-bridging oxygen formation, the glass transition temperature and the enthalpy difference between the two states are took into consideration. This model generally gives better estimation of the N_4 value comparing with the YDB model and D&S model. However, experimental measurement of the T_g makes this model a little bit complicated, since the rest two model can be calculated directly for certain compositions without any other information.

4.3. Relationship between glass composition and properties

For sodium aluminosilicate glasses, one interesting phenomenon is the so-called "aluminum avoidance", or, the Loewenstein's rule [53]. This can be expressed that the linkage Al-O-Si is more favorable than the combination of Al-O-Al and Si-O-Si linkages. In our simulations, we calculated the normalized probabilities of forming these three linkages in sodium boroaluminosilicate glasses (as shown in Fig. 13 and Fig. 14), and the simulation results show that the probability of forming Al-O-Si linkages is much higher than the combination of the Al-O-Al and Si-O-Si, with B-O-Al having the lowest probability of linkages. Thus our results support the "aluminum avoidance" phenomenon exists in both ternary and quaternary systems.

It was found that many structural features and properties of the boroaluminosilicate glasses depend on the glass composition and these dependences can be correlated to key structure features such as the percentage of silica or the percentage of four-fold coordinated boron. This is not surprising as silica is the strongest network-former among Al_2O_3, B_2O_3 and SiO_2. As we have shown earlier, addition of small amount of silica can covert aluminum from 5- and 6-fold coordination to 4-fold coordination and make them play a glass former role in rare earth aluminosilicate glasses [58]. Furthermore, four-fold coordinated boron also have a strong effect on the properties. For example, the elastic and bulk moduli of several series of the glasses were found to increase with the percentage of $^{[4]}B$ (as shown in Fig. 17).

5. Conclusions

In this paper, a set of self-consistent, compositional dependent partial charge potentials have been developed for atomistic simulations of multi-component oxide glasses with three common glass formers: SiO_2, B_2O_3 and Al_2O_3 based on the framework of the borosilicate potential proposed by Kieu et al. [24]. The aluminum related potential parameters were introduced based on the current understanding of the glass chemistry and the parameters obtained by fitting to structures and properties of crystalline and model glass compositions. The newly developed potentials were then used to study several series of sodium boroaluminosilicate glasses $16Na_2O$-$4xAl_2O_3$-$4yB_2O_3$-4(21-x-y) SiO_2 (x = 1, 2, 3, 4 and y = 3, 4, 5, 6) with varying ratios of glass formers but constant modifier concentrations. Careful comparison of both the short and medium range structures of these glasses were performed with available experimental data as well *ab initio* simulation results. It

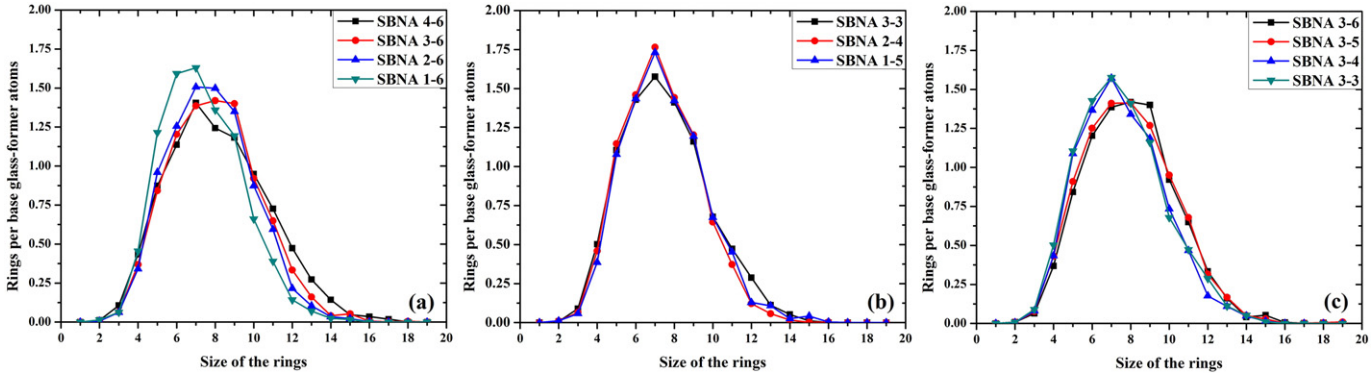

Fig. 15. Primitive ring size distribution of sodium boroaluminosilicate glasses for compositions with a) same boron oxide, b) same silica and c) same alumina contents, respectively. The rings were calculated assuming linkages of all glass formers: SiO_2, B_2O_3, and Al_2O_3. The formula of the glasses is $16Na_2O$-$4xAl_2O_3$-$4yB_2O_3$-4(21-x-y) SiO_2 (x = 1, 2, 3, 4 and y = 3, 4, 5, 6).

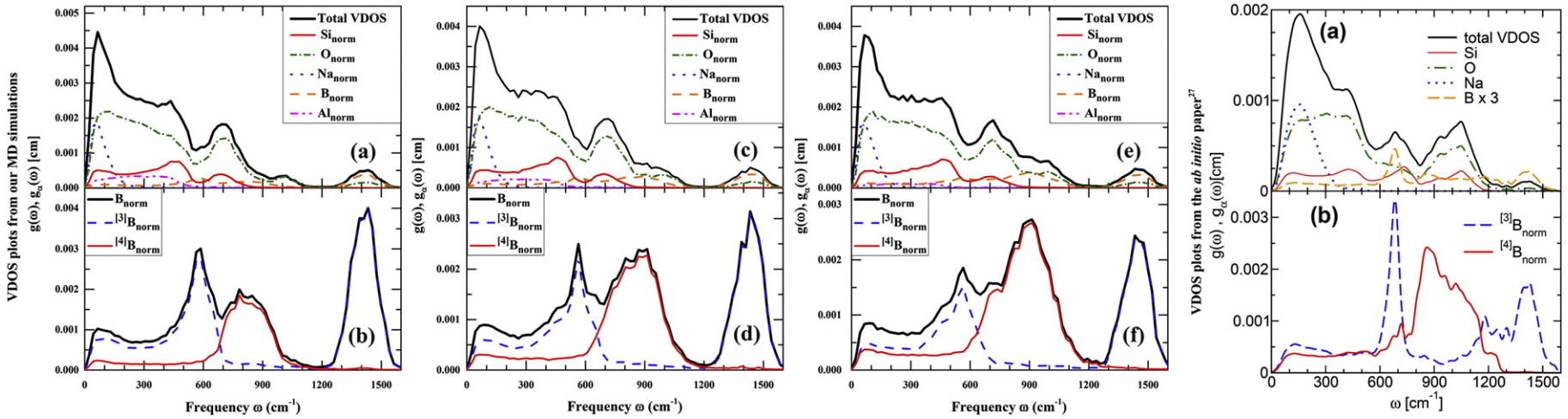

Fig. 16. Vibrational density of states (VDOS) plots: Left side a–f are from our MD simulations, and the right side a–b is from the *ab initio* calculations [27] for comparison. For our MD ones, from left to right are for compositions with same silicon content: SBNA3-4, SBNA2-5 and SBNA1-6, respectively. The top plots (a, c and e) are total and partial VDOS of the glasses with the values normalized to 1 for better comparison. The bottom ones (b, d and f) are normalized partial VDOS of trigonal $^{[3]}B$ and tetragonal $^{[4]}B$ atoms together with the normalized partial boron VDOS. The formula of the glasses is $16Na_2O\text{-}4xAl_2O_3\text{-}4yB_2O_3\text{-}4(21\text{-}x\text{-}y)\ SiO_2$ (x = 1, 2, 3, 4 and y = 3, 4, 5, 6).

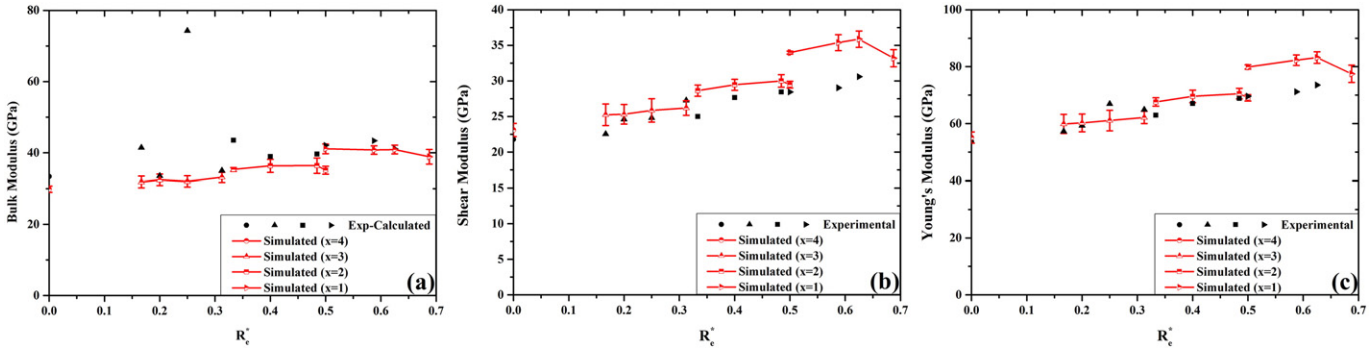

Fig. 17. Comparison of calculated and experimental mechanical properties. (a) Bulk modulus, b) shear modulus and c) Young's modulus comparisons between the experimental data and simulated results, respectively. Error bar for simulations were calculated from standard deviations of six glasses simulated. Experimental shear modulus and Young's modulus values are from Gan et al. [43], while the bulk modulus are calculated using Eq. (22). The R_e^* value is calculated through Eq. (10), and listed in Table 4.

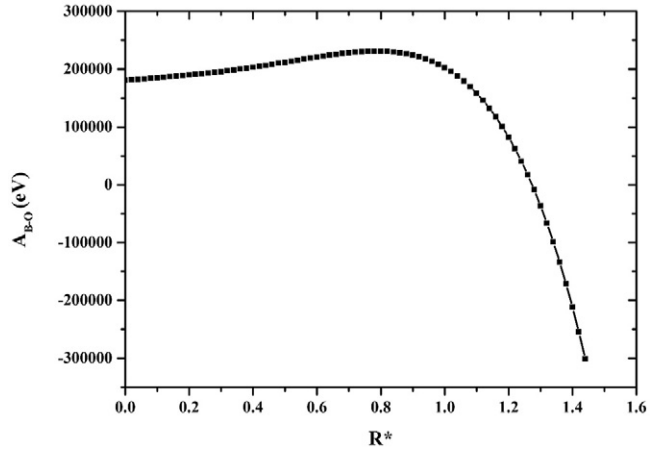

Fig. 18. $A_{B\text{-}O}$ as a function of R* curve for borosilicate glasses obtained by solving Eq. (4).

is shown this set of potential set can reproduce the coordination change of aluminum and boron as a function of composition. In addition, the mechanical properties are also in good agreement with experimental values, and the calculated vibrational spectra also agree well with previous *ab initio* simulation results. It is concluded that the developed composition-dependent partial charge pair-wise potentials are capable to deal with complex structure changes of boroaluminosilicate glasses and describe the properties. Importantly, these potentials are computationally efficient and can be employed to study simulation of large systems (*e.g.* millions of atoms) and obtain long time (*e.g.* nano to micro seconds) properties of glass, glass melts and glass formation/transition behaviors, which *ab initio* calculations cannot handle easily. Lastly, the limitation of these potential was also discussed and directions of future improvement pointed out.

Acknowledgement

This work was supported by DOE NEUP (project # DE-NE000748) and NSF DMR Ceramics program (project # 1508001).

Appendix A

The atomic charges of sodium boroaluminosilicate glasses calculated from the current model is shown in Table 1. The compositions of the sodium borosilicate glasses simulated and comparison of the simulated percentage of four coordinated B and those from the Yun, Dell and Bray model [10,11] are listed in Table 2.

The pair distribution function plots and the cutoffs for Si-O, B-O and Al-O pairs in all simulation SBNA compositions as well as the chosen cutoff values are shown in Fig. 1.

Table 1
Atomic charges for sodium boroaluminosilicate glasses $16Na_2O$-$4xAl_2O_3$-$4yB_2O_3$-$4(21\text{-}x\text{-}y)$ SiO_2 (x = 1, 2, 3, 4 and y = 3, 4, 5, 6).

SBNA x-y	Si	B	Al	O	Na
SBNA 4-6	1.890626	1.413190	1.418126	−0.94437	0.473126
SBNA 3-6	1.885460	1.448099	1.412960	−0.94954	0.467960
SBNA 3-5	1.885762	1.451831	1.413262	−0.94924	0.468262
SBNA 3-4	1.886289	1.455131	1.413789	−0.94871	0.468789
SBNA 3-3	1.886955	1.458586	1.414455	−0.94804	0.469455
SBNA 2-6	1.879532	1.486120	1.407032	−0.95547	0.462032
SBNA 2-5	1.880749	1.490579	1.408249	−0.95425	0.463249
SBNA 2-4	1.882115	1.495406	1.409615	−0.95288	0.464615
SBNA 2-3	1.883536	1.502450	1.411036	−0.95146	0.466036
SBNA 1-6	1.873734	1.521426	1.401234	−0.96127	0.456234
SBNA 1-5	1.876112	1.524443	1.403612	−0.95889	0.458612
SBNA 1-4	1.878437	1.528907	1.405937	−0.95656	0.460937
SBNA 1-3	1.881038	1.532320	1.408538	−0.95396	0.463538

Table 2
Sodium borate glass compositions and comparison of average B coordination number from simulation and those from Dell-Bray model prediction. The "SBN-a" and "SBN-b" glasses are with K = 1 and K = 2, respectively.

					Average B coord. number		
	SiO_2 mol%	Na_2O mol%	B_2O_3 mol%	ρ (g/cm^3)	This (MD)	YDB model	Diff. (%)
SBN-a0	69.5	0.0	30.5	2.042	3.03	3.00	−0.99
SBN-a3	48.0	3.3	48.7	2.069	3.07	3.07	0.00
SBN-a10	44.4	9.6	46.1	2.181	3.22	3.21	−0.31
SBN-a12	59.7	12.2	28.1	2.370	3.41	3.44	0.88
SBN-a13	75.0	12.5	12.5	2.780	3.91	3.87	−1.02
SBN-a14	67.7	14.2	18.1	2.450	3.75	3.73	−0.53
SBN-a30	55.3	30.0	14.7	2.540	3.58	3.62	1.12
SBN-b20	45.5	9.1	45.5	2.161	3.19	3.20	0.31
SBN-b30	43.5	13.0	43.5	2.261	3.30	3.30	0.00
SBN-b40	41.7	16.7	41.7	2.350	3.43	3.40	−0.87
SBN-b50	40.0	20.0	40.0	2.429	3.56	3.50	−1.69
SBN-b60	38.5	23.1	38.5	2.480	3.66	3.56	−2.73
SBN-b70	37.0	25.9	37.0	2.499	3.71	3.56	−4.04
SBN-b90	34.5	31.0	34.5	2.518	3.50	3.53	0.86
SBN-b100	33.3	33.3	33.3	2.536	3.54	3.50	−1.13
SBN-b120	31.3	37.5	31.3	2.561	3.57	3.45	−3.36
SBN-b130	30.3	39.4	30.3	2.560	3.56	3.43	−3.65
SBN-c10	64.5	3.2	32.3	2.098	3.09	3.10	0.32
SBN-c20	62.5	6.3	31.3	2.147	3.17	3.20	0.95
SBN-c30	60.6	9.1	30.3	2.237	3.27	3.30	0.92
SBN-c40	58.8	11.8	29.4	2.308	3.39	3.40	0.29
SBN-c50	57.1	14.3	28.6	2.396	3.52	3.50	−0.57
SBN-c60	55.6	16.7	27.8	2.450	3.65	3.60	−1.37
SBN-c70	54.1	18.9	27.0	2.480	3.71	3.63	−2.16
SBN-c90	51.3	23.1	25.6	2.517	3.80	3.63	−4.47
SBN-c100	50.0	25.0	25.0	2.530	3.83	3.63	−5.22
SBN-c110	48.8	26.8	24.4	2.518	3.52	3.60	2.27
SBN-c120	47.6	28.6	23.8	2.521	3.53	3.58	1.42
SBN-c130	46.5	30.2	23.3	2.526	3.56	3.56	0.00

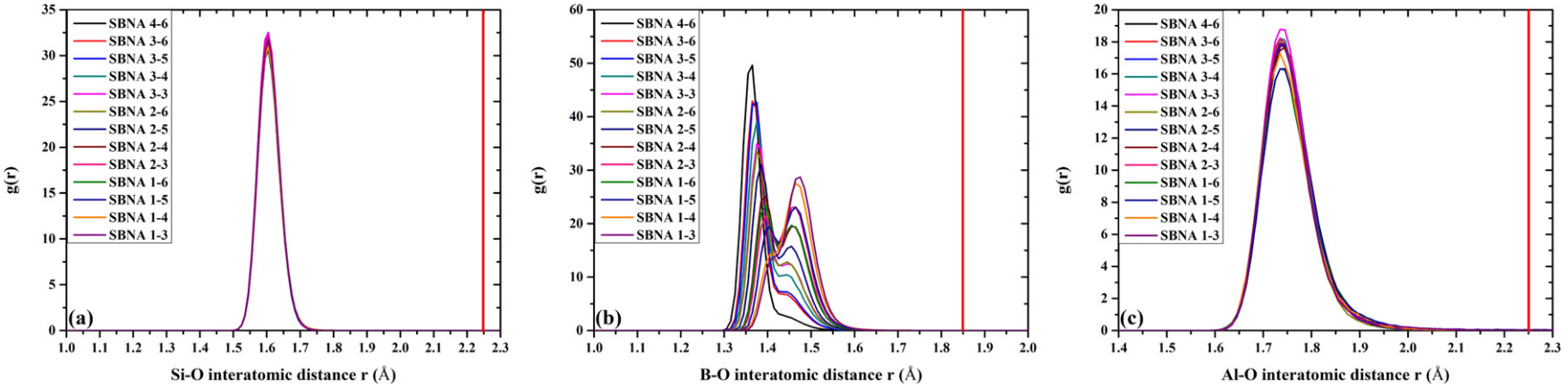

Fig. 1. Pair distribution function plots and the cutoffs for a) Si-O, b) B-O and c) Al-O pairs in all the SBNA compositions, respectively. The position of the red vertical line is the cutoff value we chose for each pair.

References

[1] H.G. Pfaender, Schott Guide to Glass, Springer Science & Business Media, 2012.
[2] G.H. Beall, D.A. Duke, D.R. Uhlmann, N.J. Kreidl, Acad. Press. New York, 1, 1983 403.
[3] L.D. Pye, V.D. Fréchette, N.J. Kreidl, Borate Glasses: Structure, Properties, Applications, Springer Science & Business Media, 2012.
[4] M.M. Smedskjaer, R.E. Youngman, J.C. Mauro, Appl. Phys. A Mater. Sci. Process. 116 (2014) 491.
[5] J. Du, Mol. Dyn. Simulations Disord. Mater, Springer, 2015 157–180.
[6] M.M. Smedskjaer, J.C. Mauro, R.E. Youngman, C.L. Hogue, M. Potuzak, Y. Yue, J. Phys. Chem. B 115 (2011) 12930.
[7] Y. Xiang, J. Du, M.M. Smedskjaer, J.C. Mauro, J. Chem. Phys. 139 (2013) 44507.
[8] L.-S. Du, J.F. Stebbins, J. Non-Cryst. Solids 351 (2005) 3508.
[9] O.V. Mazurin, J. Non-Cryst. Solids 351 (2005) 1103.
[10] Y.H. Yun, P.J. Bray, J. Non-Cryst. Solids 27 (1978) 363.
[11] W.J. Dell, P.J. Bray, S.Z. Xiao, J. Non-Cryst. Solids 58 (1983) 1.
[12] G. El-Damrawi, W. Müller-Warmuth, H. Doweidar, I.A. Gohar, Phys. Chem. Glasses 34 (1993) 52.
[13] J.M. Delaye, V. Louis-Achille, D. Ghaleb, J. Non-Cryst. Solids 210 (1997) 232.
[14] L. Cormier, D. Ghaleb, D.R. Neuville, J.-M. Delaye, G. Calas, J. Non-Cryst. Solids 332 (2003) 255.
[15] L. Huang, J. Kieffer, J. Chem. Phys. 118 (2003) 1487.
[16] L. Huang, J. Kieffer, Phys. Rev. B 74 (2006) 224107.
[17] J. Du, A.N. Cormack, J. Non-Cryst. Solids 349 (2004) 66.
[18] J. Du, A.N. Cormack, J. Am. Ceram. Soc. 88 (2005) 2532.
[19] J. Du, L. Kokou, J.L. Rygel, Y. Chen, C.G. Pantano, R. Woodman, J. Belcher, J. Am. Ceram. Soc. 94 (2011) 2393.
[20] L. Kokou, J. Du, J. Non-Cryst. Solids 358 (2012) 3408.
[21] A. Pedone, G. Malavasi, M.C. Menziani, A.N. Cormack, U. Segre, J. Phys. Chem. B 110 (2006) 11780.
[22] B. Park, Molecular Dynamics Study of the Structure of Borate Glasses(Thesis) Alfred University, 1998.
[23] H. Inoue, A. Masuno, Y. Watanabe, J. Phys. Chem. B 116 (2012) 12325.
[24] L.-H. Kieu, J.-M. Delaye, L. Cormier, C. Stolz, J. Non-Cryst. Solids 357 (2011) 3313.
[25] G. Ferlat, T. Charpentier, A.P. Seitsonen, A. Takada, M. Lazzeri, L. Cormier, G. Calas, F. Mauri, Phys. Rev. Lett. 101 (2008) 65504.
[26] L. Pedesseau, S. Ispas, W. Kob, Phys. Rev. B 91 (2015) 134201.
[27] L. Pedesseau, S. Ispas, W. Kob, Phys. Rev. B 91 (2015) 134202.
[28] B. Guillot, N. Sator, Geochim. Cosmochim. Acta 71 (2007) 4538.
[29] B.W.H. Van Beest, G.J. Kramer, R.A. Van Santen, Phys. Rev. Lett. 64 (1990) 1955.
[30] M. Matsui, Geophys. Res. Lett. 23 (1996) 395.
[31] V.V. Maslyuk, T. Bredow, H. Pfnür, Eur. Phys. J. B 41 (2004) 281.
[32] K.D. Kwon, L.J. Criscenti, J. Mineral. Soc. Korea 26 (2013) 119.
[33] J.D. Gale, A.L. Rohl, Mol. Simul. 29 (2003) 291.
[34] I.T. Todorov, W. Smith, K. Trachenko, M.T. Dove, J. Mater. Chem. 16 (2006) 1911.
[35] D. Chandler, Introduction to Modern Statistical Mechanics, 1987.
[36] A.K. Varshneya, Fundamentals of Inorganic Glasses: Arun K. Varshneya, 1994 (Access Online via Elsevier).
[37] Y. Xiang, Computational Studies on Structures and Ionic Diffusion of Bioactive Glasses(PhD Thesis) University of North Texas, 2014.
[38] J. Du, L.R. Corrales, J. Chem. Phys. 125 (2006) 114702.
[39] S. Plimpton, J. Comput. Phys. 117 (1995) 1.
[40] R. Hill, Proc. Phys. Soc. A 65 (1952) 349.
[41] V. Kahlenberg, H. Böhm, Am. Mineral. 83 (1998) 631.
[42] M. He, X.L. Chen, T. Zhou, B.Q. Hu, Y.P. Xu, T. Xu, J. Alloys Compd. 327 (2001) 210.
[43] F. Gan, Issledovanie Alyumo-Bornoi Anomalii Svoistv Silikatnykh Stekol, Thesis, Leningrad, 1959.
[44] D.M. Zirl, S.H. Garofalini, J. Am. Ceram. Soc. 73 (1990) 2848.
[45] G.N. Greaves, A. Fontaine, P. Lagarde, D. Raoux, S.J. Gurman, Nature 293 (1981) 611.
[46] R.-S. Zhou, R.L. Snyder, Acta Crystallogr. Sect. B Struct. Sci. 47 (1991) 617.
[47] C.W. Burnham, M.J. Buerger, Zeitschrift Für Krist. Mater. 115 (1961) 269.
[48] N. Ishizawa, T. Miyata, I. Minato, F. Marumo, S. Iwai, Acta Crystallogr. Sect. B Struct. Crystallogr. Cryst. Chem. 36 (1980) 228.
[49] D.A. McKeown, G.A. Waychunas, G.E. Brown, J. Non-Cryst. Solids 74 (1985) 349.
[50] D.A. McKeown, G.A. Waychunas, G.E. Brown, J. Non-Cryst. Solids 74 (1985) 325.
[51] R.L. Mozzi, B.E. Warren, J. Appl. Crystallogr. 3 (1970) 251.
[52] S. Wang, J.F. Stebbins, J. Am. Ceram. Soc. 82 (1999) 1519.
[53] W. Loewenstein, Am. Mineral. 39 (1954) 92.
[54] B. De Jong, G.E. Brown, Geochim. Cosmochim. Acta 44 (1980) 491.
[55] S.K. Lee, J.F. Stebbins, Am. Mineral. 84 (1999) 937.
[56] X. Yuan, A.N. Cormack, Comput. Mater. Sci. 24 (2002) 343.
[57] J. Du, Y. Xiang, J. Non-Cryst. Solids 358 (2012) 1059.
[58] J. Du, J. Am. Ceram. Soc. 92 (2009) 87.

Chapter 7
Challenges in Molecular Dynamics Simulations of Multicomponent Oxide Glasses

Jincheng Du

Abstract Despite tremendous progresses made in the past few decades in molecular dynamics simulations of glass and related materials, there exist a number of challenges in MD simulations of multicomponent glasses. This chapter summarizes the progresses in this field and present the challenges that include the reliable and transferable empirical potentials, cooling rate, system size and concentration effect on the simulated glass structures, and the validating structures of multicomponent oxide systems. Several practical examples on multicomponent and technologically important glass systems using classical MD simulations are also given to highlight the capabilities and challenges.

7.1 Introduction

Since its first application on silica glasses about four decades ago [1–3], molecular dynamics (MD) simulations have become an effective and almost indispensable method in studying the atomic structure and structure-property relationships in glass materials. Glass structure lacks long-range order and defies any single experimental method in structural determination, in contrast to crystalline materials where diffraction method can usually uniquely determine the atomic structures. The structure of glasses is also not random or featureless but, on the contrary, there exist plenty of short- and medium-range structure characteristics that play critical roles on the behaviors and properties of glasses. Determining these glass structure characteristics still poses as a significant challenge in modern characterizations methods and remains a frontier of physical science, although significant progresses in methods such as high energy X-ray and neutron diffraction [4], solid state NMR [5], EXAFS [6], and more recently atom tomography [7]. Atomistic simulations, especially MD based methods, have been playing a more and more important role in investigating

J. Du (✉)
Department of Materials Science and Engineering,
University of North Texas, Denton, TX, USA
e-mail: du@unt.edu

C. Massobrio et al. (eds.), *Molecular Dynamics Simulations of Disordered Materials*, Springer Series in Materials Science 215,
DOI 10.1007/978-3-319-15675-0_7

glass structure and structure-property relationships in glass research. This is due to rapid development of simulation methodologies (classical and ab initio MD methods), diversified potential models (partial charge, polarizable, reactive force fields), and accessible high performance computational facilities. As a result, MD simulations are not only practiced in university or national labs but also gradually used in industrial and companies to solve more practical problems. For example, MD simulations have recently been used to study the ion exchange processes in chemically strengthened glasses for display applications [8]. Despite these progresses, there remain several challenges in MD simulations of multicomponent oxide glasses, on which this chapter will be focused on.

Most industrial and technologically important glasses are multicomponent in nature. It is one of the major advantages of glass materials to maintain glass formability in large composition range [9]. The capability to fine-tune thermal-mechanical and other properties, to optimize processing condition, and address cost and environmental friendliness considerations by varying the glass compositions are also important in practical glass applications. It is thus critical to understand the structure of these multicomponent glasses and how each component impacts the glass structure and thus influences the physical, chemical, thermal, mechanical, optical and other properties. Earlier MD simulations involve simpler unary or binary glass compositions but significant progress has been made to study multicomponent glasses.

MD simulations involve studying an assembly of atoms or molecules [10], usually with applied periodic boundary condition for solid and melt, that interact with each other through empirical potentials. With initial positions randomly generated or from crystal structures and velocity assigned from Boltzmann distribution at given temperature, the atoms will move step by step with positions determined through solving Newton's equation of motion at time step in the order of femtosecond. This process goes iteratively until specified time steps are reached. The simulations can be run under different ensembles and the macroscopic thermodynamic properties such as pressure and heat capacity can then be calculated. The most commonly used procedure to generate glass structure is the simulated melt and quench process. Due to the application of periodic boundary condition and relatively small number of atoms as compared to the Avogadro's number used in the simulations, mechanical heating is inevitable (normal melting starts from surface and propagate to the inner part). As a result, higher than the normal melting temperatures (5000–8000 K) are required to ensure equilibration and removal of memory effects of the initial structure. The melt is then gradually cooled down to room temperature through a linear, non-linear or step cooling procedures with nominal cooling rate ranging from 0.1 to 10 K/ps. The trajectories of atoms can be recorded for structural analysis such as pair distribution functions and bond angle distributions or used for further diffusion or dynamic property calculations.

In this chapter, we will discuss some of the major challenges of the multicomponent oxide glasses using classical molecular dynamics simulations. These challengesinclude the development of reliable and transferable empirical potentials,

optimization of the glass forming procedures, and experimental validations of simulated structures. A few examples of MD simulations of several multicomponent glasses ranging from soda lime silicate glasses, sodium aluminosilicate glasses, and phosphosilicate glasses and structural information obtained will then be provided. Properties such as mechanical behaviors (Bulk, Young's and shear moduli), ionic diffusion coefficients and electrical conductivity, viscosity, vibrational spectra and others can be calculated from trajectories of structural models generated from MD simulations but they are not the focus of this chapter.

7.2 Current Challenges on MD Simulations of Multicomponent Oxide Glasses

Despite significant progresses and wide applications in different systems, MD simulations of glasses still face a number of challenges in studying glass materials, especially for multicomponent systems. These challenges include reliable and transferable potentials models for multicomponent systems, the cooling rate effect during simulated glass formation, and the system size effect on certain properties and concentration effect on the simulations of minor components. These challenges are discussed in detail below.

7.2.1 Empirical Potentials

Empirical potentials play a critical role in MD simulations. The quality of the potentials determines in large extent the accuracy and validity of the final simulated structures and properties and hence the quality of the simulations. In practice, the availability of potential models is usually the limiting factor whether a system can be simulated. As most of the early MD simulations focused on simpler unary or binary glass systems, the available potentials in the literature are also limited to these simple components and very few potential sets are applicable to multicomponent systems. Fortunately, there are some recent efforts of developing potentials for common oxides that include most of the glass component. Some of these potentials have been tested in wide compositions ranges and can be valuable in studying some practical multicomponent glass systems. One of such set of potentials was initially developed by D.M. Teter, and modified, widely tested and utilized by Cormack, Du et al. [11–21]. The potential set consists of long range Coulombic interactions with fixed partial ionic charges to account for partial covalency in silicate, aluminate, phosphate oxide systems. The charge for oxygen is −1.2 and the cation charges scale proportionally from their formal charges to ensure charge neutrality of the overall system. For example, 2.4 for Si, 1.8 for Al and 0.6 for Na. Short range interactions are in the Buckingham form, which has an exponential repulsion term and a power attractive

Table 7.1 Atomic charge and Buckingham potential parameters for oxide glasses [11–21]

Pairs	A (eV)	ρ (Å)	C (eV Å^6)
$O^{-1.2}$–$O^{-1.2}$	2029.2204	0.343645	192.58
$Si^{2.4}$–$O^{-1.2}$	13702.905	0.193817	54.681
$P^{3.0}$–$O^{-1.2}$	26655.472	0.181968	86.856
$Al^{1.8}$–$O^{-1.2}$	12201.417	0.195628	31.997
$Li^{0.6}$–$O^{-1.2}$	41051.938	0.151160	0.0
$Na^{0.6}$–$O^{-1.2}$	4383.7555	0.243838	30.70
$K^{0.6}$–$O^{-1.2}$	20526.972	0.233708	51.489
$Ca^{1.2}$–$O^{-1.2}$	7747.1834	0.252623	93.109
$Sr^{1.2}$–$O^{-1.2}$	14566.637	0.245015	81.773
$Y^{1.8}$–$O^{-1.2}$	29526.977	0.211377	50.477
$La^{1.8}$–$O^{-1.2}$	4369.39	0.2786	60.28
$Er^{1.8}$–$O^{-1.2}$	58934.851	0.195478	47.651
$Eu^{1.8}$–$O^{-1.2}$	5950.5287	0.253669	27.818
$Ce^{1.8}$–$O^{-1.2}$	11476.9522	0.242032	46.7604
$Ce^{2.4}$–$O^{-1.2}$	31697.724	0.21836	90.659

term to account for dispersion interactions, which can be expressed as

$$V_{ij}^{'}(r) = A_{ij} \cdot \exp\left(-\frac{r}{\rho_{ij}}\right) - C_{ij}/r^6 \tag{7.1}$$

where A, ρ and C are parameters, r is interatomic distance. This set of potential from the published papers is summarized in Table 7.1 [11–21]. It is worth noting that for the A parameter for O–O interaction the value of 1844.7458 eV was also used in the literature but it has been shown the updated value (2029.2233 eV, about 10 % larger than the original one) gave better agreement in terms of Si–O bond length and coordination number for silicon and other cations [12]. A correction term is usually used to modify Buckingham potential at short distances due to much faster increase of the power term than the exponential at term short interatomic distances in the Buckingham potential form. This creates an unphysical, negative infinite potential well at short interatomic distances. For systems running at high temperatures, such as the melt, in constrained dynamics or with unreasonable initial atom configurations, atoms can overcome the barrier and fall into the well that leads to "fusion" of atoms and unphysically high potential energies. This can be corrected by the addition of a separate potential function such as 12–18 Lenard-Jones potential or a splice function for shorter distances to the original Buckingham potential. The correction that Du et al. used was a splice function with the form of [22]

$$V_{ij}^{'}(r) = A_{ij} \cdot r^n + B_{ij} \cdot r^2 \tag{7.2}$$

where A, B, n are parameters. The function will be applied for distance smaller than r_0, where r_0 is defined as the r value when the second derivative of potential energy equals to 0 and the A, B, n parameters were chosen so the potential, force, and first derivative of force for V(r) and $V'(r)$ to be continuous at r_0. Other functional form such as the ZBL potential [23] can also be used for the short range corrections of the Buckingham potential. In such a case, a polynomial function will be needed to link the two potentials in the short distance range.

Water plays a critical role in many properties of glasses. Hence it is important to understand the structural role and mechanism of how water reacts and interacts with oxide glasses. While most of the earlier water and hydroxyl potentials were based on full charge models, Du and Cormack have developed a set of partial charge potentials that are compatible with the above mentioned oxide glass potentials to enable the simulations of hydroxyl groups in the bulk and on the surface of glasses. This potential takes the similar partial charge of the Buckingham form as listed in Table 7.1 for oxide, and uses the Morse potential for O–H interactions together with a screened harmonic three-body term for Si–O–H bond angles. The oxygen atom in hydroxyl group has a different charge (−0.856 vs. −1.2) as compared to the oxygen atoms in the glass [14, 24]. The potential for hydroxyl groups has the Coulomb-subtracted Morse form:

$$V(r) = D\{1 - \exp[-\beta(r - r_0)]\}^2 - D - \frac{e^2 q_O q_H}{4\pi\varepsilon_0 r_{ij}} \tag{7.3}$$

in which D, β and r_0 are parameters. A three-body term was introduced to correctly reproduce the Si–O–H bond angle on silica surfaces. The three-body term has the screened harmonic form,

$$E_{jik}(\theta) = \frac{1}{2}(\theta_{jik} - \theta_0)\exp(-(r_{ij}/\rho_1 + r_{ik}/\rho_2)) \tag{7.4}$$

in which i, j and k represent the center atom and the other two atoms, and r_{ij} and r_{ik} represent the distance between the center atom and its two neighbors, θ_{jik} is the angle between j, i and k, with i at the center. The parameters θ_0, ρ_1 and ρ_2 were obtained by fitting the structure and defect format energies of silicic acid and a number of metal hydroxides. The atomic charges and potential parameters are listed in Table 7.2 [14, 24].

Another comprehensive potential set for oxide glasses was developed by Pedone et al. [25]. This set potential used the same partial charge as the above mentioned potentials but the short range interaction has the form of Morse potential with an additional −12 power term to enhance short range repulsion [25],

$$V_{ij}(r) = D_{ij}\left[\left\{1 - e^{-a_{ij}(r-r_0)}\right\}^2 - 1\right] + \frac{C_{ij}}{r^{12}} \tag{7.5}$$

Table 7.2 Potential parameters of oxide glasses with hydroxyl groups [14, 24]

	Buckingham potential parameters			
	A (eV)	ρ (Å)		C (eV Å^6)
$Si^{2.4}$–$O^{-1.2}$	13702.905	0.193817		54.681
$Si^{2.4}$–$O^{-0.856}$	12443.824	0.193817		54.681
$Na^{0.6}$–$O^{-1.2}$	4383.7555	0.243838		30.7000
$Na^{0.6}$–$O^{-0.856}$	4096.2726	0.243838		30.7000
$Ca^{1.2}$–$O^{-1.2}$	7747.1834	0.252623		93.1090
$Ca^{1.2}$–$O^{-0.856}$	7036.7000	0.252623		93.1090
$Mg^{1.2}$–$O^{-1.2}$	7063.4907	0.210901		19.2100
$Mg^{1.2}$–$O^{-0.856}$	5754.1167	0.210901		19.2100
$H^{0.256}$–$O^{-0.856}$	100.0	0.25		0.0
$O^{-1.2}$–$O^{-1.2}$	1844.7458	0.343645		192.58
$O^{-0.856}$–$O^{-0.856}$	1844.7458	0.343645		192.58
	Morse potential parameters (Coulomb-subtracted)			
	D (eV)	B (Å^{-1})		r_0 (Å)
$H^{0.256}$–$O^{-0.856}$	7.0525	0.190		0.9485
	Screened Harmonic potential parameter			
	E_o (eV)	θ_o (°)	ρ_1 (Å)	ρ_2 (Å)
$H^{0.256}$–$O^{-0.856}$–$Si^{2.4}$	12.0	118	2.0	3.2

where D, a, r_0, and c are parameters. This set of potentials has been applied to a several multicomponent glass systems [26–28].

Despite active developments of potentials for oxides, the potentials for simulating multicomponent glasses can be improved in several ways. One of the major issues is the potential transferability. There exist potentials of various oxides in the literature but in most of the cases they are not compatible with each other. For example, the oxygen-oxygen interaction can have different functional forms or different parameters for two sets of potentials. In such a case, parameters of other cation-oxygen interactions are then not compatible and usually cannot be mixed to use together. Simultaneous fitting to a large number of crystal or minerals database can improve the transferability of a set of potential, as in the two previously mentioned potential sets [13, 25].

Another challenge on potentials is due to the fact that most of the current potential fitting for oxides was done in crystalline systems based on the structure and mechanical properties under ambient temperature and pressure. Temperature dependent properties such as melting temperature, thermal expansion coefficient and heat capacity are not commonly used in the fitting. Due to notable differences of the crystalline and glass systems, fine tuning the parameters for glass and melt to correctly describe at wide temperature range is highly desirable for the simulation

of glasses, yet only very few sets of potentials in the literature address this issue [29, 30].

Additional challenges exist when modeling glasses with components that exhibit compositional dependent coordination numbers. Boron oxide and aluminum oxide are those examples. NMR studies have shown that a boron anomaly is associated with boron coordination change as a function of composition [31–33]. For example, addition of sodium oxide to boron oxide leads to conversion of three coordinated boron to four coordinated boron. This conversion continues until sodium oxide is about 40 % and then further addition of sodium oxide creates non-bridging oxygen instead of 3–4 coordination conversion for boron ions. This becomes more complicated in borosilicate glasses, where the maximum depends on the boron oxide to silicon dioxide ratio, and in boroaluminosilicate glasses, where there is a competition among the three processes: conversion of 3 to 4-coordinated boron, creation of NBOS, and conversion of 5 and 6 to 4-coordinated aluminum. Several potentials have been applied to the aluminosilicate system which addresses well of the coordination conversion issue [26]. For borate and borosilicate glasses, Cormack and Park developed coordination dependent potentials [34], Huang and Kieffer developed charge equilibration and coordination dependent potentials [35], and more recently, Kieu et al. developed a set of fix charge potentials but the charges are adjusted depending on the composition [36]. Inoue et al. also proposed the usage of fixed charge, pair potential only to solve this issue [37]. The development of better potential for these mixed glass former glasses remain a major challenge in simulating mixed glass former glasses.

Most empirical potentials for oxide glasses adopt the Born model of solids and consist a long range Coulombic term and a short range interactions. Early simulations used formal (or full) charges but more recent potentials mainly use partial charge models. Full charge models are also usually accompanied by three body terms to correctly describe the structural unit geometry and the bond angles between the structural units. Later development based on first principles calculations and empirical fitting found that appropriate partial charges and fine tuning of short range parameters can successfully describe the coordination and bond angles of glass former cations. Another advantage of these partial charge pairwise potentials are their superior computational efficiency that enables simulations of large systems (hundreds thousands to millions of atoms) of oxide glasses. In addition to fixed charge partial charge models, recent developments include the variable charge models with the charges calculated step by step using the charge equilibrium method. This method is especially important in describing the heterogeneous structures or interfaces that include metal/oxide or oxide/water interactions. Examples of these potentials include the ReaxFF [38] and the COMB potentials [39].

It is known that the polarization effect of oxygen ions and some other large cations is important to describe the dielectric behaviors and defects in oxide ceramics. Polarizable potentials have also been used in glass simulations, where ion polarization is commonly treated by using the core-shell model. In the core-shell model, polarizability is treated by the massless shell that is linked to the core through a spring with the spring constant and shell charge determined to reflect the polarizability of the

ions. The shells are usually treated in two ways in MD simulations: dynamic shell and adiabatic shell. In a dynamic shell, a small mass is applied to the shell and it moves as other particles in the system. The time step is chosen to be small enough to separate the energy transfer between the shell vibration and the normal ionic motion. For adiabatic shell, the shell position is adjusted or equilibrated after each of MD step. Relatively larger time step can be applied to adiabatic shell simulations but extra steps of shell equilibration are needed. As a result, the polarizable potential simulations have additional computational cost. Tilocca et al. developed a set of shell model polarizable potential for silicate glasses and applied it to the simulation of soda lime silicate and bioactive glasses [40]. It was found that glass structures generated from the polarizable potential gave the silicon and phosphorus Q_n distributions closer to experimental NMR values than those from rigid ion models, although both rigid ion and polarizable potentials generated glass melt structure quite different from those from Car-Parrinello based ab initio MD (AIMD). Polarizable potentials were considered to better describe the melt to glass transition during the cooling process by keeping certain Q_n species and silicon coordination defects for longer time and better resembles those from AIMD simulations [41].

Ab initio based molecular dynamics (AIMD) [42, 43], which obtain the forces from accurate first principles calculations, should be more general and can be applied to any glass system, as long as the first principles theory can adequately describe the chemical bonding in the system. However, AIMD is still limited by the simulation system size and time (up to a few hundred atoms and tens of picoseconds) due to high computational cost. This becomes especially true for multicomponent systems. AIMD has been used in simulating silica, lithium and sodium silicate glasses, and a few other glass systems [42, 43]. The results from AIMD provide accurate trajectories and structures that can serve as a model system for comparison with and those from classical MD simulations and validate the simulation results and potential models. AIMD has also already been used to simulate to several chalcogenide glasses, for which very few empirical potentials are available due to the bonding complexity in the systems. It is expected that AIMD will be applied to more and more systems due to availability of high performance computing facilities but classical MD will not likely to be fully replaced by it in the near foreseeable future. Details regarding ab initio MD simulations can be found in other parts in this book.

7.2.2 Cooling Rate Effect

To ensure integration accuracy of equation of motions, MD simulations use time steps in the order of the femtosecond. This limits the total accessible simulation time in practical simulations ranging from hundreds pico-seconds to a few nano-seconds, which leads to cooling rate of the K/ps level during the simulated cooling process. This cooling rate is still many (6–9) orders of magnitude higher than fastest possible experimental ones. This is also one of the common criticisms of MD simulations of glasses from our experimental colleagues on glass structures generated using computer simulations by the melt-and-quench process.

However, it was observed in the study of sodium silicate glasses that simulated glass structures based on reasonable potentials and procedures are not that much different from the experimental structural data [13], suggesting that direct comparison of cooling rate values from experiment and simulations might be misleading. This was mainly explained by two reasons: firstly the number of atoms used in simulations. Although with applied periodic boundary condition, the number of atoms in glass simulations range from initially a few hundred to now a few to tens of thousands, which is many orders of magnitude smaller than real glass samples. In this situation, the atoms have higher chance to exchange energies with the boundaries so the system can achieve equilibrium faster. As a result, higher cooling rate from simulated process might not lead to drastically different glass structures, which explains the similarities of the simulated as compared to experimentally observed glass structures [44]. With increasing computing power, the trend of cooling rate can be systematically studied using relatively large system sizes.

It is worth mentioning that some structural properties are more sensitive to cooling rate than others. For example, Du and Xiang found in their MD simulations of bioactive glasses (Na_2O–CaO–P_2O_5–SiO_2) that Si Q_n distributions are fairly insensitive to cooling rate effect while minor glass former P Q_n distribution are more sensitive to cooling rate effect [21]. With decreasing cooling rate, the fraction of phosphorus Q_0 species increases (experimental NMR studies suggest that majority of phosphorus are in Q_0 species). This result was later confirmed in MD simulations of the same glass system using polarizable potentials [45]. These results suggest that different structure features equilibrate or freeze in during glass formation at different speed so the cooling rate effect is sensitive to interested structure/property features.

Although most glasses from MD simulations were generated through the melt and quench process, it will be very worthwhile to explore other methods in generating glass structure. Experimentally, the amorphous state can not only be created using the melt and quench method but also using physical or vapor deposition methods, the sol-gel method, pressure or radiation induced armorphizations. Similarly, methods other than melt and quench from simulations would be very valuable to explore. For example, Monte Carlo and MD can be combined in the process of glass formation [46].

7.2.3 Simulation Size and Concentration Effect

In the past few decades, we have witnessed the increase of size of MD simulations in terms of total atom numbers in the simulations. Starting from around 100 atoms in early MD simulations to several thousand of atoms in common practice during the past decade, today's simulations of oxide glasses with hundreds of thousands or even millions of atoms of ionic systems can be achieved. It is worth noting that millions atom simulations for metals has been achieved much earlier. This was due tothe fact

that metal potentials such as commonly used Embedded Atom Method (EAM) [47] have short cutoffs and there is no long range Coulombic force. However, simulations of a few thousands atoms are still commonly used in today's MD simulations in the literature as further increasing the system size in simulation will not influence of the structure or properties of interest in many studied systems.

Some properties, however, are more sensitive to system size than the others. One of those that is very sensitive to system size effect is the clustering behavior of minor component rare earth ions in glasses. It is known that rare earth ions have very low solubility in silica [15, 49]. A fraction of a percent will lead to clustering of rare earth ions and deterioration of properties such as optical emission due to non-radiative decay caused by energy transfer between clustered rare earth ions. In order to study the clustering behavior of low concentration components, such as rare earth (RE) oxide in silica glasses, it is necessary to use sufficiently large simulation cells to obtain statistically meaningful results. Early MD simulations of RE contained glasses use several hundred of atoms and a few RE ions. Of course, the clustering tendency cannot be investigated in these systems. In a study of clustering of europium ions in silica and silicate glasses, Kokou and Du have studied the clustering tendency as a function of system size for 1 mol% Eu_2O_3 [19, 48]. It was found that only after certain system size, namely over 6000 atoms, the trend of clustering can be reproducibly obtained in simulations. Figure 7.1 shows comparison of the probability to find a neighboring rare earth ion from random distribution and that from MD simulations. It was shown that for small system sizes (e.g. 1500 and 3000 atoms), the comparison with the random distribution is influenced by statistics and the clustering behavior is not conclusive. However, for larger system sizes where there are sufficient number of europium ions to provide better statistics, the probabilitybased on MD simulated

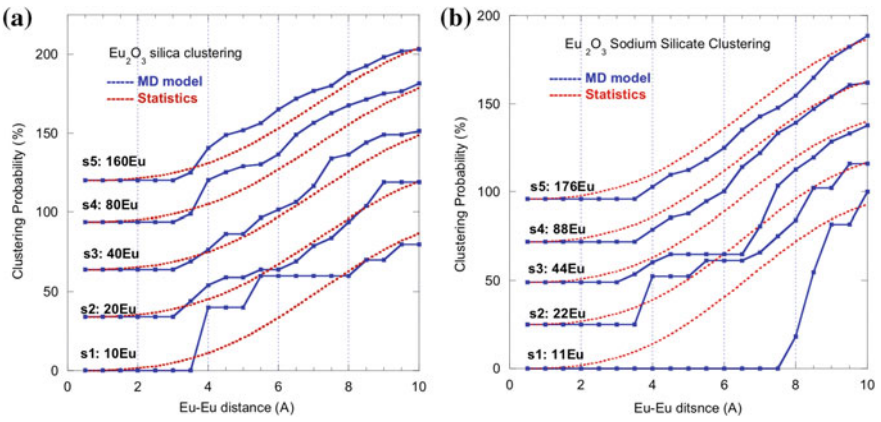

Fig. 7.1 Probabilities of finding neighboring Eu ions as a function of Eu–Eu distance in random distribution (*red curves*) and Eu ions distribution from MD simulation (*blue curves*) in Eu_2O_3 doped **a** silica and **b** sodium silicate glasses. Total number of atoms for glass s1–s5 are 1500, 3000, 6000, 12000, 24000, respectively [48]

structure is consistently higher than the random distribution in silica glass due to europium ion clustering but the probability is consistently lower than the random distribution in sodium silicate glasses. This is a classic example showing the effect of system size on simulated glass properties.

7.2.4 Validating Structure Models from Simulations

Comparing structural information from X-ray and neutron diffraction provides a very valuable way to validate MD simulation results of glasses. In some simple systems, the partial pair distribution function or partial structure factors of all atom pairs can be determined experimentally and they provide excellent validations for simulated structures. However, as the composition becomes more complicated and more elements included, larger number of pair contributions will complicate the comparison and the validation becomes more and more difficult in multicomponent glass systems. For example, for binary oxides, e.g. sodium silicate, there are six partial pair distribution functions, but for a four component systems, for example the bioactive glass composition, there are a total of fifteen partials contributions. The overlap between partial contributions makes it very challenging to assign the peaks and to determine the quality of comparison and hence the validation of the simulated structure models.

The R_x factor proposed by Wright [50] is commonly used to quantify the difference of the simulated and experimental total correlation function T(r), which is a form of pair distribution function and used in comparison with experiments due to symmetric broadening in experiments [51, 52]. The R_x is defined as [50],

$$R_X = \left[\frac{\Sigma_{i=1}^{N} (T^X(r_i) - T^S(r_i))^2}{\Sigma_{i=1}^{N} (T^X(r_i))^2} \right] \tag{7.6}$$

where $T^X(r_i)$ is the total correlation function from experiment and $T^S(r_i)$ is the total correlation function from simulations. In order to compare with experimental diffraction data, the simulated total distribution functions need to be broadened to take into consideration of the limit of momentum transfer (maximum Q value) in the diffraction experiments [51, 52]. The partial correlation function $t_{ij}(r)$ is first broadened by convoluting with the component peak function $p_{ij}^N(r)$, which defines the experimental resolution (for neutron diffraction in this case).

$$t'_{ij}(r) = \int_0^\infty t_{ij}(r')[P_{ij}^N(r - r') - P_{ij}^N(r + r')]dr' \tag{7.7}$$

The component peak function is defined as,

$$P_{ij}^N(r) = \frac{\overline{b_i}\,\overline{b_j}}{\pi} \int_0^{Q_{\max}} M(Q)\cos(rQ)dQ \tag{7.8}$$

in which $\overline{b_i}$ is the average neutron scattering length of atom i, $Q_{\max}$ is the maximum value of the experimental scattering vector, $M(Q)$ is the modification function. A common form of modification function is the Lorch function, which gives a gradual cutoff and is defined as,

$$M(Q) = \begin{cases} \frac{\sin \Delta r}{\Delta r Q} & Q \leq Q_{\max} \\ 0 & Q > Q_{\max} \end{cases} \tag{7.9}$$

The total correlation function after broadening for the neutron diffraction case is then expressed as,

$$T^N(r) = T^o(r) + D^N(r) = \sum_{i,j} c_i t'_{ij} \tag{7.10}$$

in which $T^o(r)$ equals $4\pi r \rho^o \sum_i c_i \overline{b_i}$, where c_i and b_i are atom fraction and neutron scatter length of element i and ρ^o is the atom number density of the glass.

Figure 7.2 shows the comparison of experimental and simulated total correlation function (T(r)) for 45S5 bioactive glass. The R_x value for this system is 8.0 %. The 45S5 glass has four elements and 15 partial-pair distribution functions (8 of the 15 partial-pair distribution functions are shown in the figure) [21]. The overlap of these partial distributions makes it very difficult to deconvolute the contributions from different pairs. For example, the Si–O and P–O first peak, as well as the Na–O and Ca–O first peak, are largely overlapped; so it is almost impossible to obtain information on the Si–O/P–O or Na–O/ Ca–O bond length directly from neutron diffraction studies of the bioactive glasses.

It is also possible to compare the reciprocal space structure factors, either from neutron or X-ray diffraction measurements. The partial structure factors are first calculated through Fourier transformation the partial pair distribution functions using

$$S_{ij}(Q) = 1 + \rho_o \int_0^R 4\pi r^2 [g_{ij}(r) - 1] \frac{\sin(Qr)}{Qr} \frac{\sin(\pi r/R)}{\pi r/R} dr \tag{7.11}$$

in which $g_{ij}(r)$ is the pair distribution function of atom pair i and j, Q is the scattering vector, ρ_o is the average atom number density, R is the maximum value of the integration in real space which is set to half of the size of one side of the simulation cell. The $\frac{\sin(\pi r/R)}{\pi r/R}$ part of the integrand is a Lorch-type window function, as defined earlier, to reduce the effect of finite simulation cell size. Lorch function reduces the ripples at low Q (the cutoff effect) but it also leads to some broadening of the structure factor peaks. It is valuable to study the cutoff effect by simulating several glasses with different simulation cell sizes. The partial structure factors are then added together with weighting factors to obtain the total neutron structure factor,

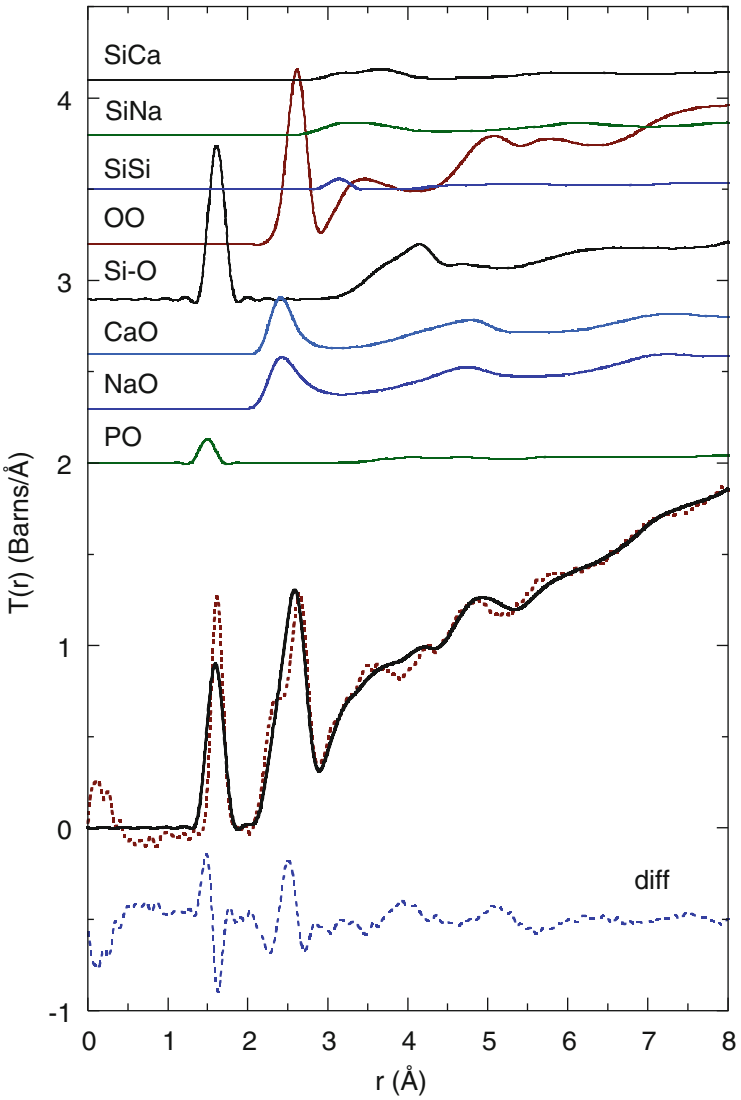

Fig. 7.2 Comparison of experimental (*dotted line*) and simulated (*solid line*) neutron total correlation function T(r) of 45S5. The difference of the two (*dash line*) and eight important (out of total fifteen) partial pair correlation functions from simulations are also shown. Q_{max} of 59 $Å^{-1}$ (the maximum Q value from experiment) and Lorch window function were used in neutron broadening of simulated structures [21]

$$S_N(Q) = (\sum_{i=1}^{n} c_i b_i)^{-2} \sum_{i,j=1}^{n} c_i c_j b_i b_j S_{ij}(Q) \tag{7.12}$$

in which c_i is the fraction of atoms in each of the species, and b_i is the neutron scattering length of the species. The contribution partial structure factors are defined as

$$S^N_{ij(i\leq j)}(Q) = (\sum_{i=1}^{n} c_i b_i)^{-2}(2-\delta_{ij})c_i c_j b_i b_j S_{ij}(Q) \tag{7.13}$$

in which δ_{ij} is a delta function. By examining the $S^N_{ij}(Q)$, one can determine how each atom pair contributes to the features of the structure factors. b_i and b_j are the neutron scattering lengths of atom type i and j. Figure 7.3 shows the comparison of the experimental neutron structure factor and those calculated from MD simulations of a lanthanum aluminate glass (37.5 % La_2O_3–62.5 % Al_2O_3) [53]. In the figure,

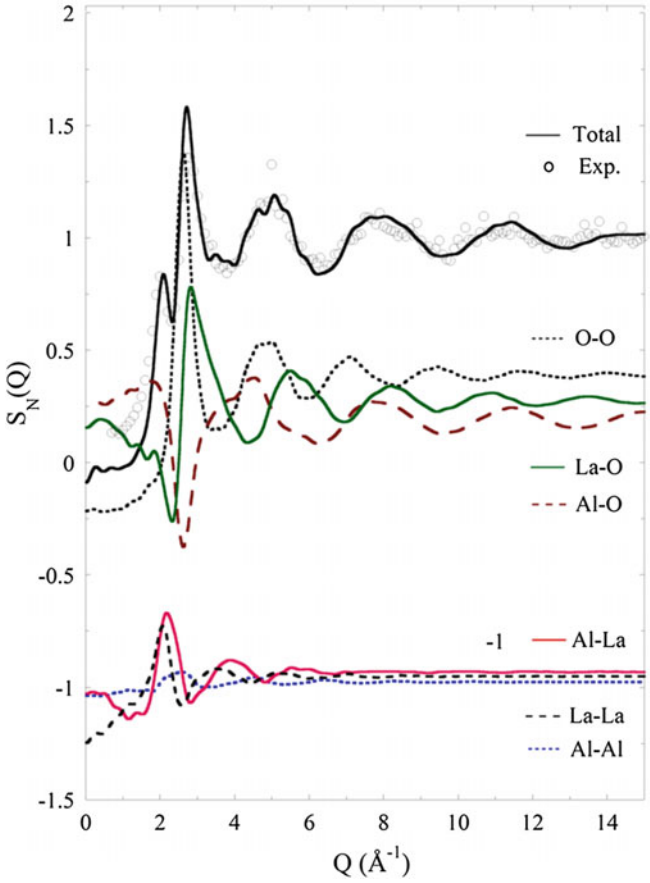

Fig. 7.3 Comparison of experimental and calculated neutron structure factor for lanthanum aluminate glasses [53]. Partial structure factors from MD simulations are also shown

it is also shown the contributions of each of the six partial structure factors. This comparison will not only provide information on how good the agreement is but also what partial contribution leads to the major differences.

There are several site specific experimental techniques such as solids state NMR, EXAFS and Raman spectroscopy that can give additional structural information to be compared directly with simulation results and thus are able to provide further validations. For example, NMR results not only provide Q_n distributions but also how the Q_n species are linked together through double or multi-quantum experiments. This kind of site specific experimental methods is an additional opportunity for detailed structure comparison and validation.

Recently, calculations of the NMR spectra using the GIPAW method based on structure models from classical MD simulations were performed and used to interpret the experimental NMR spectra for various nuclei. Insight on the network structures of complicated bioactive glasses was obtained [54]. Combination of classical MD simulations, DFT relaxation of periodic glass structure models, and GIPAW NMR spectra calculations has also been used to investigate modifier local environment in glasses [55]. For example, strontium local environment in strontium containing bioactive glasses was studied by this combination method with multiple samples. It was found that statistics from multiple glass samples are critical to generate reliable comparison of the NMR spectra [55]. This can become a powerful method in interpreting NMR results to provide rich structural information of glasses [56].

7.3 MD Simulations of Multicomponent Glasses: Practical Examples

7.3.1 Soda Lime Silicate Glasses

Soda lime silicate (Na_2O–CaO–SiO_2) glasses are the basis of a wide range of industrial glass compositions, often with addition of other minor components. Structural understanding of these glasses is thus of both scientific and technological importance. However, there are very few studies of soda lime silicate glasses from MD simulations, possibly due to the additional complexity of CaO introduced to the binary Na_2O–SiO_2 glasses which, together with other alkali silicate glasses, have been very well studied using MD simulations. Cormack and Du [57] have studied the soda lime silicate glasses in the base composition $15Na_2O$–$10CaO$–$75SiO_2$ and investigated the effect of replacing Na_2O with CaO on the short range and medium range structures using MD simulations. Partial charge pairwise potential with BKS [58] parameters were used for the Si–O and O–O interactions and Na–O and Ca–O parameters developed by fitting to the structures and properties of related crystal systems [57].

Although CaO and Na_2O both play the glass modifiers role in silicate glasses (it is confirmed from simulations that each sodium ion creates one NBO and each calcium

ion creates two NBOs, by breaking the Si–O–Si linkages), their local coordination environments are quite different. It was found that calcium ions have total coordination number of around six with around 80 % are non-bridging oxygen (NBO), while the coordination number for sodium is around 5 with a little over 50 % of them are NBO. This can be seen from pair correlation functions of Ca–O and Na–O pairs and the deconvoluted BO/NBO contributions. Similar trend was also found in bond angle distributions. This difference is mainly originated from the difference of the field strength of sodium and calcium ions. Stronger bonding to NBOs that create stronger linkage between Si–O network fragments of Ca as compared to Na leads to much improved mechanical property and chemical durability when CaO is introduced to soda silicate glasses. The primitive ring size distribution statistics, a way to measure the medium range structures, was found to be relatively insensitive to the CaO/Na_2O substitution.

Pedone et al. studied soda silicate and soda lime silicate glasses using the partial charge Morse potential with MD simulations [59]. It was found that calcium ions increases the compactness (lower free volume) and increases the cohesion energy due to stronger Ca–O bond as compared to Na–O bond. As a result, soda lime silicate glasses have higher Young's moduli and higher sodium diffusion energy barrier as compared to soda silicate glasses. The substitution of MgO with CaO in soda lime silicate glasses were also studied using MD simulations. It was found that magnesium mainly has fourfold coordination as compared to calcium with mainly sixfold coordination. MgO/CaO substation leads to decrease of diffusion energy barrier and elastic moduli.

7.3.2 Aluminosilicate Multicomponent Glasses

Alumina as a glass-forming component has been commonly used to improve the properties of soda silicate glasses. As a result, aluminosilicate glasses is a common industrial glass system that finds a number of technological applications. For example, the Corning Gorilla© glass that are widely used for display in electronic devices is aluminosilicate glass and the base glass composition of E-glass is also aluminosilicate with other components such as boron oxide. Alumina is generally considered to be a glass former when combined with other glass forming oxides as it cannot form glass by itself and, in some classifications, it is also considered to be an intermediate.

Xiang, Du, Smedskjaer and Mauro recently studied sodium aluminosilicate glasses using classical MD simulations with two sets of potentials [60]. Both sets of potentials use partial charges with -1.2 being assigned to oxygen and the charges of other ions proportionally scaled down from their formal charges. One set uses Buckingham potential format and other one uses Morse potential. Three compositions were studied with similar silica content (around 60 mol%) but different Al/Na ratios covering peralkaline (Al/Na $<$ 1) to peralumina (Al/Na $>$ 1) compositions. Aluminum ions are found to be mainly (over 95 %) fourfold coordinated and are part of the silicon-oxygen glass network. The $[AlO_{4/2}]^-$ units are mainly charge balanced

by sodium ions but oxygen triclusters [OAl_3] or [OAl_2Si] are also found to exist in the glasses. The percentage of oxygen triclusters increases from around 1 % to around 10 % with increasing Al/Na ratio. The percentage of five-coordinated Al also increases with Al/Na ratio. Depending on the potentials used, an increase from 0.4 to 1.3 % or from 1.9 to 5.5 % from peralkali (Al/Na = 0.6) to peralumina (Al/Na = 1.5) for the Buckingham and Morse potentials, respectively. Six coordinated aluminum was also observed in the structure generated using the Morse potential.

Connectivity between [AlO_x] polyhedra was analyzed to study the distribution of the glass forming units. It was found that majority linkages are [AlO_x]–[SiO_4] through corner sharing of bridging oxygen, this is followed by [SiO_4]–[SiO_4] linkages through corner sharing. [AlO_x]–[AlO_x] has the lowest possibility. However, no strict aluminum avoidance rule was observed as there are still considerable amount [AlO_x]–[AlO_x] linkage and average of such linage per [AlO_x] increase with increasing Al/Na ratio.

Mechanical properties of these glasses were also calculated based on the structures generated from MD simulations. This was done by calculating the compliance matrix, which is second derivative of potential energy versus strain. Based on the compliance matrix, bulk, Young's and shear moduli, as well as Poisson's ratio, were calculated. The increase trend of bulk and shear moduli with increasing Al/Na ratio was correctly reproduced for both potentials. While the Buckingham potential slightly overestimates both moduli, the Morse potential slightly underestimates the moduli.

Corrales and Du studied the surface of soda lime aluminosilicate glass and melt using MD simulations [61]. The base glass composition was chosen to represent one form of E-glass with an aim to understand sodium ion distribution at the glass fiber surfaces. Constant pressure simulations were used to generate the glass and glass melt. Z-density distribution was used to describe element density in directions perpendicular to the surface. It was found clear segregation and enrichment of sodium ions on the surface. This is associated with non-bridging oxygen ion segregation at the surface. The results help to explain the experimentally observed sodium emission in glass fiber surfaces. Potential of mean force was used to measure the correlation between sodium ions in this paper. Two methods were used to calculate the potential of mean forces: integration of pair distribution functions and constrained dynamic simulations, with both give similar results.

7.3.3 Aluminophosphate and Phosphosilicate Multicomponent Glasses

Phosphate glasses find wide applications as laser media and optical windows, and more recently as bioactive materials. Phosphate glasses are characterized by the chain or network structures formed by [PO_4] tetrahedrons linked through bridging oxygen ions [62]. Compared to [SiO_4] tetrahedron, there exist a terminal double bond P=O

in each [PO_4] unit. The other three bridging oxygen can be converted to non-bridging oxygen during the depolymerization of the network, depending on the O/P ratio.

There were concerns on the description of the double bonds in [PO_4] unit using classical MD simulations but it seemed that the mean field approach in pair potentials work well in phosphate glasses as in silicate glasses. Liang et al. [62] studied lithium phosphate binary glasses using MD simulations. It was found that the observed glass transition temperature minimum is related to the abundance of small-membered rings in the structures. An increase in glass stability was observed as the average ring size increased from two- to four-membered rings. Mountjoy studied the structures of rare earth (RE) phosphate glasses, $(R_2O_3)_x(P_2O_5)_{1-x}$ using MD simulations and compared with EXAFS and diffraction experimental methods [63]. It was found that RE coordination number ranges from 6 to 8 and generally decreases with decreasing RE ionic radius [63]. Du et al. studied cerium aluminophosphte glasses ($19Al_2O_3$–$76P_2O_5$–$5CeO_2$) using a set partial charge pairwise potential [20]. It was found that phosphorus ions are mainly four coordinated (99 %) and aluminum ions are four (79 %), five (20 %) and six (1 %) coordinated with an average coordination number of 4.2. Aluminum ions were found to be mostly in the glass forming network for both four and five coordinated states. For phosphorus species, there is a wide distribution of Q_n species.

Phosphosilicate and aluminophosphosilicate glasses were also modeled using MD simulations by Du et al. [20]. Figure 7.4a shows the glass forming cation-oxygen pair distributions. It can be seen that the bond lengths increase from P–O, Si–O and Al–O with peak position in 1.51, 1.62, 1.79 Å respectively. It can also be seen that the first peak of the P–O, Si–O and Al–O decrease in intensity and becomes less symmetric in the sequence, which can be related to the decreasing field strength of the three glass forming cations. Bond angle distribution analyses of the three glass forming cations show that O–P–O BAD is most symmetric at angle of 109° while O–Al–O bond angle distribution is rather broad. It is interesting that five coordinated silicon, which does not exist in usual silicate glasses, was found in cerium phosphosilcate and cerium

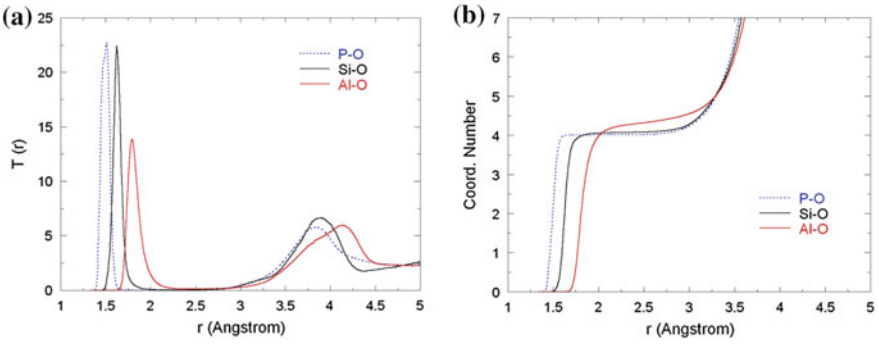

Fig. 7.4 Pair distribution function (**a**) and accumulated coordination numbers (**b**) for P, Si and Al in cerium aluminophosphosilicate glass [20]

aluminophosphosilicate glasses in the range 4–5 %. This was also observed in NMR studies of phosphosilicate glasses. This is shown in the accumulated coordination number of the three network forming cation (Fig. 7.4b).

One of the most interesting findings of the cerium phosphate glasses from MD simulations is the preference of glass forming network unit around cerium ions. Cerium ions have a coordination number of around 7 and the preference in their second coordination shell decrease in the sequence phosphorous, aluminum and silicon. The coordination numbers of Si, Al and P in the second coordination shell are 0.2, 0.5 and 6.6, respectively, for Ce^{3+} and 0, 0, 6.5 for Ce^{4+} [20]. This suggests that cerium and other rare earth ions will be preferentially surrounded by phosphorous and aluminum and forms a solvation shell to separate these high field strength ions from the rigid silicon oxygen network. These simulation results explain well the declustering effect of alumina and phosphorus oxide codopants in rare earth containing optical fibers [20].

Another group of phosphosilicate glasses that have attracted much attention in simulations is the bioactive glasses [64]. These glasses have relatively low phosphorous oxide concentration (2–3 mol%) with large amount (over 20 mol%) of sada and calcia. The compositions can be considered to be invert glass as the silica content is less than 50 %. These glasses can be partially dissolved in body fluid solutions and develop a layer of hydroxyl carbonate apatite (HCP) at the interface and are classified to be bioactive. These complicated quarterly glass system (Na_2O–CaO–P_2O_5–SiO_2) can be further modified by addition or substituting MgO, SrO or ZnO to further fine tune or add additional functionalities. The bioactivity of the glasses originates from their atomic structure and has shown strong composition, and hence structure, dependent. MD simulations have been successfully used to simulate the 45S5 bioglass [64], one of the most bioactive compositions. First reported by Zeitler and Cormack [65] and later followed by Tilocca et al. [41, 66], Pedone et al. [27], and Du and Xiang [8, 21], a number of studies on MD simulations of these and related bioactive glasses have been published. Considerable insights on the atomic structures and their bioactivity correlation have been revealed by these simulations. As a result, this special glass system has become one of the most studied multicomponent glasses.

Zeitler and Cormack [65], and later Du and Xiang [8, 21], used the partial charge pair wise potential with parameters from Table 7.1 to simulate the 45S5 bioactive glass bulk and surface structures. MD simulations using this set of potential correctly have reproduced the basic glass structure features and have shown reasonable agreement with neutron diffraction results. It was found that in 45S5, the glass network structure is highly fragmented with branched chain or small groups, with an average network connectivity of around 1.9. This fragmented network structure is one of the main reason that the glass can be easily dissolved in aqueous solutions that leads to the formation of silanol groups that further polymerize to form amorphous Si–O network, on which calcium and phosphate groups deposit and further crystallize to form HCP crystals. Pedone et al. studied the effect of MgO/CaO substitution on the structure and properties of 45S5 bioactive glasses using MD simulations [27]. Tilloca et al. have reported several papers on MD simulations of 45S5 and related

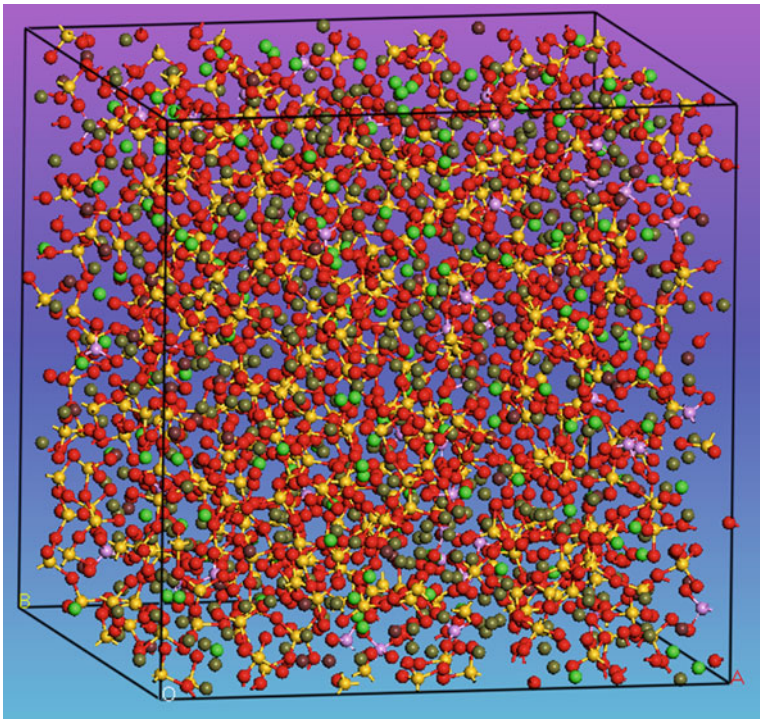

Fig. 7.5 Snapshot of bioactive glass $46.1SiO_2 \cdot 24.4Na_2O \cdot 16.9CaO \cdot 2.6P_2O_5 \cdot 10SrO$ (mol%) from MD simulations. Total number of atoms 2836. Simulation cell size $34 \times 34 \times 34$ Å^3. *Pink ball* Sr; *blue ball* Ca; *green ball* Na; *small yellow ball* Si; *small purple ball* P; *small red ball* O

bioactive glasses using a set of polarizable potentials based on the shell model [41, 66].

Du and Xiang studied the SrO/CaO substitution effect on the glass structure and diffusion of 45S5 bioactive glasses using MD simulations [21]. SrO is introduced to bioactive glasses due to the simultaneous effect of Sr ions to enhance bone growth and inhibit bone absorption. It was found that Sr ions reside in an environment similar to calcium. The substitution leads to linear increase of glass density and decrease of molar volume. However, the substitution does not considerably change the medium range structure such as network connectivity and Qn distribution. The ionic diffusion behaviors including the diffusion coefficients and diffusion energy barriers also remain constant with the substitution. Figure 7.5 shows a snapshot of 45S5 bioactive glass with 10 % SrO/CaO substitution from MD simulations. These simulation results provide further evidence that SrO/CaO substation can be a mechanism to improve efficiency of hard tissue growth and bioactivity while maintain the general dissolution behaviors and other basic physical and chemical behaviors of 45S5 glass [21].

7.4 Concluding Remarks

Classical MD simulations have been successfully used to study the structure and properties of oxide glasses including some multicomponent glass compositions. Structural, diffusion, dynamic and mechanical properties of these glasses can be systematically studied using simulations. With careful experimental validations, these simulations can be used to investigate glass the structure—property relationship and eventually design of new glass compositions. Applications of these simulations methods have now moved beyond academic laboratories and began to be used in industrial environments. There remain, however, several challenges in MD simulations of multicomponent glasses namely the reliability and transferability of empirical potentials, cooling rate and system size effect on the structure features, experimental validation of the simulated structures. Despite these challenges, it is concluded that MD simulations will play a more and more important role in fundamental and practical research of glass materials.

Acknowledgments The author gratefully acknowledges funding support of the NSF GOALI project through the Ceramic Program (project # 1105219) and the DOE NEUP project (project # DE-NE0000748).

References

1. L.V. Woodcock, C.A. Angell, P. Cheeseman, Molecular dynamics studies of the vitreous state: simple ionic systems and silica. J. Chem. Phys. **65**, 1565 (1976)
2. C. Huang, A.N. Cormack, *Computer simulation studies of the structure and transport properties of alkali silicate glasses*. Physics of Non-Crystalline Solids (Taylor & Francis, Cambridge, 1992), pp. 31–35
3. T.F. Soules, A.K. Varshneya, Molecular dynamic calculations of a sodium borosilicate glass structure. J. Am. Ceram. Soc. **64**, 145–150 (1981)
4. A.C. Wright, Neutron scattering from vitreous silica. V. The structure of vitreous silica: what have we learned from 60 years of diffraction studies? J. Non-Cryst. Solids **179**, 84–115 (1994)
5. J.F. Stebbins, Effects of temperature and composition on silicate glass structure and dynamics: SI-29 NMR results. J. Non-Cryst. Solids **106**, 359–369 (1988)
6. G.N. Greaves, EXAFS and the structure of glass. J. Non-Cryst. Solids **71**, 203–217 (1985)
7. S. Gin, J.V. Ryan, D.K. Schreiber, J. Neeway, M. Cabie, Contribution of atom-probe tomography to a better understanding of glass alteration mechanisms: application to a nuclear glass specimen altered 25 years in a granitic environment (2013)
8. Y. Xiang, J. Du, Effect of strontium substitution on the structure of 45S5 bioglasses. Chem. Mater. **23**, 2703–2717 (2011)
9. J.C. Mauro, C.S. Philip, D.J. Vaughn, M.S. Pambianchi, Glass science in the United States: current status and future directions. Int. J. Appl. glass Sci. **5**, 2–15 (2014)
10. M.P. Alan, D.J. Tildesley, *Computer Simulation of Liquids* (Oxford University Press, Oxford, 1989)
11. A.N. Cormack, J. Du, T.R. Zeitler, Alkali ion migration mechanisms in silicate glasses probed by molecular dynamics simulations, in *79th International Bunsen Discussion Meeting*, The Royal Society of Chemistry, UK, vol. 4, pp. 3193–3197 (2002)
12. A.N. Cormack, J. Du, T.R. Zeitler, Sodium ion migration mechanisms in silicate glasses probed by molecular dynamics simulations. J. Non-Cryst. Solids **323**, 147–154 (2003)

13. J. Du, A.N. Cormack, The medium range structure of sodium silicate glasses: a molecular dynamics simulation. J. Non-Cryst. Solids **349**, 66–79 (2004)
14. J. Du, A.N. Cormack, Molecular dynamics simulation of the structure and hydroxylation of silica glass surfaces. J. Am. Ceram. Soc. **88**, 2532–2539 (2005)
15. J. Du, A.N. Cormack, The structure of erbium doped sodium silicate glasses. J. Non-Cryst. Solids **351**, 2263–2276 (2005)
16. J. Du, L.R. Corrales, Compositional dependence of the first sharp diffraction peaks in alkali silicate glasses: a molecular dynamics study. J. Non-Cryst. Solids **352**, 3255–3269 (2006)
17. J. Du, L. Rene Corrales, Understanding lanthanum aluminate glass structure by correlating molecular dynamics simulation results with neutron and X-ray scattering data. J. Non-Cryst. Solids **353**, 210–214 (2007)
18. J. Du, Molecular dynamics simulations of the structure and properties of low silica yttrium aluminosilicate glasses. J. Am. Ceram. Soc. **92**, 87–95 (2009)
19. J. Du, L. Kokou, Europium environment and clustering in europium doped silica and sodium silicate glasses. J. Non-Cryst. Solids **357**, 2235–2240 (2011)
20. J. Du, L. Kokou, J.L. Rygel, Y. Chen, C.G. Pantano, R. Woodman, J. Belcher, Structure of cerium phosphate glasses: molecular dynamics simulation. J. Am. Ceram. Soc. **94**, 2393–2401 (2011)
21. J. Du, Y. Xiang, Effect of strontium substitution on the structure, ionic diffusion and dynamic properties of 45S5 bioactive glasses. J. Non-Cryst. Solids **358**, 1059–1071 (2012)
22. L.R. Corrales, J. Du, Compositional dependence of the first sharp diffraction peaks in alkali silicate glasses: a molecular dynamics study. J. Non-Cryst. Solids **352**, 3255–3269 (2006)
23. J. Du, R. Devanathan, L.R. Corrales, W.J. Weber, A.N. Cormack, Short- and medium-range structure of amorphous zircon from molecular dynamics simulations. Phys. Rev. B (Condens. Matter Mater. Phys.) **74**, 214204-1 (2006)
24. J. Du, Molecular dynamics simulations of the structure of silicate glasses containing hydroxyl groups and rare earth ions, Ph.D. Dissertation, Alfred University, 2004
25. A. Pedone, G. Malavasi, M.C. Menziani, A.N. Cormack, U. Segre, A new self-consistent empirical interatomic potential model for oxides, silicates, and silica-based glasses. J. Phys. Chem. B **110**, 11780–11795 (2006)
26. Y. Xiang, J. Du, M.M. Smedskjaer, J.C. Mauro, Structure and properties of sodium aluminosilicate glasses from molecular dynamics simulations. J. Chem. Phys. **139**, 079904 (2013)
27. A. Pedone, G. Malavasi, M.C. Menziani, Computational insight into the effect of CaO/MgO substitution on the structural properties of phospho-silicate bioactive glasses. J. Phys. Chem. C **113**, 15723–15730 (2009)
28. A. Pedone, G. Malavasi, A.N. Cormack, U. Segre, M.A. Menziani, Elastic and dynamical properties of alkali-silicate glasses from computer simulations techniques. Theor. Chem. Acc. **120**, 557–564 (2008)
29. B. Guillot, N. Sator, A computer simulation study of natural silicate melts. Part I: Low pressure properties. Geochim. Cosmochim. Acta **71**, 1249–1265 (2007)
30. B. Guillot, N. Sator, A computer simulation study of natural silicate melts. Part II: High pressure properties. Geochim. Cosmochim. Acta **71**, 4538–4556 (2007)
31. P.J. Bray, J.G. O'Keefe, NMR investigation of the structure of alkali borate glasses. Phys. Chem. Glasses **4**, 37–46 (1963)
32. J. Zhong, P.J. Bray, Change in boron coordination in alkali borate glasses, and mixed alkali effects, as elucidated by NMR. J. Non-Cryst. Solids **111**, 67–76 (1989)
33. R.E. Youngman, J.W. Zwanziger, Multiple boron sites in borate glass detected with dynamic angle spinning nuclear magnetic resonance. J. Non-Cryst. Solids **168**, 293–297 (1994)
34. A.N. Cormack, B. Park, Molecular dynamics simulations of borate glasses. Phys. Chem. Glasses **41**, 272–277 (2000)
35. L. Huang, J. Nicholas, J. Kieffer, J. Bass, Polyamorphic transitions in vitreous B2O3 under pressure. J. Phys. Condens. Matter **20**, 075107 (2008)
36. Le-Hai Kieu, J. Delaye, L. Cormier, C. Stolz, Development of empirical potentials for sodium borosilicate glass systems. J. Non-Cryst. Solids **357**, 3313–3321 (2011)

37. H. Inoue, A. Masuno, Y. Watanabe, Modeling of the structure of sodium borosilicate glasses using pair potentials. J. Phys. Chem. B **116**, 12325–12331 (2012)
38. A.C.T. van Duin, B.V. Merinov, S.J. Seung, W.A. Goddard III, ReaxFF reactive force field for solid oxide fuel cell systems with application to oxygen ion transport in yttria-stabilized zirconia. J. Phys. Chem. A **112**, 3133–3140 (2008)
39. T. Liang, T. Shan, Y. Cheng, B.D. Devine, M. Noordhoek, Y. Li, Z. Lu, S.R. Phillpot, S.B. Sinnott, Classical atomistic simulations of surfaces and heterogeneous interfaces with the charge-optimized many body (COMB) potentials. Mater. Sci. Eng. R: Rep. **74**, 255–279 (2013)
40. A. Tilocca, N.H. de Leeuw, A.N. Cormack, Shell-model molecular dynamics calculations of modified silicate glasses. Phys. Rev. B (Condens. Matter Mater. Phys.) **73**, 104209-1 (2006)
41. A. Tilloca, Short- and medium-range structure of multicomponent bioactive glasses and melts: an assessment of the performances of shell-model and rigid-ion potentials. J. Chem. Phys. **129**, 084504 (2008)
42. J. Du, L.R. Corrales, Structure, dynamics, and electronic properties of lithium disilicate melt and glass. J. Chem. Phys. **125**, 114702 (2006)
43. A. Tilocca, N.H. De Leeuw, Ab initio molecular dynamics study of 45S5 bioactive silicate glass. J. Phys. Chem. B **110**, 25810–25816 (2006)
44. L.R. Corrales, J. Du, Thermal kinetics of glass simulations. Phys. Chem. Glasses **46**, 420–424 (2005)
45. A. Tilocca, Cooling rate and size effects on the medium-range structure of multicomponent oxide glasses simulated by molecular dynamics. J. Chem. Phys. **139**, 114501 (12 pp) (2013)
46. A. Tandia, K.D. Vargheese, J.C. Mauro, Elasticity of ion stuffing in chemically strengthened glass. J. Non-Cryst. Solids **358**, 1569–1574 (2012)
47. M.I. Baskes, Modified embedded atom method, in *Proceedings of the 1994 International Mechanical Engineering Congress and Exposition*, 6–11 Nov 1994, vol. 42 (ASME, Chicago, 1994), pp. 23–35
48. L. Kokou, J. Du, Rare earth ion clustering behavior in europium doped silicate glasses: simulation size and glass structure effect. J. Non-Cryst. Solids **358**, 3408–3417 (2012)
49. J. Du, A.N. Cormack, Structure study of rare earth doped vitreous silica by molecular dynamics simulation. Radiat. Eff. Defects Solids **157**, 789–794 (2002)
50. A. Wright, The comparison of molecular dynamics simulations with diffraction experiments. J. Non-Cryst. Solids, **159**, 264–268 (1993)
51. A.C. Wright, Neutron and X-ray diffraction. J. Non-Cryst. Solids **106**(1–3), 1–16 (1988)
52. A.C. Wright, Neutron diffraction and X-ray amorphography, in *Experimental Techniques of Glass Science*, ed. by C.J. Simmons, O.H. El-Bayoumi (American Ceramic Society, Westerville, 1993)
53. J. Du, L.R. Corrales, Understanding lanthanum aluminate glass structure by correlating molecular dynamics simulation results with neutron and X-ray scattering data. J. Non-Cryst. Solids **353**, 210–214 (2007)
54. A. Pedone, T. Charpentier, G. Malavasi, M.C. Menziani, New insights into the atomic structure of 45S5 bioglass by means of solid-state NMR spectroscopy and accurate first-principles simulations. Chem. Mater. **22**, 5644–5652 (2010)
55. C. Bonhomme, C. Gervais, N. Folliet, F. Pourpoint, C.C. Diogo, J. Lao, E. Jallot, J. Lacroix, J.-M. Nedelec, D. Iuga, J.V. Hanna, M.E. Smith, Y. Xiang, J. Du, D. Laurencin, 87Sr solid-state NMR as a structurally sensitive tool for the investigation of materials: antiosteoporotic pharmaceuticals and bioactive glasses. J. Am. Chem. Soc. **134**, 12611–12628 (2012)
56. T. Charpentier, M.C. Menziani, A. Pedone, Computational simulations of solid state NMR spectra: a new era in structure determination of oxide glasses. RSC Adv. **3**, 10550–10578 (2013)
57. A.N. Cormack, J. Du, Molecular dynamics simulations of soda-lime-silicate glasses. J. Non-Cryst. Solids **293–295**, 283–289 (2001)
58. B.W.H. van Beest, G.J. Kramer, R.A. van Santen, Force fields for silicas and aluminophosphates based on ab initio calculations. Phys. Rev. Lett. **64**, 1955–1958 (1990)

59. A. Pedone, G. Malavasi, A.N. Cormack, U. Segre, M.C. Menziani, Elastic and dynamical properties of alkali-silicate glasses from computer simulations techniques. Theor. Chem. Acc. **120**, 557–564 (2008)
60. Y. Xiang, J. Du, L.B. Skinner, C.J. Benmore, A.W. Wren, D.J. Boyd, M.R. Towler, Structure and diffusion of ZnO-SrO-CaO-Na_2O-SiO_2 bioactive glasses: a combined high energy X-ray diffraction and molecular dynamics simulations study. RSC Adv. **3**, 5966–5978 (2013)
61. L.R. Corrales, J. Du, *Characterization of Ion Distributions Near the Surface of Sodium-Containing and Sodium-Depleted Calcium Aluminosilicate Melts* (Blackwell Publishing Inc, Beijing, 2006), pp. 36–41
62. J. Liang, R.T. Cygan, T.M. Alam, Molecular dynamics simulation of the structure and properties of lithium phosphate glasses. J. Non-Cryst. Solids **263–264**, 167–179 (2000)
63. G. Mountjoy, Molecular dynamics, diffraction and EXAFS of rare earth phosphate glasses compared with predictions based on bond valence. J. Non-Cryst. Solids **353**, 2029–2034 (2007)
64. L.L. Hench, Bioceramics, a clinical success. Am. Ceram. Soc. Bull. **77**, 67–74 (1998)
65. T.R. Zeitler, A.N. Cormack, Interaction of water with bioactive glass surfaces. J. Cryst. Growth **294**, 96 (2006)
66. A. Tilocca, A.N. Cormack, N.H. de Leeuw, The structure of bioactive silicate glasses: new insight from molecular dynamics simulations. Chem. Mater. **19**, 95–103 (2007)

Received: 30 June 2016 | Accepted: 10 October 2016

DOI: 10.1111/jace.14654

ORIGINAL ARTICLE

Journal of the American Ceramic Society

Surface structures of sodium borosilicate glasses from molecular dynamics simulations

Mengguo Ren | Lu Deng | Jincheng Du

Department of Materials Science and Engineering, University of North Texas, Denton, Texas

Correspondence
Jincheng Du, Department of Materials Science and Engineering, University of North Texas, Denton, TX.
Email: jincheng.du@unt.edu

Abstract

Surface plays an important role in the physical and chemical properties of oxide glasses and controls the interactions of these glasses with the environment, thus dominating properties such as the chemical durability and bioactivity. The surface atomic structures of a series of sodium borosilicate glasses were studied using classical molecular dynamics simulations with recently developed compositional dependent partial charge potentials. The surface structural features and defect speciation were characterized and compared with the bulk glasses with the same composition. Our simulation results show that the borosilicate glass surfaces have significantly different chemical compositions and structures as compared to the bulk. The glass surfaces are found to be sodium enriched and behave like borosilicate glasses with higher R (Na_2O/B_2O_3) values. As a result of this composition and associated structure changes, the amount of fourfold boron decreases at the surface and the network connectivity on the surface decreases. In addition to composition variation and local structure environment change, defects such as two-membered rings and three-coordinated silicon were also observed on the surface. These unusual surface composition and structure features are expected to significantly impact the chemical and physical properties and the interactions with the environments of sodium borosilicate glasses.

KEYWORDS

boron oxide, borosilicate glass, glass structure, glass surface, molecular dynamics, simulation

1 | INTRODUCTION

Sodium borosilicate (SBN) glasses have had wide use in everyday life and technologies, such as sealing materials and chemically resistant laboratory glass wares. They are the base composition for known industrial brands such as the Vicor and the Pyrex glasses.[1-4] They are also widely accepted as confinement matrix to immobilize medium- and high-level nuclear wastes.[5] In addition, borosilicate glasses find biomedical applications with controlled dissolution rate and bioactivity.[6,7] For many of these applications, it is critical to understand the bulk and, especially, surface glass structures as they have a strong impact on the corrosion and dissolution behaviors, bioactivity, long-term chemical durability, mechanical properties, and ion-exchange behaviors. Despite the wide applications of borosilicate glasses, the current knowledge of their structure remains limited. The presence of two glass network formers, Si and B, as well as the coexistence of different types of boron coordination states, makes the SBN glass structure significantly more complex than silicate glasses.[4,8,9] Therefore, a deeper understanding of the bulk, and especially, the surface structure of SBN glasses is important to both glass science and technologies.

Glass surfaces are critical to understanding the interactions of glass with the environment, as they are where the

reactions first take place. Detailed structural information of SBN glass surfaces and their interaction with water are thus important to a better understanding of the mechanisms of aqueous glass corrosion and alterations. Compared to the study of bulk glass structure, the analysis of glass surface is much more difficult because of limited analysis methods. Common experimental techniques that have been used to study glass surfaces include X-ray photoelectron spectroscopy (XPS), secondary ion mass spectroscopy, scanning and transmission electron microscopy, and Fourier-transform infrared spectroscopy.[10-13] The insulating and amorphous structure of glasses further complicate both analysis and data interpretation.[14,15] On the other hand, during the past few decades, molecular dynamics (MD) simulations have been effective for the surface structure study of different kinds of glasses. Numerous works on the MD simulation of silica glass surface have been reported.[15-19] For example, Du et al.[16] investigated the structure and hydroxylation of silica glass surface by MD simulation using pairwise partial charge potentials. During the surface creation process, the formation of defects (ie, nonbridging oxygen (NBO), two-membered ring, and three-coordinated silicon) was observed, and these defects are regarded as active sites for the formation of hydroxyl groups. Zeitler et al.[20] studied the interaction of water with bioactive glass surfaces whose complex compositions include SiO_2, Na_2O, CaO, and P_2O_5. They reported that defects identified in SiO_2 surface, such as three-coordinated Si, were not observed in these simulated bioactive glasses. Average reaction energies for different rings were calculated, and dramatic structural openings occurred on opening of three-membered rings. In another MD simulation surface study of multicomponent glass, Corrales and Du[21] demonstrated that after characterization of the surface state of a series of sodium-containing calcium aluminosilicate glass melts, sodium ions, and NBO near the glass surface were enriched.

Compared to wide applications of MD simulations of silica and silicate glass surfaces, simulation studies of borosilicate glass surfaces are quite limited. This dearth of studies is due mainly to the limited availability of suitable empirical potential for borosilicate glass systems because of the complexity of borosilicate glass structures and the difficulty of describing boron coordination change with composition. Recent developments of potentials have enabled simulations of borosilicate glasses. Inoue et al.[22] developed a set of partial charge pairwise potentials for SBN glasses, and were able to reproduce boron coordination change with composition. In addition, a set of composition-dependent partial charge potentials developed by Kieu et al.[23] were able to describe the boron coordination change with composition in terms of both R (Na_2O/B_2O_3) and K (SiO_2/B_2O_3) values. In addition to the structure, the equilibrium density and mechanical properties of borosilicate glasses calculated using this set of potentials also agree well with experiments. Recently, Kwon and Criscenti[24] used this set of potentials to model a few SBN glass surfaces. They reported that surface glass composition differs significantly from the bulk. Many aspects of borosilicate glass surface structures, however, remain unknown, while the structure features remain critical to understanding the interaction of these glasses with water and dissolution behaviors.

In this work, we apply molecular dynamics simulations using the recently developed potentials[23] to perform a detailed analysis of the SBN glass dry surface. The aim of these simulations is better to understand the composition and structural differences between SBN bulk glass and glass surface. This paper is arranged as follows: MD simulation details introduced in Section 2 include the potential model used here and how to generate SBN bulk glass and glass surface. Property analysis and comparisons are subsequently presented in Section 3: Z-density profile is used to determine the thickness of surface layer; and then glass surfaces compositions are calculated and compared with bulk glasses. For local glass structure study, pair distribution function, bond angle distribution, and N_4 (the fraction of tetrahedral to total boron) data are calculated; and ring size distributions are used for medium glass structure analysis. Also reported in this section are defects types and concentrations that formed on glass surfaces. Section 4 discusses the significance of these results to understanding SBN glass surface properties. Finally, Section 5 summarizes our findings.

2 | SIMULATION DETAILS

Classical molecular dynamics simulations were performed using the DL_POLY[25] package. The potentials used here were developed by Kieu et al.,[23] and was recently tested by Deng and Du by simulating sodium borosilicate glasses in wide composition ranges, which showed good agreement of boron coordination change with composition as compared to well accepted theories.[27] The potentials combine a long-range coulomb term and a short-range Buckingham term,

$$\Phi(r_{ij}) = \frac{q_i q_j}{r_{ij}} + A_{ij} e^{\frac{-r_{ij}}{\rho_{ij}}} - \frac{C_{ij}}{r_{ij}^6} \quad (1)$$

where r_{ij} is the interatomic distance between atoms i and j; q_i and r_{ij} are the effective charge for atoms i and j, respectively. A_{ij}, ρ_{ij}, and C_{ij} are the parameters for the Buckingham term. The potentials were based on a set of partial charge potentials developed by Guillot-Sator.[26] The main feature of this set of potential is their compositional-dependent atomic charges and the A_{ij} parameter for the B–O

Buckingham interactions, which enable it to correctly describe boron coordination change with composition.[23] Potential parameters were fitted to the well-accepted Dell and Bray model[8] of boron coordination change with composition and have been shown to describe the structure, including boron coordination change, and properties such as density and mechanical properties of a series of SBN glasses. Recent testing of the potentials has shown that the potentials are capable of simulations of SBN glasses in wide composition ranges.[27] In addition to structure features, the potential was also shown to be able to reproduce the experimental densities under constant pressure simulations and mechanical properties.[23] More details of the potential can be found in Refs. [23] and [27].

Borosilicate glasses are commonly described by two ratios: $R = \frac{Na_2O}{B_2O_3}$ and $K = \frac{SiO_2}{B_2O_3}$. In this work, three different SBN glass compositions with the same K (=2) but different R values were studied using MD simulations (Table 1). The initial systems, with ~3000 atoms for each composition, were generated by randomly placing all the atoms in a cubic cell with experimental glass densities. These systems were then energy minimized at 0 K and relaxed at 300 K. After relaxation, systems were heated to 6000 K to remove the memory effect of the initial configurations, and then cooled to 300 K gradually, with a nominal cooling speed of 5 K/ps. Canonical ensembles (NVT) and a time step of 1 fs were used throughout the bulk glass simulation processes.

For surface creation, the bulk structure generated above was first relaxed at 300 K for 200 000 time steps under constant (zero) pressure using an isothermal and isobaric ensemble (NPT). During this process, a small decrease in cell length observed in all three samples resulted in a 1.7%-3.1% increase in glass densities. MD simulations of glass surfaces began with cleaving the bulk structures perpendicular to the z-axis.[17] Figure 1 schematically shows the process of glass surface generation in simulations. Starting from a bulk glass structure model (Figure 1(left)) generated from the normal melt and quench process and full relaxation under constant temperature and pressure (NPT) ensemble to release stress, the surface was created by insertion of a vacuum gap followed by a series of annealing and relaxation. A vacuum gap of 20 Å along the z-axis was inserted to the simulation cell while keeping the three-dimensional periodic boundary conditions (Figure 1 (middle)). Meanwhile, the bottom quarter layer of the relaxed bulk structure was frozen to mimic the bulk. To simulate spontaneous heating during fracture and to facilitate structural relaxation, the cleaved surface was relaxed at 1000 K for 60 000 time steps and then cooled gradually to 300 K and further relaxed at 300 K for another 60 000 time steps. To obtain reliable results, for each sample, three different surfaces were generated by inserting the vacuum gap at different positions (each displaced from each other by 4 Å) along the z-axis of one bulk structure.

TABLE 1 Bulk glass composition, density, and simulation cell information (cubic cell, length of each sides) used for MD simulation

	Composition (mol%)					Density	Cell size	Atom number				
Glass	SiO_2	B_2O_3	Na_2O	R	K	(g/cm^3)	(Å)	Si	B	Na	O	Total
SBN0.2	62.50	31.25	6.25	0.2	2.0	2.147	33.28	518	518	104	1865	3005
SBN0.5	57.14	28.57	14.29	0.5	2.0	2.396	33.24	480	480	240	1800	3000
SBN1.0	50.00	25.00	25.00	1.0	2.0	2.530	32.82	428	428	428	1712	2996

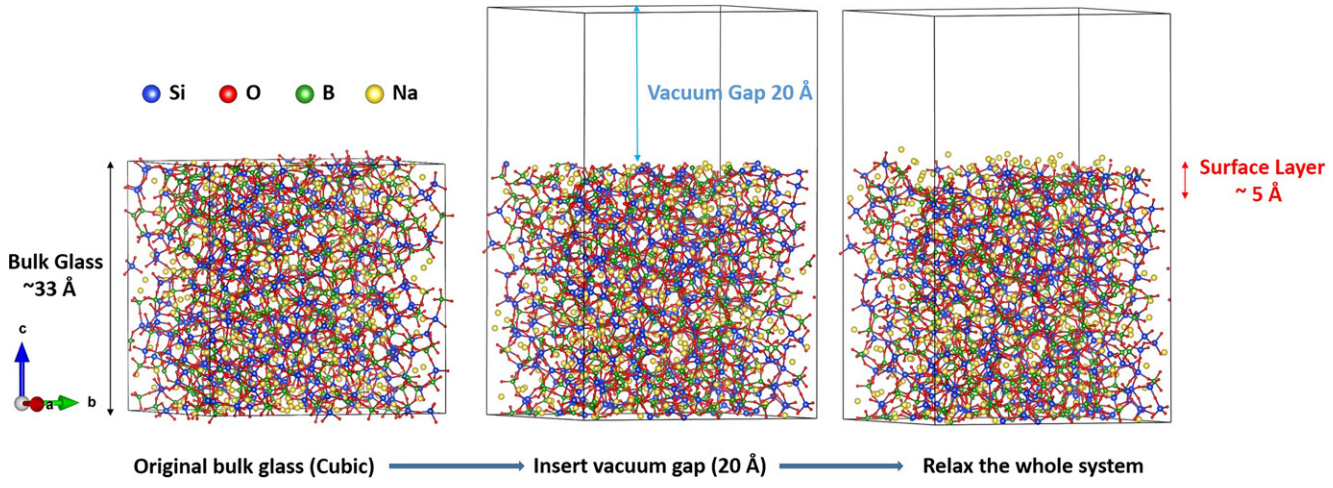

FIGURE 1 Schematic illustration of the glass surface creation process (Glass SBN1.0 is used here as an example.)

3 | RESULTS

The z-density profiles of all ion types calculated in 2 Å slabs are shown in Figure 2 for three samples. Note a distinct drop of atom densities near the surface regions. For visual assistance, a green vertical dashed line marks the starting change point. According to this atom density change, the thickness of surface regions was 4-8 Å, which is also in agreement with other simulation results.[16,28]

After determining surface region thickness, the chemical compositions at the glass surface were further calculated; those chemical compositions at the glass surface turned out to be significantly different from bulk glasses. Table 2 compares calculated R and K values between glass surfaces and bulk glasses. For bulk glass, all three samples have the same initial K value of 2. For glass surface, the K value of sample SBN0.2 was increased to 2.25, whereas surface K values of samples SBN0.5 and SBN1.0 showed almost no change. Further comparing the R value reveals a significant increase in R value at the surface of these samples and the increment for samples SBN0.2, SBN0.5, and SBN1.0 are 0.15, 0.15, and 0.50, respectively. This result indicated that Na replaces both Si and B on the surface of three samples, thereby causing the enrichment of sodium at glass surface. The increase in sodium concentration at the glass surface also has been found in ab initio simulations of 45S5 bioactive glass as well as other classic MD simulations, including 58S bioactive glass, soda-lime-silica glass, and sodium calcium aluminosilicate glass melts. The accumulation of Na^+ at the surface is recognized to compensate for the charge of NBOs caused by O–Si bond breakage.[21,29-31] The enrichment of sodium at the surface is important at the initial stage of the general glass dissolution process, where Na^+ undergoes ion exchange in solution and leads to the formation of a hydrated alteration layer on the glass surface.[32,33]

In contrast to the large difference in bulk and surface of the coordination number, bond distance, and bond angle of boron, silicon coordination remains around 4.0, and the Si–O bond distance remains around 1.61 Å (Figure 3). The large structure feature differences in boron between the bulk and surface stem from their composition differences. And, we know the boron coordination environment depends on composition, ie, both the R and K values; while the high field strength of Si^{4+} enables silicon ions to remain fourfold coordinated and to experience a relatively small change in distribution with composition. However, there the difference between bulk and surface is subtle but noticeable, even for Si–O distributions. Comparison of Si–O PDF between bulk glass and surface showed a slight decrease in peak height and an increase in peak Full Width at Half Maximum of the first peak for the surface.

To get more accurate quantitative results, the N_4 number for the surface and bulk structure is calculated and is shown in Figure 4. Theoretical trends of N_4 vs R for K=2 series SBN glasses predicted by Dell and Bray model are drawn as a reference in the blue dash line. Dell and Bray model can be used to predict N_4 based on the glass composition ($R Na_2O{\cdot}B_2O_3{\cdot}K SiO_2$). According to this model, N_4=R as $0 \le R \le R_{max}(=0.5+\frac{K}{16})$; N_4=R_{max} as $R_{max} \le R \le R_{D1}(=0.5+K/4)$; $N_4 = R_{max} - (R - R_{D1})(8+K)/[12 \times (2+K)])$ as $R \ge R_{D1}$.[8] When R=0.2 (sample SBN0.2) and R=0.5 (sample SBN0.5), the N_4 numbers of bulk structures agree well with theoretical values. However, when R value equals 1.0, the simulated bulk structure has slightly higher N_4 than that predicted by the Dell and Bray model. Surface N_4 numbers were compared with the corresponding bulk N_4 values and the results show that the number of fourfold boron decreased on surfaces. This is supported by

TABLE 2 Comparison of R (Na_2O/B_2O_3) and K (SiO_2/B_2O_3) values of bulk and surface

	SBN0.2	SBN0.5	SBN1.0
R_{bulk}	0.2	0.5	1.0
$R_{surface}$	0.35	0.65	1.50
K_{bulk}	2.0	2.0	2.0
$K_{surface}$	2.25	2.03	2.04

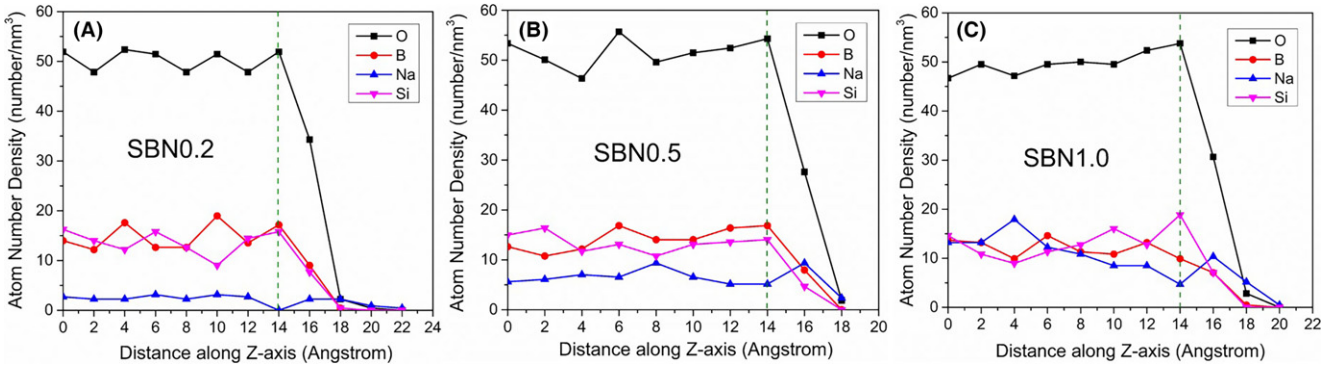

FIGURE 2 z-density profiles of (A) SBN0.2, (B) SBN0.5, and (C) SBN1.0

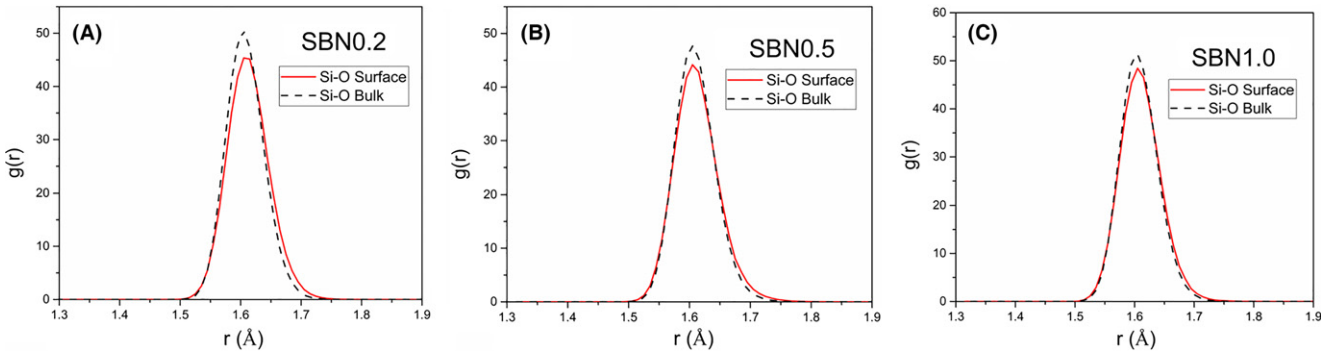

FIGURE 3 Comparison of bulk and surface Si–O pair distribution functions in (A) SBN0.2 glass; (B) SBN0.5 glass; (C) SBN1.0 glass

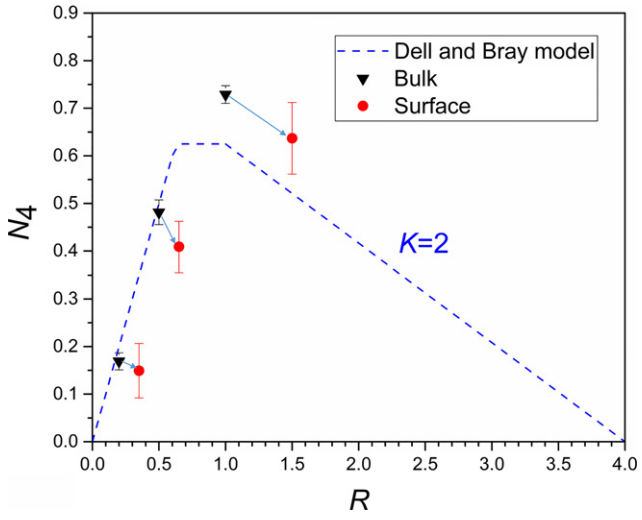

FIGURE 4 Comparison of calculated N_4 with R for surface and bulk SBN glasses (the standard deviation was calculated from three parallel samples). Trends predicted by Dell and Bray model for K=2 are shown as blue dash line

pair distribution and bond angle distribution analyses that will be presented later (Figures 5 and 6). Also, the difference in N_4 numbers between surface and bulk structure increase with the increase in R value. These results suggest that sodium ions accumulated at surface were not used to convert trigonal BO_3 units into tetrahedral BO_4 units. Instead, they were used to create non-bridging oxygen ions on [SiO4] tetrahedrons on the surface.

Bond angle distribution (BAD) of O–Si–O and Si–O–Si was also studied. Corresponding results for sample SBN0.5 are presented here as an example. As shown in Figure 7A, in the bulk structure, the O–Si–O bond angle has a symmetric distribution, with the peak position at around 109°; while for the surface, another peak appears at around 87°. Furthermore, by comparing the bulk and surface Si–O–Si bond angle distribution (Figure 7B), we learn that the Si–O–Si BAD of the bulk structure ranges from 110° to 180°, with a peak around 150°; while that of the surface shifts to lower values. A possible source of distortion in Si–O–Si angle is the concentration increase in small rings of sizes 3 and 4. (Rings are defined as the smallest loops of Si/B–O links.)[34] Additional surface effects are characterized by the emergence of a second peak at around 91° in Si–O–Si BAD for the surface. The O–Si–O and Si–O–Si bond angles in two-membered rings calculated by Bunker et al.[35] were 88.5° and 91.5°, respectively. Therefore, a reasonable inference is that the appearance of smaller bond angles around 90° on the surface is related to the formation of two-membered rings.

To better visualize the surface atomic structure and determine surface structure features, the top 5 Å surface

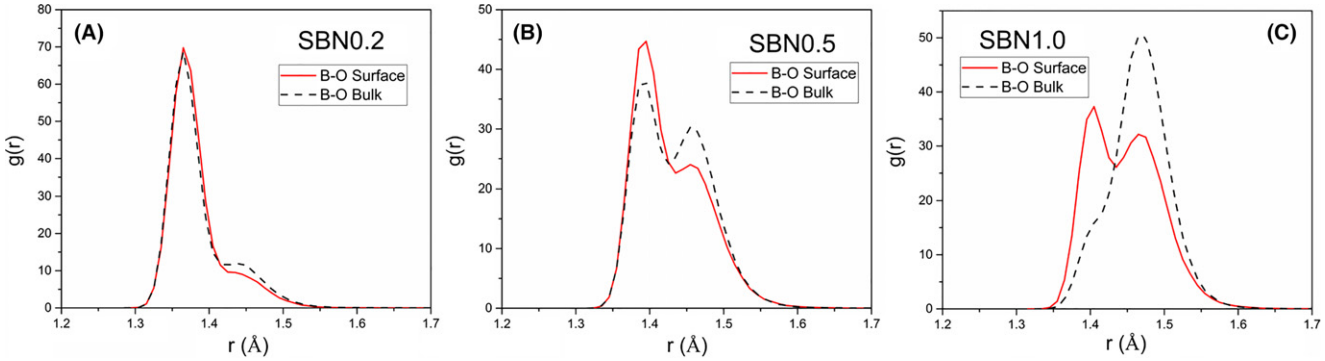

FIGURE 5 Comparison of bulk and surface B–O pair distribution functions in (A) SBN0.2 glass; (B) SBN0.5 glass; (C) SBN1.0 glass

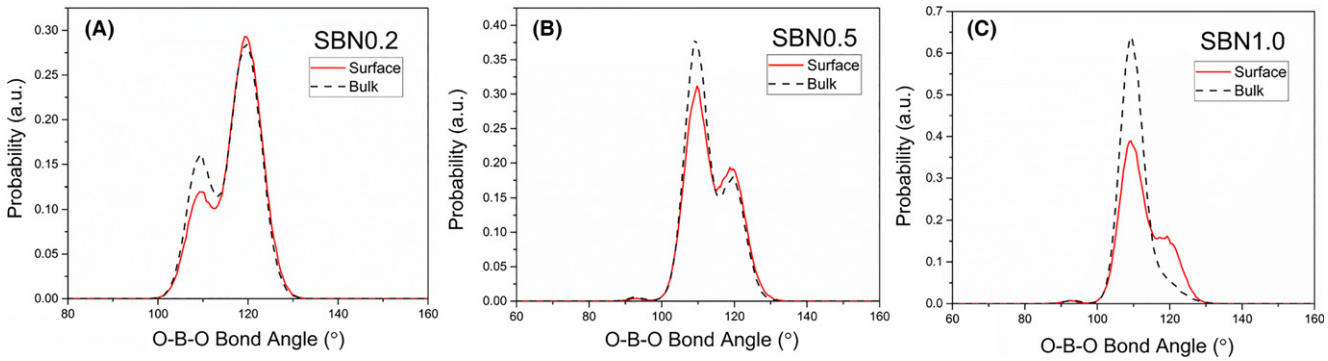

FIGURE 6 Comparison of bulk and surface O–B–O bond angle distribution functions in (A) SBN0.2 glass; (B) SBN0.5 glass; (C) SBN1.0 glass

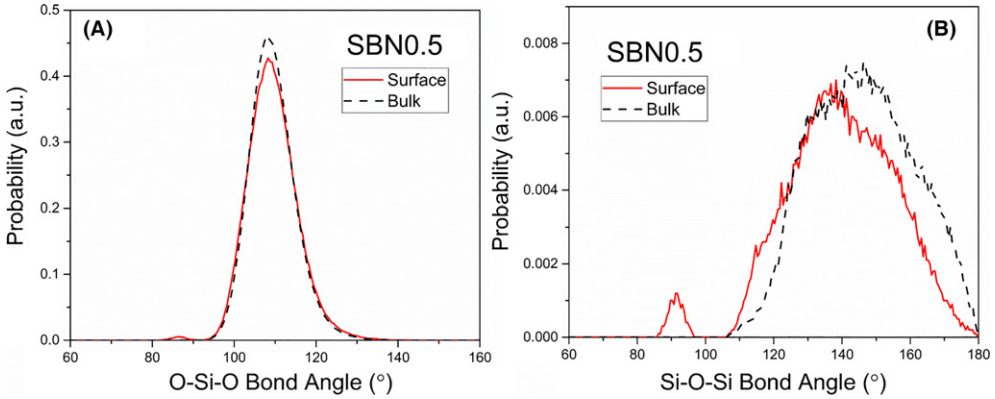

FIGURE 7 Comparison of (A) O–Si–O and (B) Si–O–Si bond angle distribution in bulk SBN0.5 glass and its surface

layer of SBN0.5 glass is shown in Fig. 8 with both the top and side views. Although we observed the existence of two-membered (2M) rings as well as three-coordinated silicon (Si^3) at the surface, the number of these defects is very low as compared to silica surfaces.[16] Table 3 summarizes calculated surface defects concentrations for SBN glass samples with different compositions. For each glass composition, three different surface models were created, and the data shown in Table 3 are the average values. Worth noting is that the formation of two-membered silicon rings at the surface is found in all glass samples, while the concentration of Si^3 decreased to 0 for the sample SBN1.0. A previous MD simulation study of pure silica surface[16] showed an average two-membered ring and Si^3 concentration of 0.884 and 0.778/nm^2, respectively, which is obviously much higher than what our study revealed for SBN glass. That defect sites are highly reactive when exposed to water, considering their high energy states, is well-accepted.[36,37] Thus, a low defect concentration of SBN glass at the surface would be attractive for their application in nuclear industry.

Figure 9 presents ring size distribution on the surface and in the bulk of SBN glass. Ring statistics were calculated from primitive ring distributions of Si–O–Si, Si–O–B, and B–O–B linkages. The bulk has a broad-ring size distribution from 3- up to 15-membered rings; while 2-membered rings showed up on the surface with quite low concentration, thereby confirming our previous results. In addition, the higher concentration of small rings is an important feature of the surface as compared to the bulk structure, and is consistent with the shift of Si–O–Si bond angle for surface (as shown in Figure 7). Formation of these small rings can be explained by the recombination of neighboring dangling bonds such as NBO and Si^3, which generated during surface formation.

4 | DISCUSSION

Compared with the bulk glass, change in composition and structure is clearly observed for the SBN glass surfaces: an increase in sodium concentration at the surfaces was observed for all three samples with different sodium contents. Sodium enrichment was also observed in boron-free E glass and melts from MD simulations.[38] On the other hand, excess NBOs created upon the formation of surface

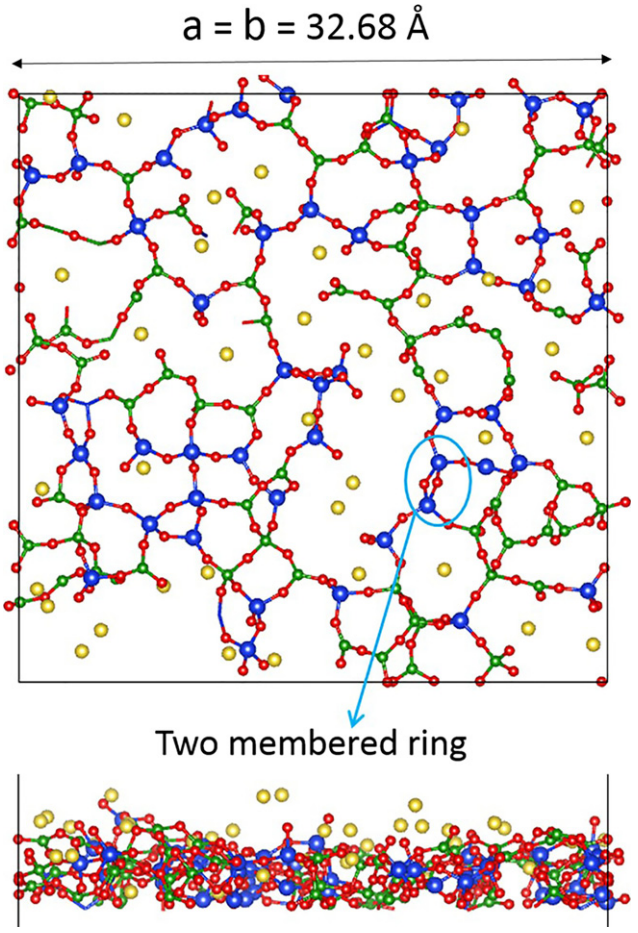

FIGURE 8 Top view and side view of one of the relaxed surface (~5 Å) of SBN0.5. Color codes are red (O), blue (Si), green (B), and yellow (Na)

can be verified by the coordination number change as shown in Table 4, where both Si–NBO bonds and B–NBO bonds concentrations increased at the surface as compared to bulk glass. The increase in NBOs tends to be the driving force behind sodium enrichment of the glass surface, as the accumulation of Na^+ at the surface can be used to compensate the charge of NBOs caused by O–Si or O–B bond breakage.

Another important feature of SBN glass surface is the decrease in N_4 value, which indicates that three-coordinated boron is more favorable at the surface. One possible reason is that the reaction $BO_4 \rightarrow BO_3$ + NBO takes place during the surface formation process, and leads to the BO_3 group as well as nonbridging oxygen increasing at the glass surface. Another possible reason is that the increase in BO_3 group at the SBN glass surface can be analog to the Si^3 formation found in pure silica glass surface studies.[15,16] As boron can form both three- and fourfold coordinated structure units, formation of $^{[3]}B$ at the boron-contained glass surface is much easier and thus preferred over the formation of Si^3. This also explained why the Si^3 defects concentration (defect numbers/surface area) at SBN surface calculated in this work (Table 3) is much lower than that for silica glass (0.6-0.8/nm^2).[15,16] Comparing the defects concentration of three samples, the trend is that as the Na_2O/B_2O_3 ratio increased from 0.2 to 1.0, Si^3 defects concentration decreased from 0.12/nm^2 to 0. This general trend shows that during the surface formation process, sodium as a network modifier is important for the elimination of defects such as ^{3}Si.

The increases in sodium ions concentration and NBOs concentration, and the decrease in N_4 value at the SBN glass surface will weaken the glass network structure and thus make the surface more vulnerable to corrosion, which clearly is not good for use as nuclear waste glass but is desirable for some bioactivity applications. The results of this work verify that bulk glass composition is an important determinant of glass surface properties. Comparison among three SBN glass samples with the same SiO_2/B_2O_3 value (K=2) but different Na_2O/B_2O_3 ratio (R=0.2, 0.5 and 1.0) shows that at glass surface, with increasing Na_2O/B_2O_3 ratio, the concentrations of Na^+, NBO, and $^{[3]}B$ continue to increase while the defects concentration decreases. All these results indicated that a special design of glasses compositions and structures is quite important for their various applications with different performance requirements.

In MD simulations of glasses, an important consideration is the simulation cell size effect as three-dimension periodic boundary condition is commonly employed. According to our study about simulation cell size effect on boron coordination in SBN glass simulation, N_4 number tends to converged as the system size reaches around 1000 atoms.[9] Considering the fact that most simulation results are based on statistical data, an increase in the system size can help improve the accuracy of predictions, especially for surface simulations. In this work, we chose a simulation box with around 3000 atoms as a consideration of both accuracy and time used for simulation. The size should be

TABLE 3 Defect concentrations on SBN glass surfaces (#/nm^2)

	SBN0.2	SBN0.5	SBN1.0
2M ring	0.060	0.063	0.031
Si^3	0.120	0.031	0
Total	0.180	0.094	0.031

TABLE 4 Comparison of Si/B–NBO bond percentage of bulk glass and glass surface

	SBN0.2 (%)	SBN0.5 (%)	SBN1.0 (%)
Si–NBO (Surface)	0.98	4.58	8.03
Si–NBO (Bulk)	0.69	0.76	4.88
B–NBO (Surface)	1.91	2.52	7.37
B–NBO (Bulk)	0.35	0.29	2.93

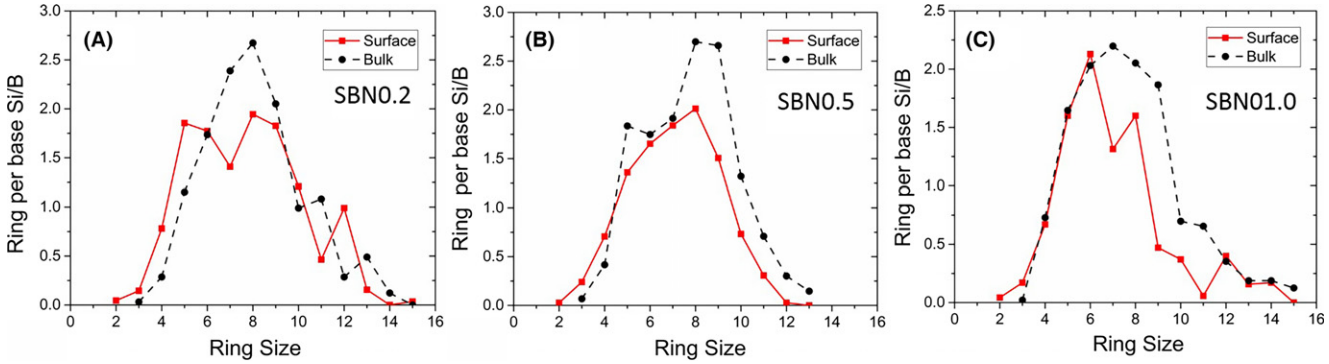

FIGURE 9 Comparison of ring size distribution of the surface and the bulk of (A) SBN0.2 glass, (B) SBN0.5 glass, and (C) SBN1.0 glass

sufficient to capture the bulk and surface structural feature changes in the borosilicate glasses studied in this work.

Another consideration in MD simulations is the cooling rate effect in simulations.[39] The bulk glass is formed at a cooling speed of 5 K/ps while the annealed surface is cooled down from 1000 K to room temperature with 10 K/ps. Both these cooling rates are much higher than experimental values and this high cooling rate in MD simulations of glasses is a common criticism of the simulation results. However, although the cooling speed is several orders higher than real systems, the number of atoms in the simulation cell, of course with three-dimensional periodic boundary condition, is much smaller than the real systems (eg, Avogadro's number). As a result of fast energy exchange of atoms with the surrounding cells,[39] the two effects tend to cancel with each other and, hence, the simulated glass structure is not too much different from experiments, as shown in the comparison of silicate glasses.[40] In a recent study of cooling rate effect on structure and properties of silica glasses, it was shown that a slower cooling rate led to a decrease in glass density (from 2.31 to 2.22 g/cc) and decrease in defect concentration for cooling rate range of 10^{13} to 10^{9} K/s.[41] As the structure of borosilicate glasses is much more complex than silica, a systematic study of both cooling rate and system size on the structure of borosilicate glasses is thus very necessary. These studies are being carried out and will be reported elsewhere (L. Deng, unpublished).

5 | CONCLUSIONS

Three sodium borosilicate glasses and their surfaces with the same K ($[SiO_2]/[B2O_3]$)=2) but different $R([Na_2O]/[B_2O_3])$ values were studied using classical molecular dynamics simulations with recently developed potentials. The composition and structure of the glass surfaces were investigated and compared with those of the bulk glasses. The surface concentration of Na^+ increased as compared to the bulk when the surfaces are formed, resulting in a glass structure with higher R values and a lower percentage of four-fold coordinated boron (N_4) due to preferential formation of NBO connected to B. Thus, the surface has a lower network connectivity, and consequently higher reactivity, as compared to the bulk. In addition, defects including two-membered silicon rings and Si^3 were formed at surface but with lower surface concentration as compared with those for pure silica glass. These surface defects provide potential active sites for the attachment or formation of hydroxyl groups and initiation of glass dissolutions. Thus, this study of the SBN glass dry surface property paves the way for better understanding of the following possible surface reaction processes. Comparisons of surfaces among three different glasses show that with the increase in R value), surface Na^+, NBO, and $^{[3]}B$ concentration increases and coordination defects concentration decreases. Lastly, intermediate-range structural analysis shows that the average ring size at the surface is decreased with a higher concentration of small rings as compared with the bulk glasses.

ACKNOWLEDGMENTS

This work was supported by National Science Foundation DMR Ceramics Program (Project number: 1508001) and Department of Energy Nuclear Energy University Program (NEUP, Project number: # DE-NE000748).

REFERENCES

1. Beales K, Day C, Duncan W, Midwinter J, Newns G. Special issue paper. Preparation of sodium borosilicate glass fibre for optical communication. *Proc Inst Electr Eng*. 1976;123:591–596.
2. Ben-Yakar A, Byer RL. Femtosecond laser ablation properties of borosilicate glass. *J Appl Phys*. 2004;96:5316–5323.
3. Bunker BC, Arnold GW, Day DE, Bray P. The effect of molecular structure on borosilicate glass leaching. *J Non Cryst Solids*. 1986;87:226–253.
4. Wu X, Dieckmann R. Sodium tracer diffusion in glasses of the type $(Na_2O)_{0.2}$ $[(BO_{1.5})_X$ $(SiO_2)_{1-X}]_{0.8}$. *J Non Cryst Solids*. 2011;357:2846–2856.

5. Kilymis D, Delaye J, Ispas S. Density effects on the structure of irradiated sodium borosilicate glass: a molecular dynamics study. *J Non Cryst Solids*. 2016;432:354–360.
6. Huang W, Day DE, Kittiratanapiboon K, Rahaman MN. Kinetics and mechanisms of the conversion of silicate (45S5), borate, and borosilicate glasses to hydroxyapatite in dilute phosphate solutions. *J Mater Sci Mater Med*. 2006;17:583–596.
7. Pan HB, Zhao XL, Zhang X, et al. Strontium borate glass: potential biomaterial for bone regeneration. *J R Soc Interface*. 2010;7:1025–1031.
8. Dell W, Bray PJ, Xiao S. ^{11}B NMR studies and structural modeling of $Na_2O–B_2O_3–SiO_2$ glasses of high soda content. *J Non Cryst Solids*. 1983;58:1–16.
9. Yun Y, Bray P. Nuclear magnetic resonance studies of the glasses in the system $Na_2O–B_2O_3–SiO_2$. *J Non Cryst Solids*. 1978;27:363–380.
10. D'Souza AS, Pantano CG, Kallury KM. Determination of the surface silanol concentration of amorphous silica surfaces using static secondary ion mass spectroscopy. *J Vac Sci Technol, A*. 1997;15:526–531.
11. D'Souza AS, Pantano CG. Mechanisms for silanol formation on amorphous silica fracture surfaces. *J Am Ceram Soc*. 1999;82:1289–1293.
12. Sprenger D, Bach H, Meisel W, Gütlich P. XPS study of leached glass surfaces. *J Non Cryst Solids*. 1990;126:111–129.
13. Zhuravlev L. The surface chemistry of amorphous silica. Zhuravlev model. *Colloids Surf Physicochem Eng Aspects*. 2000;173:1–38.
14. Pantano C, Kelso J, Suscavage M. Surface studies of multicomponent silicate glasses: quantitative analysis, sputtering effects and the atomic arrangement. *Adv Mater Charact*. 1983;15:1–38.
15. Garofalini SH. Molecular dynamics computer simulations of silica surface structure and adsorption of water molecules. *J Non Cryst Solids*. 1990;120:1–12.
16. Du J, Cormack AN. Molecular dynamics simulation of the structure and hydroxylation of silica glass surfaces. *J Am Ceram Soc*. 2005;88:2532–2539.
17. Feuston B, Garofalini S. Topological and bonding defects in vitreous silica surfaces. *J Chem Phys*. 1989;91:564–570.
18. Roder A, Kob W, Binder K. Structure and dynamics of amorphous silica surfaces. *J Chem Phys*. 2001;114:7602–7614.
19. Rimola A, Costa D, Sodupe M, Lambert J, Ugliengo P. Silica surface features and their role in the adsorption of biomolecules: computational modeling and experiments. *Chem Rev*. 2013;113:4216–4313.
20. Zeitler TR, Cormack A. Interaction of water with bioactive glass surfaces. *J Cryst Growth*. 2006;294:96–102.
21. Corrales LR, Du J. Characterization of ion distributions near the surface of sodium-containing and sodium-depleted calcium aluminosilicate melts. *J Am Ceram Soc*. 2006;89:36–41.
22. Inoue H, Masuno A, Watanabe Y. Modeling of the structure of sodium borosilicate glasses using pair potentials. *J Phys Chem B*. 2012;116:12325–12331.
23. Kieu L, Delaye J, Cormier L, Stolz C. Development of empirical potentials for sodium borosilicate glass systems. *J Non Cryst Solids*. 2011;357:3313–3321.
24. Kwon KD, Criscenti LJ. Na borosilicate glass surface structures: a classical molecular dynamics simulations study. *J Miner Soc Korea*. 2013;26:119–127.
25. Smith W, Forester T. DL_POLY_2. 0: a general-purpose parallel molecular dynamics simulation package. *J Mol Graph*. 1996;14:136–141.
26. Guillot B, Sator N. A computer simulation study of natural silicate melts. Part I: low pressure properties. *Geochim Cosmochim Acta*. 2007;71:1249–1265.
27. Deng L, Du J. Development of Effective empirical potentials for molecular dynamics simulations of the structures and properties of boroaluminosilicate glasses. *J Non-Cryst Solids*. 2016;453:177–194.
28. Feuston B, Garofalini SH. Water-induced relaxation of the vitreous silica surface. *J Appl Phys*. 1990;68:4830–4836.
29. Yuan X, Cormack AN. MD simulated structures of soda-lime-silica glass and its surface. *Ceram Trans*. 1997;82:281–286.
30. Tilocca A, Cormack AN. Modeling the water−bioglass interface by *ab initio* molecular dynamics simulations. *ACS Appl Mater Interfaces*. 2009;1:1324–1333.
31. Tilocca A, Cormack AN. Surface signatures of bioactivity: MD simulations of 45S and 65S silicate glasses. *Langmuir*. 2009;26:545–551.
32. Pierce EM, Frugier P, Criscenti LJ, Kwon KD, Kerisit SN. Modeling interfacial glass-water reactions: recent advances and current limitations. *Int J Appl Glass Sci*. 2014;5:421–435.
33. Gin S, Jollivet P, Fournier M, et al. The fate of silicon during glass corrosion under alkaline conditions: a mechanistic and kinetic study with the international simple glass. *Geochim Cosmochim Acta*. 2015;151:68–85.
34. Ganster P, Benoit M, Delaye J, Kob W. Surface of a calcium aluminosilicate glass by classical and *ab initio* molecular dynamics simulations. *Surf Sci*. 2008;602:114–125.
35. Bunker B, Haaland D, Ward K, et al. Infrared spectra of edge-shared silicate tetrahedra. *Surf Sci*. 1989;210:406–428.
36. Morrow B, Cody I. Infrared studies of reactions on oxide surfaces. 6. Active sites on dehydroxylated silica for the chemisorption of ammonia and water. *J Phys Chem*. 1976;80:1998–2004.
37. Tilocca A, Cormack AN. Exploring the surface of bioactive glasses: water adsorption and reactivity. *J Phys Chem C*. 2008;112:11936–11945.
38. Corrales LR, Du J. Characterization of ion distributions near the surface of sodium containing and sodium depleted calcium aluminosilicate glass melts. *J Am Ceram Soc*. 2006;89:36–41.
39. Corrales LR, Du J. Thermal kinetics of glass simulations. *Phys Chem Glasses*. 2005;46:420–424.
40. Du J, Cormack AN. The medium range structure of sodium silicate glasses. *J Non-Cryst Solids*. 2004;349:66–79.
41. Lane JD. Cooling rate and stress relaxation in silica melts and glasses via microsecond molecule dynamics. *Phys Rev E*. 2015;92:012320.
42. Deng L, Du J, 'Simulation cell size and cooling rate effect on boron coordination in borosilicate glasses from MD simulations", in preparation.

How to cite this article: Ren M, Deng L, Du J. Surface structures of sodium borosilicate glasses from molecular dynamics simulations. *J Am Ceram Soc*. 2017;100:2516–2524.

journal

J. Am. Ceram. Soc., 99 [8] 2823–2833 (2016)
DOI: 10.1111/jace.14292

Structural Origin of the Thermal and Diffusion Behaviors of Lithium Aluminosilicate Crystal Polymorphs and Glasses

Mengguo Ren, and Jincheng Du†

Department of Materials Science and Engineering, University of North Texas, Denton, Texas

Lithium aluminosilicate polymorphs α–$LiAlSi_2O_6$, β–$LiAlSi_2O_6$, and the $LiAlSi_2O_6$ glass have been studied comparatively using classical molecular dynamics (MD) simulations with an aim to better understand the structural origin of the different thermo-mechanical behaviors and lithium ion diffusion properties. The melting behaviors and structural evolution were investigated for the three phases using MD simulations. The structural features of the three simulated samples were analyzed using coordination number, pair and bond angle distributions. The results showed that β-$LiAlSi_2O_6$ and the $LiAlSi_2O_6$ glass had similar melting behavior, had more random short-range atomic structures, and lower densities as compared to the α-$LiAlSi_2O_6$ phase, which has a more ordered and compact structure. The lithium ion diffusion behavior in α–$LiAlSi_2O_6$, β–$LiAlSi_2O_6$, and $LiAlSi_2O_6$ glass and their melts are determined and compared by calculating the mean square displacements. It was found that at high temperatures, the melts of α–$LiAlSi_2O_6$, β–$LiAlSi_2O_6$, and $LiAlSi_2O_6$ glass had similar diffusion properties. While at low temperatures, α–$LiAlSi_2O_6$ had the lowest diffusion coefficient and highest diffusion energy barrier due to its more close-packed structure and lacking of defects to facilitate lithium ion diffusion. Both the β–$LiAlSi_2O_6$ and glass show high ionic conductivity even at low temperatures. This originates from their lower density and thus relatively open structures, but slightly different diffusion mechanisms. Lithium ion diffusion in β–$LiAlSi_2O_6$ is through the large available interstitial sites while that in the glass is through vacancies due to high free volume. The glass phase had slightly lower lithium ion diffusion energy barrier and higher lithium ion diffusion coefficients as compared to the β–$LiAlSi_2O_6$ phase, indicating the glass phase can achieve high ionic diffusion and, in some cases, even higher than the crystalline phases with similar densities and short-range structures.

Keywords: *aluminosilicates; glass–ceramics; simulation; diffusion/diffusivity*

I. Introduction

Lithium aluminosilicate (LAS) materials find wide applications in glasses and glass–ceramics and as potential lithium ion solid-state electrolytes due to their high ionic conductivities. Spodumene $LiAlSi_2O_6$ (1:1:4 Li_2O:Al_2O_3:SiO_2) is one of the most important phases of the LAS system and is the main mineral phase for lithium deposit on earth.[1,2] LAS glass–ceramics have high composition tolerance, high chemical and thermal stability, and thus find various technological applications.[3,4] There exist wide solid solution formations of LAS with the silica polymorph structures and they show peculiar properties such as negative or zero thermal expansion coefficients due to thermal expansion anisotropy along different crystallographic orientations.[5,6] For example, average linear thermal expansion coefficient of β-spodumene ($LiAlSi_2O_6$) is only 0.9×10^{-6} K^{-1} and β-eucryptite ($LiAlSiO_4$) even has a negative average thermal expansion coefficient (-6.2×10^{-6} K^{-1}).[7] The low thermal expansion property of LAS have wide range of commercial and technological applications, ranging from thermal shock-resistant stove cooktop plates, telescope mirrors, to high-temperature furnace windows.[8]

LAS glasses and crystalline materials also have been considered as solid-state electrolytes due to their high lithium ion conductivity.[9,10] Garcia et al. synthesized a series of lithium ion conductors on the join Li_4SiO_4–$Li_5AlSi_2O_8$ solid solutions.[11] The results showed that the highest conductivity could reach ~$3 \times 10^{-5}\Omega^{-1}$ cm^{-1} at 100°C, and the variation in conductivity with composition was due to changes in both the conduction activation energy and the mobile ion concentration. Welsch et al. performed diffusion and ionic conductivity studies on $LiAlSi_2O_6$ glass and it was found that the lithium self-diffusivity in $LiAlSi_2O_6$ glass was very similar to that in lithium silicate glasses.[12] Despite wide range of experimental studies, detailed understanding of the structure–property relationship, especially on the ionic diffusion and thermal mechanical behaviors, in LAS materials is still missing.

Molecular dynamics (MD) simulations have also been used to study lithium containing silicate glasses. However, most work so far focused on the binary lithium silicate systems,[13–16] while studies on LAS ternary system are very limited. Li and Garofalini[17] used MD simulations to investigate the structure and the lithium ions diffusion behavior of Li_2O–Al_2O_3–SiO_2 glasses with the same amount of SiO_2 but different R (mole ratio of Al_2O_3/Li_2O) vales using a set of pair potentials with three-body terms. Aluminum was found to be mainly four coordinated and did not change with composition, which can be due to the usage of three-body potential on Al that constrained the aluminum ions to be four coordination. The simulated results show that with the increase of R, lithium ions alter from bonding to nonbridging oxygen to bonding to the bridging oxygen in $[AlO]^{4-}$ tetrahedra, and when $R = 1$, lithium ions has the lowest diffusion energy barrier. Xiang et al.[18] recently studied the sodium aluminosilicate glasses using MD simulations with partial charge effective two-body potentials and compared the effect of potentials on the generated structures of compositions ranging from peralkali to peralumina. The results show that the partial charge pairwise potentials work well for the aluminosilciate system. The results also show that for the composition with Al/Na ration equals 1 and the peralkali compositions, aluminum ions are mainly four coordinated, while small amount of five coordinated Al are formed in peralumina compositions. Oxygen triclusters were found to exist in the glasses as a charge compensation mechanism for high coordinated aluminum ions. Narayanan et al.[19] have developed a set of potentials in the framework of reactive force

J. Mauro—contributing editor

Manuscript No. 38098. Received January 25, 2016; approved April 13, 2016.
†Author to whom correspondence should be addressed. e-mail: Jincheng.du@unt.edu

field (ReaxFF) for the LAS systems. This set of potentials was shown to be able to correctly reproduce the relative stability of α-, β-, γ-eucryptite ($LiAlSiO_4$) polymorphs and the mechanical properties of the crystals.[19] However, the suitability of these potentials to simulate the melting behaviors of the crystals and glass formation is yet to be tested. Earlier potentials for silicates utilized full ionic charges and, as a result, three-body terms were required to reproduce the tetrahedron shapes of the glass former cation oxygen polyhedrons (e.g. [SiO4]) building blocks. More recent potential developments[20–22] showed that, when partial charges are used to describe the partially covalent and partially ionic bonds in silicates, effective pairwise potentials are capable of describing the structure and properties silicate and aluminosilicate crystalline[23,24] and glass systems.[18,25–27] More complicated potentials that include polarization, charge transfer, or many body effect provide more accurate descriptions of interatomic bonding, but they also have lower computational efficiency. As a result, the partial charge-effective two-body potentials were chosen to study the structure and thermal-mechanical behaviors of LAS crystal and glass materials in this work.

The spodumene phase with the $LiAlSi_2O_6$ (or Li_2O–Al_2O_3–$4SiO_2$) composition represents one of the most important LAS crystalline phases. Natural spodumene is mostly found as α-$LiAlSi_2O_6$ with $C2/c$ symmetry ($Z = 4$; $a = 9.48$ Å, $b = 8.40$ Å, $c = 5.22$ Å, $\beta = 110°$.[28]) In this structure, silicon is in the center of tetrahedral sites and there are two kinds of six coordinated sites, M1 and M2 [Fig. 1(a)]. The M1 sites are occupied by Al^{3+} and M2 by Li^+ ions.[29] The high-temperature phase β-$LiAlSi_2O_6$ (Fig. 2) belongs to the tetragonal space group $P4_12_12$ ($Z = 4$; $a = 7.541$ Å, $c = 9.156$ Å.[30]) Compared to α-$LiAlSi_2O_6$, both Si^{4+} and Al^{3+} are fourfold coordinated and resides in oxygen tetrahedrons in β–$LiAlSi_2O_6$, resulting a less densely packed structure. The structure of β–$LiAlSi_2O_6$ can also thought of as the three-dimensional network structure of silica made by corner-sharing [SiO_4] tetrahedrons (in the structure of high-pressure keatite phase) with one-third of Si^{4+} being randomly replaced by Al^{3+} and each $[AlO_4]^-$ group charge compensated by one Li^+ ion.[31.]

In this work, we studied α, β-spodumene and the $LiAlSi_2O_6$ glass using classical molecular dynamics (MD) simulations with a set of effective partial charge pairwise potentials that have been used in a number of silicate and alumionsilicate glass systems. The aim of these simulations is gain better understanding of the structural differences in the phases, the thermomechanical behaviors as a function of temperature, and the influence of structure on lithium diffusion behaviors. This paper is arranged as follows: MD simulation details are introduced in the Section II, including the potential model used here, how the crystal and glass structures are generated, and the methods used to calculated diffusion properties and structural analysis. The results of simulation are subsequently presented in the Section III. Here, we first compared the structures of α-$LiAlSi_2O_6$, β–$LiAlSi_2O_6$, and $LiAlSi_2O_6$ glass by analyzing the pair distribution function and bond angle distribution data. Then, we further deal with the diffusion properties derived based on mean square displacement (MSD) calculations. In the Section IV, discussions on the significance of these results in understanding the ionic diffusion behaviors are presented. Finally, in the section V, we summarized our findings in this work.

II. Simulation Details

α–$LiAlSi_2O_6$, β–$LiAlSi_2O_6$, and $LiAlSi_2O_6$ glass were studied using classic molecular dynamic (MD) simulations that performed using the DL-POLY program.[32] Simulation boxes with a total number of 4000 atoms were used in the MD simulation. The initial input structures of α–$LiAlSi_2O_6$[28] and β–$LiAlSi_2O_6$[30] were from the Inorganic Crystal Structure Database. The initial $LiAlSi_2O_6$ glass was generated by randomly put atoms, with the experimental measured density (2.374 g/cm^3),[33] in cubic simulation boxes. Then, the glass structures were generated by the simulated melt and quench process.

A set of partial charge pairwise potentials has been used in all the simulations of this work, which is similar to the widely used BKS and TTAM potentials.[20] The charges of O, Si, Al, and Li are assigned to −1.2, 2.4, 1.8 and 0.6, respectively. Short-range potentials acting between pairs of atoms include both repulsive (due to electron cloud overlap) and attractive terms (due to Van der Waals or dispersion interaction). The short-range interactions of the potentials have the Buckingham form,

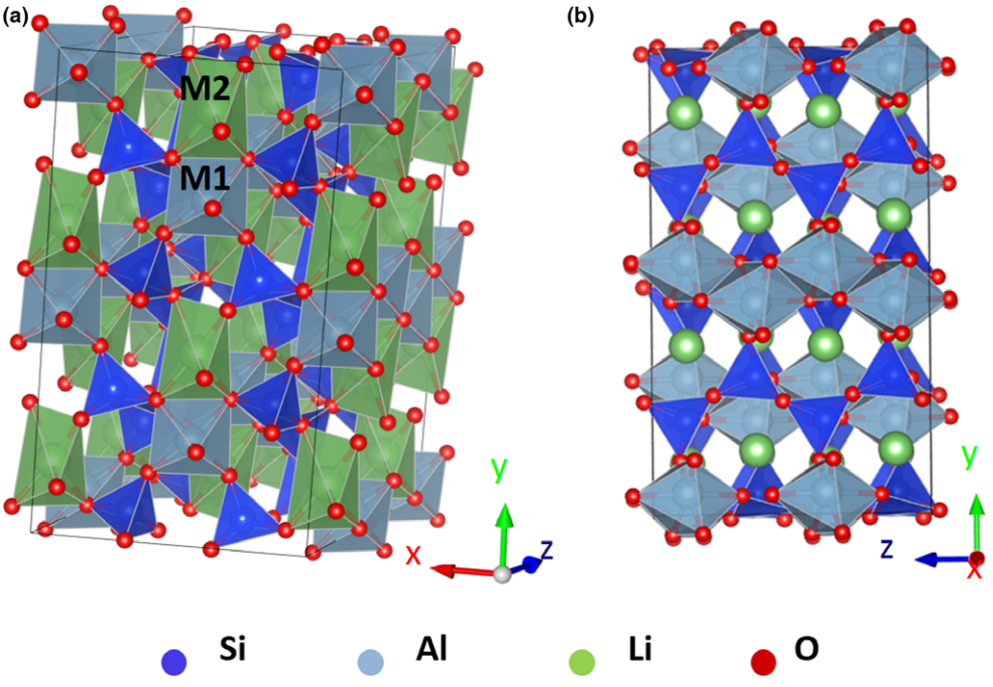

Fig. 1. Crystal structure of α–$LiAlSi_2O_6$.

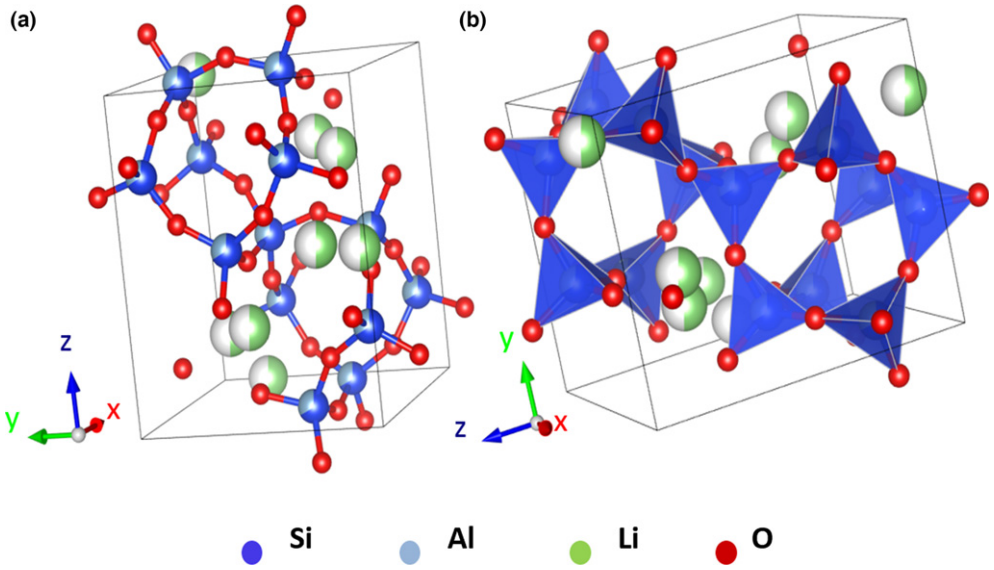

Fig. 2. Crystal structure of β–$LiAlSi_2O_6$.

$$V(r) = A \cdot \exp(-r/\rho) - C/r^6$$

where r is the distance between the two atoms and A, C, and ρ are parameters. The parameters for this potential (as shown in Table I) were initially fitted to both structure and physical properties of various minerals.[22,34] In the original form of Buckingham potential, the energy diverges to negative infinity at small distances. To solve this problem, a repulsion function $V(r) = B/r^n + Dr^2$ for the r values smaller than r_c was introduced to replace the original potential to maintain repulsion at short distances. Here, r_c is defined as the r value where the third derivative of potential energy was zero and B, n, and D are fitted parameters that make the potential, force (first derivative of potential), and first derivative of force continuous from both functions at r_c; hence, the potential and force functions are smooth after the corrections.

Long-range Coulomb interactions were calculated using the Ewald summation method. The Verlet Leapfrog algorithm with a time step of 1 fs was used to integrate the equation of motion. The isothermal and isobaric ensemble (NPT) with Berendsen thermostat and barostat was used in the simulations. After NPT run for 60 000 steps (a time range of 60 ps), a MD run with microcanonical ensemble (NVE) was performed for another 60 000 steps to further equilibrate the system at each temperature.

Tables II and III show the comparison of the structures and properties of α–$LiAlSi_2O_6$ and β–$LiAlSi_2O_6$ calculated using the potential parameters listed in Table I and those from experiments. The results show that the cell parameters and average bond distances from our simulation are in good agreement with experiments. The calculated bulk modulus of α–$LiAlSi_2O_6$ is 129.5 Gpa, which is quite closed to the average experimental value.[35,36] The general good agreement with the experiments on both the calculated structure and the properties of α–$LiAlSi_2O_6$ and β–$LiAlSi_2O_6$ indicates that the potential parameters work well for the LAS system.

Mean square displacements (MSDs) have been calculated at different temperature to obtain the diffusion and dynamic properties of the ions in crystals and glass, which is defined as the distance ion travels over a time interval t averaged over all ions of the same type, that is:

Table I. Buckingham Potential Parameters[22]

Paris	A (eV)	ρ (Å)	C (eV Å^6)
$Si^{2.4}$–$O^{-1.2}$	13702.905	0.193817	54.681
$Al^{1.8}$–$O^{-1.2}$	12201.417	0.195628	31.997
$Li^{0.6}$–$O^{-1.2}$	41051.938	0.151160	0.0
$O^{-1.2}$–$O^{-1.2}$	2029.2204	0.343645	192.58

Table II. Comparison of Simulated and Experimental Cell Parameters, Bond Distances, Bulk Modulus, Shear Modulus, and Young's Modulus for α–$LiAlSi_2O_6$

	Simulation (this work)	Experimental
a (Å)	9.668	9.479[28]
b (Å)	8.403	8.403[28]
c (Å)	5.360	5.223[28]
α = γ (°)	90	90[28]
β (°)	110.25	110.14[28]
Ave. Al–O distance (Å)	1.902	1.923[28]
Ave. Si–O distance (Å)	1.605	1.622[28]
Ave. Li–O distance (Å)	2.245	2.214[28]
Bulk modulus (Gpa)	129.5	116.8–146.1[35,36]
Shear modulus (Gpa)	75.5	–
Young's modulus (Gpa)	141.0/102.9/ 132.3†	–

†For a, b, and c direction, respectively.

Table III. Comparison of Simulated and Experimental Cell Parameters, Bond Distance, Bulk Modulus, Shear Modulus, and Young's Modulus for β–$LiAlSi_2O_6$

	Simulation (this work)	Experimental[30]
$a = b$ (Å)	7.718	7.541
c (Å)	8.895	9.156
Ave. Al–O distance (Å)	1.656	1.643
Ave. Si–O distance (Å)	1.656	1.643
Ave. Li–O distance (Å)	2.015	2.081
Bulk modulus (Gpa)	102.5	–
Shear modulus (Gpa)	40.4	–
Young's modulus (Gpa)	147.1/147.1/102.7†	–

†For a, b, and c direction, respectively.

$$<r^2(t)> = \frac{1}{n}\langle\sum_{i=1}^{n} | r_i(t) - r_i(t_0) |^2\rangle \quad (1)$$

The NVE trajectories after NPT runs at each temperature were recorded for MSD calculations. Specifically, after the initial 20 000 steps equilibration with the NVE ensemble, the following 200 000 steps (a time range of 200 ps) performed with configurations recorded every 10 steps. At long enough times, MSD exhibits a linear relationship versus time and self-diffusion coefficients (D) were calculated from the linear regime of the MSD versus time curve via the Einstein equation:

$$D = \frac{1}{6}\lim_{t\to\infty}\frac{<r^2>}{t} \quad (2)$$

where $<r^2>$ is the MSD and t is the time.[37] To ensure statistical meaningful results, MSD calculations are usually averaged over the same type particles and over large number of origins. In this work, we averaged over all lithium ions in the system and 200 origins during MSD calculation.

Based on Arrhenius relationship of diffusion coefficient, we got:

$$D = D_0 \exp(-\Delta E_a/RT) \quad (3)$$

where E_a is the diffusion energy barrier, T is the temperature in kelvin, and R is the gas constant. Take the logarithm on both sides of the Eq. (3), it is obtained:

$$\ln D = \ln D_0 - \frac{\Delta E_a}{RT} \quad (4)$$

Therefore, the activation energy can be calculated from the slop of the linear fitting of $\ln D$ relative to $1/T$.

III. Results

(1) Short- and Medium-Range Atomic Structures in Crystalline and Glass Spodumene

The structure analysis at room temperature was performed for α- and β-spodumene, as well as those for the $LiAlSi_2O_6$ glass from MD simulations. Figure 3 shows a snapshot of the simulated $LiAlSi_2O_6$ glass structure.

(A) Local Environment Around Si and Al: The local structures around silicon and aluminum were well captured by the pair distribution functions (PDF) (Fig. 4), bond angle distributions (Figs. 6–8) as well as by the accumulation coordination number of oxygen around silicon and aluminum ions (Fig. 5) calculated from the models obtained by the MD simulations. For all the three samples, silicon is 100% four coordinated to oxygen [Fig. 5(a)] with an average Si–O bond length of 1.61 Å, suggesting that the local structure around silicon is not sensitive to the changes in structure. Al–O PDFs of β–$LiAlSi_2O_6$ and $LiAlSi_2O_6$ glass have primary peaks with similar amplitude and both located at ~1.77 Å. Compared to Al–O primary peaks of β–$LiAlSi_2O_6$ and $LiAlSi_2O_6$ glass, the Al–O first peak of α–$LiAlSi_2O_6$ is broader and with smaller amplitude. It is centered at larger r value around 1.90 Å indicating a longer Al–O bond length. The experimental Al–O distance for tetrahedral and octahedral coordinated aluminum are 1.76 Å[38] and 1.91 Å[39], respectively, confirming that the structures simulation agree well with experiments. Figure 5(b) shows the accumulated coordination number of oxygen around aluminum ions, calculated as the integration of partial pair distribution functions (T(r)) over pair distance r. Using the first minimum as the integration of pair correlation (2.60 Å for α–$LiAlSi_2O_6$, 2.20 Å for β–$LiAlSi_2O_6$ and $LiAlSi_2O_6$ glass), the coordination numbers of Al was found to be 4 in β–$LiAlSi_2O_6$ as well as in $LiAlSi_2O_6$ glass, and 6 in α-$LiAlSi_2O_6$. The increase in oxygen coordination numbers around aluminum in α–$LiAlSi_2O_6$ indicating a much more compacted structure compared with β–$LiAlSi_2O_6$ and $LiAlSi_2O_6$ glass.

It can be seen from Fig. 6(a) that the O–Si–O bond angle distributions (BADs) for α–$LiAlSi_2O_6$, β–$LiAlSi_2O_6$, and $LiAlSi_2O_6$ glass are quite similar. Peaks of the three BADs are all centered around 109° while the intensity of the peak decrease according to the order of α–$LiAlSi_2O_6$, β–$LiAlSi_2O_6$, and $LiAlSi_2O_6$ glass. The O–Al–O BADs are shown in Fig. 6(b). There are two peaks in the O–Al–O BAD for α–$LiAlSi_2O_6$: the major peak at 89° and the broad peak with lower intensity at around 170°. This result reflects the six-coordination states of aluminum ions in α-$LiAlSi_2O_6$ structure. For β–$LiAlSi_2O_6$ and $LiAlSi_2O_6$ glass, the O–Al–O BADs are featured with peaks around 107°, proving the tetrahedral coordination of aluminum ions in these two structures.

For the understanding of how the aluminum oxygen polyhedrons are connected, we obtained the Al–O–Al BADs as shown in Fig. 7. Al–O–Al BAD of α–$LiAlSi_2O_6$ shows a peak at 96° indicating that the aluminum oxygen polyhedrons in α-$LiAlSi_2O_6$ structure are edge shared. Compared with α–$LiAlSi_2O_6$, the Al–O–Al BAD peak of β–$LiAlSi_2O_6$ located around 140° is much broad. This suggested that β–$LiAlSi_2O_6$ possesses the corner-sharing aluminum oxygen polyhedral. There are two peaks in the Al–O–Al BAD of $LiAlSi_2O_6$ glass: one centered at around 90° and the other at around 120°. So, it can be known that both edge-sharing and corner-sharing aluminum oxygen polyhedrons exist in the $LiAlSi_2O_6$ glass structure.

The Si–O–Si BADs are shown in Fig. 8(a). There is only one peak for each sample. α–$LiAlSi_2O_6$ has a peak centered at 143° with the largest intensity. The Si–O–Si BAD peaks for β–$LiAlSi_2O_6$ and $LiAlSi_2O_6$ glass centered around 155° and 150°, respectively. Figure 8(b) shows the Si–O–Al BADs for three samples. For α–$LiAlSi_2O_6$, there are two peaks in the Si–O–Al BAD: one centered at 122° and the other centered at 150°. The Si–O–Al BAD peaks for β–$LiAlSi_2O_6$ and $LiAlSi_2O_6$ glass centered around 148° and 133°, respectively. It can be noticed that the Si–O–Al bond angle for β–$LiAlSi_2O_6$ and $LiAlSi_2O_6$ glass are smaller than their Si–O–Si bond angles, which is because compared with Si^{4+}, Al^{3+} has smaller positive charge and thus also the smaller repulsion between the cations.

(B) Local Environment Around Li: Figure 9 compares the Li–O and Li–Li pair distribution functions of α–$LiAlSi_2O_6$, β–$LiAlSi_2O_6$, and $LiAlSi_2O_6$ glass. Bond lengths of

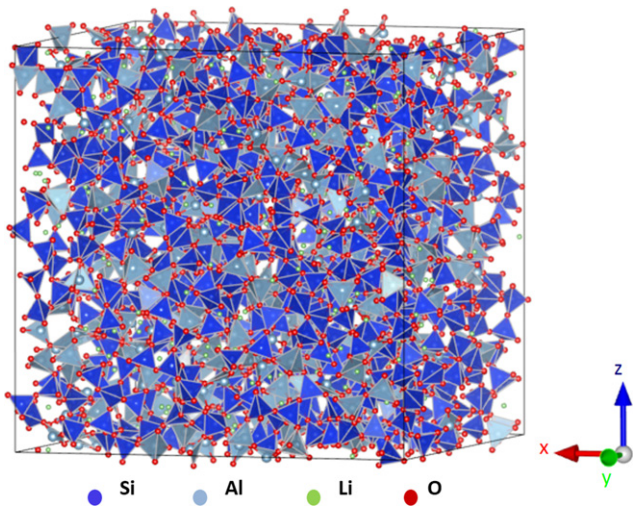

Fig. 3. Snapshot of the structure of $LiAlSi_2O_6$ glass from MD simulations

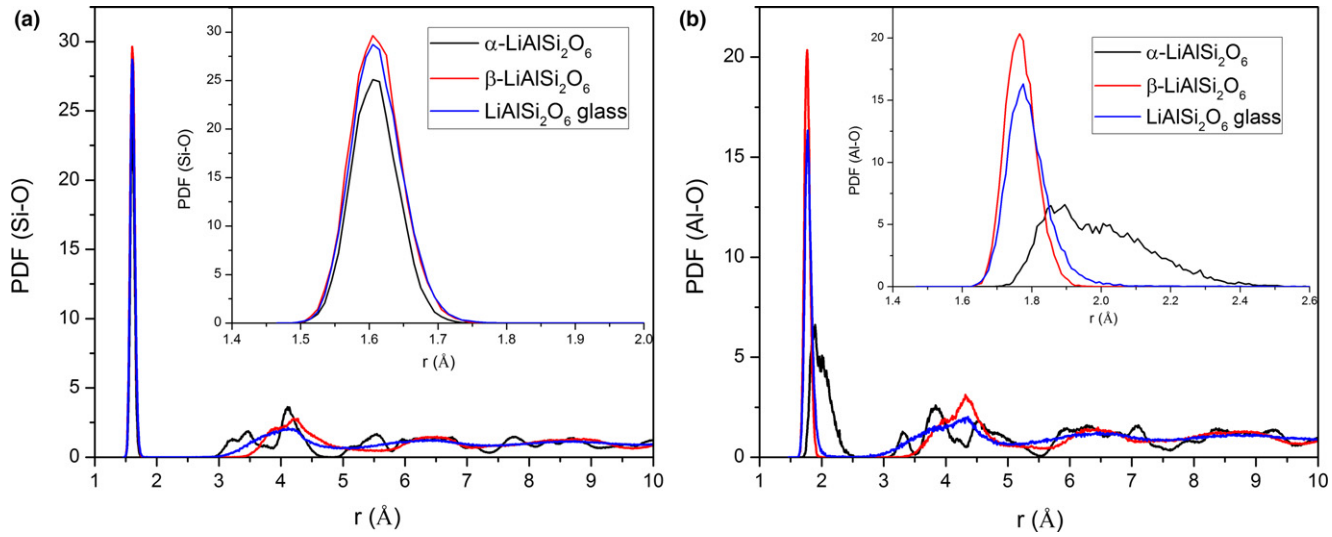

Fig. 4. (a) Si–O (b) Al–O pair distribution functions for α–$LiAlSi_2O_6$, β–$LiAlSi_2O_6$ and $LiAlSi_2O_6$ glass.

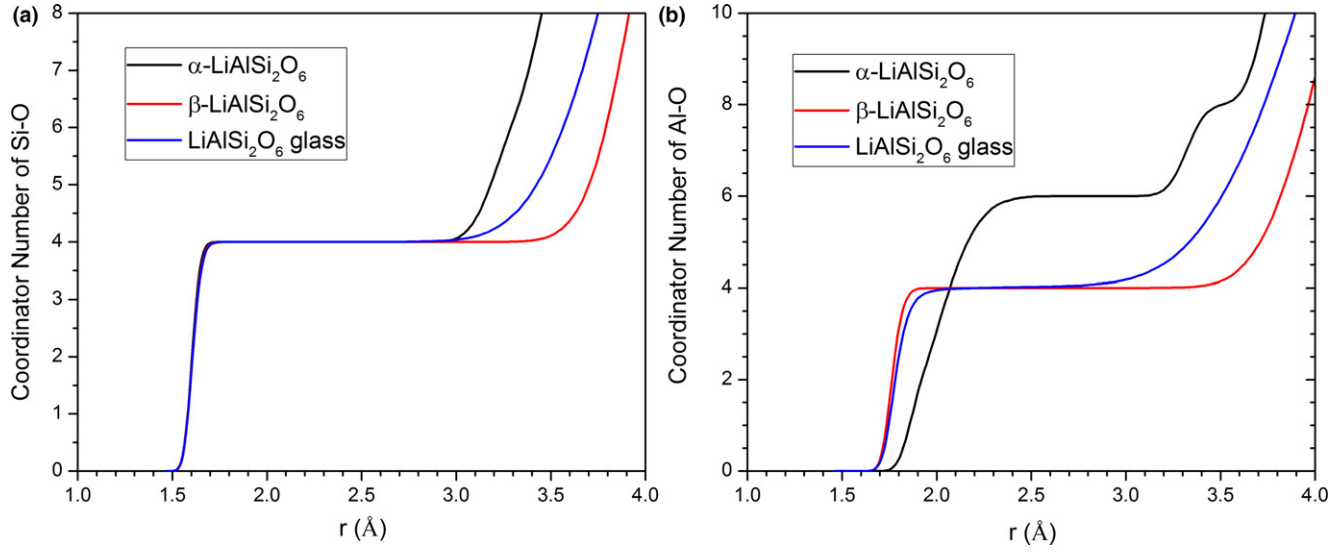

Fig. 5. Accumulation coordination number of (a) oxygen around silicon ions; (b) oxygen around aluminum ions for α–$LiAlSi_2O_6$, β–$LiAlSi_2O_6$ and $LiAlSi_2O_6$ glass.

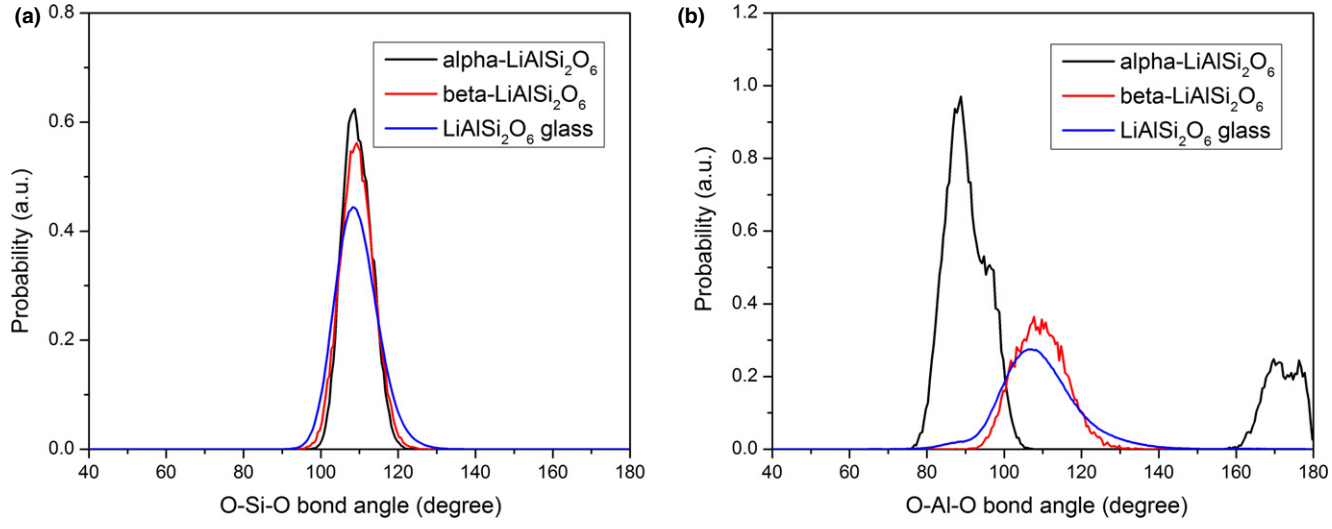

Fig. 6. (a) O–Si–O (b) O–Al–O bond angle distribution for α–$LiAlSi_2O_6$, β–$LiAlSi_2O_6$ and $LiAlSi_2O_6$ glass.

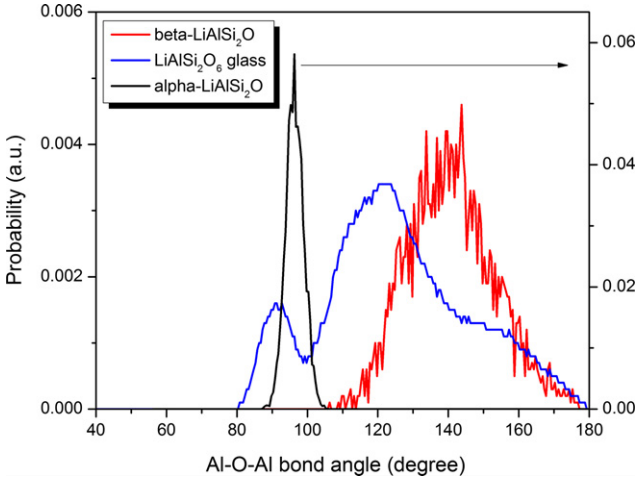

Fig. 7. Al–O–Al bond angle distribution for α–$LiAlSi_2O_6$, β–$LiAlSi_2O_6$, and $LiAlSi_2O_6$ glass.

Li–O obtained from Fig. 9(a) show that average Li–O bond length in α–$LiAlSi_2O_6$ (2.245 Å) is larger than that in β–$LiAlSi_2O_6$ (2.015 Å) and $LiAlSi_2O_6$ glass (2.005 Å). It can be further known from the Fig. 10(a) that the lithium coordination number of α–$LiAlSi_2O_6$ is 6 while the lithium coordination number of β–$LiAlSi_2O_6$ and $LiAlSi_2O_6$ glass are around 4. On the experimental side, Li ions were found to be coordinated by four oxygen with an average Li–O bond length of 2.081 Å for β–$LiAlSi_2O_6$ and lithium coordination number of 8 with an average Li–O bond length of 2.214 Åwas found in α–$LiAlSi_2O_6$,[28,30] confirming the reasonability of corresponding results that got from our simulation.

Analysis of Li–Li pair distribution functions [Fig. 9(b)] can be used to predict clustering formation of lithium ions. The Li–Li pair distribution function of α–$LiAlSi_2O_6$ has the first peak at around 5.10 Å, which is corresponding to the nearest Li–Li distance. The existence of distinct peaks at over 10 Å suggests that the lithium is distributed in a very ordered manner in α–$LiAlSi_2O_6$ crystalline structures. However, in β–$LiAlSi_2O_6$ and $LiAlSi_2O_6$ glass, Li–Li pair distribution functions are very broad and less intensive, indicating that the lithium distributions in these two structures are much more random. Figure 10(b) shows that the Li–Li coordination number of α–$LiAlSi_2O_6$ was steady around 8 at the cut-off range of 5.89 Å. While for β–$LiAlSi_2O_6$ and $LiAlSi_2O_6$ glass, the Li–Li coordination numbers keep increasing and do not show any plateau at certain cut-off range. Comparing the Li–Li coordination number for β–$LiAlSi_2O_6$ and $LiAlSi_2O_6$ glass, it can be noticed that the line representing $LiAlSi_2O_6$ glass is always above that for β–$LiAlSi_2O_6$. This result

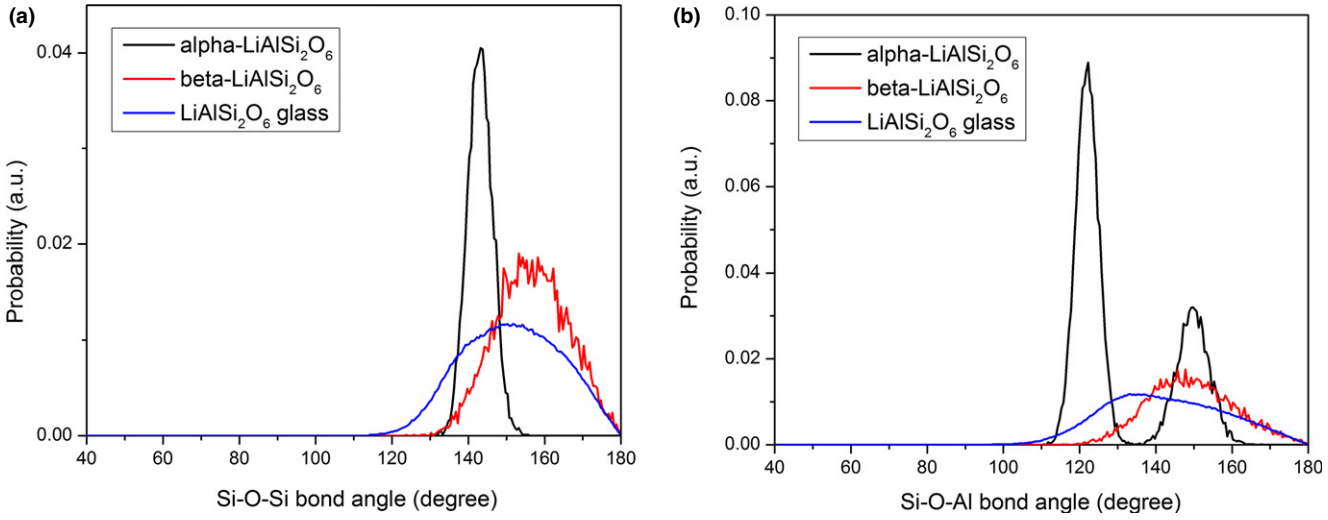

Fig. 8. (a) Si–O–Si and (b) Si–O–Al bond angle distribution for α–$LiAlSi_2O_6$, β–$LiAlSi_2O_6$, and $LiAlSi_2O_6$ glass.

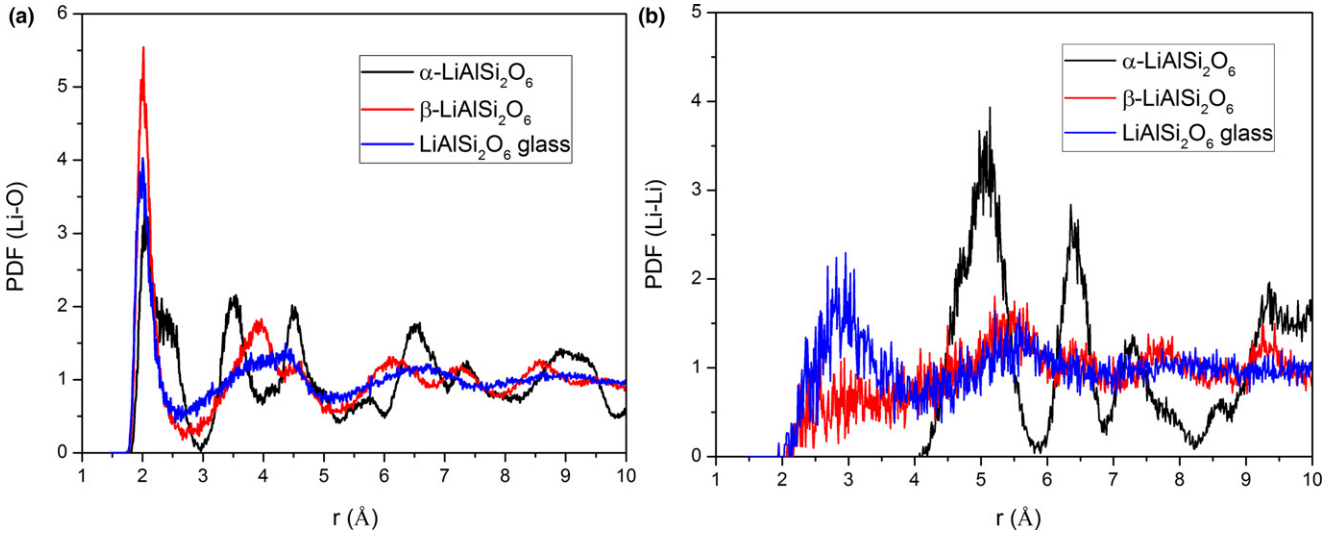

Fig. 9. (a) Li–O (b) Li–Li pair distribution functions for α–$LiAlSi_2O_6$, β–$LiAlSi_2O_6$, and $LiAlSi_2O_6$ glass.

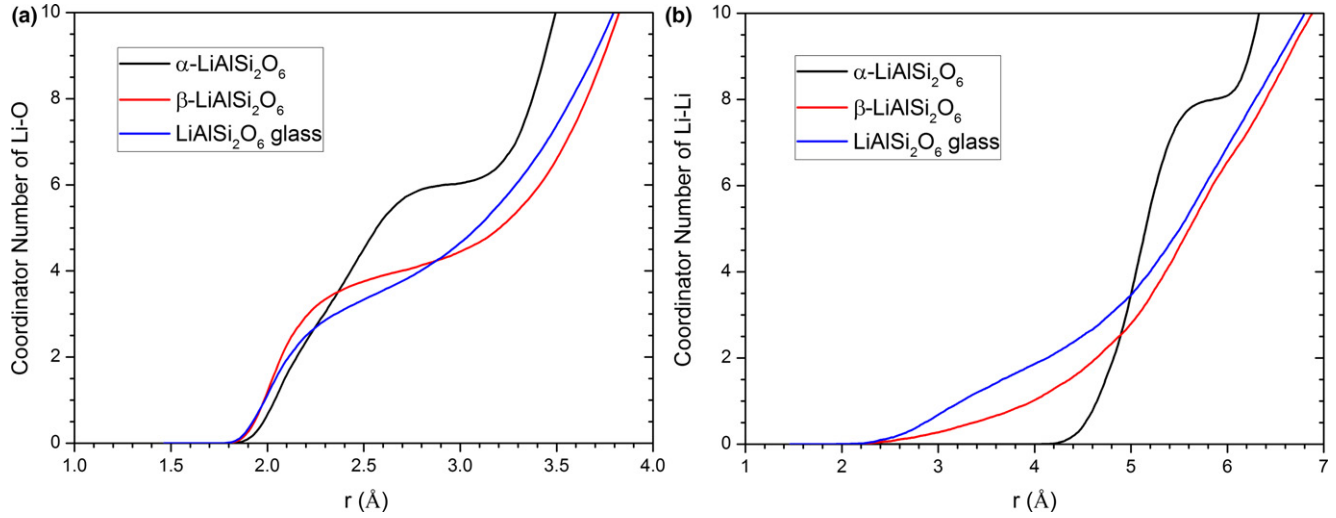

Fig. 10. Accumulation coordination number of (a) oxygen around lithium ions; (b) lithium around lithium ions for α–$LiAlSi_2O_6$, β–$LiAlSi_2O_6$, and $LiAlSi_2O_6$ glasses

indicates that the probability to find other lithium ions around a given one at shorter distance in $LiAlSi_2O_6$ glass is higher than the corresponding probabilities in β–$LiAlSi_2O_6$.

(C) Cation–Cation Distribution: The comparison of the Li–Al, Li–Si, Al–Si, and Al–Al pair distribution functions among α–$LiAlSi_2O_6$, β–$LiAlSi_2O_6$, and $LiAlSi_2O_6$ glass is shown in Fig. 11. The general trend from all these cation–cation pair distribution functions is that the quantity, intensity, and sharpness of peaks are decreased in the sequence of α–$LiAlSi_2O_6$, β–$LiAlSi_2O_6$, and then $LiAlSi_2O_6$ glass. Unlike in α–$LiAlSi_2O_6$ structure where all the atoms are arranged in an ordered way, position of aluminum in β–$LiAlSi_2O_6$ is not

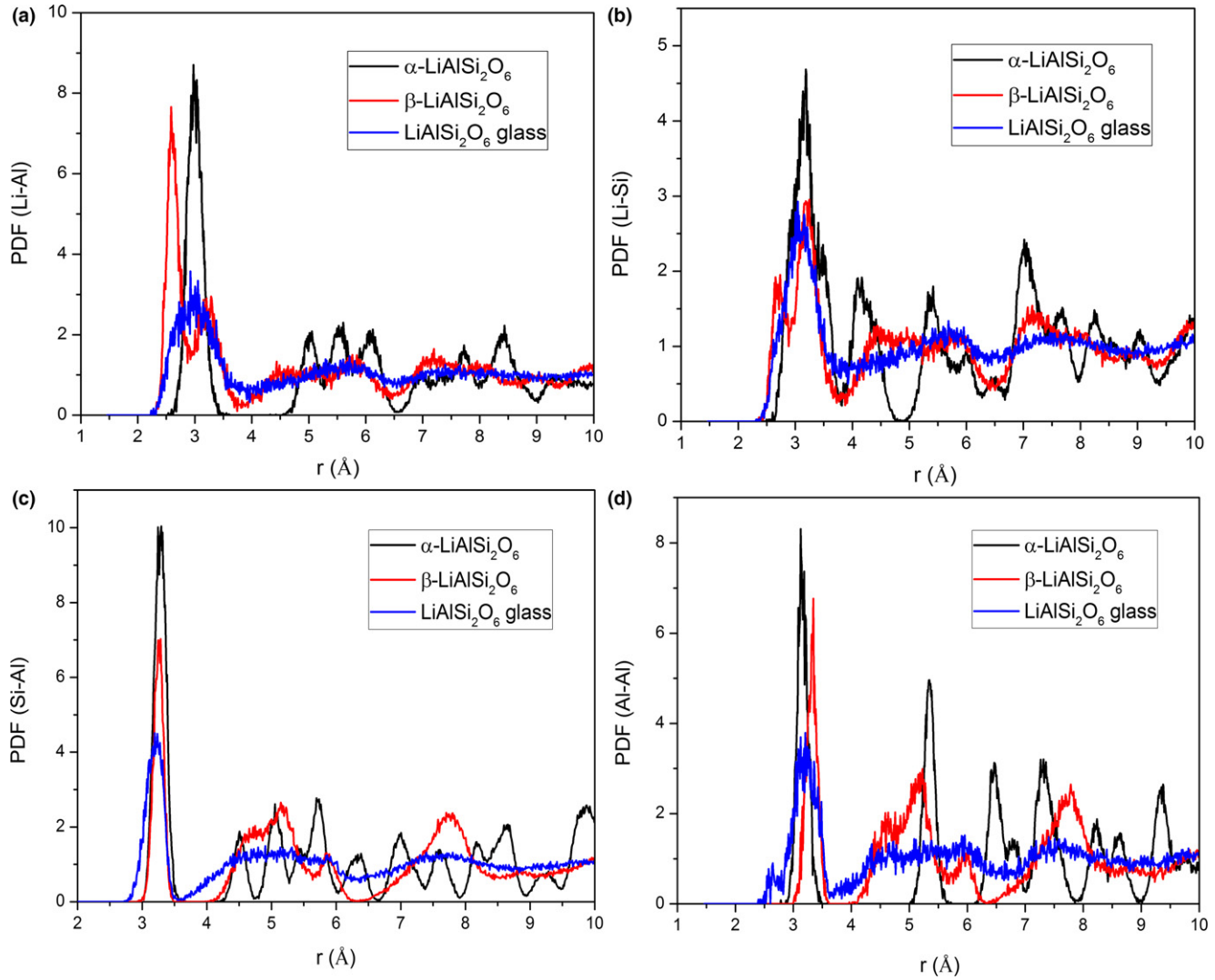

Fig. 11. Cation–Cation pair distribution functions for (a) Li–Al (b) Li–Si (c) Al–Si (d) Al–Al of α–$LiAlSi_2O_6$, β–$LiAlSi_2O_6$, and $LiAlSi_2O_6$ glass.

fixed. They take 1/3 of the tetrahedral sites at random and the other 2/3 sites are occupied by silicon. Due to such randomness introduced in the structure, β–$LiAlSi_2O_6$ shows overall similar behaviors of PDFs as compared to the $LiAlSi_2O_6$ glass.

The Al–Al pair distribution functions [Fig. 11(d)] shows that β–$LiAlSi_2O_6$ has the largest Al–Al distance, indicating that when aluminum takes the 1/3 tetrahedral sites randomly, they will try to avoid to get too close with each other. As the aluminum is sitting at the tetrahedral site in β–$LiAlSi_2O_6$, each $[AlO_4]^-$ need to be charge compensated by a Li^+. So, from Fig. 11(a), we can notice that the Al–Li distance for β–$LiAlSi_2O_6$ is the smallest one with a value of 2.59 Å.

(2) Melting Behaviors of the Three Phases

For visualization and better understanding of the simulated melting process, structure change of β–$LiAlSi_2O_6$ during the increase in temperature is shown in Fig. 12 as a representation. Figure 13(a) and (b) show the volume and configurational (or potential) energy change of three samples during the temperature rise process using constant ambient pressure simulations, respectively. The temperature was increased from 300 to 500 K and then gradually to 4500 K with an interval of 500 K. While around the phase transition point (glass transition temperature and crystal melting temperature) for each sample, additional temperatures with a smaller interval of 100 or 200 K were used to get detailed information of volume and energy changes around the transition. At each temperature, 20 000 steps (a time range of 20 ps) equilibration with the NPT ensemble were performed with a time step of 0.5 fs. The volumes of all three samples keep expansion with temperature suggesting an overall positive thermal expansion coefficient in the three systems. At low temperature range (300–2000 K), β–$LiAlSi_2O_6$ and $LiAlSi_2O_6$ glass have similar volume change while α–$LiAlSi_2O_6$ has much small volume change, suggesting a lower thermal expansion coefficient in the latter. At the temperature range of 2000–3000 K, both α–$LiAlSi_2O_6$ and β–$LiAlSi_2O_6$ go through a sudden change in volume and configurational energy. The abrupt change in volume as well as configurational energy for α–$LiAlSi_2O_6$ happens between 2700 and 2800 K, indicating that the melting temperature of α–$LiAlSi_2O_6$ lies between these two temperatures. Similarly, the melting temperature of β–$LiAlSi_2O_6$ can be determined as between 2900 and 3000 K, showing that β–$LiAlSi_2O_6$ as a high-temperature phase also has a calculated melting temperature which is about 200 K higher than that of the low temperature α–$LiAlSi_2O_6$ phase. For $LiAlSi_2O_6$ glass, not surprisingly, instead of an abrupt change in volume, there is only a gradual increase in volume at this temperature range since melting temperature for glass or amorphous phase is not a fix value. As the temperature keeps increasing, all the three samples are melted and share the same volume of the melt phase, indicating that the simulation scheme correctly reproduce the melt behavior although they start from very different initial cell parameters and atom positions. It is worth pointing out that the experimental melting temperature of β–$LiAlSi_2O_6$ is around 1703 K,[40] which is about 1000 K lower than the one determined from MD

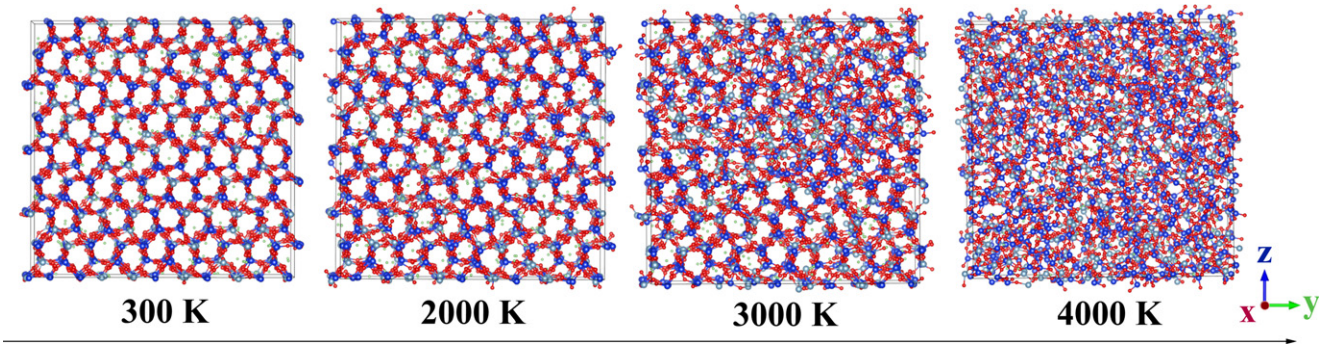

Fig. 12. Structure change of β–$LiAlSi_2O_6$ as the temperature increases.

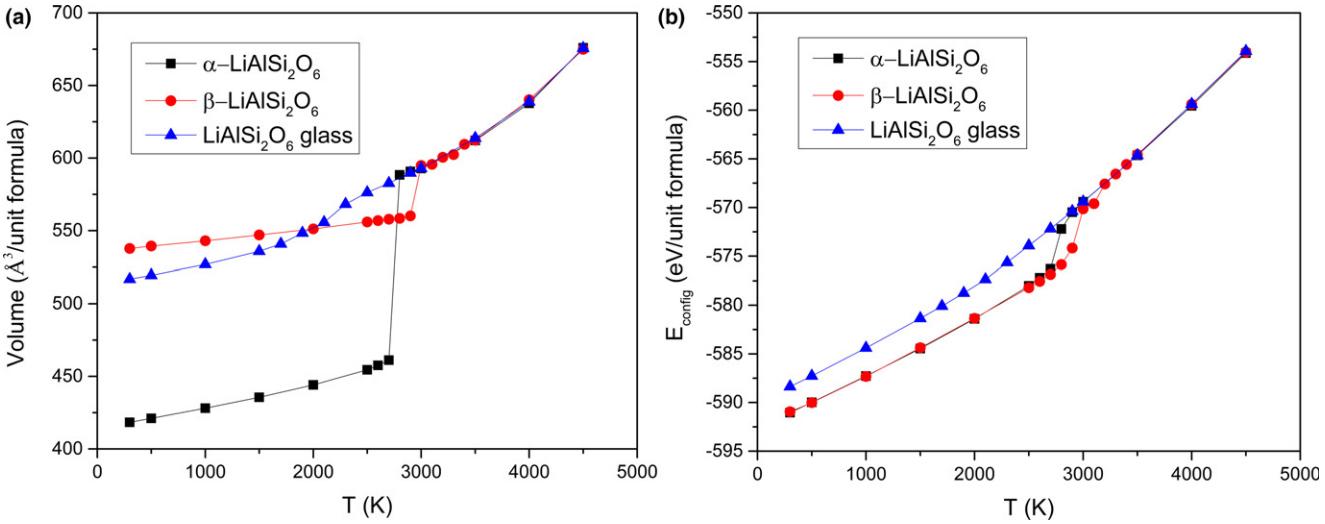

Fig. 13. (a)Volume (b) Configurational energy changes of α–$LiAlSi_2O_6$, β–$LiAlSi_2O_6$ and $LiAlSi_2O_6$ glass unit formula ($LiAlSi_2O_6$) as the temperature increases.

simulations. The main reason of this difference is due to the fact that the melting temperature is not one of the fitting parameters for the potential development and this can be corrected by the adjusting the partial charge values and short-range interaction parameters.[26] Additionally, the melting process in the simulations represents a mechanical melting process where three-dimensional periodic boundary condition is applied throughout the simulation process while, in practice, melting usually starts from free surfaces or other defects such as grain bondaries.[41,42]

Based on the above volume change data [Fig. 13(a)], volume thermal expansion coefficients can be easily achieved and the calculated result for β–$LiAlSi_2O_6$ is 1.43×10^{-5}, which is an order of magnitude lager than the experimental measured value (2.32×10^{-6}).[43] The reason of this difference can be explained by the difference of experimental and simulated linear thermal expansion coefficients. Although the simulated and experimental coefficients of linear thermal expansion (CTE) are very similar along c axis of around 6×10^{-6}, the experimental CTE of β–$LiAlSi_2O_6$ along *a* axis is negative (as shown in Table IV). This anisotropy of thermal expansion led to the averaged low volume expansion in β–$LiAlSi_2O_6$ glass–ceramics. While in MD simulation, the CTE of β–$LiAlSi_2O_6$ along *a* and *c* axes tend to be same, i.e., suggesting an isotropic behavior. This might be due to the empirical potential used for the simulations. More complicated potentials that take into account for the polarizability such as those use shell model[44] or charge transfer such as the reactive force field (ReaxFF)[45] might help to reproduce the trend of the thermal expansion of the crystals; however, other general structure features obtained using the current potentials should still be valid.

(3) Lithium Ion Diffusion in the Three Structures

The MSDs were calculated from NVE trajectories to quantify the lithium diffusion behavior of α–$LiAlSi_2O_6$, β–$LiAlSi_2O_6$, and $LiAlSi_2O_6$ glass. All the lithium ions in each simulated structure were used and averaged over large number of origins to obtain statistically meaningful results.[24] Figure 14 shows the logarithm scale of MSDs for lithium ions in $LiAlSi_2O_6$ glass which can be classified into three characteristic regions.[46] The first region is a ballistic region for short times where MSD is proportional to t^2. This is followed by a flat region in between ballistic region and diffusion region. The plateau becomes more pronounced as the temperature decreases.[47] The last region is a diffusion region for long times where MSD is proportional to t. This long-time diffusion stage was used to calculate the self-diffusion coefficients by evaluating the slope of MSDs versus time based on Einstein's equation, $D = \frac{1}{6}\lim_{t\to\infty}\frac{<r^2>}{t}$.

Figure 15 shows the lithium diffusion coefficients of three samples as a function of temperature. A temperature range of 2000–3700 K was chosen here since there is no obvious diffusion of lithium within 100 ps was observed in the α–$LiAlSi_2O_6$ under 2000 K. As can be seen from Fig. 15, the lithium diffusion in α–$LiAlSi_2O_6$ shows a two-range Arrhenius behavior. The lithium activation energy barriers for these two ranges are 1.00 eV for 2000–2700 K and 0.61 eV for 3000–3700 K (Table V). For easier comparison, the lithium diffusion properties of β–$LiAlSi_2O_6$ and $LiAlSi_2O_6$ glass are also shown here. It can be seen that at the higher temperature range (3000–3700 K), these three samples become liquid and the melt phase has almost identical lithium diffusion coefficients as well as diffusion energy barriers.

Considering that β–$LiAlSi_2O_6$ and $LiAlSi_2O_6$ glass show much similar diffusion behavior in the whole investigated temperature range of 800–3700 K, we further compared the diffusion coefficients of these two samples in Fig. 16. It is found that both β–$LiAlSi_2O_6$ and $LiAlSi_2O_6$ glass have a two-range Arrhenius behavior. For temperature between 800 and 1450 K, the fitting results shown in Table V give a lithium diffusion energy barrier of around 0.50 eV for β–

Table IV. Coefficient of Linear Thermal Expansion of β–$LiAlSi_2O_6$

α	Along *a* axis	Along *c* axis
Simulation (this work)	$+5.66 \times 10^{-6}$	$+5.66 \times 10^{-6}$
Experimental[37]	-2.02×10^{-6}	$+6.45 \times 10^{-6}$

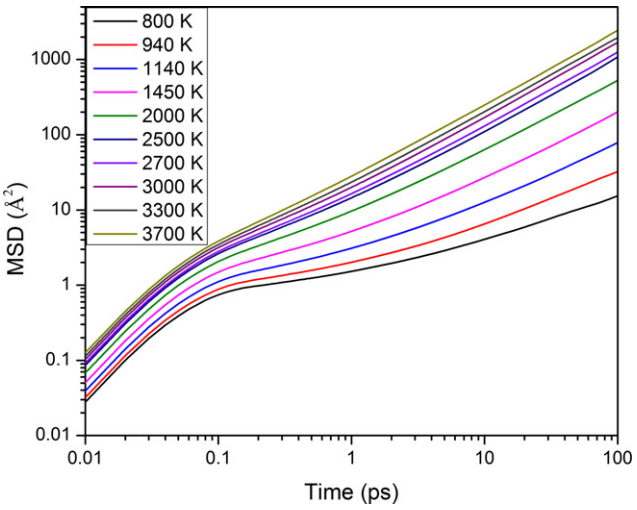

Fig. 14. Lithium mean square displacements in $LiAlSi_2O_6$ glass.

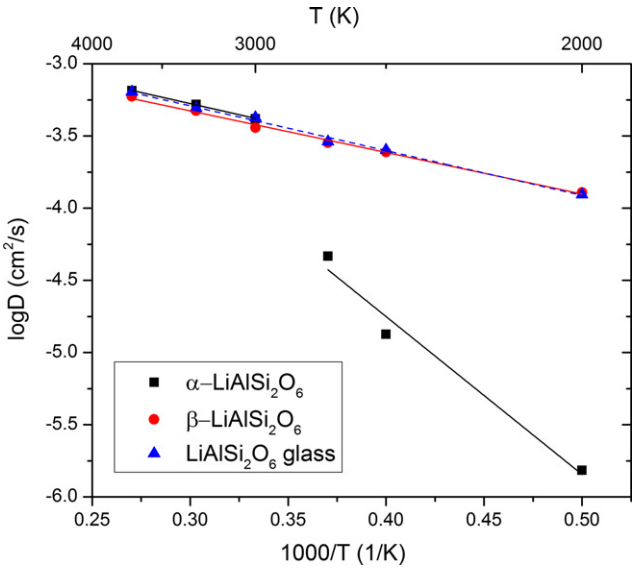

Fig. 15. Li ions diffusion coefficients in α–$LiAlSi_2O_6$, β–$LiAlSi_2O_6$, and $LiAlSi_2O_6$ glass for 2000–3700 K.

Table V. Diffusion Energy Barriers in eV for Lithium Aluminosilicate Crystals and Glasses

Samples	E_a (eV)	Temp. range (*K*)
α–$LiAlSi_2O_6$	1.00	2000–2700
	0.61	3000–3700
β–$LiAlSi_2O_6$	0.50	800–1450
	0.57	2000–3700
$LiAlSi_2O_6$ glass	0.48	800–1450
	0.62	2000–3700

$LiAlSi_2O_6$ and 0.48 eV for $LiAlSi_2O_6$ glass. Although the diffusion energy barriers in this lower temperature range for these two samples are quite similar, the diffusion coefficients for $LiAlSi_2O_6$ glass are slightly higher than that for β–$LiAlSi_2O_6$. For temperature range 2000–3700 K, the lithium diffusion energy barrier is about 0.57 eV for β–$LiAlSi_2O_6$ and 0.62 eV for $LiAlSi_2O_6$ glass and the diffusion coefficients of these two samples are quite close.

IV. Discussion

The structure of α–$LiAlSi_2O_6$ is quite ordered as shown from the pair distribution function (PDF) (Figs 9 and 11) results where distinct peaks existed over 10 Å range. Those peaks in PDFs are sharp and with high intensity and is quite different from that for β–$LiAlSi_2O_6$ and $LiAlSi_2O_6$ glass. In β–$LiAlSi_2O_6$, the position of aluminum is not fixed, they take 1/3 of the tetrahedral sites at random, and lithium ions tend to associate with alumina tetrahedron as a charge compensator. Due to the uncertain of the atom positions, the structure of β–$LiAlSi_2O_6$ is much less ordered and has some similarities with $LiAlSi_2O_6$ glass. In both β–$LiAlSi_2O_6$ and $LiAlSi_2O_6$ glass, aluminum is four coordinated and the distribution of lithium ions in these two structures are also quite similar.

The diffusion coefficients of lithium in α–$LiAlSi_2O_6$ are very low (much lower than the beta and glass phase) at low temperatures (below 2000 K in simulations). The low diffusion coefficient in the alpha phase can be understood by the more compact structure in the alpha phase and well-defined lithium site (M2) and the lack of defects to assist the diffusion. In real materials, α–$LiAlSi_2O_6$ may contain various kinds and amounts of impurities and vacancies that can assist lithium ion diffusion and change the mobility of lithium in the crystals. As the temperature increase to 2000–2700 K, lithium ions in α–$LiAlSi_2O_6$ are now movable. However, compared with β–$LiAlSi_2O_6$ and $LiAlSi_2O_6$ glass, α–$LiAlSi_2O_6$ still exhibits the lowest diffusion coefficients, which is not surprising considering its close-packed structure and the largest Li–Li sites distance among these three samples. The experimental diffusion energy barriers derived from ionic conductivity for single crystal α–$LiAlSi_2O_6$ are 1.04 eV perpendicular to *c*-axis and 0.89 eV along the *c*-axis.[33] Our simulation result gives an average diffusion energy barrier value around 1.00 eV, which is good agreement to the experimental results. If we continue to increase the temperature to above 3000 K where all three samples are become melts, the lithium diffusion properties become the same.

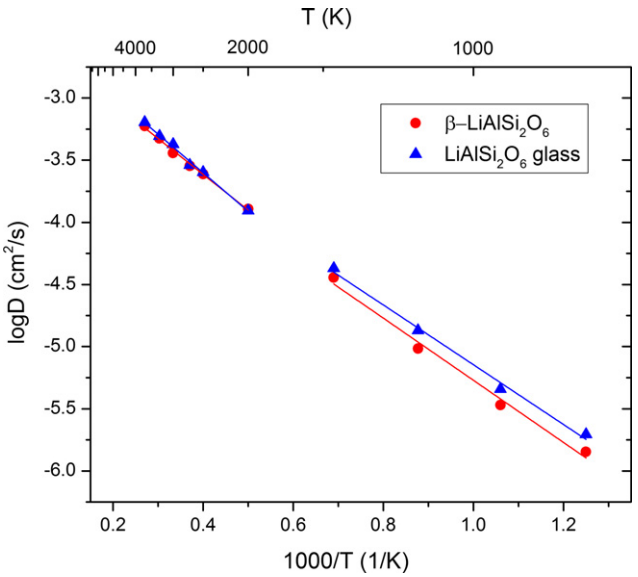

Fig. 16. Li ions diffusion coefficients in β–$LiAlSi_2O_6$ and $LiAlSi_2O_6$ glass for 800–3700 K.

Contrary to α–$LiAlSi_2O_6$, β–$LiAlSi_2O_6$ crystals have much more open three-dimensional network structure which offers possible interstitial sites for lithium ion diffusion. Thus, lithium interstitial diffusion is proposed to be the dominant mechanism for charge transfer in β–$LiAlSi_2O_6$. Considering the nature of glass and the similar density value with β–$LiAlSi_2O_6$, it is reasonable to assume that lithium migration in $LiAlSi_2O_6$ glass takes place by a similar process to that in β–$LiAlSi_2O_6$ crystals.[48] The exact mechanism of alkali ion diffusion in glasses are still a matter of debate, but it is generally believed that alkali ions and NBO segregate and form channels as in the structure picture of modified random network model.[49,50] Alkali ions are generally considered to diffuse through the vacancy model (instead of the interstitial model as alkali ions are integral part of the glass structure). More detailed analyses of the MD trajectories in this work can shed light on the diffusion mechanism of lithium ions in different phases and will be reported in future studies. The results from this work clear show that lithium ions have similar diffusion behavior to the more open beta $LiAlSi_2O_6$ phase than the alpha counterparts.

For temperature between 800 and 1450 K, the simulation results give a lithium diffusion energy barrier of around 0.50 eV for β–$LiAlSi_2O_6$ and 0.48 eV for the $LiAlSi_2O_6$ glass. These values are slightly lower compared to the ones determined from conductivity measurements at room temperature which yielded 0.71 eV for β–$LiAlSi_2O_6$ and 0.61 eV for $LiAlSi_2O_6$ glass. While in both simulation and experimental results, when compared with β–$LiAlSi_2O_6$, the $LiAlSi_2O_6$ glass always exhibits a lower diffusion energy barrier and higher diffusivity. The reason may be that in glass, there are more sites which can host lithium and only slightly differ in bonding energy, so the division between interstitial sites and regular sites of lithium in glass structure is not as sharp as that in crystal structure.[51] In addition, it can be known from Figs 9(b) and 10(b) that the average distance between lithium and lithium ions in $LiAlSi_2O_6$ glass is smaller than that in β–$LiAlSi_2O_6$, which is also a possible reason for the larger lithium diffusion coefficients for $LiAlSi_2O_6$ glass.

V. Conclusions

Molecular dynamics simulations with effective partial charge potentials have been used to understand the structural, thermal mechanical, and diffusion behaviors of spodumene ($LiAlSi_2O_6$) crystalline phases and glasses. It was found that β–$LiAlSi_2O_6$ has a structure much closer to the glass phase. For example, aluminum ions in the $LiAlSi_2O_6$ glass are mostly four coordinated with the Al–O bond distance being around 1.77 Å, which resembles those in β–$LiAlSi_2O_6$, but different from α–$LiAlSi_2O_6$ where aluminum is six coordinated and has a longer Al–O distance of 1.90 Å. Overall, β–$LiAlSi_2O_6$ as a solid-solution phase still possesses relatively ordered structure as compared with $LiAlSi_2O_6$ glass. One distinctive feature that differs in the two materials is that all the $[AlO_4]^-$ tetrahedrons in β–$LiAlSi_2O_6$ are connected through corner-sharing, while both edge-sharing and corner-sharing aluminum oxygen polyhedrons are founded in the simulated $LiAlSi_2O_6$ glass structures.

Lithium diffusion properties derived from the MSDs show that at the low temperature range (800–1450 K), the $LiAlSi_2O_6$ glass has similar but slightly lower lithium ion diffusion energy barrier and higher lithium ion diffusion coefficients as compared with β–$LiAlSi_2O_6$, while essentially no lithium diffusion was observed in α–$LiAlSi_2O_6$ until the temperature was increased to 2000 K. The diffusion behaviors were found to be closely related to the atomic structures: random substitution of Al for Si in the relatively open Si–O network in β–$LiAlSi_2O_6$ creates multiple sites and channels for charge compensating lithium ions which lead to high lithium ion diffusion even at low temperature; the lithium alumionsilicate glass structure, on other hand, provides free volumes that

lithium ions can diffuse through the vacancy mechanism; the α–$LiAlSi_2O_6$ phase, however, has a more close-packed structure and higher density than the other two phases. When no defects introduced to provide a diffusion mechanism, lithium shows minimum diffusivity in this phase.

The current MD simulations using the effective partial charge pairwise potentials generated consistent structure features and trends of lithium ion conductivity and energy barriers. However, there are several notable differences as compared to experimental values: for example, the melting temperature of β–$LiAlSi_2O_6$ determined from MD is about 1000 K higher than the experimental value; also, the negative thermal expansion along the *a* (or *b*) axis in β–$LiAlSi_2O_6$ was not reproduced. These point the direction of improvement of the current potential models.

Acknowledgments

This work was supported by NSF DMR (project # 1508001) and DOE NEUP (project # 13-5494).

References

[1]B. Munro, M. Schrader, and P. Heitjans, "AC Impedance Studies of Glassy and Crystalline Lithium Aluminosilicate Compounds," *Ber. Bunsenges. Phys. Chem.*, **96** [11] 1718–23 (1992).

[2]S. E. Kesler, P. W. Gruber, P. A. Medina, G. A. Keoleian, M. P. Everson, and T. J. Wallington, "Global Lithium Resources: Relative Importance of Pegmatite, Brine and Other Deposits," *Ore Geol. Rev.*, **48**, 55–69 (2012).

[3]R. Roy, D. M. Roy, and E. Osborn, "Compositional and Stability Relationships Among the Lithium Aluminosilicates: Eucryptite, Spodumene, and Petalite," *J. Am. Ceram. Soc.*, **33** [5] 152–9 (1950).

[4]D. Tulyaganov, S. Agathopoulos, H. Fernandes, and J. Ferreira, "Synthesis of Lithium Aluminosilacate Glass and Glass-Ceramics From Spodumene Material," *Ceram. Int.*, **30** [6] 1023–30 (2004).

[5]G. Barrera, J. Bruno, T. Barron, and N. Allan, "Negative Thermal Expansion," *J. Phys.: Condens. Matter*, **17** [4] R217–52 (2005).

[6]S. Mandal, S. Chakrabarti, S. Das, and S. Ghatak, "Synthesis of low Expansion Ceramics in Lithia–Alumina–Silica System with Zirconia Additive Using the Powder Precursor in the Form of Hydroxyhydrogel," *Ceram. Int.*, **33** [2] 123–32 (2007).

[7]R. Roy, D. K. Agrawal, and H. A. McKinstry, "Very low Thermal Expansion Coefficient Materials," *Annu. Rev. Mater. Sci.*, **19** [1] 59–81 (1989).

[8]M. Laczka, K. Laczka, K. Cholewa-Kowalska, A. B. Kounga, and C. Appert, "Mechanical Properties of a Lithium Disilicate Strengthened Lithium Aluminosilicate Glass-Ceramic," *J. Am. Ceram. Soc.*, **97** [2] 361–4 (2014).

[9]R. T. Johnson, R. Biefeld, M. Knotek, and B. Morosin, "Ionic Conductivity in Solid Electrolytes Based on Lithium Aluminosilicate Glass and Glass-Ceramic," *J. Electrochem. Soc.*, **123** [5] 680–7 (1976).

[10]I. Raistrick, C. Ho, and R. A. Huggins, "Ionic Conductivity of Some Lithium Silicates and Aluminosilicates," *J. Electrochem. Soc.*, **123** [10] 1469–76 (1976).

[11]A. Garcia, G. Torres-Trevino, and A. R. West, "New Lithium ion Conductors Based on the γ-LiAlO 2 Structure," *Solid State Ionics*, **40**, 13–17 (1990).

[12]A. Welsch, H. Behrens, I. Horn, S. Ross, and P. Heitjans, "Self-Diffusion of Lithium in LiAlSi2O6 Glasses Studied Using Mass Spectrometry," *J. Phy. Chem. A*, **116** [1] 309–18 (2011).

[13]J. Habasaki and Y. Hiwatari, "Molecular Dynamics Study of the Mechanism of ion Transport in Lithium Silicate Glasses: Characteristics of the Potential Energy Surface and Structures," *Phy. Rev. B*, **69** [14] 144207, 8pp (2004).

[14]R. P. Rao, T. Tho, and S. Adams, "Ion Transport Pathways in Molecular Dynamics Simulated Lithium Silicate Glasses," *Solid State Ionics*, **181** [1] 1–6 (2010).

[15]J. Du and L. R. Corrales, "Compositional Dependence of the First Sharp Diffraction Peaks in Alkali Silicate Glasses: A Molecular Dynamics Study," *J. Non Cryst. Solids*, **352** [30] 3255–69 (2006).

[16]H. Lammert, M. Kunow, and A. Heuer, "Complete Identification of Alkali Sites in ion Conducting Lithium Silicate Glasses: A Computer Study of ion Dynamics," *Phys. Rev. Lett.*, **90** [21] 215901, 4pp (2003).

[17]W. Li and S. H. Garofalini, "Molecular Dynamics Simulation of Lithium Diffusion in Li_2O–Al_2O_3–SiO_2 Glasses," *Solid State Ionics*, **166** [3] 365–73 (2004).

[18]Y. Xiang, J. Du, M. M. Smedskjaer, and J. C. Mauro, "Structure and Properties of Sodium Aluminosilicate Glasses From Molecular Dynamics Simulations," *J. Chem. Phys*, **139** [4] 044507, 17pp (2013).

[19]B. Narayanan, A. C. van Duin, B. B. Kappes, I. E. Reimanis, and C. V. Ciobanu, "A Reactive Force Field for Lithium–Aluminum Silicates With Applications to Eucryptite Phases," *Modell. Simul. Mater. Sci. Eng.*, **20** [1] 015002, 24pp (2012).

[20]B. Van Beest, G. Kramer, and R. Van Santen, "Force Fields for Silicas and Aluminophosphates Based on *ab Initio* Calculations," *Phys. Rev. Lett.*, **64** [16] 1955–8 (1990).

[21]S. Tsuneyuki, M. Tsukada, H. Aoki, and Y. Matsui, "First-Principles Interatomic Potential of Silica Applied to Molecular Dynamics," *Phys. Rev. Lett.*, **61** [7] 869–72 (1988).

[22]J. Du, "Challenges in Molecular Dynamics Simulations of Multicomponent Oxide Glasses"; pp. 157–80 in *Molecular Dynamics Simulations of Disordered Materials*, Edited by C.. Massobrio, J.. Du, M.. Bernasconi and P. S.. Salmon. Springer, Switzerland, 2015.

[23]J. Du, "Molecular Dynamics Simulations of the Structure and Properties of low Silica Yttrium Aluminosilicate Glasses," *J. Am. Ceram. Soc.*, **92** [1] 87–95 (2009).

[24]C. Chen and J. Du, "Lithium Ion Diffusion Mechanism in Lithium Lanthanum Titanate Solid-State Electrolytes From Atomistic Simulations," *J. Am. Ceram. Soc.*, **98** [2] 534–42 (2015).

[25]J. Du and A. Cormack, "The Medium Range Structure of Sodium Silicate Glasses: A Molecular Dynamics Simulation," *J. Non Cryst. Solids*, **349**, 66–79 (2004).

[26]J. Du and Y. Xiang, "Effect of Strontium Substitution on the Structure, Ionic Diffusion and Dynamic Properties of 45S5 Bioactive Glasses," *J. Non Cryst. Solids*, **358** [8] 1059–71 (2012).

[27]J. Du, L. Kokou, J. L. Rygel, Y. Chen, C. G. Pantano, et al., "Structure of Cerium Phosphate Glasses: Molecular Dynamics Simulation," *J. Am. Ceram. Soc.*, **94** [8] 2393–401 (2011).

[28]M. Tribaudino, F. Nestola, M. Prencipe, and H. Rundlof, "A Single-Crystal Neutron-Diffraction Investigation of Spodumene at 54 K," *Can. Mineral.*, **41** [2] 521–7 (2003).

[29]W. A. Deer, R. A. Howie, and J. Zussman, *An Introduction to the Rock-Forming Minerals*. Longman, London, 1992.

[30]C. Li and D. R. Peacor, "The Crystal Structure of $LiAlSi_2O_6$-II ("β Spodumene")," *Zeitschrift für Kristallographie-Crys. Mater.*, **126** [1–6] 46–65 (1968).

[31]P. Clarke and J. Spink, "The Crystal Structure of β Spodumene, $LiAlSi_2O_6$-II," *Zeitschrift für Kristallographie-Crys. Mater.*, **130** [1–6] 420–6 (1969).

[32]W. Smith and T. Forester, "DL_POLY_2. 0: A General-Purpose Parallel Molecular Dynamics Simulation Package," *J. Mol. Graph.*, **14** [3] 136–41 (1996).

[33]A. Welsch, H. Behrens, S. Ross, and D. Murawski, "Structural Control of Ionic Conductivity in $LiAlSi_2O_6$ and $LiAlSi_4O_{10}$ Glasses and Single Crystals," *Zeitschrift für Physikalische Chemie Int. J. Res. Phys. Chem. Chem. Phys.*, **226** [5–6] 491–511 (2012).

[34]J. Du and A. N. Cormack, "Molecular Dynamics Simulation of the Structure and Hydroxylation of Silica Glass Surfaces," *J. Am. Ceram. Soc.*, **88** [9] 2532–9 (2005).

[35]K. Aleksandrov and G. Prodaivoda, "Elastic Properties of Minerals," *Crystallogr. Rep.*, **38** [5] 214–34 (1993).

[36]P. Sondergeld, B. Li, J. Schreuer, and M. A. Carpenter, "Discontinuous Evolution of Single-Crystal Elastic Constants as a Function of Pressure Through the C2/c↔ P21/c Phase Transition in Spodumene ($LiAlSi_2O_6$)," *J. Geophys. Res.: Solid Earth (1978–2012)*, **111** [B7] B07202, 14pp (2006).

[37]B. O. Mysen, D. Virgo, and I. Kushiro, "The Structural Role of Aluminum in Silicate Melts; a Raman Spectroscopic Study at 1 Atmosphere," *Am. Mineral.*, **66** [7–8] 678–701 (1981).

[38]J. Jones, "Al-O and Si-O Tetrahedral Distances in Aluminosilicate Framework Structures," *Acta. Cryst. B*, **24** [3] 355–8 (1968).

[39]N. Ishizawa, T. Miyata, I. Minato, F. Marumo, and S. Iwai, "A Structural Investigation of α-Al2O3 at 2170 K," *Acta Cryst. B*, **36** [2] 228–30 (1980).

[40]M. Takabatake, "Aluminum Titanate Composition Being Stable at High Temperature"; U. S. Patent No. 4,118,240, 1978.

[41]J. Du, R. Devanathan, L. R. Corrales, W. J. Weber, and A. N. Cormack, "Short-and Medium-Range Structure of Amorphous Zircon from Molecular Dynamics Simulations," *Phys. Rev. B*, **74** [21] 214204, 14pp (2006).

[42]S. Phillpot, J. Lutsko, D. Wolf, and S. Yip, "Molecular-Dynamics Study of Lattice-Defect-Nucleated Melting in Silicon," *Phys. Rev. B*, **40** [5] 2831–40 (1989).

[43]W. Ostertag, G. Fischer, and J. Williams, "Thermal Expansion of Synthetic β-Spodumene and β-Spodumene—Silica Solid Solutions," *J. Am. Ceram. Soc.*, **51** [11] 651–4 (1968).

[44]A. Tilocca, N. H. de Leeuw, and A. N. Cormack, "Shell-Model Molecular Dynamics Calculations of Modified Silicate Glasses," *Phys. Rev. B*, **73** [10] 104209, 14pp (2006).

[45]A. C. Van Duin, A. Strachan, S. Stewman, Q. Zhang, X. Xu, and W. A. Goddard, "ReaxFFSiO Reactive Force Field for Silicon and Silicon Oxide Systems," *J. Phys. Chem. A*, **107** [19] 3803–11 (2003).

[46]J. Du and L. R. Corrales, "Structure, Dynamics, and Electronic Properties of Lithium Disilicate Melt and Glass," *J. Chem. Phys*, **125** [11] 114702, 12pp (2006).

[47]X. Han and H. Schober, "Transport Properties and Stokes-Einstein Relation in a Computer-Simulated Glass-Forming $Cu_{33.3}Zr_{66.7}$ Melt," *Phys. Rev. B*, **83** [22] 224201, 13pp (2011).

[48]J. Isard, "Electrical Conduction in the Aluminosilicate Glasses," *J. Soc. Glass Technol.*, **43**, 113T–23T (1959).

[49]A. Cormack, J. Du and T. Zeitler, "Alkali ion Migration Mechanisms in Silicate Glasses Probed by Molecular Dynamics Simulations," *Phys. Chem. Chem. Phys.*, **4** [14] 3193–7 (2002).

[50]A. Cormack, J. Du, and T. Zeitler, "Sodium ion Migration Mechanisms in Silicate Glasses Probed by Molecular Dynamics Simulations," *J. Non Cryst. Solids*, **323** [1] 147–54 (2003).

[51]F. Qi, C. Rier, R. Böhmer, W. Franke, and P. Heitjans, "Ion Hopping in Crystalline and Glassy Spodumene $LiAlSi_2O_6$:^{7}Li Spin-Lattice Relaxation and ^{7}Li Echo NMR Spectroscopy," *Phys. Rev. B*, **72** [10] 104301, 11pp (2005). □

journal

J. Am. Ceram. Soc., 98 [12] 3748–3757 (2015)
DOI: 10.1111/jace.13731

Ab initio Molecular Dynamics Simulations of the Hydroxylation of Nanoporous Silica

J.M. Rimsza, and Jincheng Du†

Department of Materials Science and Engineering, University of North Texas, Denton, Texas 76203

Accurate information on the interactions between water and silica is critical to the understanding of its properties including mechanical strength under stress and long-term chemical durability of silica and silicate glasses. In this study, interactions between water and nanoporous amorphous silica models were investigated using density functional theory (DFT) based *ab initio* molecular dynamics (AIMD) simulations which accurately describe bond breakage and formation as well as chemical reactions. AIMD simulations up to 30 ps were performed for systems containing water and nanoporous silica with a wide range of porosities (31%–67%). Partial removal of defects, such as two-membered rings, was observed during the AIMD runs whereas more reactive coordination defects were removed during the initial geometry optimization. The limited two-membered ring removal can be attributed to restricted water-defect movement or the increased stability of rings located on concave surfaces. Two-membered ring removal mechanisms included the formation of an overcoordinated silicon (Si^5) intermediate defect from the dynamic simulations. Si^5 defects continued to develop throughout the simulations, indicating a thermodynamic drive for two-membered ring removal which is kinetically limited. Changes in the electronic structures, such as atomic charges, and bond length-bond angle correlation functions were monitored during the hydroxylation process.

I. Introduction

Interactions and reactions between silica and water are commonly occurring in natural systems and has many implications in science and technology fields. For example, water–silica interactions have been widely considered to be the cause of hydraulic weakening of minerals, as well as in silica or silicate glasses.[1,2] The stress corrosion of glasses, which determines its long-term mechanical properties, is due to the chemical reaction of water molecules from the environment with silicate glasses at the crack tips. Understanding silica and silicate glass–water interactions is also critical as vitrification is widely accepted for the disposal of medium and high level nuclear waste materials, a scenario where the stability of the host glass material is paramount to avoid leeching of nuclear waste into the surrounding systems.[3–5] The dissolution rate of glass waste forms in ground water determines its long-term stability in geological environments and ultimately its effectiveness.[5] Detailed mechanistic understanding of water–silica interactions will lead to more accurate prediction of the behaviors of vitrified nuclear wastes during geological long-term storage.

Reaction of water with silica involves the breakage of Si–O–Si (siloxane) linkages and formation of silanol groups described by the following equation[6]:

$$\mathrm{Si-O-Si + H_2O \rightarrow Si-OH + HO-Si} \quad (1)$$

The energy barrier of the reaction depends on the Q_n speciation, that is, number of bridging oxygen, "n", per [SiO_4] tetrahedron and the stress state (and hence bond length) of Si–O bonds. At a crack tip where the Si–O bonds are under stress, the reaction has a lower energy barrier. Similarly, on fresh surfaces where highly strained two-membered rings, described as a set of edge rather than corner sharing [SiO_4] tetrahedron, exist the reaction barrier is lower as compared to unstrained Si–O bonds in larger rings. Not only does the short-range structure play a role on the reactivity of Si–O bonds, the medium-range structure such as Q_n speciation also plays a role on the water–silica reaction barrier.

The activation energies for silica dissolution in water have been investigated through both experimental and computational methods. Experimentally, Icenhower and Dove investigated the changing dissolution rates of quartz at varying temperatures and identified the activation energy for dissolution of silica in water as 74.5 ± 1.4 kJ/mol (0.77 eV) through the analysis of the reaction kinetics.[7] An energy barrier of 0.77 eV is well within the activation energy range reported by other experimental research groups of 60.9–89.0 kJ/mol (0.63–0.92 eV).[7] Computational work by Kagan et al. used MD simulations to investigate the dissolution of a silica surface when in contact with water and calculated the activation energies for the breakage of siloxane bonds of Q_n species (meaning [SiO_4] tetrahedron with n bridging oxygen) using the potential of mean force method.[6] Kagan et al. reported the limiting step in the dissolution reaction of silica as the $Q_3 \rightarrow Q_2$ or $Q_2 \rightarrow Q_1$ step in the dissolution process with an energy barrier of around 14 kcal/mol (0.61 eV), whereas the $Q_1 \rightarrow Q_0$ and $Q_4 \rightarrow Q_3$ transitions exhibiting lower energy barriers of ~13 kcal/mol (0.56 eV) and 11 kcal/mol (0.48 eV), respectively.[6] As the bond angles present in two-membered experience significant strain, measured as 1.38 eV/ring on a β-cristobalite surface, it is expected that energy barriers would be even lower for these ring defects.[8]

Two-membered ring defects on silica surfaces have been identified in experiments using both secondary ion mass spectroscopy[9,10] and ^{29}Si DAS NMR (dynamic angle spinning nuclear magnetic resonance).[11,12] The investigation of two-membered ring hydroxylation performed by D'Souza and Pantano was under ultrahigh vacuum conditions.[10] To create the ring structures the surface was fractured in high vacuum and the dangling oxygen bonds (NBO) and undercoordinated silicon (Si^3) from freshly fractured surface bonded to form two-membered rings, as no hydrogen or water were available to form silanols. The generation of the silanol groups on freshly fractured silica surfaces under lower vacuum conditions have been identified, but measuring their reaction rate has proven to be more complex.[9] Two hydroxylation rates

W.-Y. Ching—contributing editor

Manuscript No. 36111. Received December 26, 2014; approved May 28, 2015.
†Author to whom correspondence should be addressed. e-mail: jincheng.du@unt.edu

were identified for the hydroxylation and dehydroxylation behavior of silica fracture glass surfaces.[9]

The first was a reaction governed by first-order kinetics and characterized by fast reaction times, anticipated to be the result of the annihilation of two-membered ring defects.[9] In contrast, the second stage of the reaction was much slower and is hypothesized to be the result of bond breakage in three-membered rings, resulting in slower reaction rates.[9] Three-membered rings exhibit more constrained bonds as compared to larger rings, although not as reactive compared to two-membered rings, and this has been shown in Si–O–Si bond angles obtained from ^{29}Si DAS NMR: 127° for three-membered rings as compared to 147° for five-membered rings.[11] While the work by D'Souza and Pantano provides insight into the hydroxylation rate,[9,10] the techniques and methods used cannot probe the reaction mechanisms and fast reactions rates of two-membered ring removal, demonstrating the role which computational methods can play in further investigating silica hydroxylation.

In addition to experimental investigations, classical and first principles simulations have been widely used to study water–silica reactions. These simulations complement the experimental efforts where study of the water–silica reactions is challenging due to the complexity of the bulk amorphous structure, the short-time frame of the reactions, and the lack of methods available to quantify the reactant/product speciation. While significant interest and work has been invested in the development of molecular dynamics (MD) force fields, which have been effective in describing the structure and properties bulk silica, first principles calculations provide advantages for analyzing water–silica reactions, especially when significant bond breakage and formation is anticipated.[13,14] Garofalini and coworkers have developed force fields for the water–silica systems which can be used to study the hydroxylation of silica in relatively large systems, whereas DFT calculations were used extensively to provide fitting variables and validations of the simulation results.[15,16] Van Duin and coworkers have developed Reactive Force Field which is capable of describing the chemical reactions and has been used to study the water/silica interfaces but focused on large scale dynamics.[17] Even these force fields are often developed by fitting to first principles energetic data and are capable of simulating large systems, their validity in simulations, especially when simulating reactions of complex systems, usually needs to be carefully benchmarked with first principles calculations. Thus dynamics simulations based on first principles Density Functional Theory (DFT) will provide accurate reaction pathways and unambiguous reaction mechanisms of water/silica interactions. Ever increasing computational efficiency of DFT algorithms and computing power of parallel computers also makes *ab initio* molecular dynamics (AIMD) simulations of systems with a few hundred atoms possible. There are large number of publications in the literature employing computational methods to study water–silica interactions. For example, silica surfaces/water interfaces were studied using classical MD[16,18–20] and *ab initio* methods[21–24]; in addition, nano confined water,[25] hydrophobic surfaces,[26] and bio glass–water interactions[27] have also been studied using different simulation methods. Long-term dynamics simulations of water/silica interaction using AIMD is still missing in the literature. These results will otherwise be highly valuable for mechanistic understanding of the water interaction and can serve as model data for classical simulations using empirical potentials.

Despite large number of studies of water–silica interactions including hydroxylation of silica, the detailed reaction mechanism of water with silica is relatively unstudied. For instance, Masini and Bernasconi, who investigated reaction mechanisms, did not allow the reaction to naturally develop during their simulations.[24] Likewise, work by Du and Cormack artificially formed the silanol bonds and measured the secondary energetic effects.[20] Even recent work by Kagan et al. placed water molecules in an ideal configuration to cause breakage of unstrained siloxane bonds.[6] Lopez et al. used DFT to study H_2 interactions with two-membered rings and manually added hydrogen atoms into the system to avoid bond breakage concerns with cluster calculations.[28] Tilocca and Cormack investigated the interaction of two-membered rings in 45S5 bioglass with water using CPMD (Car-Parrinello molecular dynamics) simulation methods by placing water molecules adjacent to two-membered ring sites to facilitate reactions.[27] One exception is work by Du et al. who performed analysis of two-membered ring dissolution using mixed quantum mechanical and molecular mechanical (QM/MM) simulations to investigate the natural hydroxylation process without placing atoms to facilitate two-membered ring removal.[22,23] The results were shown to be sensitive to the portion of the surface which is treated with quantum mechanics, with increasing quantum mechanical treatment resulting in lowering of energy barriers, especially compared to cluster calculations.[22] While placement of water molecules and constrained dynamics facilitate the reactions, few studies investigate the direct dynamic simulations of water–silica interactions.

In this study, we have studied the interaction of water-amorphous silica with different porosities by using AIMD simulations. The investigation focuses on the natural reaction pathways without presetting the initial configuration through relatively long AIMD simulations. The effect of porosity of amorphous silica on water–silica reaction behaviors was investigated. In particular, the hydroxylation process and associated atomic and electronic structural changes, reaction pathways for surface defect sites such as two-membered rings and coordination defects are studied in detail.

This study begins with a discussion of the computational methodologies employed, followed by an analysis of the hydroxylation process of silica including extensive structural and mechanistic analysis (charge analysis, reaction rates, two-membered ring concentrations, and bond angle-bond distance correlations). Finally, a discussion and conclusions are presented.

II. Methodologies

Two different computational methods, classical MD with effective partial charge empirical potentials and DFT based AIMD simulations, were employed in this work to generate nanoporous amorphous silica structures and study the water–silica interactions, respectively.[20] The development of the nanoporous silica structure was performed using classical MD methods implemented in the DLPOLY 2.20 code and has been previously described.[29,30] The simulations of the water–silica interactions were modeled using Gaussian type localized basis set periodic DFT-based AIMD simulations implemented in the CP2K code. CP2K has been shown to provide accurate descriptions and computationally effective for insulating materials and water containing systems.[31]

(1) Nanoporous Silica Structure Generation

Nanoporous amorphous silica structures were generated using the lattice expansion method for a system of ~100 atoms, with the consideration of a system that is large enough to represent the amorphous structure and feasibility of computationally intensive AIMD simulations in subsequent studies of water/silica interactions.[32,33] The protocol begins with a 99 atom bulk silica structure with experimental density of 2.2 g/cc, which was generated through a melt and quench procedure using classical MD with a partial atomic charge pair wise potential with short-range interactions in the Buckingham form described by Du and Cormack.[34] Linear lattice expansion was used followed by several relaxation steps to generate porous structures. In this method, all

atomic positions scaled with simulation box length increases around 20%, stepwise for each level of porosity. The lattice expansion results in artificial Si–O bond breakages which were restored after relaxations in MD simulations with canonical (NVT) ensemble where the number of atoms (N) and the volume (V) are geometrically constrained along with temperature (T) control at 300 K through the application of a Nosé–Hoover thermostat. The resulting nanoporous silica systems included voids scattered throughout the structure, producing the randomized porosity. For the generation of nanoporous silica systems at higher porosities the expansion process is repeated after each NVT relaxation to develop systems with porosities between 30% and 70%, specifically sets of 31%, 42%, 52%, 60%, and 67% nanoporous silica systems. In the nanoporous silica systems, the porosity is the free volume added to the system through the lattice expansion and is described by following equation[30]:

$$\frac{V - V_0}{V} = P(\%) \tag{2}$$

with V as the volume of the nanoporous silica structure and V_o is the volume of the dense silica system. The porosity range studied here was selected to be consistent with porosity ranges reported experimentally for nanoporous silica generated through plasma-enhanced chemical vapor deposition and sol–gel techniques.[30] Though the system size of silica used in this study is only ~100 atoms (total number of atoms are 300–400 atoms with water molecules in AIMD simulations), the same procedure was used to reproduce much larger systems (with several thousand atoms), and it is expected that the systems used here will replicate the porous structures of the larger systems, though the pore size will be inherently limited by the system size. For a more detailed discussion of the structure of the nanoporous silica and their comparison to experiment the reader is directed to Ref. [30]. Additional relaxation was performed on all the porous structures under isothermal and isobaric conditions (NPT) to develop a relaxed nanoporous silica system at ambient pressure. A detailed discussion of the role of the relaxation steps and analysis of the resultant nanoporous silica structure is included in Ref. [30]. To ensure accurate statistical analysis of the structures all simulations were performed in triplicate with different initial bulk silica structures and all reported standard deviations are equal to the standard error:

$$\mathrm{SE} = \frac{s}{\sqrt{n}} \tag{3}$$

where SE is the standard error, s is the standard deviation of the measurement and n is the number of unique systems.

Due to the tortuosity of the nanoporous silica systems generated using the protocol described above, a series of flat surfaces were also produced to provide comparative systems. Flat surfaces were created by using the initial dense silica systems and adding 10 Å of vacuum in the z-direction through adjustment of the periodic boundary conditions. The addition of the vacuum layer effectively sliced through the system, creating the flat surfaces. Five unique surfaces were generated and underwent further geometry optimization using the first principles DFT methods described in Section II(2) to remove the high-energy sites before water was introduced to the surface.

(2) Water–Nanoporous Silica Interactions

Water was introduced into the system by generating a box of water molecules at a density of 1.0 g/cc and overlapping the pure water system with the nanoporous silica structure. Any water molecules which were within 1.0 Å of the silica structure were removed to ensure that they did not inadvertently create high-energy sites within the system. Due to increasing free space in the porous systems with increasing porosity the number of water molecules added to the systems varied between 20 ± 2 molecules at 31% porosity to 85 ± 3 molecules at 67% porosity. The standard deviation in the number of molecules added arises from the variability in the porous structure, which results in a slight changes in the number of water molecules which can be introduced into the system. Initially, a geometry optimization within DFT was performed for 500 steps to remove high-energy strained sites which arise from the introduction of water.[35] Following the geometry optimization under DFT Born–Oppenheimer AIMD run was performed for 30 ps (30 000 steps with 1 fs time step) at 300 K in a canonical (NVT) ensemble. The temperature was controlled by a Nosé–Hoover thermostat. Periodic boundary conditions and a time step of 1.0 fs were also employed. DZVP basis sets and a generalized gradient approximation functional of the BLYP form were implemented.[36] Snapshots of the hydroxylated nanoporous silica systems before and after the inclusion of water are included in Fig. 1.

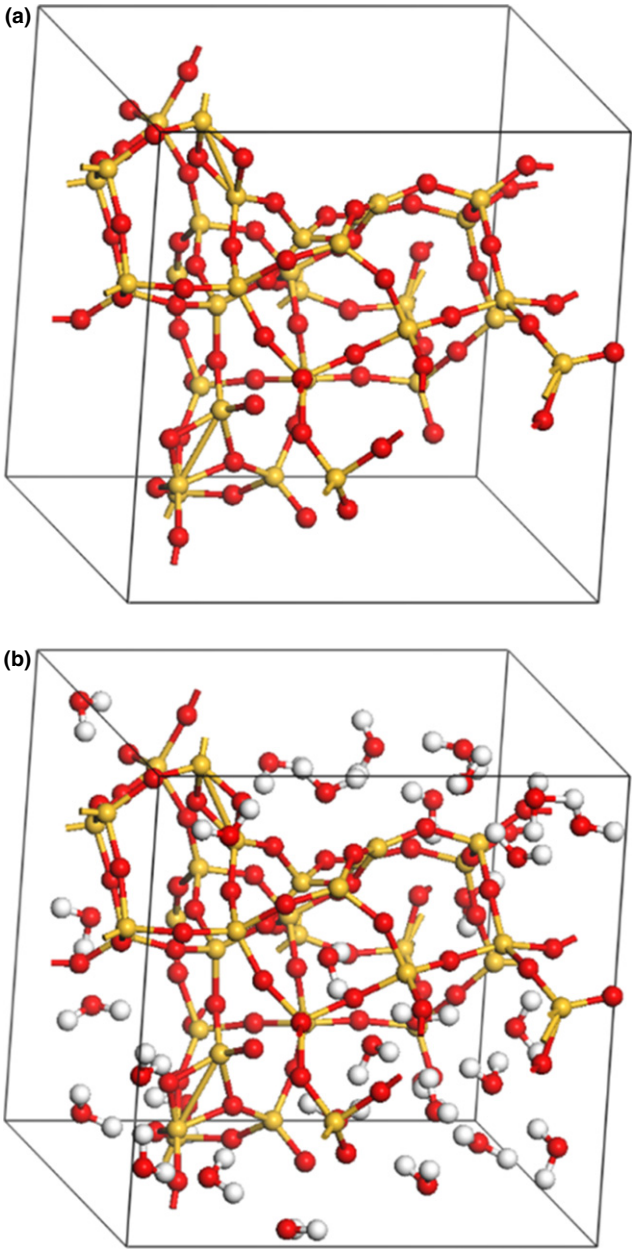

Fig. 1. Snapshot of 42% nanoporous silica systems (a) unhydrated and (b) hydrated. Red is oxygen, yellow is silicon, and white is hydrogen.

III. Results and Discussion

(1) Water–Silica Reaction Mechanisms

The first principles MD simulations performed in this work provide an excellent opportunity to investigate mechanisms of water–silica reactions, especially internal surface defect removal, when the system is in contact with water. The coordination defects present in silica have the highest energy and the largest energetic drive for removal. These included nonbridging oxygen (NBO), described by an oxygen atom bonded to only one silicon atom, three-bonded oxygen, an oxygen atom bonded to three silicon atoms, under bonded silicon (Si^3), a silicon atom which is bonded to only three oxygen, and an overcoordinated silicon (Si^5), where a silicon atoms is bonded to five oxygen. The removal of the coordination defects is fast and the majority of such defects were removed during the initial geometry optimization step before AIMD simulations. In the case of the NBO defects, a water molecule donates a hydrogen to terminate the bond and the remaining OH^- may experience limited localized diffusion before receiving a proton via hydrogen hopping to complete the water molecule.[16,17] In the case of Si^3 defects, an OH^- terminates the dangling bond and the remaining proton is free to travel through the solvent, via hydrogen hopping, before it forms a H_3O^+ ion or is absorbed onto a separate defect.[16,17] It should be noted that when the term hydrogen hopping is used it indicates the transfer of a hydrogen atom throughout the water through successive donation of a hydrogen to neighboring water molecule, resulting in rapid transfer of excess hydrogen in the solution.[17,22]

The mechanism of two-membered ring removal is more complex as breaking the siloxane bond will form two defects, a Si^3 and a NBO and often includes more than one water molecule.[37] Masini and Bernasconi performed constrained DFT studies on the removal of two-membered rings on flat silica surfaces and postulated two separate reaction mechanisms.[24] In the first, the oxygen in a water molecule absorbs onto one of the silicon in the two-membered ring, resulting in a temporary Si^5 defect, causing the two-membered ring to open.[24] In the second, the oxygen atom in the water molecule interacts with a bridging oxygen, causing a temporary three bonded oxygen defect, resulting in two-membered ring opening.[24] Even though the second oxygen-based mechanism has a lower activation energy (0.32 eV) the lower physisorption energy of the first Si^5-based mechanism (0.11 eV) makes it more energetically favorable, despite having a larger activation energy of 1.1 eV.[22,24] In addition, the Si^5 reaction mechanisms was observed in the classical MD analysis of hydroxylation of flat silica surfaces by Mahadevan and Garofalini, in mixed quantum and molecular mechanics simulations by Du et al. and in investigations of the dissolution of flat silica surfaces using classical MD methods by Kagan et al.[6,16,22] In the AIMD simulations performed here, three instances of two-membered ring breakage were identified but only the first mechanism, which generates a temporary Si^5 defect, was observed. The Si^5 defect is stable for 0.1–0.2 ps before the almost simultaneous removal of the extra hydrogen in the Si–OH_2 defect and the breaking of the Si–O bond. Snapshots of the reaction are included in Fig. 2. As the extra hydrogen, which is present from the disassociation of the water molecule, is unable to terminate the developed NBO defect due to its diffusion away from the reaction site, the NBO is not immediately terminated. Rather, hydrogen is transported via hydrogen hopping to the defect site, which is consistent with previously reported results.[16,22]

The flat silica surfaces did not exhibit any two-membered ring breakage during the simulations. This is consistent with reaction rates suggested by D'Souza and Panatano for the second stage of hydroxylation of experimental silica surface and adjusting by 10^4–10^5 times for the strain of the two-membered rings, the total number of siloxane bonds which should be broken is 3×10^{-10} for the simulations studied here.[9] Therefore, it is significant that two-membered ring removal occurs in the porous systems, indicating the high level of stress around the location of the defect. A more

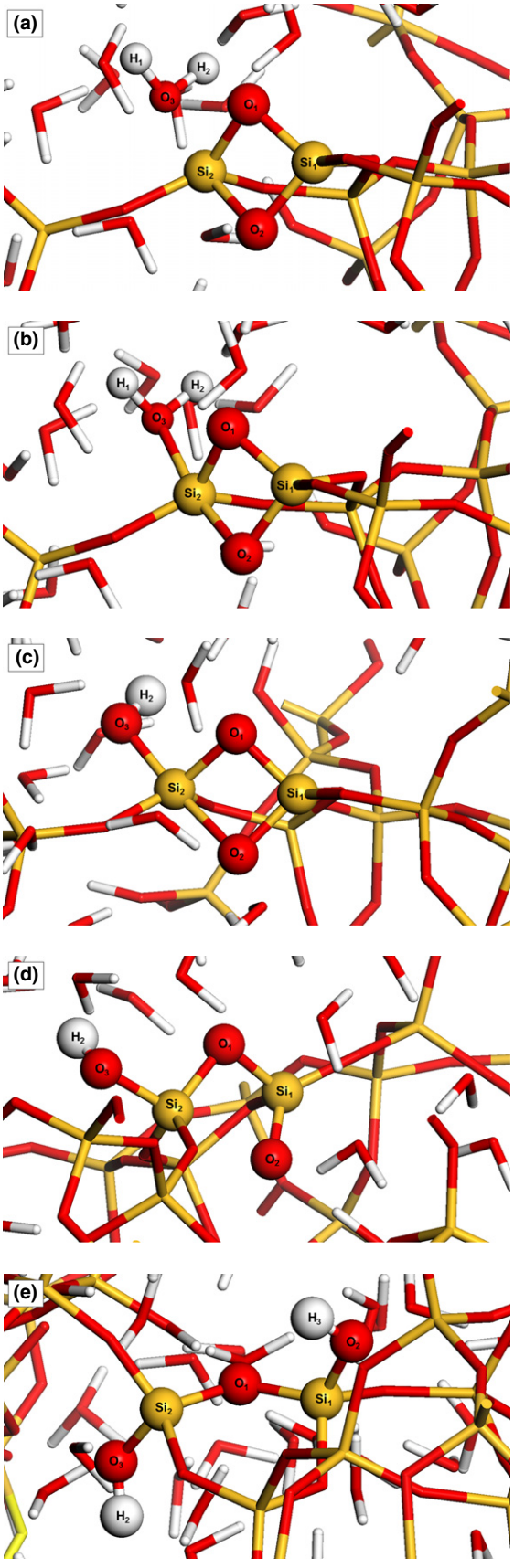

Fig. 2. Snapshots of the five representing steps of the mechanism of two-membered ring breakage in a 60% nanoporous silica system in the presence of water.

detailed discussion of the reaction rates for the computational systems is included in Section III(4).

(2) Atomic Charge Transfer During Hydroxylation

Analysis of the changes in the atomic charges of the individual atoms during the hydroxylation reaction provides insight into the electronic structure of the defect during the reaction. Very little information of charge transfer during the hydroxylation reaction is available, which is primarily due to the fact that classical simulations typically use fixed charges and cannot take into account the changing charge states, though this information is available from analysis of AIMD trajectories. Thus far, investigation of atomic charges has been the focused on the analysis of silanol structures in clusters, such as orthosilicic acid (SiO_4H_4) with respect to water molecule orientation as part of the characterization of hydrogen bonds.[38,39] Even so, some charge transfer from the water to the silica network is observed.[22] The investigation of the charge states in the silanol group represent analysis of the final structure, rather than the hydroxylation of the defect which generates the silanol group.

Du et al. did investigate the charge states of the hydroxylation of two-membered rings but focused on the charge of the hydronium ion involved in proton transfer during the hydrogen hopping process rather than the charge of the defect.[22] Regardless, *ab initio* computational studies have identified charge transfer between silanol groups and adjacent water molecules, which provides some insight into the expected charge of the water molecule during the hydroxylation reaction. In addition, Bredas et al. noted that slight geometry distortions can cause significant changes in atomic charge densities over entire molecules, indicating that once charge has been added or removed to a structure charge transfer can be expected throughout the system.[40]

Mulliken population analysis was performed at five points along the water–silica defect reaction pathway to identify changes in the partial atomic charges. To calculate the partial atomic charges the molecular orbitals, which are calculated to complete the DFT simulation, are integrated to describe the electron density of an atom.[41] In the case where a complete atomic orbital, described by the basis function, is located on a single atom, the entire electron density is assigned to that atom.[41] If the basis function is assigned to multiple atoms then the electron density is divided equally among the atoms.[41] All partial atomic charges reported here are referenced to Fig. 2 with average atomic charges being included in Table I. The reader should note that H_1 and H_3 are not involved in the entire reaction, with H_1 diffusing away from the silica surface at step 2 and H_3 terminating the NBO in step 5. Therefore, the analysis of their partial atomic charges should be considered in the context of their role in the reaction. Changing atomic charges of the Si, H, and O atoms in the defect with reaction step are included in Fig. 3 and Table I.

The silicon atoms experience a loss of electronic charge, identified as a less negative charge, between reaction step 1 and 2 when there is a Si^5 defect associated with the ring structure as seen in Table I. The difference in Si_1 and Si_2 charges in step 1 and step 2 is less drastic than the less negative charge in the silicon in the network structure between steps 1 and 2, indicating that it is not the change in the charge of the silica structure as a whole which is responsible for the less negative charge of Si_1 and Si_2 [Table I and II Fig. 3(a)]. The less negative charge of the network silicon between steps 1 and 2 can be attributed to removal of various coordination defects elsewhere in the silica structure during the time that the two-membered ring reaction is taking place. The less negative charge in the Si_1 and Si_2 in step 2 is balanced by a more negative charge of the bridging oxygen (O_1 and O_2), giving the two-membered ring structure a net charge of 0.929 in step 1 and a charge of 0.926 in step 2 as seen in Table II. During the initial two steps the charge of the water molecule becomes significantly less negative, −0.050 at step 1 to 0.106 in step 2 (Table II). The change in the charge indicates that the interaction of the water molecule with the two-membered ring results in transfer of electrons to the silica structure. The charge transfer from the water to the silica ring structure was also noted in mixed QM/MM studies of two-membered ring breakage by Du et al.[22] The transfer of charge from the water molecule to the silica structures comes from both the water and the hydrogen atoms in the molecule, with a more negative charge of ~0.05 from all three atoms [Figs. 3(b) and (c)].

After the initial charge transfer, from the water molecule absorbing on the Si atom, the charge of both the structure and the absorbed water molecule are constant until the formation of the NBO. The NBO formation causes a more negative charge of the silicon atoms independent of the network silicon, an effect which decreases with the formation of the silanol group in step 5. The reaction of the two silicon in the structure with NBO formation is indicative of the generalized charge transfer which can occur in molecular structures from the formation of localized defects. In addition, previous work by Hamann investigated the charge state of a two-membered ring using Mulliken population analysis but focused on the existence of an unsupported pi bond between the two silicon, rather than changes in the charge state during defect removal.[42] The existence of a latent bond between the silicon may facilitate the charge transfer between the silicon atoms during the reaction [Fig. 3(a)], causing the changes in the silicon charges to occur in tandem until the formation of the NBO defect during step 4, at which the two-membered ring is effectively broken and the pi-bond would dissolve.

The oxygen atoms exhibit a clear difference in charge states between the various oxygen environments, O_1 and O_2, which are part of the two-membered ring defect and O_3, as part of the water molecule, with O_3 exhibiting a consistently less negative charge [Fig. 3(b)]. The effect decreases in step 5 where the water molecule has been completely integrated into

Table I. Atomic Charges of Si, O, and H Atoms Involved in Two-Membered Ring Breakage During the Five Steps Pictured in Figs. 2(a)–(e) (Reaction step 1–5)

Step	1		2		3		4		5	
Si_1	0.913	±0.030	0.967	±0.011	0.970	±0.008	0.910	±0.015	0.945	±0.003
Si_2	0.995	±0.025	1.024	±0.010	1.025	±0.015	0.982	±0.008	0.981	±0.010
O_1	−0.449	±0.039	−0.550	±0.019	−0.551	±0.040	−0.589	±0.023	−0.450	±0.029
O_2	−0.481	±0.022	−0.516	±0.008	−0.515	±0.023	−0.535	±0.004	−0.486	±0.005
O_3	−0.332	±0.058	−0.279	±0.018	−0.297	±0.049	−0.370	±0.022	−0.375	±0.059
H_1	0.137	±0.007	0.192	±0.006	0.172	±0.08	0.165	±0.005	0.172	±0.015
H_2	0.145	±0.013	0.194	±0.013	0.151	±0.014	0.157	±0.002	0.169	±0.007
H_3	0.119	±0.024	0.148	±0.004	0.150	±0.004	0.159	±0.005	0.159	±0.014

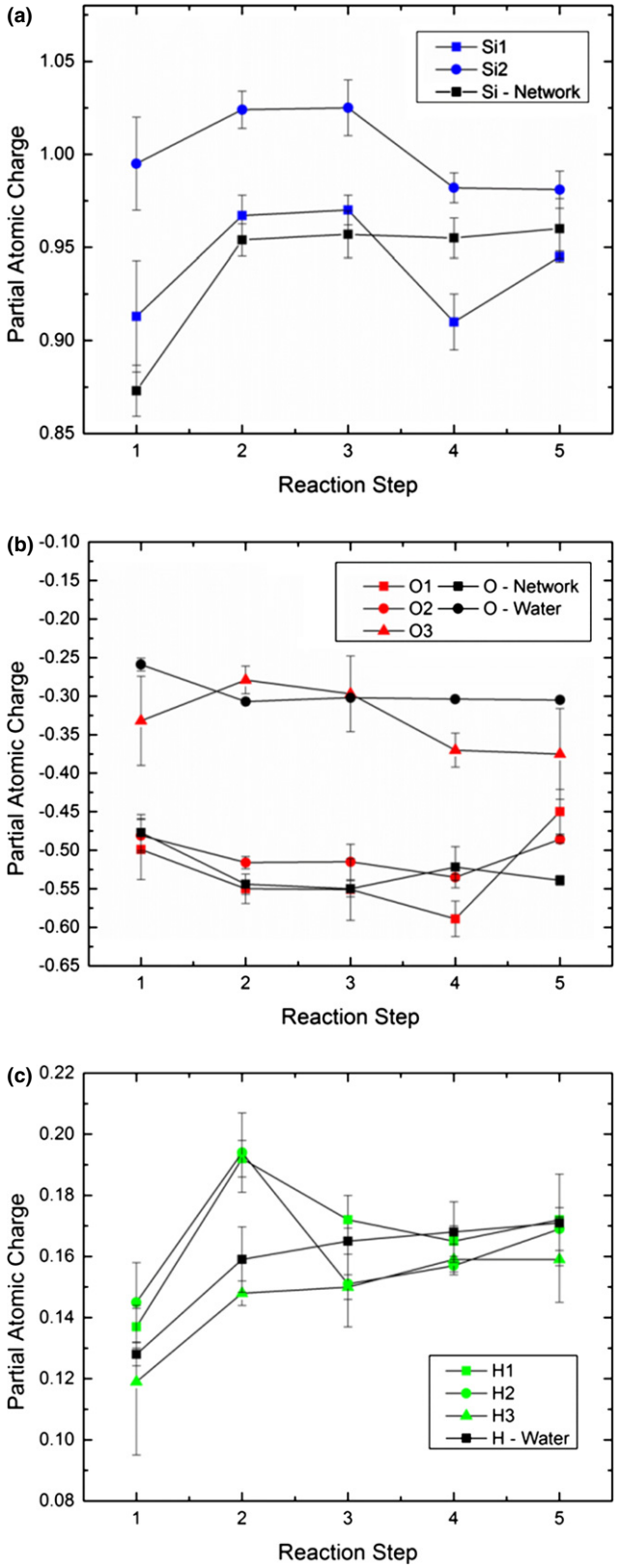

Fig. 3. Changing atomic charges of (a) Si, (b) O, and (c) H atoms involved in the two-membered ring breakage mechanism outlined in Fig. 2. The error bars are equal to the standard error of the charges.

the silica surface, demonstrating the difference in the charge of the O_3 atom and the oxygen in the water molecules [Fig. 3(b)]. Also, the formation of the NBO defect causes the most dramatic charge difference on the silicon atom associated with the defect, with little effect on the involved oxygen. Initially, the charges on the hydrogen atoms exhibit a clear distinction between atoms which are part of the water molecule compared to the silica structure, with H_1 and H_2 atoms exhibiting a less negative charge, especially during the formation of the Si–OH_2 defect (step 2). After the disassociation of the water molecule the charges on the hydrogen start to converge, until step 5 of the reaction at which point the charge transfer is complete.

Table II. Atomic Charges of the Water Molecule and the Two-Membered Ring Structures During Two-Membered Ring Opening at the Five Stages Pictured in Figs. 2(a)–(e) (Step 1–5)

Step	1	2	3	4	5
Two-Membered Ring	0.929	0.926	0.930	0.767	0.989
Water	−0.050	0.106	0.026	−0.048	−0.035

Analysis of the partial atomic charges indicate the level of charge transfer that is occurring during the annihilation of the two-membered ring defect, including transfer of charge from the water molecule to the surface and the effect on the atoms surrounding the defect site.

(3) Bond Distance-Bond Angle Correlations: Finger Prints of Reactions from Short Range Atomic Structures

Bond angle-bond distance correlations provide an opportunity to investigate how constraints in the O–Si–O bond angle affects the Si–O distance in a snapshot of the simulation. Typically, bond angle distributions (BAD) and radial/pair distribution functions (RDF/PDF) are presented independently of one another. By investigating both distributions simultaneously it is possible to identify outliers in either the BAD or PDF data and how they relate to one another. Figures 4 and 5 are the contour plots of the Si–O bond lengths in the nanoporous silica and surface silica models with the three O–Si–O bond angles which are related to the bond length. In some cases, a fourth angle is included, which only occurs if the Si in the [SiO_4] tetrahedron is five coordinated. The bond length and BAD are included along the *x*- and *y*-axis, respectively, and are centered around the Si–O bond length of 1.61 Å and the ideal O–Si–O bond angle of 109.5°.[30]

Initially, both the 31% nanoporous silica surface and the flat surface have a broad distribution of the bond lengths (*x*-axis) and bond angles (*y*-axis). The nanoporous silica surface has significantly more outliers in the initial configurations due to the introduction of water into the system, generating defects [Figs. 4(a) and 5(a)]. After the geometry optimization has been performed [Figs. 4(b) and 5(b)] there is a decrease in the distribution of the bond angles and bond distances for both systems, indicating that relaxation of the silica surfaces is occurring. Further simulation time results in decreases in the distributions of the bond lengths and bond angles [Figs. 4(c) and 5(c)]. Interestingly, a number of outliers remain in the silica surface simulation after the 30 ps of AIMD have been completed, consisting of O–Si–O bond angles above 140° and below 100° coupled with disproportionally long bond lengths above 1.75 Å. These outliers can be attributed to the temporary formation of a Si^5 defect by introduction of a water molecule, identified both from the simulations performed here and noted by Kagan et al. [Figs. 2(b) and (c)].[6] As the formation of a Si^5 defect is the primary method through which bond breakage occurs (for instance in the opening of two-membered and three-membered ring) their continued formation indicates that there is a drive to break the siloxane bond and open the ring, but that insufficient energy is available to overcome the energy barrier. In addition, the reader should note the existence of a shoulder in the BAD (on the *y*-axis) in Figs. 4 and 5 which can be attributed to a bond angle of ~80° which occurs in both two-membered and three-membered rings.[30]

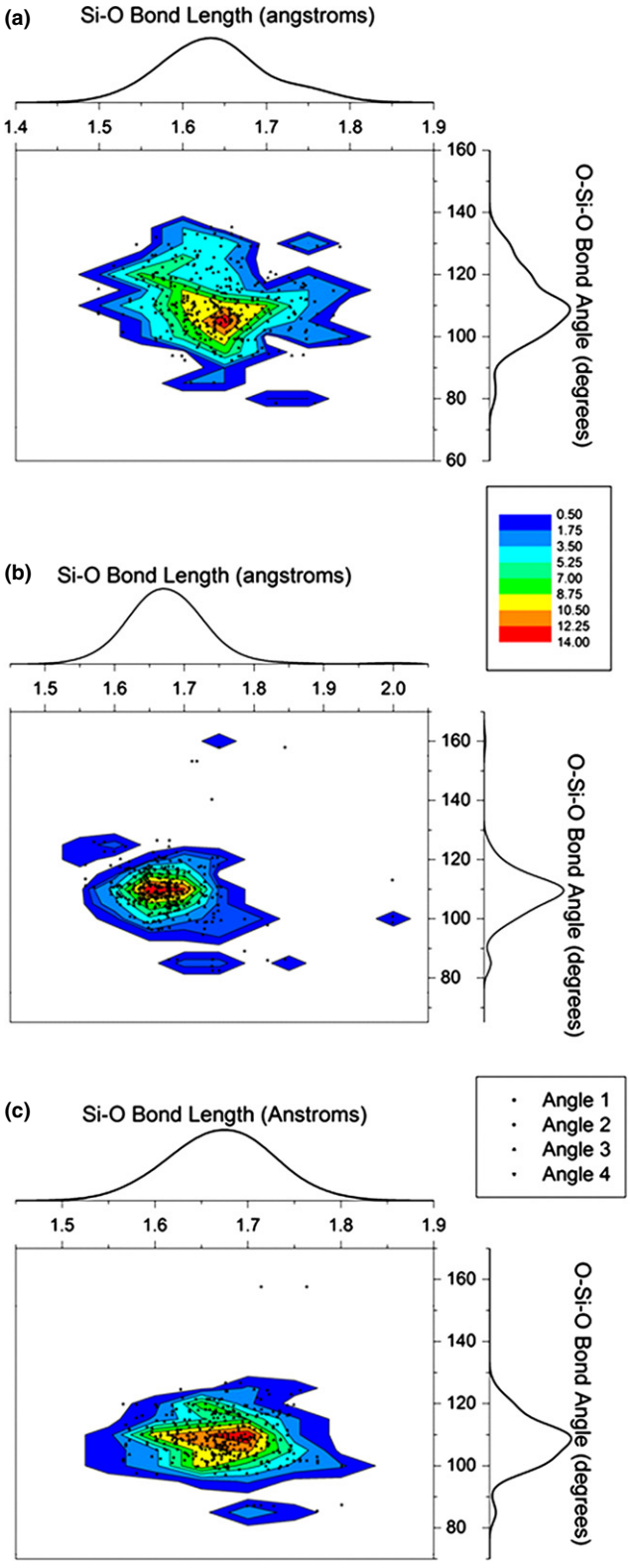

Fig. 4. O–Si–O bond angle Si–O bond length plots of 31% nanoporous silica computational systems (a) initial configuration, (b) after geometry optimizations, and (c) after 30 ps of *ab initio* molecular dynamics. The Si–O pair distribution function and the O–Si–O bond angle distribution are plotted on the *x*- and *y*-axis, respectively.

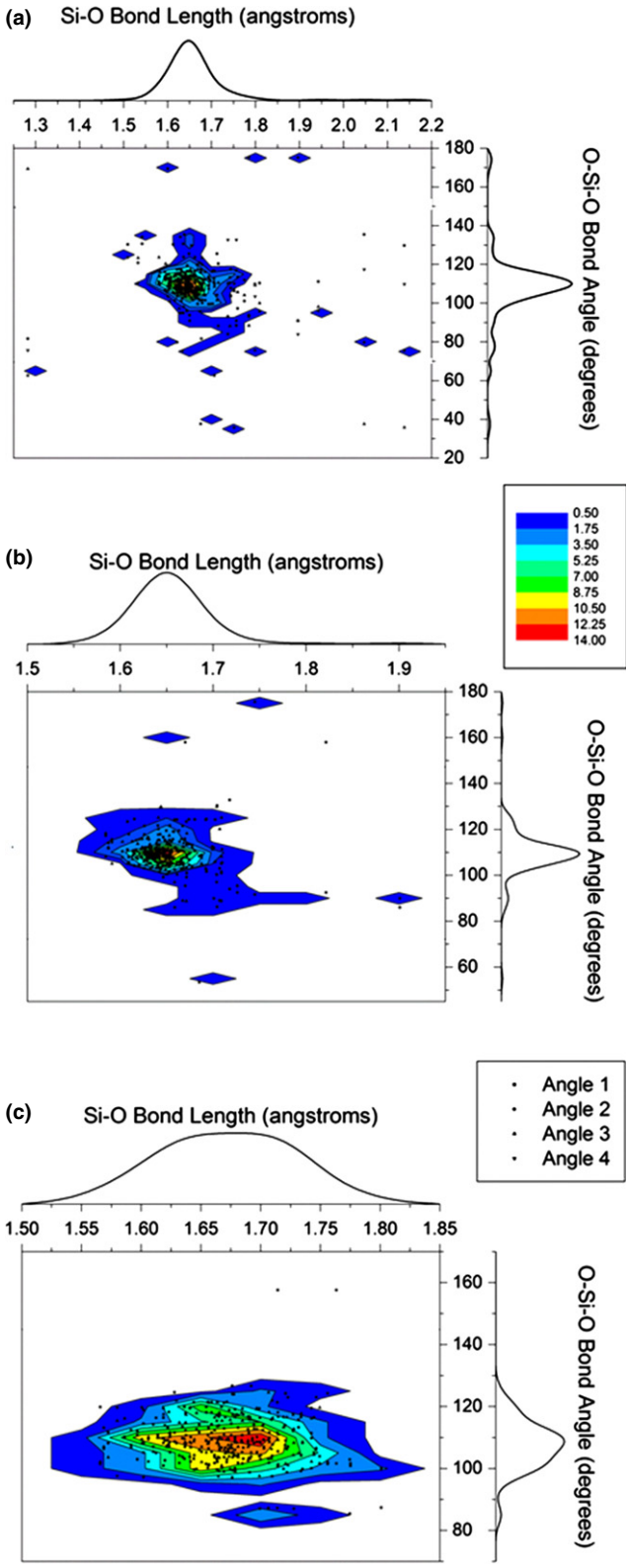

Fig. 5. O–Si–O bond angle Si–O bond distance plots of nanoporous silica surfaces (a) initial configuration, (b) after geometry optimizations, and (c) after 30 ps of *ab initio* molecular dynamics. The Si–O pair distribution function and the O–Si–O bond angle distribution are plotted on the *x*- and *y*-axis, respectively.

(4) Two-Membered Ring Concentrations in Hydroxylated Silica

Two-membered rings, described by the number of silicon involved in the ring structure, are high energy surface defects which occur in both computational and experimental systems. Thermodynamically, these high-energy defects will be removed from the silica systems when it interacts with water molecules present in the atmosphere. Kinetically, two-membered ring removal is complex due to the role of the water molecules in facilitating the reaction. Tilocca and Cormack identified some kinetic stability in two-membered ring—water

reactions during their computational investigations of bioactive glasses.[27] The two-membered ring reactions were hypothesized to depend on water–water and water–defect interactions and as smaller rings only react with 1–2 water molecules at a time their reactivity is limited.[27] Such an effect would be exacerbated in a nanoporous system where water molecules will have limited access to the two-membered ring defects due to the complexity of the porous system. In addition, Kagan et al. investigated the energy barriers of silica dissolution in water by classical MD methods and found that energy barriers increased when the silicon reaction sites were in slightly concave surface contours, which caused the water molecule to interact with additional atoms from the silica structure.[6] Due to the highly variable positions of the two-membered rings in the porous silica structure it is possible that some are part of concave surfaces, leading to their increased stability. As seen in Fig. 6, there is limited change in the two-membered ring concentration in both the nanoporous silica systems and the silica surfaces with time. The two-membered ring annihilation which does occur is restricted to the highest porosity systems (52%, 60%, and 67%) where the two-membered rings would be most easily accessed by the water molecules and where there is a higher probability that a two-membered ring is located on flatter surfaces. The removal of two-membered rings in the highest porosity nanoporous systems but not in the flat surfaces can be attributed to the higher strain which rings in the porous system experience. The added curvature of the system induces extra strain, leading to an increased energetic drive for their removal. Therefore, in the nanoporous silica systems there is a set of competing mechanisms to describe two-membered ring removal, the limiting factor of the water-two-membered ring interactions and two-membered ring positions in concave surfaces as well as the driving force of the added strain from the curvature of the porosity.

(5) Silanol Concentration on Hydroxylated Silica Surfaces

Silanol concentrations (Si–OH) on silica surfaces has been used as a method of investigating the defects concentrations as the hydroxylation groups are formed through the annihilation of common defect species (NBO, Si^3, Si^5, and two-membered rings). Silanol concentrations were calculated by identifying the number of Si–OH groups present in the nanoporous silica systems. The internal surface area was calculated by generating a Connolly (solvent excluded) surface using MaterialStudio.[43,44] The Connolly surface is identified by "rolling" a simulated solvent molecule with a 1 Å radius along the nanoporous silica surface of the structure and the surface of the molecule fitting against the structure generates the surface.[43]

Du and Cormack demonstrated that the total silanol concentration of ~4.6 nm^{-2} for both computational and experimental systems can be separated by defect species with different percentage of silanol groups being the result of annihilation of different defect species.[20] The low level of silanol concentrations in the nanoporous systems studied here, and seen in Fig. 7, indicates that there is limited termination of ring defects in the structure, which is consistent with data presented in Section III(4). The computational silica surfaces investigated in this study would exhibit hydroxylation of 3.92 ± 0.11 #/nm^2 assuming complete defect removal, whereas for the nanoporous silica systems the range was much broader with final theoretical silanol concentrations between 2.8 and 3.7 #/nm^2, varying with porosity. The difference in the theoretical maximum hydroxylation concentration for the porous systems compared to the flat surfaces can be attributed to the different surface morphology causing fewer defects per nm^2 compared to the flat surfaces. As ring defects are responsible for ~60% of the silanol concentration the final silanol concentrations of 0.9–1.5 #/nm^2 are expected (Fig. 7).

Concentrations of silanol groups on freshly fractured surfaces have been quantified experimentally and used to predict reaction kinetics of hydroxyl formation by D'Souza and Pantano.[9,10] They noted two ranges of hydroxylation kinetics, initially a very rapid hydroxylation process which was attributed to the breaking of two-membered rings followed by a slower hydroxylation rate from the breakage of three-membered rings.[9,10] Similar differences in silanol formation rates exist in the computational data presented here, through rather than two- and three-membered rings being broken it is the immediate termination of coordination defects during the geometry optimization followed by the slower breaking of the two-membered rings during AIMD which is responsible for the differences in hydroxylation rates. D'Souza et al. suggested that first order reaction kinetics can be applied to these reactions using the following equation[9,10]:

$$c(t) = c_0 e^{kt} \tag{4}$$

with $c(t)$ as the concentration of silanol groups at time t, c_o as the initial concentration of silanol groups at the begin-

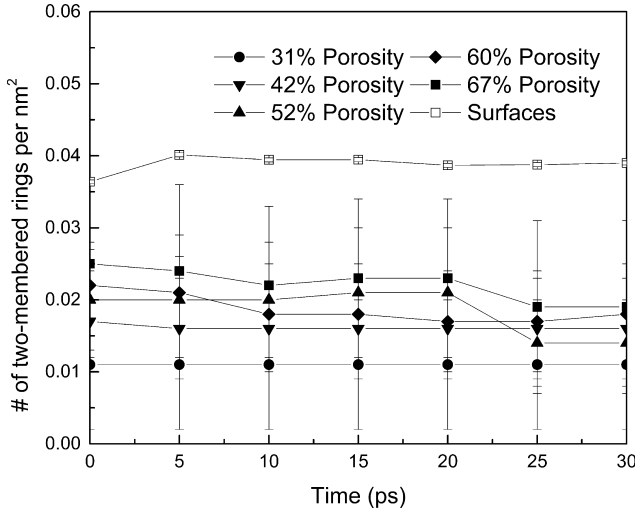

Fig. 6. Changes in two-membered ring concentrations per nm^2 of surface area for nanoporous silica systems with porosities between 31% and 67% and flat surfaces. Standard deviation is equal to the standard error.

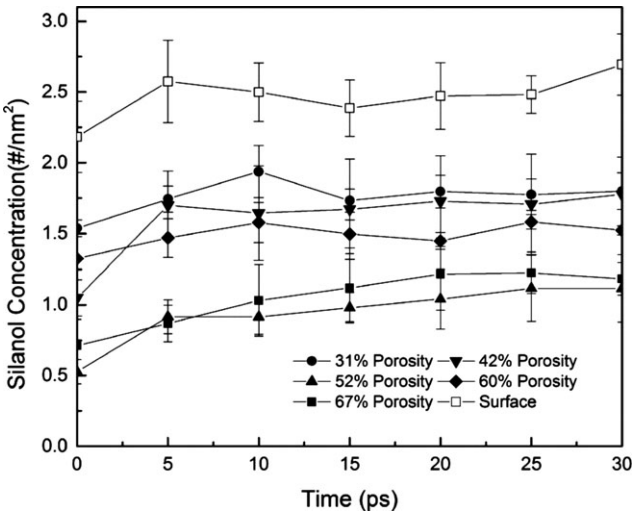

Figure 7. Silanol concentrations in #/nm^2 for nanoporous silica systems with porosities between 31% and 67% and flat surface with time. Standard deviation is equal to the standard error.

ning of the AIMD simulation, t as time and k as the reaction rate constant. Using Eq. (4) and the maximum silanol concentrations that can be expected in the simulated structures, the amount of time required to reach maximum silanol concentration was estimated. It was found that the time required to remove all the two-membered ring defects ranged from 63 ± 23 ps to 472 ± 137 ps for porous systems and 1011 ±380 ps for flat surfaces, which is significantly higher than the 30 ps AIMD simulation performed in this work. This estimation suggests that hydroxylation, even for highly strained two-membered rings, has relatively large energy barriers and are rare events requiring long MD simulations.

Bulk silica has a wide ring size distribution ranging from three to ten membered rings with a Gaussian type distribution centered on six-membered rings.[45] The stability of the rings increases with ring sizes hence larger rings have much lower energy barrier to open the Si–O–Si linkage by reaction with water. Therefore, direct simulation of hydroxylation or dissolution using MD simulations will be very difficult due to long simulation time required for those rare events. Other techniques must be used to study the water reaction of these rings. These methods include transition state theory with the Nudged Elastic Band[45] or the Dimer[46] method, or constrained MD simulations with potential of mean force[3] to address these challenges.

IV. Conclusions

The interactions between water molecules and nanoporous amorphous silica models with porosities between 31% and 67% were investigated through the application of DFT based AIMD simulations to allow for accurate description of bond breakage and formation during water–silica reactions. 30 ps AIMD trajectories were used to analyze the dynamics of defect reactions with water. It was found that coordination defects such as NBO and under/over coordinated silicon were removed during the geometry optimization stage suggesting fast reactions with water. For other surface defects, such as two-membered rings, only partial reactions were observed after 30 ps AIMD at 300 K and no reactions were observed for larger rings during the AIMD simulations. The limited two-membered ring removal can be explained by the restricted movement of water molecules in the nanopores and the higher energy barriers reported for siloxane bond breakage reactions present on concave surfaces.[6]

The observed mechanism of two-membered ring defect removal from AIMD simulations is consistent with a previously proposed mechanism which includes the formation of an intermediate Si^5 defect.[24] The formation of the Si^5 defect was found to be associated with charge transfer from the absorbed water molecule to the silica structure. In addition, the development of Si^5 defects in the Si–OH_2 structure can be identified through bond angle-bond distance correlation plots. Though the Si^5 defects continued to persist in the AIMD simulations the energy required to cause siloxane bond breakage was not present. Analysis of the silanol concentrations with time indicated that full hydroxylation of the surface was anticipated to occur between 60 and 470 ps in nanoporous silica systems and around 1100 ps on silica surfaces.

Acknowledgments

This work was supported by the DOE NEUP project. We want to thank Dr. Joe Ryan for helpful discussions. J.M. Rimsza acknowledges that this material is based upon work supported by the National Science Foundation Graduate Research Fellowship under Grant No. DGE-1144248. Computational resources are from the UNT high performance computing cluster.

References

[1]K. Davis and M. Tomozawa,"Water Diffusion into Silica Glass: Structural Changes in Silica Glass and Their Effect on Water Solubility and Diffusivity," *J. Non Cryst. Solids*, **185** [3] 203–20 (1995).
[2]D. Griggs, "Hydrolytic Weakening of Quartz and Other Silicates" *Geophys. J. Roy. Astron. Soc.*, **14** [1–4] 19–31 (1967).
[3]C. M. Jantzen and M. J. Plodinec, "Thermodynamic Model of Natural, Medieval and Nuclear Waste Glass Durability," *J. Non Cryst. Solids*, **67** [1–3] 207–23 (1984).
[4]S. Gin, et al., "An International Initiative on Long-Term Behavior of High-Level Nuclear Waste Glass," *Mater. Today*, **16** [6] 243–8 (2013).
[5]E. M. Pierce, P. Frugier, L. J. Criscenti, K. D. Kwon, and S. N. Kerisit, "Modeling Interfacial Glass-Water Reactions: Recent Advances and Current Limitations," *Inter. J. Appl. Glass Sci.*, **5** [4] 421–35 (2014).
[6]M. Kagan, G. K. Lockwood, and S. H. Garofalini, "Reactive Simulations of the Activation Barrier to Dissolution of Amorphous Silica in Water,"*Phys. Chem. Chem. Phys.*, **16** [20] 9294–301 (2014).
[7]J. P. Icenhower and P. M. Dove, "The Dissolution Kinetics of Amorphous Silica into Sodium Chloride Solutions: Effects of Temperature and Ionic Strength," *Geochim. Cosmochim. Acta*, **64** [24] 4193–203 (2000).
[8]D. Ceresoli, M. Bernasconi, S. Iarlori, M. Parrinello, and E. Tosatti, "Two-Membered Silicon Rings on the Dehydroxylated Surface of Silica," *Phys. Rev. Lett.*, **84** [17] 3887–90 (2000).
[9]A. S. D'Souza and C. G. Pantano, "Hydroxylation and Dehydroxylation Behavior of Silica Glass Fracture Surfaces," *J. Am. Ceram. Soc.*, **85** [6] 1499–504 (2002).
[10]A. S. D'Souza and C. G. Pantano, "Mechanisms for Silanol Formation on Amorphous Silica Fracture Surfaces," *J. Am. Ceram. Soc.*, **82** [5] 1289–93 (1999).
[11]T. Charpentier, P. Kroll, and F. Mauri, "First-Principles Nuclear Magnetic Resonance Structural Analysis of Vitreous Silica," *J. Phys. Chem. C*, **113** [18] 7917–29 (2009).
[12]T. M. Clark, P. J. Grandinetti, P. Florian, and J. F. Stebbins, "Correlated Structural Distributions in Silica Glass," *Phys. Rev. B*, **70** [6] 064202, 8pp (2004).
[13]S. H. Garofalini, "Molecular Dynamics Computer Simulations of Silica Surface Structure and Adsorption of Water Molecules," *J. Non Cryst. Solids*, **120** [1] 1–12 (1990).
[14]S. Levine and S. H. Garofalini, "A Structural Analysis of the Vitreous Silica Surface Via a Molecular Dynamics Computer Simulation," *J. Chem. Phys.*, **86**, 2997–3003 (1987).
[15]T. Mahadevan and S. Garofalini, "Dissociative Water Potential for Molecular Dynamics Simulations," *J. Phys. Chem. B*, **111** [30] 8919–27 (2007).
[16]T. Mahadevan and S. Garofalini, "Dissociative Chemisorption of Water onto Silica Surfaces and Formation of Hydronium Ions," *J. Phys. Chem. C*, **112** [5] 1507–15 (2008).
[17]J. C. Fogarty, H. M. Aktulga, A. Y. Grama, A. C. Van Duin, and S. A. Pandit, "A Reactive Molecular Dynamics Simulation of the Silica-Water Interface," *J. Chem. Phys.*, **132**, 174704, 10pp (2010).
[18]E. B. Webb and S. H. Garofalini, "Relaxation of Silica Glass Surfaces Before and After Stress Modification in a Wet and Dry Atmosphere: Molecular Dynamics Simulations," *J. Non Cryst. Solids*, **226** [1] 47–57 (1998).
[19]B. Feuston and S. H. Garofalini, "Water-Induced Relaxation of the Vitreous Silica Surface," *J. Appl. Phys.*, **68** [9] 4830–6 (1990).
[20]J. Du and A. N. Cormack, "Molecular Dynamics Simulation of the Structure and Hydroxylation of Silica Glass Surfaces," *J. Am. Ceram. Soc.*, **88** [9] 2532–9 (2005).
[21]T. Bakos, S. Rashkeev, and S. Pantelides, "H_2O and O_2 Molecules in Amorphous SiO_2: Defect Formation and Annihilation Mechanisms," *Phys. Rev. B*, **69** [19] 195206, 9pp (2004).
[22]M. Du, A. Kolchin, and H. Cheng, "Hydrolysis of a Two-Membered Silica Ring on the Amorphous Silica Surface," *J. Chem. Phys.*, **120**, 1044–54 (2004).
[23]M. Du, A. Kolchin, and H. Cheng, "Water–Silica Surface Interactions: A Combined Quantum-Classical Molecular Dynamic Study of Energetics and Reaction Pathways," *J. Chem. Phys.*, **119**, 6418–22 (2003).
[24]P. Masini and M. Bernasconi, "Ab Initio Simulations of Hydroxylation and Dehydroxylation Reactions at Surfaces: Amorphous Silica and Brucite," *J. Phys.: Condens. Matter*, **14** [16] 4133–44 (2002).
[25]S. H. Garofalini, T. S. Mahadevan, S. Xu, and G. W. Scherer, "Molecular Mechanisms Causing Anomalously High Thermal Expansion of Nanoconfined Water," *Chem. Phys. Chem.*, **9** [14] 1997–2001 (2008).
[26]V. Bakaev and W. Steele, "On the Computer Simulation of a Hydrophobic Vitreous Silica Surface," *J. Chem. Phys.*, **111**, 9803–12 (1999).
[27]A. Tilocca and A. N. Cormack, "Modeling the Water– Bioglass Interface by *Ab Initio* Molecular Dynamics Simulations," *ACS Appl. Mater. Interfaces*, **1** [6] 1324–33 (2009).
[28]N. Lopez, M. Vitiello, F. Illas, and G. Pacchioni, "Interaction of H_2 with Strained Rings at the Silica Surface from *Ab Initio* Calculations," *J. Non Cryst. Solids*, **271** [1] 56–63 (2000).
[29]T. Forester and W. Smith, *The DL_POLY_2 Reference Manual*. Daresbury Laboratory, Daresbury, 2000.
[30]J. Rimsza and J. Du, "Structural and Mechanical Properties of Nanoporous Silica," *J. Am. Ceram. Soc.*, **97** [3] 772–81 (2014).
[31]J. VandeVondele, F. Mohamed, M. Krack, J. Hutter, M. Sprik, and M. Parrinello, "The Influence of Temperature and Density Functional Models in *Ab Initio* Molecular Dynamics Simulation of Liquid Water," *J. Chem. Phys.*, **122**, 014515, 6pp (2005).

[32]J. Sarnthein, A. Pasquarello, and R. Car, "Structural and Electronic Properties of Liquid and Amorphous SiO_2: An *Ab Initio* Molecular Dynamics Study," *Phys. Rev. Lett*., **74** [23] 4682–5 (1995).

[33]J. Du and L. R. Corrales, "Structure, Dynamics, and Electronic Properties of Lithium Disilicate Melt and Glass," *J. Chem. Phys*., **125**, 114702, 12pp (2006).

[34]J. Du, C. J. Benmore, R. Corrales, R. T. Hart, and J. K. R. Weber, "A Molecular Dynamics Simulation Interpretation of Neutron and X-ray Diffraction Measurements on Single Phase Y_2O_3–Al_2O_3 Glasses," *J. Phys.: Condens. Matter*, **21** [20] 205102, 9pp (2009).

[35]C. Bonhomme, et al., "^{87}Sr Solid-State NMR as a Structurally Sensitive Tool for the Investigation of Materials: Antiosteoporotic Pharmaceuticals and Bioactive Glasses," *J. Am. Chem. Soc*., **134** [30] 12611–28 (2012).

[36]S. Kurth, J. P. Perdew, and P. Blaha, "Molecular and Solid-State Tests of Density Functional Approximations: LSD, GGAs, and Meta-GGAs," *Inter. J.Quantum Chem*., **75** [4–5] 889–909 (1999).

[37]A. Tilocca, "Structure and Dynamics of Bioactive Phosphosilicate Glasses and Melts From *Ab Initio* Molecular Dynamics Simulations," *Phys. Rev. B*, **76** [22] 10429, 14pp (2007).

[38]J. Sauer, "Molecular Structure of Orthosilicic Acid, Silanol, and $H_3SiOH{\cdot}AlH_3$ Complex: Models of Surface Hydroxyls in Silica and Zeolites," *J. Phys. Chem*., **91** [9] 2315–9 (1987).

[39]P. Ugliengo, V. Saunders, and E. Garrone, "Silanol as a Model for the Free Hydroxyl of Amorphous Silica: *Ab-Initio* Calculations of the Interaction with Water," *J. Phys. Chem*., **94** [6] 2260–7 (1990).

[40]J. Brédas, D. Beljonne, V. Coropceanu, and J. Cornil, "Charge-Transfer and Energy-Transfer Processes in π-Conjugated Oligomers and Polymers: A Molecular Picture," *Chem. Rev*., **104** [11] 4971–5004 (2004).

[41]F. Jensen, *Introduction to Computational Chemistry*. John Wiley & Sons, Hoboken, NJ, 2007.

[42]D. Hamann, "Energies of Strained Silica Rings," *Phys. Rev. B*, **55** [22] 14784–93 (1997).

[43]M. L. Connolly, "Analytical Molecular Surface Calculation," *J. Appl. Crystallogr*., **16** [5] 548–58 (1983).

[44]*Manual of MaterialStudio 3.0*. Accelyrys, Inc, San Diego, California, 2004.

[45]P. Zapol, H. He, K. D. Kwon, and L. J. Criscenti, "First-Principles Study of Hydrolysis Reaction Barriers in a Sodium Borosilicate Glass," *Inter. J. Appl. Glass Sci*., **4** [4] 395–407 (2013).

[46]F. Gao, J. Du, E. J. Bylaska, M. Posselt, and W. J. Weber, "*Ab Initio* Atomic Simulations of Antisite Pair Recovery in Cubic Silicon Carbide," *Appl. Phys. Lett*., **90** [22] 221915, 3pp (2007). □

THE JOURNAL OF PHYSICAL CHEMISTRY C

Article

pubs.acs.org/JPCC

Water Interactions with Nanoporous Silica: Comparison of ReaxFF and *ab Initio* based Molecular Dynamics Simulations

J. M. Rimsza,[†,#] Jejoon Yeon,[‡,⊥] A. C. T. van Duin,[‡] and Jincheng Du*[,†]

[†]Department of Materials Science and Engineering, University of North Texas, Denton, Texas 76203, United States

[‡]Department of Mechanical and Nuclear Engineering, The Pennsylvania State University, University Park, Pennsylvania 16802, United States

Supporting Information

ABSTRACT: Detailed understanding of the reactions and processes which govern silicate−water interactions is critical to geological, materials, and environmental sciences. Interactions between water and nanoporous silica were studied using classical molecular dynamics with a Reactive Force Field (ReaxFF), and the results were compared with density functional theory (DFT) based *ab initio* molecular dynamics (AIMD) simulations. Two versions of ReaxFF Si/O/H parametrizations (Yeon et al. *J. Phys. Chem. C* **2016**, *120*, 305 and Fogarty et al. *J. Chem. Phys.* **2010**, *132*, 174704) were compared with AIMD results to identify differences in local structures, water dissociation mechanisms, energy barriers, and diffusion behaviors. Results identified reaction mechanisms consisting of two different intermediate structures involved in the removal of high energy two-membered ring (2-Ring) defects on complex nanoporous silica surfaces. Intermediate defects lifetimes affect hydroxylation and 2-Ring defect removal. Additionally, the limited internal volume of the nanoporous silica results in decreased water diffusion related to the development of nanoconfined water. Hydrogen atoms in the water diffused 10−30% faster than the oxygen atoms, suggesting that increased hydrogen diffusion through hydrogen hopping mechanisms may be enhanced in nanoconfined conditions. Comparison of the two different ReaxFF parametrizations with AIMD data indicated that the Yeon et al. parameters resulted in reaction mechanisms, hydroxylation rates, defect concentrations, and activation energies more consistent with the AIMD simulations. Therefore, this ReaxFF parametrization is recommended for future studies of water−silica systems with high concentrations of surface defects and highly strained siloxane bonds such as in complex silica nanostructures.

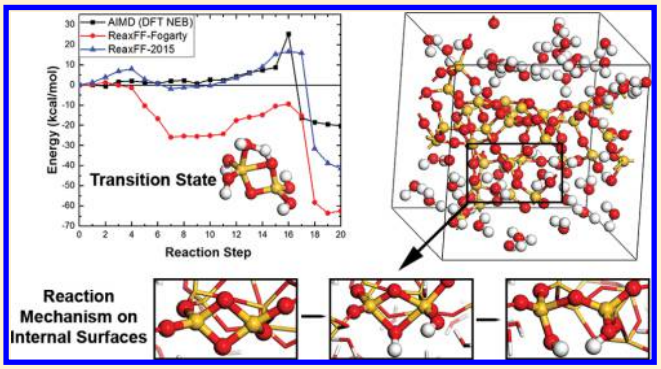

1. INTRODUCTION

Nanoporous silica commonly occurs in natural systems and can be found in biomedical, microelectronic, environmental, and energy applications. The high surface area and variable pore structure, in both size and morphology, make nanoporous silica well suited for catalysis supports, gas phase separation, hydrogen storage, and thermal insulation.[1−3] Interactions between water and internal surfaces formed in nanoporous silica are of interest due to the omnipresence of water in the environment and its effect on the dissolution behavior, long-term stability, and mechanical properties of silica.

Recent experimental work has identified fast hydroxylation of fractured silica surfaces,[4,5] structure and dynamics of interfacial water in nanoporous silica,[6,7] and various bonding environments in the water−silica system[8] using secondary ion mass spectroscopy, nuclear magnetic resonance spectroscopy, and sum-frequency generation spectroscopy. Atomistic computer simulations provide information on water−silica systems that are not available from experiment due to characterization difficulties of the amorphous structure, randomized pore morphology, and short reaction times. The identification of reaction mechanisms, varying stability of defect species, and the hydroxylation rate of reactive silica surfaces are all of interest.

Both density functional theory (DFT) and classical molecular dynamics (MD) studies have been employed to perform atomistic investigation of water−silica systems. DFT simulations analyzed hydrogen bond networks, surface silanol concentrations, development of structured water, energetics of silica monomer and dimer formation, and the protonation of silanol groups.[9−12] Reaction mechanisms and energy barriers responsible for siloxane bond breakage in strained and unstrained silica sites have been reported by Rimsza and Du,[13] Zapol et al.,[14] and Rimola and Ugliengo[15] among others, demonstrating the importance of *ab initio* simulations in identifying details of the water−silica interface.

Despite the success with the application of DFT methods to water−silica system, classical MD methods have a clear advantage in terms computational efficiency. As a result much

Received: August 5, 2016
Revised: September 26, 2016
Published: October 3, 2016

DOI: 10.1021/acs.jpcc.6b07939
J. Phys. Chem. C 2016, 120, 24803−24816

larger systems can be studied compared to first-principles based simulations. ReaxFF simulations are estimated to be ~5x faster than DFT simulations of a 350 atom system using a Silicon Graphics Origin-computer for the original hydrocarbon ReaxFF force field.[16] Since then additional improvements, such as the reax/c style implemented in LAMMPS has resulted in greater increases in efficiency over quantum mechanical methods.[17]

A challenge of classical MD simulations is the development of potentials capable of accurately describing interatomic interactions. For the mixed covalent and ionic bonding in water−silica systems the potential should include different charge states and polarization of oxygen atoms depending on the chemical environments, and be capable of describing the chemical reactions of water with silica. Early potentials that are successful in the simulations of the structure and properties of bulk silica include two-bodied Buckingham potentials by van Beest, Kramer, and van Santen (BKS) and Tsenueyki and colleagues (TTAM).[18,19] Additional regulation of the O−Si−O and Si−O−Si bond angles was included through the use of three-bodied terms.[20,21] Water molecules further complicate potential development due to hydroxylation reactions, the formation of hydronium (H_3O^+) ions, and proton transfer in bulk water.

There are a number of empirical potentials developed to study water−silica systems. One of the first used a dissociative water potential by Feuston and Garofalini.[20] The Feuston-Garofalini potential focused on the simulation of polymerization reactions, but inconsistencies in the structure of bulk water, including the formation of symmetric hydrogen bonds and low H−O−H bond angles, indicated the need for additional refinement.[20] Mahadevan and Garofalini developed another potential which focuses on the disassociation of water molecules in bulk water systems, which has been applied to the investigate the lifetime of hydronium ions,[22] hydroxylation,[23] thermal expansion of nanoconfined water,[24] and silica dissolution.[25] Du and Cormack developed a set of partial charge potentials to study the hydroxylation of silica and silicate surfaces with a Morse potential for O−H interactions.[26] Silanol concentration of the silica surface was close to experimental values; however, no water parameters were included in the potentials set. Another potential developed for water−silica simulations was published by Hassanali and Singer, who used a BKS model for silica and a SPC/E model for water with Buckingham interactions to describe the water−silica interface.[27] Several other water−silica potentials have been developed;[28−30] however, truly reactive potentials that can reproduce the bulk silica and water structures and properties as well as their reaction energetics are rare in the literature.

ReaxFF, a reactive force field initially developed by van Duin, Goddard and co-workers was a significant advancement in the simulations of water−silica interactions.[16,31] ReaxFF is a bond-order based potential which uses a complex series of partial energy terms to describe the total system energy and bonding states of a material.[31] ReaxFF utilizes a charge equilibration (QEq) method to calculate geometry dependent charges.[32] Advantages of the ReaxFF potential model include the indistinguishability of atomic species in the force field−only one atom type is used for atoms of a single element, regardless of their coordination - and the smooth transition from one chemical species to another.[33] Additionally, charges in the systems vary depending on the local geometry and chemical environment.[33] The first ReaxFF potential for Si/O/H systems was developed in 2003.[31] This potential was aimed at describing silica/silicon interfaces and did not have a capability for describing a liquid water phase. The initiation of the ReaxFF "water-branch" (see Reference[34] for a recent review) enabled the inclusion of a reactive liquid water phase. ReaxFF/SiO was reparameterized for water−silica systems in 2010 by Fogarty et al. (ReaxFF-Fogarty) and successfully reproduced structural features and diffusion coefficients for water and silica.[33] A detailed comparison indicated that the ReaxFF-Fogarty potential is well suited to the simulation of both bulk silica and hydroxylated silica surfaces.[33,35] In 2015, the parameters described by Fogarty et al. were adjusted by Yeon and van Duin (ReaxFF-2015) to improve activation energies for Si−O bond breakage,[36] specifically including local strain influence on silica hydrolysis activation energies. The underlying chemistry of the ReaxFF potential allows for high accuracy with a relatively small penalty in computational efficiency, but is more complicated to parametrize than the two- and three-body potentials described previously. In the relatively short time that the ReaxFF potential has been available, it has demonstrated its application in a variety of silica-related studies and has quickly become one of the most widely implemented silica potentials. Examples of its application in recent years include silica crack propagation,[37] O_2 and H_2 interactions with silica surfaces,[38,39] investigation of friction and wear on silica surfaces,[40] as well as its use in the simulation of mixed silica−hydrocarbon systems.[41,42]

However, current ReaxFF simulations investigated focused on flat surfaces or silica nanorods.[33] Simulations of the interactions of truly nanoporous structures of silica and water are limited. Nanoporous silica more closely resemble corrosion fronts than gel structures, so validation the of water−silica interactions on these surfaces is critical. In addition, most of the ReaxFF development was based on the geometry and energetics of static DFT based quantum mechanical simulations. The simulations are rarely compared with dynamic *ab initio* molecular dynamic (AIMD) simulations. Comparisons between the results from ReaxFF based MD simulations and dynamic data from AIMD simulations assists in establishing the accuracy of the potential. The validation of these methods provides direct comparison of the performance of the two versions of ReaxFF and selection criterion for the future use of the force field in complex structures. The purpose of this paper is to provide a systematic comparison of MD simulation results of water−nanoporous silica interaction from two versions of the ReaxFF potentials and those from the AIMD simulations through the short and medium range structure, water diffusion behaviors, water−silica reaction mechanisms, hydroxylation of defect species, lifetimes of coordination defects, and activation energies for siloxane bond breakage. This will not only provide insight of the chemical reaction process of water−silica interactions but also the relative accuracy of the two sets of ReaxFF potentials. The results indicate that the 2015 ReaxFF potential improves the activation energy and mechanisms of water−silica reactions as well as the stability of coordination defect structures while accurately reproducing structural and dynamic features of complex nanoporous silica systems.

This paper is organized in the following way. After introducing the computational methodologies, the results on the test of the silica dimers are first reported. A comparison of activation energies for siloxane bond breakage between the ReaxFF potentials and *ab initio* simulations is then given. An analysis of the 2-Ring defect reaction mechanisms, three-bonded oxygen defect lifetimes, hydroxylation rates, and

DOI: 10.1021/acs.jpcc.6b07939
J. Phys. Chem. C 2016, 120, 24803−24816

diffusion coefficients provides insight into the kinetics of water−silica interactions. Lastly, conclusions are presented.

2. COMPUTATIONAL METHODS

Several computational methods, ranging from classical MD with fixed partial charge and ReaxFF potentials to DFT based *ab initio* MD simulations, were used in this work to develop the hydrated nanoporous silica structures and to investigate the reactivity and dynamic properties. These mixed methods are required to take advantage of accuracy in describing the chemical reactions of *ab initio* and ReaxFF based methods and the computational efficiency of the classical MD simulations. As compared to many static transition state calculations of water−silica reactions,[15,43−46] this work focused on the dynamic simulations of the hydrated nanoporous silica systems to identify water−silica reactions and water diffusion behaviors.

2.1. Nanoporous Silica Structure Generation. A classical MD potential parametrized by Teter for silica was used for generation of the nanoporous silica.[26] A 99 atom silica model with a density of 2.2 g/cm^3 was used as the base structure and was created through a melt and quench procedure. The small system sizes allow for efficient simulations using DFT methods. To introduce volume into the silica, a four step protocol was implemented.

First, the dense silica underwent a linear lattice expansion by 20%, increasing the cell volume from 1500 Å^3 to 1800 Å^3 and the Si−O bond length from 1.6 to1.9 Å. Next, the expanded silica structure was relaxed with a NVT ensemble for 30 ps with a 1 fs time step at 300 K using a Nosé−Hoover thermostat. The number of atoms (N), volume (V), and temperature (T) were kept constant, to retain the added volume in the system. Atomic movement recreated some of the SiO_4 tetrahedra and incorporated free space into the system as voids. After relaxation, ∼20% porosity was scattered throughout the structure. To create higher porosity models, the relaxed systems were expanded again, adding additional volume and increasing the porosity. By repeating the expansion and relaxation process iteratively, systems with different porosities were created. To account for a range of porous structures, systems between 30% and 70% porosity were generated. Variation in the nanoporous silica system is from the unique silica structures used for the development of the porous systems. Higher porosities, such as occur in silica aerogels, result in completely fragmented structures at this system size and current DFT methods are not sufficiently efficient to allow for increases in simulation cell dimensions.

The final step was an isothermal−isobaric (NPT) relaxation performed with a Nosé−Hoover thermostat and barostat to bring the system to a thermomechanical equilibrium. This step was critical in removing the negative pressure regions which can form due to the added vacuum space in the simulation cell.[47] The final nanoporous silica systems have porosities of 31%, 42%, 52%, 60%, and 67% with densities of 1.53 g/cm^3, 1.27 g/cm^3, 1.06 g/cm^3, 0.88 g/cm^3, and 0.74 g/cm^3, respectively. The same method of generating nanoporous silica was used for larger systems (∼3000 atoms), and the short- and long-range structural features of those structures are included in ref 48.

Hydration of the nanoporous silica structure was performed by overlaying a simulation cell of pure water on the nanoporous silica models. Any water molecules outside the boundary of the simulation cell or overlapping with the silica backbone were removed, resulting in a hydrated nanoporous silica structure. Due to the larger volume of free space available in highly porous systems, the number of water molecules increases with porosity. Simulation sizes varied between 150 and 370 atoms. Snapshots of a nanoporous silica structure before and after hydration are included in Figure 1.

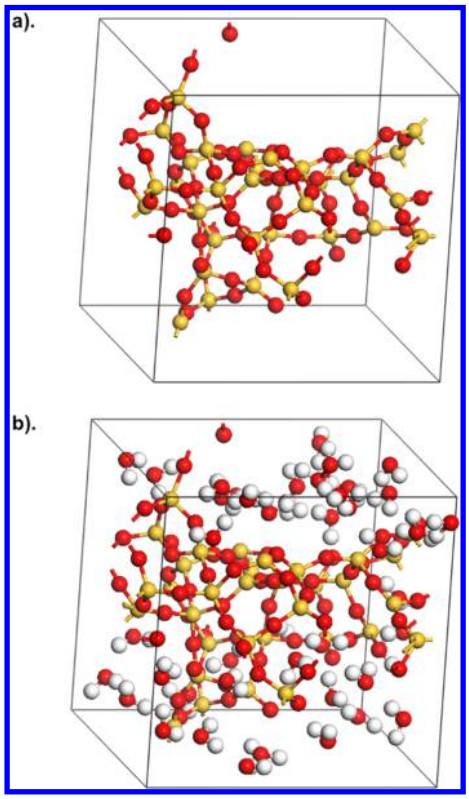

Figure 1. Snapshot of the 52% nanoporous silica systems (a) unhydrated and (b) hydrated. Colors: red (oxygen), yellow (silicon), white (hydrogen).

Simulations were performed in triplicate with different initial dense silica structures to account for variances in the amorphous porous system. Results are reported as the average with the standard error. The standard error is described by eq 1, with SE as the standard error, SD as the standard deviation, and n as the number of unique systems.[13]

$$SE = \frac{SD}{\sqrt{n}} \quad (1)$$

All the hydrated nanoporous silica systems underwent 500 steps of DFT geometry optimization before further simulations were performed to eliminate inconsistencies in the minimization routines between the classical MD and DFT simulations. Details on the DFT methods used for the relaxation and AIMD simulations are included in Section 2.3. The geometry optimization allowed for removal of high energy structures formed by the introduction of water. An analysis of the effect of the geometry optimization on similar systems is included in ref 13.

The same hydrated nanoporous silica structures were used as the initial conditions for all simulation methods, both DFT and classical MD simulations with the ReaxFF-Fogarty and ReaxFF-2015 potentials. Identical initial structures allowed for the comparison of the results across simulation methods.

2.2. Reactive Force Field (ReaxFF) Potentials. ReaxFF is a complex bond order based potential in which the system

DOI: 10.1021/acs.jpcc.6b07939
J. Phys. Chem. C 2016, 120, 24803−24816

energy is the sum of several partial energy contributions (eq 2).[31]

$$E_{system} = E_{bond} + E_{over} + E_{under} + E_{lp} + E_{val} + E_{pen} + E_{tors} + E_{conj} + E_{vdWaals} + E_{Coulomb} \quad (2)$$

In ReaxFF, atomic bond order is calculated directly from the interatomic distances rather than using fixed chemical bonds. The bond order is recalculated after every simulation step to allow for the formation and breakage of bonds.

Additional partial energy terms were added during parametrization of ReaxFF for silica systems.[16,31] Separate disassociation energies for different bonding states (single, double, and triple), an energy term for the treatment of lone pairs, and an adjusted valence angle term to account for the effect of the different bonding states were all introduced.[31] Details and functional forms for these adjustments are included in the original paper, ref 31.

Fogarty et al. in 2010 parametrized the ReaxFF potential for the water−silica systems, including additional *ab initio* data. The process included parametrization to quantum mechanical data of water clusters and proton transfer in acidic and basic systems, after which the silica parameters were refit to a silica training set.[16,33] The resulting water−silica simulation matched well with DFT simulations or experimental results on the structural features, diffusion coefficients, and partial charge distributions.[33] The ReaxFF-Fogarty force field was also used for the identification of water diffusion by proton transfer through a silica slab and polarization of the water molecules during interaction with silica surfaces.[33] In the ReaxFF-Fogarty potential, the activation energy for the breakage of strained siloxane bonds, such as those in high energy 2-Ring defects, is underestimated.[36] The low activation energy results in faster hydroxylation of strained Si−O bonds and affects the stability of strained ring defects, which is inconsistent with DFT data.[33,36,42] Reaction pathways from the DFT simulation of water with strained and unstrained siloxane bonds were added to the training set for the ReaxFF potential parametrization to correct the activation energies. A discussion of the effect of the reparametrization on strained and unstrained siloxane bond breakage is included in Section 3.2.

Hydrated nanoporous silica systems were simulated using both ReaxFF-Fogarty and ReaxFF-2015 potentials for 30 ps of classical MD using a 0.35 fs time step at 300 K controlled by a Nosé−Hoover thermostat. In some instances, longer simulations (1 ns or more) were performed to investigate the stability of certain defect structures, and are discussed in Section 3.3. The ReaxFF simulations were performed in the MD simulation package LAMMPS using the USER-REAXC package.[49] The coordinates of the hydrated nanoporous silica systems before and after simulation are included in the Supporting Information.

2.3. *Ab Initio* Molecular Dynamics (AIMD) Simulations. DFT AIMD simulations were performed in parallel using the same initial nanoporous silica systems for comparison with ReaxFF classical MD simulations. A mixed Gaussian and plane wave basis set was implemented in the QUICKSTEP routine in CP2K to provide increased efficiency over the use of pure plane wave codes.[50,51] The QUICKSTEP method has been previously applied to the simulation of water, silica, and water−silica systems.[9,10,52,53] DZVP basis sets and the BLYP functional were used due to their ability to reproduce both the diffusional and structural properties of liquids[52] and silica[53] with an energy cutoff of 280 Ry. Similar computational parameters have been used to identify the structure of water inside a silica nanopore, the acidity of silanol species, and 2-Ring defect reactions.[9,10,13] Hydrated nanoporous silica underwent 30 ps of AIMD using a 1 fs time step at 300 K, controlled by a Nosé−Hoover thermostat. The coordinates of the hydrated nanoporous silica systems before and after simulation are included in the Supporting Information.

3. RESULTS

3.1. Short Range Structures of Strained and Unstrained Silica Dimers and Silica Surfaces. Analysis of the strained and unstrained silica dimers provides insight into how the local structure of the SiO_4 tetrahedron and Si−O−Si bridges vary with simulation method and classical MD potential. A silica dimer (Figure 2a) and a hydroxylated 2-Ring defect structure (Figure 2b) were selected as representative systems for unstrained and strained siloxane bonds, respectively. Similar models were used to reparametrize the ReaxFF potentials with improved energetics for 2-Ring defect removal (ReaxFF-2015 potential).[36] The strained silica dimer is representative of a 2-Ring defect, which is a set of edge sharing SiO_4 tetrahedra. 2-Ring defects are more reactive than Si−O bonds in three-membered or four-membered rings, and are therefore commonly used in atomistic simulations to investigate kinetics of siloxane bond breakage in computational time frames. 2-Ring defects have been identified experimentally during the fracturing of silica in high vacuum.[4,54−56] To form the dimer for the cluster calculations, all the dangling oxygen bonds were hydrogen terminated.

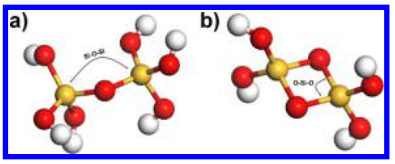

Figure 2. Snapshots of the (a) unstrained and (b) unstrained silica dimers. Colors: red (oxygen), yellow (silicon), white (hydrogen).

All simulations were performed in 25 Å × 25 Å × 25 Å cells, and the energies of the structures were minimized through geometry optimization before analysis. Bond angle distributions (BAD) and pair distribution functions (PDF) were generated from a 15,000 step NVT classical MD or AIMD simulation to identify equilibrium bond lengths and angles at 300 K. The use of BAD and PDF accounts for variations in the bond length due to thermal vibrations. Interatomic distances and bond angles are reported as the peak of the BAD or PDF value, as well as the full-width-at-half maximum (fwhm) in Table 1 and Table 2.

The Si−O, O−O, and O−H interatomic distances are consistent between both the strained and unstrained siloxane dimers and the different simulation methods (Table 1, Table 2). Experimental variation in the Si−O−Si bond angles depends on the characterization methods used and the thermal history of the glass, and both AIMD and ReaxFF simulations are within the range noted experimentally.[33,58,61] Differences in the Si−O−Si bond angles between AIMD and ReaxFF may be due to the variation in the structure due to thermal effects during the simulation. Previous DFT methods have identified that the Si−O−H bond angle is ∼118°, suggesting that ReaxFF-Fogarty had an underestimation of the bond angle while ReaxFF-2015 experienced a slight overestimation in both

DOI: 10.1021/acs.jpcc.6b07939
J. Phys. Chem. C 2016, 120, 24803−24816

Table 1. Interatomic Distances and Bond Angles of the Unstrained Silica Dimer and Experimental Values from Bulk Amorphous Silica

Property	AIMD		ReaxFF-Fogarty		ReaxFF-2015		Expt.
	Dimer	Surface	Dimer	Surface	Dimer	Surface	Silica
Si−O dist. (Å)	1.64 (0.07)	1.65 (0.08)	1.55 (0.07)	1.58 (0.09)	1.57 (0.09)	1.59 (0.11)	1.61[b]
O−O dist. (Å)	2.69 (0.20)	2.68 (0.20)	2.55 (0.19)	2.56 (0.29)	2.58 (0.38)	2.58 (0.30)	2.65[c]
O−H dist. (Å)	0.97 (0.03)	1.01[a] (0.08)	0.96 (0.07)	0.99[a] (0.07)	0.98 (0.05)	1.01[a] (0.08)	0.98[d]
Si−Si dist. (Å)	3.09 (0.19)	3.20 (0.32)	2.91 (0.06)	3.06 (0.12)	3.06 (0.11)	3.12 (0.15)	3.1[e]
Si−O−Si angle (deg)	142 (20)	142 (38)	140 (9)	150 (22)	153 (26)	154 (37)	144[c] 152[f]
O−Si−O angle (deg)	110 (12)	108 (12)	108 (11)	108 (17)	109 (12)	108 (15)	109.4[c]
Si−O−H angle (deg)	116 (14)	117[a] (17)	107 (7)	112[a] (9)	124 (9)	123[a] (7)	118.1[g]

[a]From Si−OH located on internal surfaces of nanoporous silica. [b]Neutron diffraction.[57] [c]Electron diffraction.[58] [d]Electon diffraction.[59] [e]Large angle X-ray scattering.[60] [f]Neutron diffraction.[61] [g]DFT with 6-31G** Gaussian basis set.[62]

Table 2. Interatomic Distances and Bond Angles of the Strained Silica Dimer and Experimental Values from Bulk Amorphous Silica

Property	AIMD		ReaxFF-Fogarty		ReaxFF-2015		Expt.
	Dimer	Surface	Dimer	Surface	Dimer	Surface	Silica
Si−O dist. (Å)	1.69 (0.07)	1.66 (0.13)	1.59 (0.09)	1.56 (0.08)	1.57 (0.10)	1.58 (0.09)	1.61[b]
O−O dist. (Å)	2.81 (0.15)	2.68 (0.20)	2.70 (0.45)	2.56 (0.29)	2.68 (0.42)	2.58 (0.30)	2.65[c]
O−H dist. (Å)	0.97 (0.06)	1.01[a] (0.08)	0.97 (0.07)	0.99[a] (0.07)	0.98 (0.07)	1.01[a] (0.08)	0.98[d]
Si−Si dist. (Å)	2.39 (0.09)	2.42 (0.09)	2.82 (0.08)	2.83 (0.06)	2.76 (0.06)	2.80 (0.08)	3.1[e]
Si−O−Si angle (deg)	91 (4)	91 (4)	106 (5)	105 (6)	104 (6)	103 (6)	144[c] 152[f]
O−Si−O angle (deg)	89 (4)	89 (4)	74 (5)	74 (4)	76 (5)	76 (6)	109.4[c]
Si−O−H angle (deg)	117 (13)	117[a] (17)	108 (8)	112[a] (9)	124 (9)	123[a] (7)	118.1[g]

[a]From Si−OH located on internal surfaces of nanoporous silica. [b]Neutron diffraction.[57] [c]Electron diffraction.[58] [d]Electon diffraction.[59] [e]Large angle X-ray scattering.[60] [f]Neutron diffraction.[61] [g]DFT with 6-31G** Gaussian basis set.[62]

models studied.[63] The Si−O−H bond angle from AIMD simulations of this work is close to earlier DFT calculations, while the difference between AIMD and ReaxFF simulations within 5%.

In the strained silica structure, the Si−Si interatomic distance is 2.4 Å by AIMD methods, ∼0.40 Å smaller than the ReaxFF simulation values of ∼2.8 Å in both the dimer and the dense systems (Table 2). The Si−Si interatomic distance of 2.4 Å is consistent with previous DFT investigations using Gaussian 6-31G basis sets.[64] Additionally, in the AIMD simulations both the Si−O−Si and O−Si−O bond angles experience strain with bond angles of 90−94°, less than ∼145° and ∼109° reported for Si−O−Si and O−Si−O unstrained bond angles, respectively.[26] Compression of both bond angles to ∼90° is consistent with previous DFT calculations and forms a relatively symmetric 2-Ring defect.[64−66] In the ReaxFF methods, both angles are compressed by ∼35° in the 2-Ring defects, with O−Si−O and Si−O−Si bond angles of ∼74° and 105°, respectively, creating a rhombohedral 2-Ring defect. In previous simulations of nanoporous silica surfaces using classical MD methods with a silica force field and fixed partial charges parametrized by Teter, the O−Si−O and Si−O−Si bond angles were ∼85° and ∼90°, respectively, which is consistent with AIMD simulations.[48]

Discrepancies between the ReaxFF simulations and the AIMD data can be attributed to features in the ReaxFF force field. For instance, a strict distribution of charges may prevent the formation of a Si−Si unsupported π-bond described by Hamann.[66] Alternatively, the ability of the systems to form fully strained 2-Ring defects may be limited by control of the Si−Si interatomic distances. The effect of the varying strain of the O−Si−O and Si−O−Si bond angles on the reactivity is unknown, but future users of the potential should be aware that some small structural details of the highly strained bonds are different between AIMD and classical MD simulations using the ReaxFF potentials.

3.2. Activation Energies for Siloxane Bond Breakage in Cluster Models. A number of *ab initio* computational studies have been performed to investigate the activation energies related to 2-Ring defect removal, and values between 7.38 kcal/mol (0.32 eV) and 29.29 kcal/mol (1.27 eV) have been reported (Table 3). Activation energies for siloxane bond breakage are complicated by variations in simulation methods, surface models, hydration levels, and 2-Ring defect locations. For instance, activation energies for 2-Ring defect structures located on concave surfaces are reported to be higher than those on flat surfaces.[25] Du et al. and Tilocca and Cormack suggested that an increasing number of water molecules involved in the reaction decreases the reaction barrier.[67,68] Additionally, cluster calculations or bulk surface models has an effect on the activation energy of 2-Ring defect removal, as does the type of reaction mechanism.[67]

When the ReaxFF-Fogarty force field was used to simulate water reactions with the strained silica dimer (Figure 2b), an activation energy of −8.07 kcal/mol (−0.35 eV) was identified, far below the range reported by *ab initio* methods (Table 3). In the ReaxFF-2015 parametrization, the reaction pathway for Si−O bond breakage in a strained silica dimer using DFT with a B3LYP functional and a 6-311++G(d,p) basis set and an activation energy of ∼20 kcal/mol (0.87 eV) was used.[36] The result is an activation energy of 16.6 kcal/mol (0.72 eV) for Si−

DOI: 10.1021/acs.jpcc.6b07939
J. Phys. Chem. C 2016, 120, 24803−24816

Table 3. Activation Energies for Siloxane Bond Breakage in a 2-Ring Defect Structure by Classical MD and *ab Initio* Simulation Methods

Author	E_a (kcal/mol)	System	Method	ref.
This work (AIMD)	25.1	Dimer	DFT	
Yeon and van Duin	20.1	Dimer	DFT	36
	20.1	Dimer	Classical MD ReaxFF-2015	
	−8.1	Dimer	Classical MD ReaxFF-Fogarty	
Rimola and Uglinego	24.9−29.3	Cluster	DFT	15
Walsh, Wilson, and Sutton	16.4−25.6	Cluster	DFT	43
Masini and Bernasconi	7.4−25.4	Bulk surface	CPMD[a]	44
Mischler et al	20.8	Bulk surface	CPMD[a]	45
Du et al.	9.5	Bulk surface	QM/MM	67

[a]Carr-Parrinello molecular dynamics.

O bond breakage in a strained silica dimer using ReaxFF-2015, within the range of previous investigations.

DFT climbing image nudged-elastic-band (NEB) simulations were performed to identify the activation energies for the breakage of strained and unstrained Si−O bonds. NEB methods are used to identify the minimum energy path (MEP) between initial and final states, with the transition state (or saddle point) identified as the highest energy structure along the MEP.[69] The NEB simulations used the same parameters as the AIMD simulations, including exchange-correlation functional, basis set, and energy cutoff with a k-spring coefficient of 0.05. The steps of the reaction were identified from the breaking of strained and unstrained silica dimers used in the parametrization of the ReaxFF-2015 force field. The reaction pathways for water reaction with silica dimers through the use of the ReaxFF force fields were obtained from ref 36, which had been calculated through DFT simulations with a B3LYP functional and a 6-311G(d,p) basis set. From these coordinates, the energy for each point using the ReaxFF potentials was calculated and used to identify the energy barriers for the reaction. This method was selected to be consistent with the work done by Yeon and van Duin in the parametrization of the ReaxFF-2015 force field. The reactions between the water molecule and the silica dimers are included in Figure 3a and Figure 3b for the strained and unstrained dimers, respectively.

The ability of the AIMD methods to replicate the bond breakage properties in the ReaxFF and DFT simulations implemented by Yeon and van Duin can be identified through an analysis of the activation energies for Si−O bond breakage.[36] From the NEB simulations, the strained siloxane bond activation energy is 25.1 kcal/mol (1.09 eV) (Figure 4a),

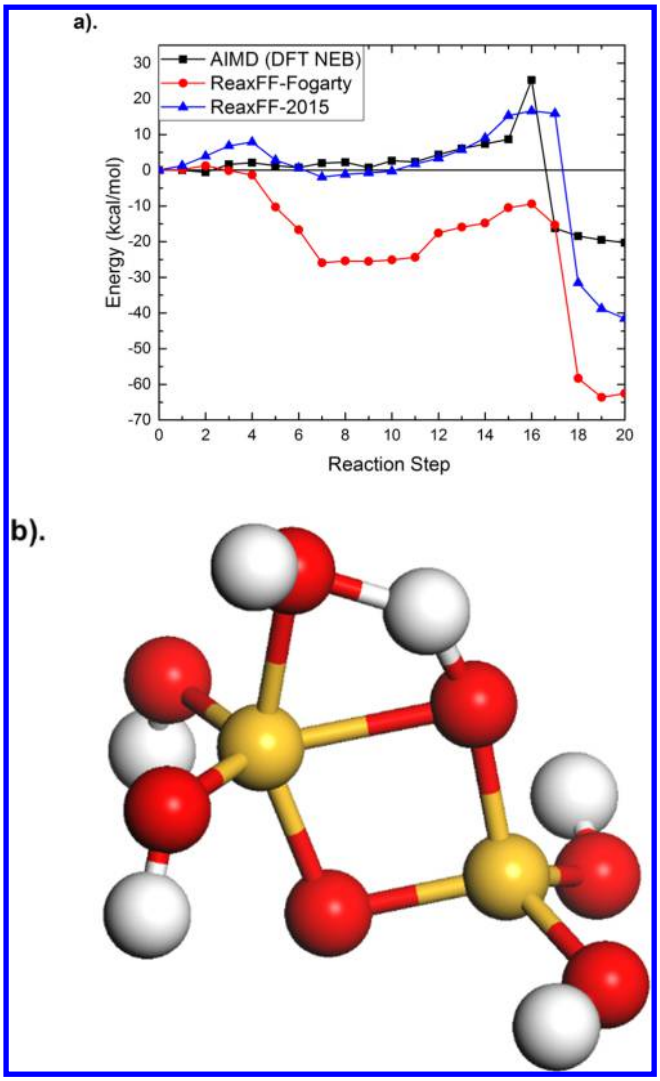

Figure 4. (a) Energy barrier for the breakage of strained Si−O bonds in silica dimers by water and (b) snapshot of the transition state for the reaction from NEB AIMD simulations. Colors: red (oxygen), yellow (silicon), white (hydrogen).

within the energy range of other computational studies (Table 3). The 25.1 kcal/mol (1.09 eV) activation energy in the AIMD

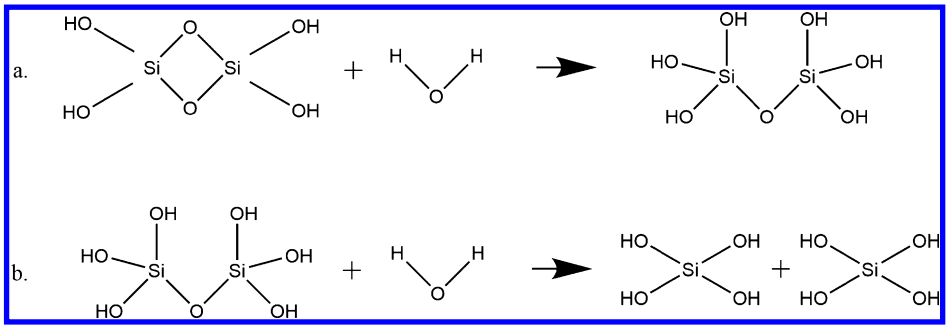

Figure 3. Sketches of reactions between water and (a) strained and (b) unstrained silica dimers.

DOI: 10.1021/acs.jpcc.6b07939
J. Phys. Chem. C 2016, 120, 24803−24816

simulations is ∼4.6 kcal/mol (0.2 eV) higher than in the ReaxFF simulations, which may be due to differences in reaction mechanisms between the different methods.

The transition state for the reaction between a water molecule and the strained silica dimer is included in Figure 4b. It occurs during the transfer of a hydrogen atom from the absorbed water molecule to a bridging oxygen (BO), and it is consistent with the transition states from previous DFT calculations.[36] The ReaxFF-2015 simulations exhibit a small prepeak of ∼11 kcal/mol (0.5 eV) along the reaction pathway, which is associated with the bonding of the water to a silicon, forming an overcoordinated silicon defect. Previous investigations of silica−water energy barriers in cluster calculations identified peaks associated with different phases of the reactions and which are more pronounced in basic systems.[15,70] The relative height of the prepeak in the ReaxFF-2015 simulations may indicate an added stability in the 2-Ring defect structure between the different simulation methods.

The similarities in the activation energy and transition state for water reaction with a strained silica dimer indicate that AIMD methods can be used for large complex simulations of water−silica interactions and provide insight into the accuracy of the ReaxFF force fields.

3.3. Two-Membered Ring Defect Removal Mechanisms in Nanoporous Silica. Reaction energies for strained siloxane bonds are found to vary with reaction mechanism and position of the strained Si−O bonds in the system. This is due to kinetic limitations, which affect the accessibility 2-Ring defect sites by one or more water molecules in the reaction. Experimental reaction rates suggest that, regardless of the reaction mechanism, 2-Ring defects are removed from surfaces through the formation of silanol groups within the first few seconds of the surface being in contact with the atmosphere.[4] In computational time frames (<1 ns), 2-Ring defects have some stability due to their high activation energies relative to the energy gain associated with their removal.

Figure 5 demonstrates the varying stability of 2-Ring structures across all the hydrated nanoporous silica systems investigated. Different rates of 2-Ring removal occurred depending on the computational methods used. The AIMD simulations exhibit an almost 50% reduction in 2-Ring concentrations within the first 30 ps of the simulation (Figure 5), while the ReaxFF simulations require more than 100 ps of simulation time to exhibit the same reduction in 2-Ring defect concentration. Therefore, AIMD simulations are more reactive, and the ReaxFF potentials require ∼4−5 times as much simulation time to develop comparable 2-Ring defect concentrations. Simulating the systems for longer time frames, including up to 2 ns, did not result in further reduction in 2-Ring defect concentrations.

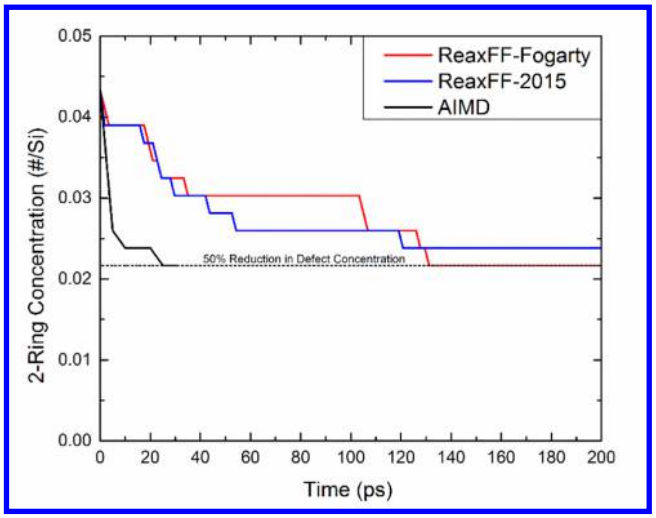

Figure 5. Concentration of 2-Ring defects structures (#/Si) in the hydrated nanoporous silica systems.

The complex nanoporosity of the silica structure may also be a factor in limiting removal of 2-Ring defects. First, the 2-Ring defect must be accessible to allow for the formation of one of the intermediate defects necessary for bond breakage. 2-Ring defects have been identified as a surface defect[26] and should therefore be water accessible on flat surfaces. The curved surfaces in nanoporous systems are more complex, and previous classical MD simulations have suggested that 2-Ring defects on concave surfaces can experience increases in energy barriers for removal.[23] Increased energy barriers are attributed to interactions between the water molecules and the side of the concave silica surface, limiting the movement of water molecules into the position required to break the Si−O bond. While the location of the defects may explain why only 50% of the 2-Ring defects are removed from the nanoporous silica systems, it does not explain why the rate of defect removal is different between the simulations methods. The mechanisms which are responsible for the removal of 2-Ring defects provide insight into this process.

Previous first-principles calculations have shown two different mechanisms responsible for the 2-Ring breakage in water−silica systems.[44] The most common is the absorption of a water molecule onto one of the silicon atoms, causing the formation of a five-coordinated silicon (Si^5) defect ($Si{-}OH_2$). Eventually, Si−O bond breakage leads to removal of the 2-Ring defect structure. Of the 14 2-Ring defect reactions which occur in the AIMD simulations, all of them are the result of this mechanism. Previous *ab initio* simulation studies have identified similar mechanisms, and a detailed analysis is summarized in ref 13. When only a single water molecule is present, a hydrogen from the absorbed water molecule can be transferred to the nonbridging oxygen (NBO) formed from the Si−O bond scission. Alternatively, when two or more water molecules are present, a hydrogen is transferred through the water to terminate the NBO.

The second reaction mechanism of 2-Ring defect removal includes the absorption of a hydrogen onto one of the BO. The absorbed hydrogen causes the simultaneous generation of a silanol during Si−O bond scission.[44] The breakage of a Si−O bond by absorption of a hydrogen onto a BO has an activation energy of ∼7.4 kcal/mol (0.32 eV) for the entire defect. The formation of a Si^5 intermediate defect has an activation energy of only 2.5 kcal/mol (0.11 eV), despite the entire reaction mechanism, including Si−O bond breakage, having an activation energy of 25.4 kcal/mol (1.10 eV). As a result, Si^5 defects are preferentially formed. Therefore, the mechanisms which include Si^5 formation as an intermediate defect are more common.[44]

When 2-Ring defects are removed in the ReaxFF simulations, the most common reaction mechanism is a combination of the two discussed above. It includes the formation of both a Si^5 intermediate defect and the absorption of a hydrogen onto a BO. Absorption of the hydrogen results in an extension of the Si−O bond from ∼1.6 Å to ∼2.2 Å and an expansion of the Si−

DOI: 10.1021/acs.jpcc.6b07939
J. Phys. Chem. C 2016, 120, 24803−24816

O−Si bond angle to ∼125°. The changes in the bond angles and distances may relieve strain in the defect, creating energetic drive for the absorption of a hydrogen onto a BO.

Snapshots of a combined reaction for 2-Ring defect removal in ReaxFF simulations are included in Figure 6a−e.

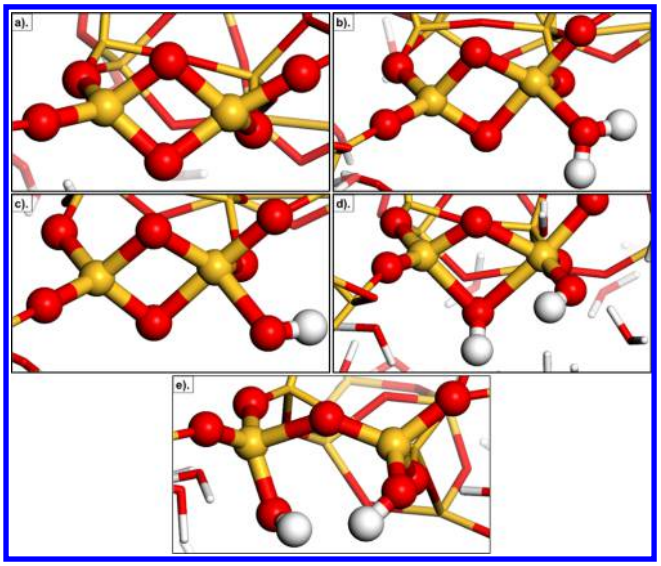

Figure 6. Snapshots of the (a) initial and (b−d) intermediate defect structures and (e) final structure during the breakage of a 2-Ring defect in a 67% hydrated nanoporous silica system simulated using the ReaxFF-2015 potential. Colors: red (oxygen), yellow (silicon), white (hydrogen).

In Figure 6 the Si^5 intermediate defect is formed from the absorption of a water onto a silicon (Figure 6b). Shortly after, a hydrogen breaks off (Figure 6c). This is followed by the absorption of a hydrogen onto one of the BO (Figure 6d). Eventually the Si−O bond breaks, resulting in the formation of two vicinal silanols (Figure 6e). The lifetimes and formation order of the two intermediate defects is variable, and in some cases, the hydrogen absorbs onto the BO before the formation of the Si^5 defect. Figure 7 demonstrates the long lifetimes of the intermediate defect structures in three of the 2-Ring defect removal reaction mechanisms which occur in the first 30 ps of the simulation. For simulations which used the ReaxFF-Fogarty potential, two of the three reactions exist for longer than 30 ps, indicating the high stability of the intermediate structures. In the ReaxFF-2015 simulations, the lifetimes of the intermediate defects are shortened, particularly when both intermediate defects, hydrogen absorbed onto a BO and the Si^5 defect, are present. Select ReaxFF simulations were run for longer time frames, and intermediate defects can exist for hundreds of picoseconds. In the AIMD simulations, intermediate defect lifetimes are less than 1 ps, indicating this is what causes the stability of the 2-Ring defects in the ReaxFF simulations.

For the 2-Ring defect to be removed in the ReaxFF simulations, both the Si^5 intermediate defect and the absorption of a hydrogen onto a BO must be present before Si−O bond scission. This may be due to the inclusion of the reaction pathway in the ReaxFF-2015 parametrization which contains both intermediate defect structures, as seen in the snapshot of the transition state in Figure 4b, creating a thermodynamic drive for their formation. The incorporation of the trajectory for 2-Ring defect removal in the ReaxFF-2015 parametrization has resulted in an improved reaction mechanism compared to AIMD simulations.

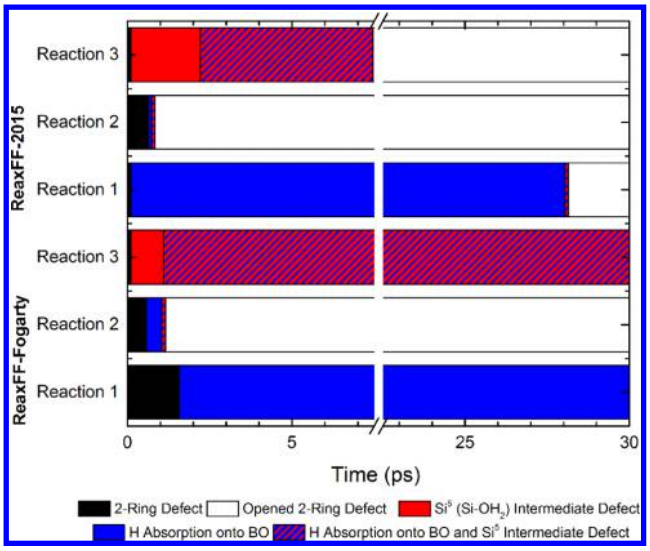

Figure 7. Lifetimes of the intermediate defect structures in the 2-Ring defect reaction mechanisms in nanoporous silica simulated using ReaxFF-Fogarty and ReaxFF-2015 classical MD potentials. All reactions occurred in the first 30 ps of the simulation.

3.4. Stability of Three-Bonded Oxygen Defects in Nanoporous Silica. During the formation of the nanoporous silica structures, a number of high energy defects are generated. These include under bonded silicon (Si^3), NBO, and the aforementioned ring structure defects. Another rarely occurring defect is the three-bonded oxygen (TBO) or oxygen tricluster, which occurs when an oxygen is bonded with three network formers in glasses. In the nanoporous silica systems studied here, low concentrations of TBO (<1%) were identified (Figure 8a).

TBO is known to occur in other amorphous oxide systems, such as sodium aluminosilicates, with concentrations as high as 30%.[71,72] Classical MD simulations on sodium aluminosilicates noted that the oxygen in the TBO were always bonded to a minimum of one aluminum atom.[71] This is due to TBO acting as a charge compensating mechanism for a lack of Na^+ to neutralize the NBO in an AlO_4 tetrahedron.[71] TBO bonded exclusively to silicon did not occur.[71] In nanoporous silica systems, the TBO defect is unstable and should be removed quickly in both AIMD and ReaxFF simulations.

In the AIMD simulations, TBO are stable for the first 20 ps, with a consistent decrease in their concentration with time (Figure 8a). TBO are more stable in simulations using the ReaxFF-Fogarty potential with increasing concentrations after 15 ps (Figure 8a). The ReaxFF-2015 parametrization is an improvement over the ReaxFF-Fogarty version, with lower concentration of TBO, which decrease with time.

Examination of the location of the TBO indicates that they occur primarily as part of a 2-Ring defect (Figure 8b), also identified in classical MD simulations.[73] Therefore, their removal can be attributed to decreases in 2-Ring defects as well as TBO from the system. Stable TBO in pure silicate systems simulated with ReaxFF may be due to the decrease in energy associated with perturbation of the 2-Ring structure. The Si−O−Si bond angle expands from ∼105° to ∼125°, and the Si−O bond distances increase to ∼2.2 Å, relieving strain in the defect. The mechanism for TBO removal does not require a

DOI: 10.1021/acs.jpcc.6b07939
J. Phys. Chem. C 2016, 120, 24803−24816

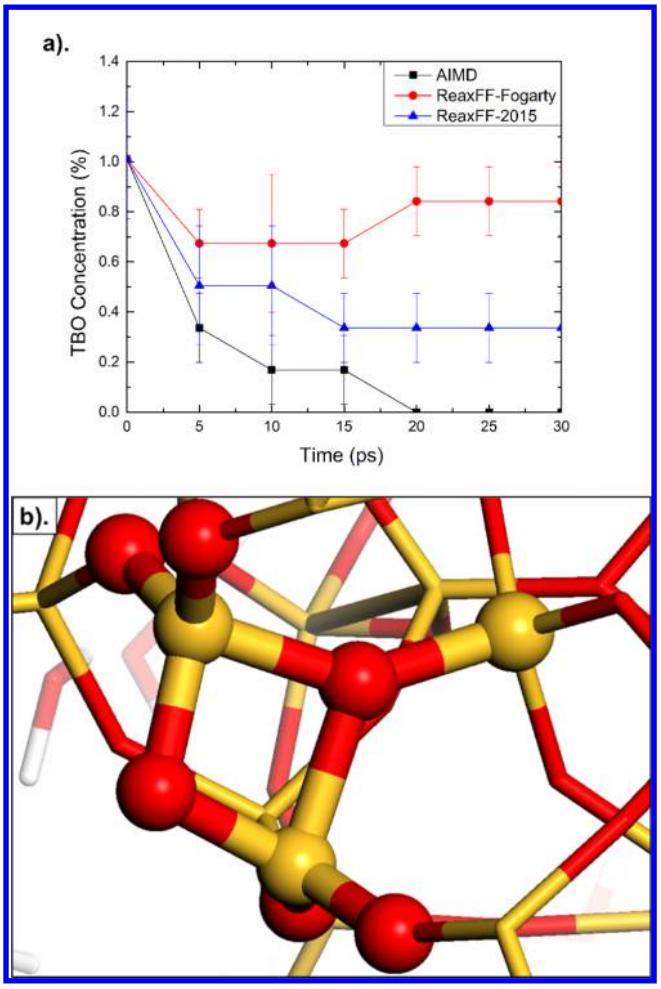

Figure 8. (a) Concentration TBO defects in the hydrated nanoporous silica systems simulated using AIMD or classical MD simulations. (b) 2-Ring defect through the formation of a TBO defect in the hydrated nanoporous silica systems. Colors: red (oxygen), yellow (silicon), white (hydrogen).

water molecule to facilitate the reaction, and is caused by a thermodynamic drive to decrease the energy of the system.

The ReaxFF-2015 force field resulted in faster removal of the TBO defects, an improvement over the ReaxFF-Fogarty force field and more consistent with the AIMD simulation results.

3.5. Hydroxylation Rates in Nanoporous Silica. The hydroxylation rates of the internal surface area of the nanoporous silica structures provide insight into the dynamics of the water−silica interface. The silanol concentration on silica surfaces is ∼4.6/nm^2 due to the termination of coordination and ring structure defects.[26] After 30 ps of AIMD, the nanoporous silica has a final silanol concentration of 1.37 ± 0.05 silanol/nm^2. The silanol concentration is significantly lower than the experimental value reported for hydroxylation of a flat surface and ∼0.1−0.2 silanol/nm^2 higher than the ReaxFF simulations (Table 4). Due to the relatively short time frames of the simulations and the complexity of the internal surface area, the system is unable to be fully hydroxylated. Previous studies indicated that between 50 and 500 ps of AIMD simulation time is required for the hydroxylation of nanoporous silica systems depending on the porosity.[13] Due to the longer simulation times required for comparable 2-Ring defect removal in the ReaxFF simulations, it is estimated that full hydroxylation would require tens of nanoseconds of simulation time or more.

Reaction rates were calculated using a first order reaction rate equation to describe the hydroxylation behavior in computational and experimental systems.[4,5,13] The reaction rate is described by eq 3, with $C(t)$ as the silanol concentration at t = 0.03 ns (30 ps), C_0 as the concentration at the beginning of the MD simulation time, t as the elapsed time (0.03 ns), and k as the reaction rate:[5]

$$C(t) = C_o e^{kt} \tag{3}$$

The hydroxylation rate of 17.0 silanol/ns for the AIMD simulation is higher than the values of 8.7 and 10.7 silanol/ns for the ReaxFF-Fogarty and ReaxFF-2015 simulations, respectively. The reparametrization of the ReaxFF force field appears to have increased the hydroxylation rate for the ReaxFF-2015 systems, which results in an improvement relative to the AIMD results.

The result is unexpected, since there was an increase in the activation energy for the removal of 2-Ring defects, which affects the silanol concentration. Hydroxylation rates are also dependent on the termination or removal of defect species. An analysis of changing defect concentrations with time highlights varying defect stability in the nanoporous silica structures.

Defect concentrations are broken down into coordination defects (Si^3, Si^5, NBO) and ring structure defects (2-Ring and 3-Ring defects), and are included in Figure 9. The decreasing concentration of coordination defects in the structure is well represented by both ReaxFF force fields and is in close agreement with the AIMD simulations (Figure 9a). This indicates that the initial rate of hydroxylation is consistent between the AIMD and ReaxFF simulations. There is little tendency to maintain the coordination defects in the structure beyond the low levels of TBO which were discussed previously.

The AIMD simulations have more reactive ring structure defects, resulting in a greater decrease in 2-Ring and 3-Ring defect concentrations with time. The ReaxFF-2015 potential exhibits higher 3-Ring defect removal with time compared with the ReaxFF-Fogarty force field (Figure 9b). Overall, the ReaxFF-Fogarty and ReaxFF-2015 potentials result in similar

Table 4. Silanol Concentration with Time for Hydrated Nanoporous Silica Systems Using AIMD Methods and Classical MD Potentials[a]

								Reaction Rate (silanol/ns)	
Time (ps)	0	10	20	30	100	250	500	t = 0.03 ns	t = 0.5 ns
AIMD	0.87 ± 0.09	1.32 ± 0.06	1.33 ± 0.05	1.37 ± 0.05	N/A	N/A	N/A	17.00 ± 3.37	N/A
ReaxFF-Fogarty	0.87 ± 0.09	1.08 ± 0.09	1.10 ± 0.09	1.10 ± 0.09	1.21 ± 0.07	1.29 ± 0.10	1.31 ± 0.10	8.70 ± 2.09	0.87 ± 0.13
ReaxFF-2015	0.87 ± 0.09	1.08 ± 0.08	1.08 ± 0.08	1.16 ± 0.08	1.32 ± 0.07	1.35 ± 0.07	1.34 ± 0.06	10.70 ± 2.13	0.97 ± 0.18

[a]Error bars are the standard error.

DOI: 10.1021/acs.jpcc.6b07939
J. Phys. Chem. C 2016, 120, 24803−24816

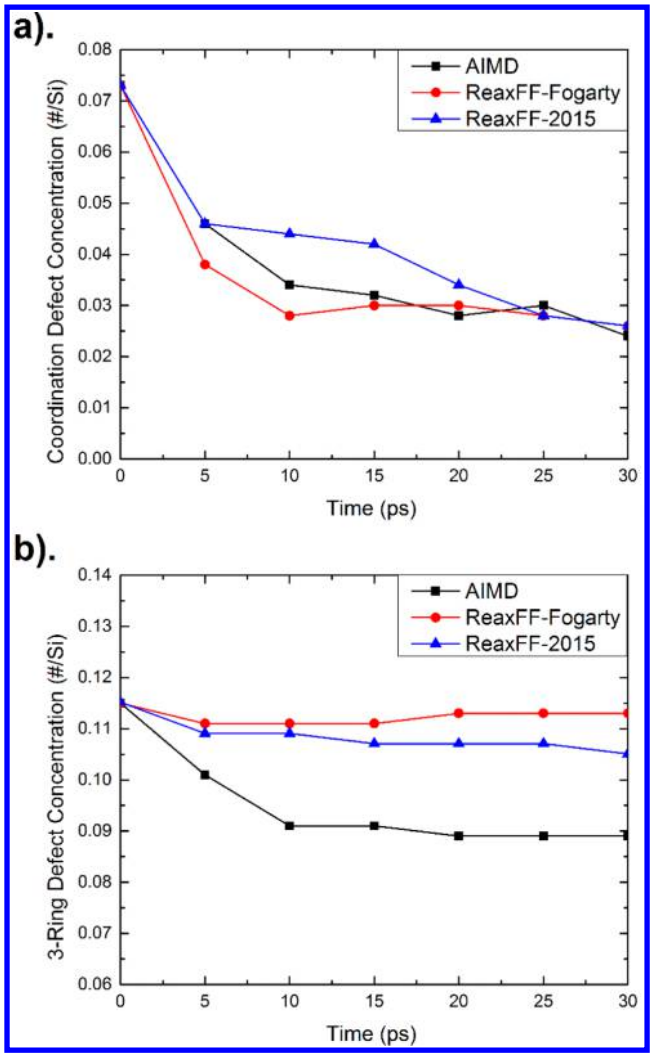

Figure 9. Concentration of (a) coordination defects (Si^3, Si^5, NBO) and (b) three-membered ring structure defects with time. Error bars are the standard error.

hydroxylation rates, which slight improvements in the 3-Ring removal rate in the ReaxFF-2015 version, compared to the AIMD simulations.

3.6. Water Diffusion in Nanoporous Silica. An important aspect of water−silica interactions is the diffusion of water molecules through the nanoporous silica structure. Changing diffusion rates have a significant effect on the reaction rate, since water molecules diffuse to coordination or 2-Ring defects before they are terminated or removed. The constraints of the nanoporous silica on the dynamics of the water molecules affect the movement of water through the system.

Several previous studies using NMR[7,74,75] and differential scanning calorimetry[76] identified a region of frozen or structured water next to silica surfaces. This region of kinetically limited water results in slower atomic movement and diffusion compared to bulk values. Simulations suggest the interfacial region extends a minimum of 10 Å into the liquid.[10,77,78] Based on this criterion, nearly all of the water molecules in the nanoporous silica studied here would be considered interfacial water. Therefore, the diffusion coefficient of water in the nanoporous silica is expected to be lower than in pure water due to nanoconfinement effects. The monolayer of water molecules adjacent to the silica surface experience almost no diffusion due to the formation of a hydrogen bonding network between the water molecules and surface silanol groups.[79] In subsequent layers farther from the surface, increasing diffusion of the water molecules occurs along with less orientation of the water molecules.[80] As more free space is introduced into the system, the diffusion coefficient is expected to increase, since a lower percentage of the water molecules exist in the interfacial region.

Diffusion coefficients were calculated from the 30,000 steps recorded during the 30 ps simulation of the hydrated nanoporous silica systems. A mean squared displacement (MSD) was calculated using eq 4, where $x_i(0)$ is the position of particle i at time = 0, $x_i(t)$ is the position of particle i at t = time, and n is the number of particles in the system.[81]

$$MSD = \frac{1}{n}\left\langle \sum_{i=1}^{n} |x_i(0) - x_i(t)|^2 \right\rangle \tag{4}$$

Using the MSD, the diffusion coefficient can be calculated from the Einstein diffusion equation in eq 5.[81]

$$D = \frac{1}{6}\lim_{t\to\infty} \frac{d}{dt}|x(0) - x(t)| \tag{5}$$

The different atomic species are separated by their bonding environments to allow for the identification of changing diffusion rates between atomic species. Several previous investigations of water diffusion have separated the hydrogen atoms and oxygen atoms in water molecules for analysis to identify the level of disassociation of the water molecule during the diffusion process or to calculate electrical conductivity.[33,82,83] By separating the hydrogen and oxygen atoms, the relative diffusion of each species can be identified, indicating if faster hydrogen atom transport occurs in the hydrated nanoporous systems.

Table 5 indicates that the diffusion coefficients for both the hydrogen and oxygen atoms which compose the water

Table 5. Diffusion Coefficients (10^{-9} m^2/s) of Hydrogen and Oxygen in the Water Molecules in the Hydrated Nanoporous Structures Reported as the Average of Three Simulations with the Standard Error

	AIMD			ReaxFF-Fogarty			ReaxFF-2015		
Porosity (%)	D_H	D_O	D_H-D_O	D_H	D_O	D_H-D_O	D_H	D_O	D_H-D_O
31	0.47 ± 0.04	0.40 ± 0.06	0.07 ± 0.04	0.34 ± 0.06	0.25 ± 0.04	0.09 ± 0.03	0.40 ± 0.03	0.27 ± 0.01	0.13 ± 0.07
42	0.39 ± 0.11	0.27 ± 0.09	0.12 ± 0.04	0.69 ± 0.11	0.53 ± 0.14	0.16 ± 0.04	0.49 ± 0.04	0.33 ± 0.03	0.16 ± 0.05
52	0.50 ± 0.09	0.32 ± 0.04	0.18 ± 0.11	0.78 ± 0.13	0.65 ± 0.15	0.13 ± 0.08	0.75 ± 0.06	0.63 ± 0.07	0.12 ± 0.02
60	0.60 ± 0.08	0.50 ± 0.07	0.09 ± 0.02	1.08 ± 0.10	0.95 ± 0.09	0.13 ± 0.04	1.01 ± 0.09	0.86 ± 0.09	0.15 ± 0.02
67	0.49 ± 0.03	0.40 ± 0.03	0.08 ± 0.01	1.22 ± 0.11	1.05 ± 0.11	0.17 ± 0.02	1.18 ± 0.22	1.01 ± 0.17	0.17 ± 0.09
100 (H_2O)	3.13 ± 0.03	2.94 ± 0.02	0.19 ± 0.01	2.73 ± 0.38	2.59 ± 0.35	0.14 ± 0.03	2.90 ± 0.73	2.82 ± 0.72	0.09 ± 0.03

DOI: 10.1021/acs.jpcc.6b07939
J. Phys. Chem. C 2016, 120, 24803−24816

molecules are lower than in bulk systems (Table 5). Decreased water diffusion is due to the formation of the aforementioned hydrogen bonding network which limits atomic movement. In classical MD simulation using ReaxFF, diffusion coefficients increase with increasing porosity, since a lower percentage of the water molecules are within the first monolayer adjacent to the silica surface (Figure 10a). The AIMD simulations also

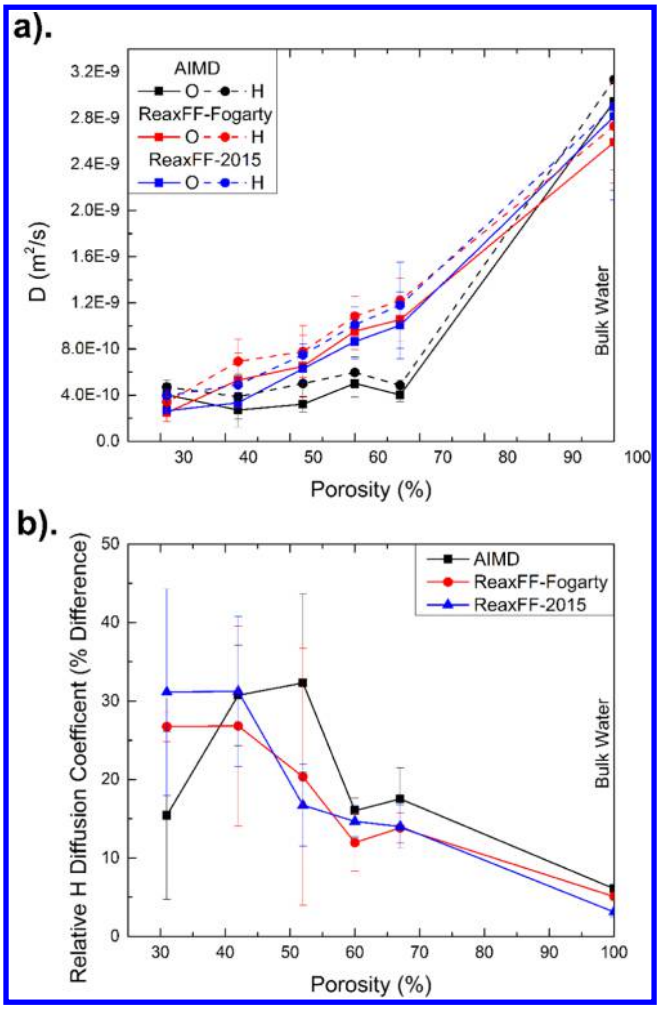

Figure 10. (a) Diffusion coefficient for water molecules, separated into hydrogen and oxygen atoms; (b) percent difference in D_H and D_O values in hydrated nanoporous silica systems. The error bars are the standard error.

exhibit increasing diffusion coefficients with increasing porosity, but the trend is not as clear. This may be due to the higher concentration of silanol groups on the surface in the AIMD simulations, resulting in the formation of a stronger hydrogen bond network. Previous classical MD simulations have noted that hydrophobic surfaces with a few silanol groups experience less trapping of water molecules, while hydrophilic surfaces develop transient binding between the water and the silanol groups, limiting diffusion.[84,85]

Separate from overall diffusion rates, hydrogen atoms appear to diffuse faster than the oxygen atoms and are consistent across all simulation methods. The difference in the hydrogen diffusion coefficient (D_H) relative to the oxygen diffusion coefficient (D_O) is included in Figure 10.b. In bulk water, both atomic species diffuse at similar rates, indicating a low level of disassociation, which is consistent with previous ReaxFF studies.[33] In the nanoporous silica systems hydrogen diffuses 10−30% faster than the oxygen. Several features of the simulation could be causing this trend. The first is that when diffusion of the entire water molecule is limited, the water molecule may disassociate into hydrogen and hydroxides to allow for diffusion through small spaces. In this case the lightness of the hydrogen relative to the hydroxide may result in increased average diffusion of the hydrogen atoms in the system. Bakos et al. suggested a similar mechanism for movement of water through small membered rings.[86]

Alternatively, diffusion of hydrogen atoms to terminate NBO defects in the system may result in an increased hydrogen diffusion coefficient. When the water molecules react with the unhydroxylated surface, both Si^3 and NBO coordination defects are terminated. Previous studies have indicated a slight preference for Si^3 bond termination compared to NBO, creating a temporary increase in hydrogen atoms in solution before diffusion allows for termination of the NBO defect.[20,87] Additionally, previous AIMD analysis of the breakage of 2-Ring defects found that diffusion of hydrogen atoms to terminate the NBO defects occurs, especially in systems with multiple water molecules involved in the reaction.[13] Finally, analysis of hydrogen hopping in bulk water through the use of dissassocaitve water potentials finds that when hydrogen is bonded strongly to oxygen in a water or hydronium molecule, the diffusion is controlled by the heavy oxygen atoms.[22,88] During hydrogen transfer events, there is an increase in the diffusion until a new complete water molecule is formed. Diffusion coefficients for proton exchange in bulk water of 9.32 $\times 10^{-9}$ m^2/s have been identified through both computational and experimental investigations.[89] The increased D_H values for hydrogen involved in transfer events may account for the relative D_H/D_O values in Table 5.

Additionally, the difference in D_H and D_O values decreases as the porosity increases for the ReaxFF-Fogarty and ReaxFF-2015 classical MD simulations. This suggests that as more free space becomes available, diffusion of the entire water molecule is taking place, rather than disassociation or hydrogen transport to allow for atomic movement throughout the system.

Further analysis of the mechanisms of water diffusion through nanoporous silica systems and along complex interfaces would benefit the understanding of the kinetics of hydroxylation and siloxane bond breakage.

4. CONCLUSIONS

Through application of ReaxFF based classical and *ab initio* molecular dynamics simulations, the interactions between water and the complex internal porosity in nanoporous silica were investigated. Two versions of the ReaxFF potentials (ReaxFF-Fogarty and ReaxFF-2015) were compared with the AIMD simulations to identify differences in localized structure, activation energy barriers, reaction mechanisms, and diffusion coefficients.

Structural comparisons indicate that both ReaxFF parametrizations do an excellent job of simulating the short-range order of the water molecules and SiO_4 tetrahedron in unstrained silica dimers. In the strained 2-Ring defect structures, the contraction of the O−Si−O and Si−O−Si bond angles to 75° and 105°, respectively, forms a rhombohedral 2-Ring defect. The 2-Ring defect structures from other two-bodied potentials[48] or AIMD simulations form more symmetric structures with O−Si−O and Si−O−Si bond

DOI: 10.1021/acs.jpcc.6b07939
J. Phys. Chem. C 2016, 120, 24803−24816

angles of ~90°, and as a result, small differences in strain may occur.

For siloxane bond breakage, complex multistep reaction mechanisms consisting of the formation of two different intermediate defects of five coordinated silicon and hydrogen bonded to bridging oxygen occur in the ReaxFF simulations during the removal of 2-Ring surface defects. Similar mechanisms were observed in AIMD simulations, but the latter has a higher reaction rate as compared to those using ReaxFF. The development of the intermediate defects affects the lifetimes of the 2-Ring defects and hydroxylation rates.

Additionally, water molecules in the nanoporous silica exhibit lower diffusivity relative to bulk water, possibly due to nanoconfinement effects as a result of the nanoporous silica structures. The confined water molecules also show increased hydrogen diffusion as compared to oxygen, suggesting more pronounced hydrogen transport when water is confined.

Comparison of the simulation results using the two ReaxFF parametrizations with the AIMD results identifies improvements in the reaction mechanisms, hydroxylation rates, defect concentrations, and activation energies for Si−O bond scission in the most recent version of the ReaxFF Si/O/H potential by Yeon and van Duin.[36] The new parametrization is recommended for the study of water−silica reactions over the ReaxFF-Fogarty parametrization, especially when the system contains 2-Ring defects, highly strained Si−O bonds, or complex coordination defects.

Inclusion of AIMD simulation results into parametrization of classical MD force fields provides important validation and input into force field development beyond the conventional static energy and barrier calculations which are currently implemented. Due to the complexities associated with introducing more complex and dynamic data into the potential development process, there is a significant need for the creation of algorithms for including AIMD results into empirical force field development efforts.

■ ASSOCIATED CONTENT

Supporting Information

The Supporting Information is available free of charge on the ACS Publications website at DOI: 10.1021/acs.jpcc.6b07939.

Coordinates for the initial hydrated nanoporous silica system (TXT)

Coordinates for the final hydrated nanoporous silica system after ReaxFF-Fogarty simulation (TXT)

Coordinates for the final hydrated nanoporous silica system after ReaxFF-2015 simulation (TXT)

Coordinates for the final hydrated nanoporous silica system after AIMD simulation (TXT)

■ AUTHOR INFORMATION

Corresponding Author

*E-mail: Jincheng.du@unt.edu, Phone: (940)369-8184.

Present Addresses

[#]J. M. Rimsza, School of Engineering, University of California Merced.

[⊥]Jejoon Yeon, Geochemistry Department, Sandia National Laboratory.

Notes

The authors declare no competing financial interest.

■ ACKNOWLEDGMENTS

This work is supported by the US Department of Energy (DOE) Nuclear Energy University Project (Project No. 13-5494) and National Science Foundation (NSF) DMR Ceramics Program (Project No. 1508001). J.M.R. acknowledges that this material is based on work supported by the National Science Foundation Graduate Research Fellowship Program under Grant No. DGE-114248. Computational resources are provided by the University of North Texas high performance computing cluster.

■ REFERENCES

(1) Gopalakrishnan, S.; Diniz da Costa, J. C. Hydrogen Gas Mixture Separation by CVD Silica Membrane. *J. Membr. Sci.* **2008**, *323*, 144−147.

(2) Nair, B. N.; Yamaguchi, T.; Okubo, T.; Suematsu, H.; Keizer, K.; Nakao, S. I. Sol-Gel Synthesis of Molecular Sieving Silica Membranes. *J. Membr. Sci.* **1997**, *135*, 237−243.

(3) Li, J. J.; Xu, X. Y.; Jiang, Z.; Hao, Z. P.; Hu, C. Nanoporous Silica-Supported Nanometric Palladium: Synthesis, Characterization, and Catalytic Deep Oxidation of Benzene. *Environ. Sci. Technol.* **2005**, *39*, 1319−1323.

(4) D'Souza, A. S.; Pantano, C. G. Hydroxylation and Dehydroxylation Behavior of Silica Glass Fracture Surfaces. *J. Am. Ceram. Soc.* **2002**, *85*, 1499−1504.

(5) D'Souza, A. S.; Pantano, C. G. Mechanisms for Silanol Formation on Amorphous Silica Fracture Surfaces. *J. Am. Ceram. Soc.* **1999**, *82*, 1289−1293.

(6) Rosenstihl, M.; Kämpf, K.; Klameth, F.; Sattig, M.; Vogel, M. Dynamics of Interfacial Water. *J. Non-Cryst. Solids* **2015**, *407*, 449−458.

(7) Kinney, D. R.; Chuang, I. S.; Maciel, G. E. Water and the Silica Surface as Studied by Variable-Temperature High-Resolution Proton NMR. *J. Am. Chem. Soc.* **1993**, *115*, 6786−6794.

(8) Kim, H. N.; Lee, S. K. Atomic Structure and Dehydration Mechanism of Amorphous Silica: Insights from 29 Si and 1 H Solid-State MAS NMR Study of SiO 2 Nanoparticles. *Geochim. Cosmochim. Acta* **2013**, *120*, 39−64.

(9) Sulpizi, M.; Gaigeot, M.; Sprik, M. The Silica−Water Interface: How the Silanols Determine the Surface Acidity and Modulate the Water Properties. *J. Chem. Theory Comput.* **2012**, *8*, 1037−1047.

(10) Allolio, C.; Klameth, F.; Vogel, M.; Sebastiani, D. Ab Initio H2O in Realistic Hydrophilic Confinement. *ChemPhysChem* **2014**, *15*, 3955−3962.

(11) Doltsinis, N.; Burchard, M.; Maresch, W.; Boese, A.; Fockenberg, T. Ab Initio Molecular Dynamics Study of Dissolved SiO 2 in Supercritical Water. *J. Theor. Comput. Chem.* **2007**, *6*, 49−62.

(12) Lowe, B. M.; Skylaris, C.; Green, N. G. Acid-Base Dissociation Mechanisms and Energetics at the Silica−water Interface: An Activationless Process. *J. Colloid Interface Sci.* **2015**, *451*, 231−244.

(13) Rimsza, J.; Du, J. Ab Initio Molecular Dynamics Simulations of the Hydroxylation of Nanoporous Silica. *J. Am. Ceram. Soc.* **2015**, *98*, 3748−3757.

(14) Zapol, P.; He, H.; Kwon, K. D.; Criscenti, L. J. First?Principles Study of Hydrolysis Reaction Barriers in a Sodium Borosilicate Glass. *Int. J. Appl. Glass Sci.* **2013**, *4*, 395−407.

(15) Rimola, A.; Ugliengo, P. A Quantum Mechanical Study of the Reactivity of (SiO)-Defective Silica Surfaces. *J. Chem. Phys.* **2008**, *128*, 204702.

(16) Van Duin, A. C.; Dasgupta, S.; Lorant, F.; Goddard, W. A. ReaxFF: A Reactive Force Field for Hydrocarbons. *J. Phys. Chem. A* **2001**, *105*, 9396−9409.

(17) Zheng, M.; Li, X.; Guo, L. Algorithms of GPU-Enabled Reactive Force Field (ReaxFF) Molecular Dynamics. *J. Mol. Graphics Modell.* **2013**, *41*, 1−11.

DOI: 10.1021/acs.jpcc.6b07939
J. Phys. Chem. C 2016, 120, 24803−24816

(18) Van Beest, B.; Kramer, G.; Van Santen, R. Force Fields for Silicas and Aluminophosphates Based on Ab Initio Calculations. *Phys. Rev. Lett.* **1990**, *64*, 1955.
(19) Tsuneyuki, S.; Tsukada, M.; Aoki, H.; Matsui, Y. First-Principles Interatomic Potential of Silica Applied to Molecular Dynamics. *Phys. Rev. Lett.* **1988**, *61*, 869.
(20) Feuston, B.; Garofalini, S. Oligomerization in Silica Sols. *J. Phys. Chem.* **1990**, *94*, 5351−5356.
(21) Stillinger, F. H.; Weber, T. A. Computer Simulation of Local Order in Condensed Phases of Silicon. *Phys. Rev. B: Condens. Matter Mater. Phys.* **1985**, *31*, 5262.
(22) Lockwood, G. K.; Garofalini, S. H. Lifetimes of Excess Protons in Water using a Dissociative Water Potential. *J. Phys. Chem. B* **2013**, *117*, 4089−4097.
(23) Mahadevan, T.; Garofalini, S. Dissociative Chemisorption of Water Onto Silica Surfaces and Formation of Hydronium Ions. *J. Phys. Chem. C* **2008**, *112*, 1507−1515.
(24) Garofalini, S. H.; Mahadevan, T. S.; Xu, S.; Scherer, G. W. Molecular Mechanisms Causing Anomalously High Thermal Expansion of Nanoconfined Water. *ChemPhysChem* **2008**, *9*, 1997−2001.
(25) Kagan, M.; Lockwood, G. K.; Garofalini, S. H. Reactive Simulations of the Activation Barrier to Dissolution of Amorphous Silica in Water. *Phys. Chem. Chem. Phys.* **2014**, *16*, 9294−9301.
(26) Du, J.; Cormack, A. N. Molecular Dynamics Simulation of the Structure and Hydroxylation of Silica Glass Surfaces. *J. Am. Ceram. Soc.* **2005**, *88*, 2532−2539.
(27) Hassanali, A. A.; Singer, S. J. Model for the Water-Amorphous Silica Interface: The Undissociated Surface. *J. Phys. Chem. B* **2007**, *111*, 11181−11193.
(28) Rustad, J. R.; Hay, B. P. A Molecular Dynamics Study of Solvated Orthosilicic Acid and Orthosilicate Anion using Parameterized Potentials. *Geochim. Cosmochim. Acta* **1995**, *59*, 1251−1257.
(29) Bakaev, V.; Steele, W. On the Computer Simulation of a Hydrophobic Vitreous Silica Surface. *J. Chem. Phys.* **1999**, *111*, 9803.
(30) Lopes, P. E.; Murashov, V.; Tazi, M.; Demchuk, E.; MacKerell, A. D. Development of an Empirical Force Field for Silica. Application to the Quartz-Water Interface. *J. Phys. Chem. B* **2006**, *110*, 2782−2792.
(31) Van Duin, A. C.; Strachan, A.; Stewman, S.; Zhang, Q.; Xu, X.; Goddard, W. A. ReaxFFSiO Reactive Force Field for Silicon and Silicon Oxide Systems. *J. Phys. Chem. A* **2003**, *107*, 3803−3811.
(32) Aktulga, H. M.; Fogarty, J. C.; Pandit, S. A.; Grama, A. Y. Parallel Reactive Molecular Dynamics: Numerical Methods and Algorithmic Techniques. *Parallel Comput.* **2012**, *38*, 245−259.
(33) Fogarty, J. C.; Aktulga, H. M.; Grama, A. Y.; Van Duin, A. C.; Pandit, S. A. A Reactive Molecular Dynamics Simulation of the Silica-Water Interface. *J. Chem. Phys.* **2010**, *132*, 174704.
(34) Senftle, T. P.; Hong, S.; Islam, M. M.; Kylasa, S. B.; Zheng, Y.; Shin, Y. K.; Junkermeier, C.; Engel-Herbert, R.; Janik, M. J.; Aktulga, H. M. The ReaxFF Reactive Force-Field: Development, Applications and Future Directions. *npj Computational Materials* **2016**, *2*, 15011.
(35) Yu, Y.; Wang, B.; Wang, M.; Sant, G.; Bauchy, M. Revisiting Silica with ReaxFF: Towards Improved Predictions of Glass Structure and Properties Via Reactive Molecular Dynamics. *J. Non-Cryst. Solids* **2016**, *443*, 148−154.
(36) Yeon, J.; van Duin, A. C. ReaxFF Molecular Dynamics Simulations of Hydroxylation Kinetics for Amorphous and Nano-Silica Structure, and its Relations with Atomic Strain Energy. *J. Phys. Chem. C* **2016**, *120*, 305−317.
(37) Zhang, Y.; Tao, J.; Chen, X.; Liu, B. Mixed-Pattern Cracking in Silica during Stress Corrosion: A Reactive Molecular Dynamics Simulation. *Comput. Mater. Sci.* **2014**, *82*, 237−243.
(38) Kulkarni, A. D.; Truhlar, D. G.; Goverapet Srinivasan, S.; van Duin, A. C.; Norman, P.; Schwartzentruber, T. E. Oxygen Interactions with Silica Surfaces: Coupled Cluster and Density Functional Investigation and the Development of a New ReaxFF Potential. *J. Phys. Chem. C* **2013**, *117*, 258−269.
(39) El-Sayed, A.; Watkins, M. B.; Grasser, T.; Afanas'ev, V. V.; Shluger, A. L. Hydrogen-Induced Rupture of Strained Si? O Bonds in Amorphous Silicon Dioxide. *Phys. Rev. Lett.* **2015**, *114*, 115503.
(40) Li, A.; Liu, Y.; Szlufarska, I. Effects of Interfacial Bonding on Friction and Wear at Silica/Silica Interfaces. *Tribol. Lett.* **2014**, *56*, 481−490.
(41) Chenoweth, K.; Cheung, S.; Van Duin, A. C.; Goddard, W. A.; Kober, E. M. Simulations on the Thermal Decomposition of a Poly (Dimethylsiloxane) Polymer using the ReaxFF Reactive Force Field. *J. Am. Chem. Soc.* **2005**, *127*, 7192−7202.
(42) Rimsza, J.; Deng, L.; Du, J. Molecular Dynamics Simulations of Nanoporous Organosilicate Glasses using Reactive Force Field (ReaxFF). *J. Non-Cryst. Solids* **2016**, *431*, 103−111.
(43) Walsh, T. R.; Wilson, M.; Sutton, A. P. Hydrolysis of the Amorphous Silica Surface. II. Calculation of Activation Barriers and Mechanisms. *J. Chem. Phys.* **2000**, *113*, 9191−9201.
(44) Masini, P.; Bernasconi, M. Ab Initio Simulations of Hydroxylation and Dehydroxylation Reactions at Surfaces: Amorphous Silica and Brucite. *J. Phys.: Condens. Matter* **2002**, *14*, 4133.
(45) Mischler, C.; Horbach, J.; Kob, W.; Binder, K. Water Adsorption on Amorphous Silica Surfaces: A Car−Parrinello Simulation Study. *J. Phys.: Condens. Matter* **2005**, *17*, 4005.
(46) Du, M.; Kolchin, A.; Cheng, H. Hydrolysis of a Two-Membered Silica Ring on the Amorphous Silica Surface. *J. Chem. Phys.* **2004**, *120*, 1044.
(47) Kieffer, J.; Angell, C. A. Generation of Fractal Structures by Negative Pressure Rupturing of SiO2 Glass. *J. Non-Cryst. Solids* **1988**, *106*, 336−342.
(48) Rimsza, J.; Du, J. Structural and Mechanical Properties of Nanoporous Silica. *J. Am. Ceram. Soc.* **2014**, *97*, 772−781.
(49) Plimpton, S. Fast parallel algorithms for short-range molecular dynamics. *J. Comput. Phys.* **1995**, *117*, 1−19.
(50) Hutter, J.; Marcella, I.; Florian, S.; Joost, V. CP2K: atomistic simulations of condensed matter systems. *WIREs Comput. Mol. Sci.* **2014**, *4*, 15−25.
(51) VandeVondele, J.; Krack, M.; Mohamed, F.; Parrinello, M.; Chassaing, T.; Hutter, J. Quickstep: Fast and Accurate Density Functional Calculations using a Mixed Gaussian and Plane Waves Approach. *Comput. Phys. Commun.* **2005**, *167*, 103−128.
(52) VandeVondele, J.; Mohamed, F.; Krack, M.; Hutter, J.; Sprik, M.; Parrinello, M. The Influence of Temperature and Density Functional Models in Ab Initio Molecular Dynamics Simulation of Liquid Water. *J. Chem. Phys.* **2005**, *122*, 014515.
(53) Dračínský, M.; Benda, L.; Bouř, P. Ab Initio Modeling of Fused Silica, Crystal Quartz, and Water Raman Spectra. *Chem. Phys. Lett.* **2011**, *512*, 54−59.
(54) D'Souza, A. S.; Pantano, C. G.; Kallury, K. M. Determination of the Surface Silanol Concentration of Amorphous Silica Surfaces using Static Secondary Ion Mass Spectroscopy. *J. Vac. Sci. Technol., A* **1997**, *15*, 526−531.
(55) Charpentier, T.; Kroll, P.; Mauri, F. First-Principles Nuclear Magnetic Resonance Structural Analysis of Vitreous Silica. *J. Phys. Chem. C* **2009**, *113*, 7917−7929.
(56) Clark, T. M.; Grandinetti, P. J.; Florian, P.; Stebbins, J. F. Correlated Structural Distributions in Silica Glass. *Phys. Rev. B: Condens. Matter Mater. Phys.* **2004**, *70*, 064202.
(57) Wright, A. C. Diffraction Studies of Glass Structure. *J. Non-Cryst. Solids* **1990**, *123*, 129−148.
(58) Mozzi, R.; Warren, B. The Structure of Vitreous Silica. *J. Appl. Crystallogr.* **1969**, *2*, 164−172.
(59) Shibata, S.; Bartell, L. Electron-Diffraction Study of Water and Heavy Water. *J. Chem. Phys.* **1965**, *42*, 1147−1151.
(60) Graetsch, H.; Mosset, A.; Gies, H. XRD and 29 Si MAS-NMR Study on some Non-Crystalline Silica Minerals. *J. Non-Cryst. Solids* **1990**, *119*, 173−180.
(61) Da Silva, J.; Pinatti, D.; Anderson, C.; Rudee, M. A Refinement of the Structure of Vitreous Silica. *Philos. Mag.* **1975**, *31*, 713−717.
(62) Sauer, J. Molecular Structure of Orthosilicic Acid, Silanol, and H3SiOH. Cntdot. AlH3 Complex: Models of Surface Hydroxyls in Silica and Zeolites. *J. Phys. Chem.* **1987**, *91*, 2315−2319.

DOI: 10.1021/acs.jpcc.6b07939
J. Phys. Chem. C 2016, 120, 24803−24816

(63) Civalleri, B.; Garrone, E.; Ugliengo, P. Vibrational Modes of Isolated Hydroxyls of Silica Computed Ab Initio in a Cluster Approach. *Chem. Phys. Lett.* **1998**, *294*, 103−108.
(64) O'Keeffe, M.; Gibbs, G. Ab Initio MO Calculations on Cyclodisiloxanes and Other Si-X-Si-X Rings and the Problem of″ Silica-W″. *J. Phys. Chem.* **1985**, *89*, 4574−4577.
(65) Nedelec, J.; Hench, L. Ab Initio Molecular Orbital Calculations on Silica Rings. *J. Non-Cryst. Solids* **1999**, *255*, 163−170.
(66) Hamann, D. Energies of Strained Silica Rings. *Phys. Rev. B: Condens. Matter Mater. Phys.* **1997**, *55*, 14784.
(67) Du, M.; Kolchin, A.; Cheng, H. Water−silica Surface Interactions: A Combined Quantum-Classical Molecular Dynamic Study of Energetics and Reaction Pathways. *J. Chem. Phys.* **2003**, *119*, 6418.
(68) Tilocca, A. Models of Structure, Dynamics and Reactivity of Bioglasses: A Review. *J. Mater. Chem.* **2010**, *20*, 6848−6858.
(69) Henkelman, G.; Uberuaga, B. P.; Jónsson, H. A Climbing Image Nudged Elastic Band Method for Finding Saddle Points and Minimum Energy Paths. *J. Chem. Phys.* **2000**, *113*, 9901−9904.
(70) Nangia, S.; Garrison, B. J. Reaction Rates and Dissolution Mechanisms of Quartz as a Function of pH. *J. Phys. Chem. A* **2008**, *112*, 2027−2033.
(71) Xiang, Y.; Du, J.; Smedskjaer, M. M.; Mauro, J. C. Structure and Properties of Sodium Aluminosilicate Glasses from Molecular Dynamics Simulations. *J. Chem. Phys.* **2013**, *139*, 044507.
(72) McKeown, D.; Galeener, F.; Brown, G. Raman Studies of Al Coordination in Silica-Rich Sodium Aluminosilicate Glasses and some Related Minerals. *J. Non-Cryst. Solids* **1984**, *68*, 361−378.
(73) Winkler, A.; Horbach, J.; Kob, W.; Binder, K. Structure and Diffusion in Amorphous Aluminium Silicate: A Molecular Dynamics Computer Simulation. *J. Chem. Phys.* **2004**, *120*, 384−393.
(74) Pajzderska, A.; Bilski, P.; Wąsicki, J. Phase Diagram of Water Confined in MCM-41 Up to 700 MPa. *J. Chem. Phys.* **2015**, *142*, 084505.
(75) Bronnimann, C. E.; Zeigler, R. C.; Maciel, G. E. Proton NMR Study of Dehydration of the Silica Gel Surface. *J. Am. Chem. Soc.* **1988**, *110*, 2023−2026.
(76) Takamuku, T.; Yamagami, M.; Wakita, H.; Masuda, Y.; Yamaguchi, T. Thermal Property, Structure, and Dynamics of Supercooled Water in Porous Silica by Calorimetry, Neutron Scattering, and NMR Relaxation. *J. Phys. Chem. B* **1997**, *101*, 5730−5739.
(77) Bonnaud, P.; Coasne, B.; Pellenq, R. J. Molecular Simulation of Water Confined in Nanoporous Silica. *J. Phys.: Condens. Matter* **2010**, *22*, 284110.
(78) Bourg, I. C.; Steefel, C. I. Molecular Dynamics Simulations of Water Structure and Diffusion in Silica Nanopores. *J. Phys. Chem. C* **2012**, *116*, 11556−11564.
(79) Faux, D.; Cachia, S.; McDonald, P.; Bhatt, J.; Howlett, N.; Churakov, S. Model for the Interpretation of Nuclear Magnetic Resonance Relaxometry of Hydrated Porous Silicate Materials. *Phys. Rev. E* **2015**, *91*, 032311.
(80) Chiavazzo, E.; Fasano, M.; Asinari, P.; Decuzzi, P. Scaling Behaviour for the Water Transport in Nanoconfined Geometries. *Nat. Commun.* **2014**, *5*, 3565.
(81) Chen, C.; Du, J. Lithium Ion Diffusion Mechanism in Lithium Lanthanum Titanate Solid-State Electrolytes from Atomistic Simulations. *J. Am. Ceram. Soc.* **2015**, *98*, 534−542.
(82) Zhang, L.; Davis, H. T.; Kroll, D.; White, H. S. Molecular Dynamics Simulations of Water in a Spherical Cavity. *J. Phys. Chem.* **1995**, *99*, 2878−2884.
(83) Mattsson, T. R.; Desjarlais, M. P. Phase Diagram and Electrical Conductivity of High Energy-Density Water from Density Functional Theory. *Phys. Rev. Lett.* **2006**, *97*, 017801.
(84) Sendner, C.; Horinek, D.; Bocquet, L.; Netz, R. R. Interfacial Water at Hydrophobic and Hydrophilic Surfaces: Slip, Viscosity, and Diffusion. *Langmuir* **2009**, *25*, 10768−10781.
(85) Allen, T.; Kuyucak, S.; Chung, S. The Effect of Hydrophobic and Hydrophilic Channel Walls on the Structure and Diffusion of Water and Ions. *J. Chem. Phys.* **1999**, *111*, 7985−7999.
(86) Bakos, T.; Rashkeev, S.; Pantelides, S. H_ {2} O and O_ {2} Molecules in Amorphous SiO_ {2}: Defect Formation and Annihilation Mechanisms. *Phys. Rev. B: Condens. Matter Mater. Phys.* **2004**, *69*, 195206.
(87) Hamad, S.; Bromley, S. T. Low Reactivity of Non-Bridging Oxygen Defects on Stoichiometric Silica Surfaces. *Chem. Commun.* **2008**, *35*, 4156−4158.
(88) Hofer, T. S.; Hitzenberger, M.; Randolf, B. R. Combining a Dissociative Water Model with a Hybrid QM/MM Approach A Simulation Strategy for the Study of Proton Transfer Reactions in Solution. *J. Chem. Theory Comput.* **2012**, *8*, 3586−3595.
(89) Wraight, C. A. Chance and Design—proton Transfer in Water, Channels and Bioenergetic Proteins. *Biochim. Biophys. Acta, Bioenerg.* **2006**, *1757*, 886−912.

DOI: 10.1021/acs.jpcc.6b07939
J. Phys. Chem. C 2016, 120, 24803−24816

npj | Materials Degradation

www.nature.com/npjmatdeg

REVIEW ARTICLE OPEN

Atomistic computer simulations of water interactions and dissolution of inorganic glasses

Jincheng Du[1] and Jessica M. Rimsza[1,2]

Computer simulations at the atomistic scale play an increasing important role in understanding the structure features, and the structure–property relationships of glass and amorphous materials. In this paper, we reviewed atomistic simulation methods ranging from first principles calculations and ab initio molecular dynamics (AIMD) simulations, to classical molecular dynamics (MD), and meso-scale kinetic Monte Carlo (KMC) simulations and their applications to study the reactions and interactions of inorganic glasses with water and the dissolution behaviors of inorganic glasses. Particularly, the use of these simulation methods in understanding the reaction mechanisms of water with oxide glasses, water–glass interfaces, hydrated porous silica gels formation, the structure and properties of multicomponent glasses, and microstructure evolution are reviewed. The advantages and disadvantageous of these simulation methods are discussed and the current challenges and future direction of atomistic simulations in glass dissolution presented.

npj Materials Degradation (2017)1:16 ; doi:10.1038/s41529-017-0017-y

The corrosion or degradation of glasses in aqueous solutions are critical in a number of engineering and technological processes ranging from microelectronic packaging, glass reaction chambers, and the immobilization of nuclear waste materials, as well as in healthcare and biomedical fields such as dissolution of inhaled glass fibers and bioactive glasses for biomedical applications. In particular, immobilizing radioactive waste in borosilicate glasses is widely accepted as a preferred method to treat nuclear waste materials generated from civilian and military sources. This process, also known as vitrification, is a critical component of the cycle of nuclear energy to combat global environmental and energy challenges. Researchers from around the world have extensively invested in understanding glass corrosion in an effort to predict the long-term stability and release rate radionuclides to the environment during nuclear waste storage.[1,2]

Various mechanisms for glass corrosion have been proposed and despite intensive experimental investigations with advanced characterization techniques results are unclear. It is generally accepted that the corrosion of glass consists of a set of complex processes including hydration, hydrolysis, and ion-exchange that are coupled during glass dissolution. The initial stage is inter-diffusion of proton or hydronium ions from the solution with sodium or other alkali ions in the glass.[3] This is followed by the hydrophilic attack of water on the Si-O-Si or Si-O-Al linkages that lead to hydroxylation of the silicate glass network. The remaining hydrolyzed glass skeleton then undergoes condensation and repolymerization to form the hydrated nanoporous silica rich gel layer which can be protective, decreasing dissolution to a residual rate.[4–6] The morphology of the gel layer, such as thickness, pore structure, and chemical composition, depends on the original glass composition and the pH, temperature, and composition of the solution. The resulting alteration layer is thus composed of an inter-diffusion region, an amorphous hydrated layer, and the crystalline reaction product layer schematically shown in Fig. 1.[7] A more accurate picture of the regions has been obtained by advanced characterization techniques such as atom probe tomography on corroded glasses[8,9] so that the nature of the alteration layer and related interface morphology can be more clearly understood.

Despite progress of experimental investigations of glass dissolution using advanced characterization methods such as atom probe tomography, high-resolution transmission electron microscopy, nano-secondary ion mass spectrometry (nanoSIMS), nuclear magnetic resonance spectroscopy (NMR), sum-frequency generation etc., it is still challenging to study detailed reaction mechanisms, hydrated glass and gel layers structure with nano- and mirco-porosity, as well as kinetic and transport behaviors. Atomistic computer simulations can provide detailed mechanistic information to refine our understanding of glass dissolution and shed light on key processes that control dissolution behaviors. Figure 2 shows the multiscale simulation approaches in materials modeling, which consists of methodologies ranging from quantum mechanics, to atomistic/molecular level simulations, to mesoscale and macroscale methods. At the longest time and length scales are continuum simulations that include finite element analysis, fluid dynamics, and reaction rate calculations based on rate theories.

Such higher scale models are extremely valuable, particularly on more applied aspects of research such as predicting the response of glass to long-term geological disposal. For example, Grambow and Müller initially proposed that the dissolution rate of glass is controlled by the level of silica saturation in the solution and can be described by first order rate law on the foundation of chemical reaction affinity of equilibrium thermodynamics and transition state theory.[10,11] Further development resulted in the formation of the GRAAL model (Glass Reactivity with Allowance for the

[1]Department of Materials Science and Engineering, University of North Texas, Denton, TX, USA and [2]Geochemistry Department, Sandia National Laboratories, Albuquerque, NM, USA
Correspondence: Jincheng Du (du@unt.edu)

Received: 26 January 2017 Revised: 7 June 2017 Accepted: 23 August 2017
Published online: 13 November 2017

Published in partnership with CSCP and USTB

npj nature partner journals

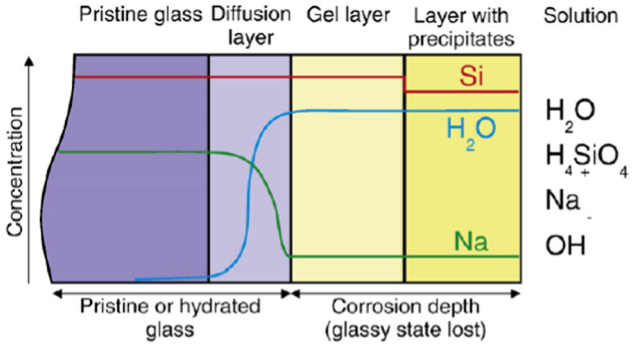

Fig. 1 Regions alteration layer (not to scale) of glass after corrosion (reprinted from ref. 7 Copyright 2010, with permission from Elsevier)

Alteration Layer) of nuclear waste glass dissolution, which include the formation of a passivating reactive interphase (PRI) formed through hydrolysis and condensation in the hydrated gel layer.[3,4,12] The PRI has been identified as a barrier to water transport into the glass and solvated ions into the solution, resulting in transport inhibition effect on glass alteration. While evidence of PRI is limited, Gin et al.[13] used nanoSIMS to identify a dense region 0.5 micron thick between the glass and gel regions, reported to be the first direct evidence of PRI from experiment. While analytical models are critical to developing an understanding of long-term glass dissolution model, atomistic simulations are also extremely powerful in highlighting the reaction mechanisms, structural, and compositional differences, which control dissolution at the small scale and have compounding effects on large scale systems over long time frames.

This review will focus on atomistic scale simulations ranging from electronic, atomistic, and mesoscale methods. In order of decreasing accuracy and increasing computational efficiency, quantum mechanical (QM) simulation methods, classical molecular dynamics (MD) simulations, and kinetic Monte Carlo (KMC) methods have all be extensively applied to understanding the mechanisms and process, which control glass dissolution. Details of these methods, including the advantages, disadvantages, and recent successes in the field of glass dissolution by the use of first-principles (ab initio), classical MD, and KMC simulation methods are discussed in subsequent sections. These include the QM level static transition state first principles simulations to identify the detailed water–glass reactions and fully dynamic simulations using ab initio MD simulations. Furthermore, classical MD simulations using empirical potentials to study multicomponent borosilicate glasses, silica–water interfaces and fully hydrated nanoporous silica structures will be reviewed. Additionally, future challenges and opportunities for simulations to provide added insight into the mechanisms and processes of glass dissolution are included.

FIRST-PRINCIPLES-BASED SIMULATIONS OF GLASS–WATER INTERACTIONS

Interactions and reactions in the water–silica system

First principles calculations provide the most accurate energies and forces and thus the most reliable reaction pathways and energetics for water–silica interactions. However, due to the high computational cost to solve time independent Schrödinger equation of electrons, approximations must be used. For liquid water and water–solid interactions, density functional theory (DFT) is the mostly widely used approximation. Earlier first principles calculations used cluster models that consists of a small group of atoms with hydrogen saturated dangling bonds to represent a surface or bulk material.[14,15] Due to localized charge transfer, cluster calculations provided reasonable analog to real situations

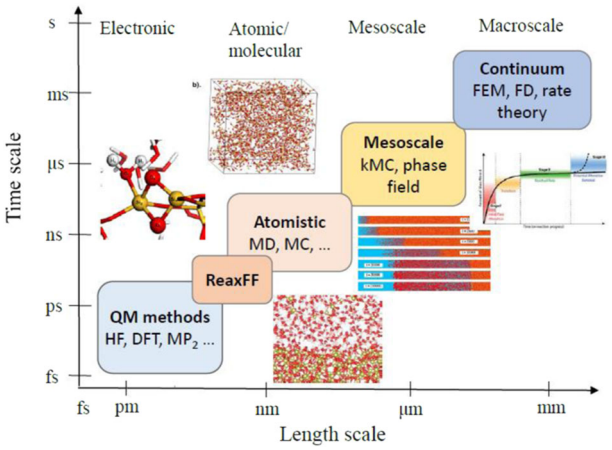

Fig. 2 Multiscale simulation methods and applications to water/glass interactions and glass dissolution (reprinted with permission from: ref. 82 copyright 2004, with permission from Elsevier and ref. 98 copyright 2016, with permission from Elsevier; reprinted with permission from ref. 23 copyright John Wiley and Sons 2015, and ref. 2 copyright John Wiley and Sons 2013)

but often constrain surface or bulk effects.[16] Only in recent years has computational efficiency increased to allow for simulation of surfaces and water–solid interfaces.[17] Recent calculations have also considered the effect of pH on the reaction energy barriers to break covalent network former–oxygen–network former linkages.[18,19]

In silicate glass dissolution, silica is the most durable component due to the stable siloxane bonds that form the backbone of the glass network, thus breakage of the Si–O–Si linkages is considered a rate limiting step.[20] DFT-based first principles calculations have been widely used to investigate the reaction mechanisms and energies for hydrolysis of the siloxane bonds (Eq.1).

$$(\equiv Si - O - Si \equiv) + H_2O \rightarrow 2(Si - OH) \quad (1)$$

Due to its high strain energy, two-membered ring (2-Ring) defects, two SiO_4 tetrahedron connected though edge sharing, are often selected for investigation of reaction mechanisms.[14,16,21,22] Two different reaction mechanisms for siloxane bond breakage were proposed by Masini and Bernasconi (Fig. 3).[22] The first involves an oxygen atom in a water molecule creating a short lived pentacoordinated silicon defect (Si^5), which causes siloxane bond rupture and the transfer of a proton to the non-bridging oxygen formed during bond breakage, forming two silanol groups (outlined in Fig. 3).[23] In the second mechanism, one of the two hydrogen in the water molecule bonds with a bridging oxygen, forming a protonated bridging oxygen, causing siloxane bond breakage and disassociation of the water molecule through formation of two silanol groups. The first reaction, which includes the formation of a Si^5 intermediate defect, has been the most commonly reported. Energy barriers for the breakage of 2-Ring defects are between 0.3–1.27 eV, and vary with simulation method and cluster size.[14,15,22] Differing energetics of the formation of the intermediate defect, either Si^5 or protonated bridging oxygen, are credited with preference for Si^5 reaction mechanism.[22] Silica linkages with defects in the local coordination environment are even more reactive with undercoordinated silicon decreasing the siloxane energy barrier by ~0.3 eV.[15] This work highlighted the variability in the siloxane bond energies, and that selective bond breakage can alter the structure of interfaces and gel structures.

While the above analysis focuses on siloxane bonds in clusters or flat surfaces, surface curvature also can affect both accessibility of defects and the stress state of the surface siloxane bonds.[24] Due

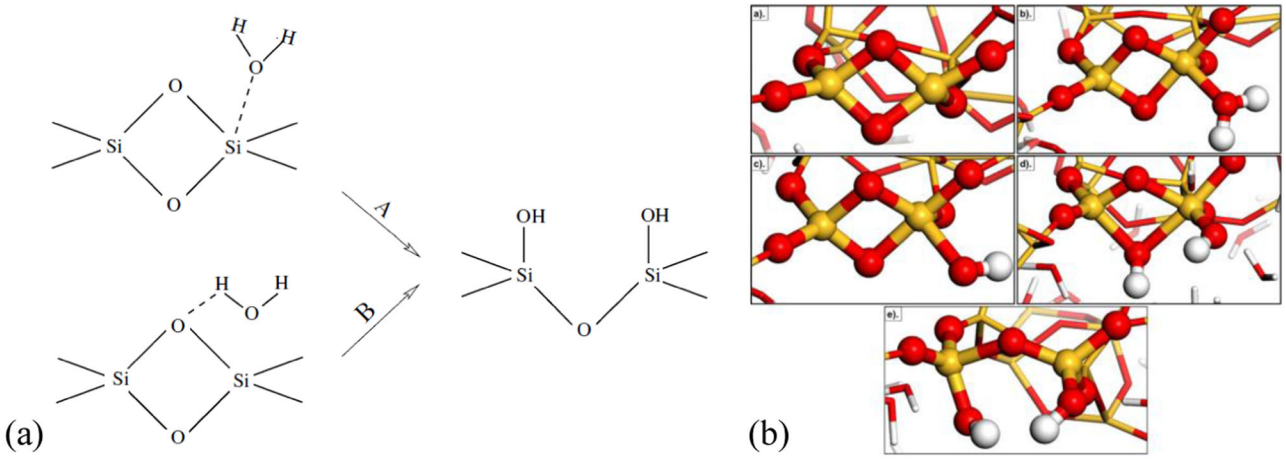

Fig. 3 **a** Two proposed reaction mechanism of water with two-membered ring defects in silica that lead to breaking of the Si–O–Si bond and defect removal (ref. 22 copyright IOP. Reproduced with Permission. All rights reserved). **b** Reaction mechanism of two-membered ring opening from AIMD simulations (adapted with permission from ref. 99 Copyright 2016 American Chemical Society)

to the development of complex silica gel structures during dissolution, a single bond on a flat surface is not a realistic view of defect sites. For example, removal of 2-Ring defects decrease in nanoporous silica systems where defects are located on complex internal pore surfaces, affecting the reactivity of silica gel.[23] Atomistic simulations are well positioned to investigate the role of surface character on the reactivity of siloxane bonds exposed to the environment. Experimental evidence demonstrates that dissolution develops preferentially at sharp points, smoothing the corners of jagged particles[25] and ledges.[26] Concave surface are more difficult to investigate, but in complex nanoporous silica systems, which include small pore sizes with highly curved internal surfaces, reactivity of 2-Ring defects is much lower.[23] Further investigations of the atomistic scale can highlight surface defects or features are most vulnerable to water attack, which can then inform microstructural engineering of glasses. For example, if small pores are resistant to dissolution, templating glasses with pores may alter the residual dissolution rate. This is just one avenue through which atomistic modeling of glass dissolution can provide unique and valuable insight, which can be incorporated into the development of corrosion resistant glasses.

Activation energies and siloxane bond stability also changes with the coordination of the silicon, which can be investigated in detail by atomistic simulations. Theoretical dissolution begins with a perfectly coordinated Q_4 species, a silicon bonded to four bridging oxygen, and then siloxane bonds break one by one, forming a Q_3, then a Q_2, a Q_1, and finally a Q_0 species (SiO_4H_x).[12] During each siloxane bond breakage a NBO and a under-coordinated silicon defect will form and are hydroxylated through consumption of water molecules. The energy barrier for different siloxane bond breakages cannot be identified experimentally, but energetics for removal of SiO_4 units are measured as 0.62–1.12 eV.[26,27] Activation energies vary with solution compositions, temperature, and the use of bulk or powdered samples.[28,29] Energy barriers are lower than the Si–O bond energies of 5–6 eV[30] indicating the important role that water plays in lowering energy barriers. Criscenti et al.[19] attempted to identify a connection between the connectedness of the silicon and stability of related siloxane bonds but did not find a clear relationships, indicating the complexity of the silica dissolution mechanisms. Identifying the changing stability of the siloxane bonds with environment would allow for engineering-specific glass compositions, which contain specific Q_n ratios to alter dissolution rates. Therefore, detailed high-accuracy investigations of changing bond stability can be an effective method of understanding glass dissolution and working to create unique glass systems, which allow for controlled dissolution.

Interactions and reactions of the water-multicomponent oxide glass systems

Ultimately, nuclear waste glasses are not composed solely of silica, and boron and aluminum are also present as network forming species along with network modifiers, such as alkali and alkali earth oxides.[20] Among the three critical processes of glass dissolution: hydration, hydrolysis, and ion-exchange, hydrolysis is a critical step. In multicomponent glasses, hydrolysis occurs in multiple cation–oxygen–cation linkages with varying energy barriers. The changing stability of M–O–M linkages in glasses is implicated from the creation of the silica rich remnant structure during glass dissolution.[12] Stability of Al–O–Si linkages was performed by Xiao and Lasaga[31,32] and Kubicki,[33,34] and Bouyer [35,36] for investigation of the weathering and hydrolysis of aluminosilicates. Borosilicates are not as well studied, though Lee and Stebbins as well as Tossell and Saghi-Szabo investigated Si–O–B linkage stability in clusters with Zapol et al. extending the analysis to surfaces.[1837,38]

M–O–M linkage stability is affected by the pH of the surrounding fluid, with both protonated and deprotonated systems investigated to approximate acidic or basic conditions. Data compiled in Fig. 4 demonstrates that all linkages exhibit the most stability at neutral conditions, with both protonation and deprotonation affecting the energy barrier. The introduction of a proton results in a decrease in the energy barriers and alters the relative stability of the network formers. Geneste et al.[36] investigated hydronium interactions with Si–O–B linkages identifying and ranked reactivity of types of bonds under protonation conditions, with B–O–B linkages appearing to be the least stable, followed by Si–NBO, and then Si–O–B structures. Protonation effects are also clearly seen in the case of Al–O–Si linkages, with hydroxyls of the Al–O–Si structures by proton absorption onto the bridging oxygen.[35]

Conversely, deprotonation conditions decrease the energy barriers though the effect is not as severe. Identifying the changing mechanisms of water interactions with M–O–M linkages can identify differences in the stability of different M–O bonds, which can be used to predict the response to different glass compositions to the resulting residual rate. Combing activation results for M-O-M linkages with changing coordination environments has indicated which are more or less stable in particular solutions, which can be used to predict glass dissolution under

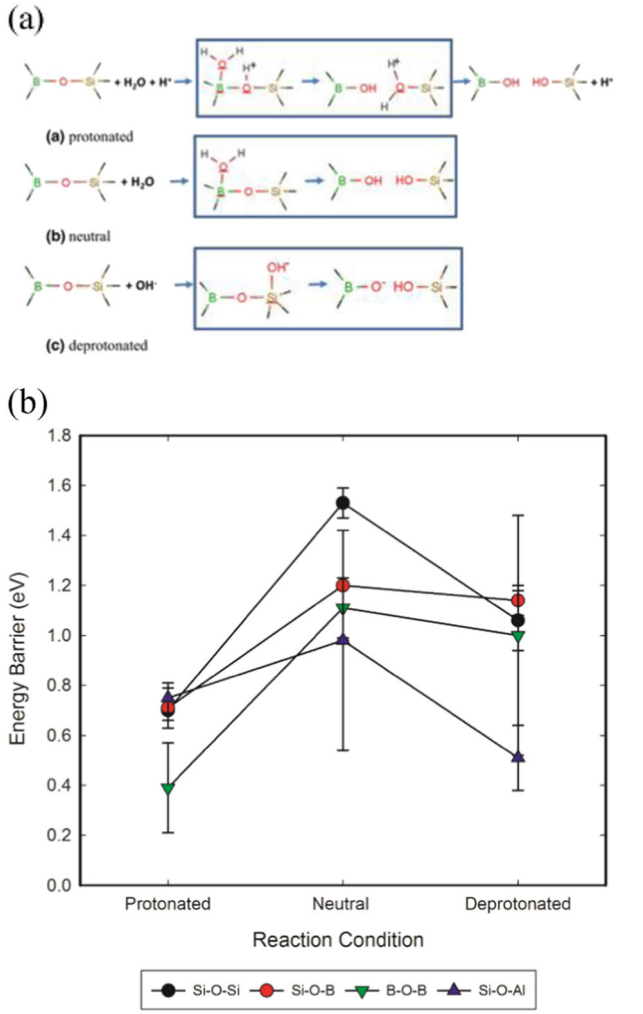

Fig. 4 **a** Introduction of the effect of pH on the energy barrier of breaking cation–oxygen–cation linkages (reprinted with permission from ref. 18 copyright John Wiley and Sons 2017). **b** Summary of energy barrier for breakage of network former linkages. Data from refs. 18, 31, 95, 99

changing environments. This demonstrates the power of DFT methods in understanding the role of localized pH and mixed network formers on the stability of multicomponent glasses.

As DFT efficiencies continue to improve it is becoming possible to investigate the surface reactivity of multicomponent glasses with water for larger systems. The majority of this work has been performed by Tilocca and colleagues[39] who investigated the stability of multicomponent bioactive glasses in aqueous environments. Many of the lessons learned and best practices from the investigation of bioactive glasses can be extended, and will provide insight into the role of surfaces on the dissolution behaviors of complex nuclear waste glass compositions.

Classical MD simulations of water/glass interactions and dissolution

Forcefield development for multicomponent oxide glasses. Classical MD employs analytical empirical potentials to describe interatomic interactions resulting in higher computational efficiency and larger system sizes. Classical MD is an attractive option to extend the time and length scale of ab initio simulations (Fig. 1). Classical MD is an effective method to generate atomic structures of glasses, in which larger system sizes and longer time scales allow for description of medium range structural features in glasses and reaction kinetics. In addition, potentials that enable description of chemical reactions can be used to study water–glass interaction and interfaces, as well as water behaviors in porous glass structures. These two types of simulations: glass structure generation and glass–water interactions represent two common classical MD simulations used to understand glass dissolution.

MD simulations have been extensively applied to study the structure and properties of glasses, which lack long range order and pose significant challenge in experimental investigations. Early potentials of silica include long range Coulombic forces and short range two-body and three-bodied interactions in various forms.[40,41] Potentials were then developed for more complex silica glasses including alkali silicates and aluminosilicate glasses.[42,43] Particularly, D.M. Teter developed a set of empirical potentials for oxides by parametrization to mineral structures and properties.[44] These potentials have been tested in wide range silicate, aluminosilicate, and phosphosilicate glasses with alkali, alkali earth, transition metal, and rare earth oxides by Du and co-workers.[44,45] Pedone et al.[46] developed a set of partial charge potential with the Morse potential form for silicate glasses that include a number of the common alkali, alkali earth, and aluminum oxides. Tilocca also developed a set of full charge potential that included polarization of oxygen ions using the Shell model [47] to model bioactive glasses.

Nevertheless, many of these potentials do not include parameters of boron oxide due to the composition dependent coordination change of boron. However, boron oxide is commonly included in nuclear waste glasses due to its capability to lower the melting temperature and viscosity of the melt. Hence, modeling multicomponent nuclear waste glasses is particularly challenging. Some potentials exits for alkali borates but only a few for borosilicate glasses. Recently, Kieu et al.[48] developed a set of two-body potential with composition dependent parameters for atomic charges and B–O interaction parameters by fitting to the boron coordination change from Dell and Bray model based on NMR studies. The Kieu potential was able to describe changing boron coordination with composition. Deng and Du tested wide composition range of the validity of the Kieu potential [49] and extended the potential to include alumina.[49] These potentials have been used to study the surface structure of sodium borosilicate glasses (Fig. 5). It can be seen that the boron coordination of the bulk glass agree well with the Dell and Bray model.[50] The glass surface has shown an enrichment of sodium and compositional changes as compared to the bulk.[51] Therefore, the glass surfaces show different chemistry and structure from the bulk, features which were also observed by Criscenti et al.[19] in MD simulations of sodium borosilicate glass surfaces.

Investigation of the changing coordination of boron in the multicomponent glasses used for nuclear waste disposal can serve as a representative study of how classical MD investigations can provide unique insight into glass structure. With recently developed potentials by Deng and Du,[49] sodium boroaluminosilicate glasses that represented simplified version of the International Simple Glass (ISG), a model glass developed by the international community to understand physical and corrosion behaviors of nuclear waste glasses, were studied using MD simulations through the simulated melt and quench process (Fig. 6 shows the snapshot of the final simulated glass structure). It can be seen that these glass former oxygen polyhedrons consisting of $[SiO_4]$, $[AlO_4]$, $[BO_3]$, and $[BO_4]$ connect together through bridging oxygen to form a three dimensional network. The cation oxygen pair distribution functions identify Si–O, Al–O, and Na–O bond distances of 1.61 Å, 1.73 Å, and 2.50 Å, respectively (Fig.7a). The B–O pair distribution (Fig. 7b) shows an average B-O bond distance of 1.47 Å with a shoulder due to shorter B–O bond distances in threefold coordinated boron (^{3}B). From the

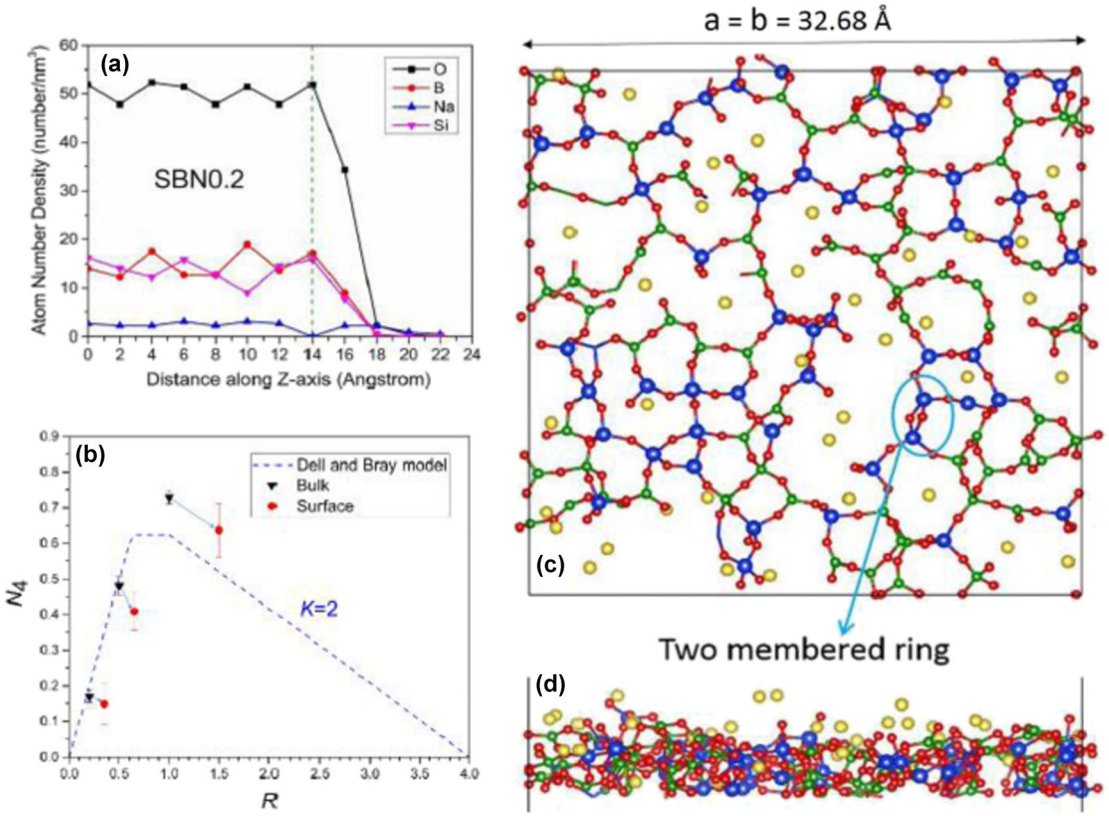

Fig. 5 Sodium borosilicate glass from MD simulations.[51] Surface composition profile **a** and boron N^4 as a function of R (soda to boron oxide ratio) for the bulk and surface **b**. Surface structure of sodium borosilicate glasses: top view (**c**) and side view of top 5 Å (**d**) (reprinted with permission from ref. 51 copyright John Wiley and Sons 2017)

deconvolution, the percentage of fourfold coordinated boron (^{4}B) can also be determined to be around 80%. Thus, in the ISG composition, majority of boron is in fourfold coordination state. With carefully developed and validated potentials, the complex structures of the mixed glass former nuclear waste glasses can be generated with structure features in good agreement with experimental data. These structures can provide a foundation of other studies such as radiation effects, diffusion behaviors, surface, and surface reactions. After the successful development of multicomponent glass model, the role of structural changes of the glass on dissolution rates can be further established so that glass dissolution can be predicted on geological time scales.

Forcefield development for the water–silica systems. Including water–silica interactions into classical MD forcefields is critical in allowing for the atomistic simulation of glass dissolution on a larger scale. Many attempts have been made to develop such a forcefield, including Feuston and Garofalini, who performed water–silica simulations using a dissociative water–silica potential in the early 1990s.[52] Recently, Mahadevan and Garofalini developed a dissociative water–silica forcefield based on water potentials by Guillot and Guissani.[53] Another forcefield used the BKS potential for silica and a SPC/E water model with Buckingham interactions for water–silica interfaces was developed by Hassanali and Singer.[54] Other water–silica potentials have been developed;[55,56] however, truly reactive potentials that can describe silica and water structures, reaction pathways, and energetics are rare.

One forcefield that includes water–silica reactions is a bond order based reactive force field (ReaxFF) with dynamic charge equilibration developed by Goddard, van Duin, and coworkers.[57] ReaxFF includes indistinguishable atomic species, thus oxygen atoms in water and oxygen in silica are of the same species, and atoms smoothly transition from one chemical species to another.[58] Additionally, charges in the systems are not fixed, but vary depending on local geometry and chemical environment. ReaxFF was first parameterized for water–silica systems in 2010 by Fogarty et al.[58] then readjusted by Yeon and van Duin to provide greater accuracy in water–silica reaction energy barriers.[59] Rimsza et al. used DFT-based ab initio MD simulations of water–nanoporous silica interactions to validate two versions of ReaxFF potentials for water–silica interactions.[60] It was shown that the new refined model (ReaxFF-2015) can describe the reaction energy barrier of Si–O–Si breakage (hydrolysis reaction) much better than the 2010 version (Fig. 8a). Also, the comparison shows the reactivity is different between the two versions of the parameters as shown in the concentration of the 2-Ring defects (Fig. 8b). Overall, the two ReaxFF potentials were able to describe the water–silica interfacial structure well but could improve the description of the water–silica reaction energetics and kinetics.

The ReaxFF has been used to identify the reactivity of the silica-gel formed during glass dissolution through interfacial gel models developed by Rimsza and Du.[61] By inserting a silica-gel structure between dense silica and bulk water, the dissolution of the silica from the gel to the water regions can be monitored.[61] Results found the removal of low coordinated silica out of the gel, resulting in an increased connectivity of the remaining gel structure, as well as the development of high silica concentrations adjacent to the water–gel interfaces.[61] Such simulations can be extremely powerful in identifying the evolution of changes of the interface during glass dissolution, and provide information on how the composition and structure of the gel affects the residual

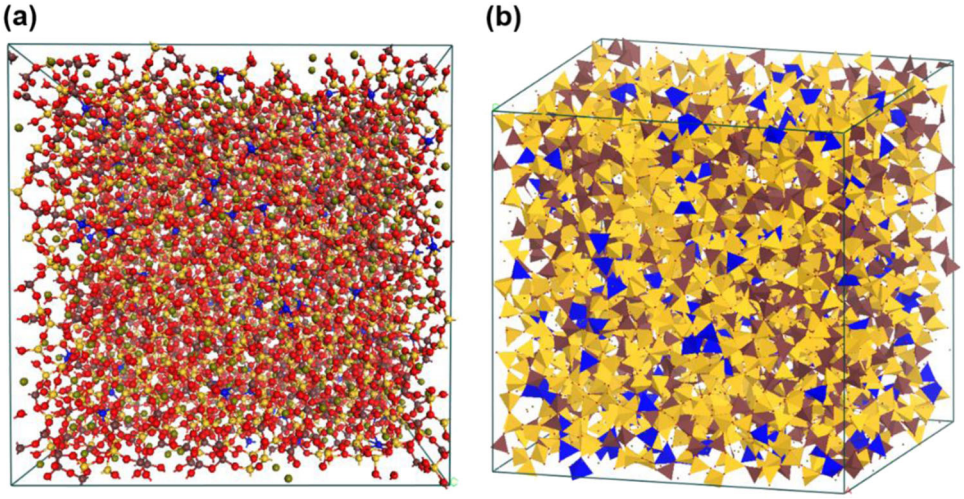

Fig. 6 Snapshot of ISG glass structure from MD simulations. **a** Ball and stick representation: red: oxygen, orange: silicon, blue: aluminum, brown: boron, green: sodium. **b** polyhedron representation. Yellow tetrahedron: SiO_4, blue tetrahedron: AlO_4, brown triangle and tetrahedron: BO_3 and BO_4

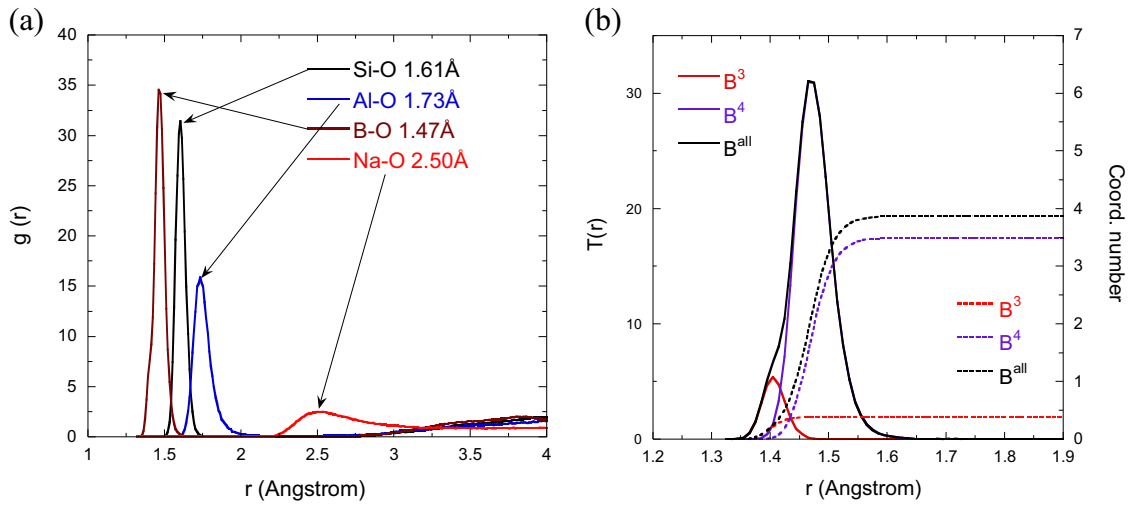

Fig. 7 **a** Pair distribution functions (PDF) of cation–oxygen pairs **b** deconvoluted boron–oxygen total correlation function and accumulated boron coordination number of ISG glass

dissolution rate. Expansion of this work into multicomponent systems would allow for the identification of the role of different network modifiers and formers can glass dissolution.

MD simulations of water–silica interactions. By using the above-mentioned forcefields, the water–silica interactions and reactions have been studied using classical MD simulations. Garofalini and co-authors performed some of the early MD simulations of water–silica glass interactions. They analyzed the structure and hydroxylation of silica surfaces[62] as well as silica polymerization.[63] With advances in potential development the role of the original defective surface in forming silanol concentrations were identified.[54,56,64] Classical MD simulations have also been able to reproduce both of the silica–water reaction mechanisms found in ab initio simulations[65,66] due to the inclusion of DFT reaction pathways and energies.[59] Classical MD simulations tend to favor siloxane bond breakage by absorption of a proton onto a bridging oxygen site, noted by Lockwood and Garofalini[65] and Rimsza, van Duin, and Du.[66]

Later simulations looked into the gradual dissolution of silica glasses. Dissociation energy barriers of different Si Q_n species (silicon oxygen tetrahedron with n bridging oxygen) on silica glass surfaces were investigated using the potential mean force approach with MD simulations. By using the dissociative water–silica potential developed by Mahadevan and Garofalini,[53] it was found that among the four ($Q_4 \rightarrow Q_3$, $Q_3 \rightarrow Q_2$, $Q_2 \rightarrow Q_1$, or $Q_1 \rightarrow Q_0$) reactions, the $Q_3 \rightarrow Q_2$ and $Q_2 \rightarrow Q_1$ reactions have the highest activation energy of ~ 14.1 kcal/mol, and is the rate limiting step in bulk silica dissolution.[19,24] These barriers are in the lower range of the experimental energy barriers of 14–24 kcal/mol and below values from cluster-based ab initio calculations (18–39 kcal/mol).[19,24] Similar differences in energy barriers for siloxane bond breakage were identified by Du and de Leeuw on quartz surfaces.[67] Understanding how the local environment alters stability of siloxane bonds is critical to understanding how silica dissolves. If certain conditions/environments leads to increased stability, that is a structural or compositional feature, which can be targeted in the development of nuclear waste glasses.

In addition to investigating activation energies, classical MD simulations have been used to study other aspects of the water–silica interface. For example, structured water has been identified adjacent to the silica interface and extends 10 Å into the

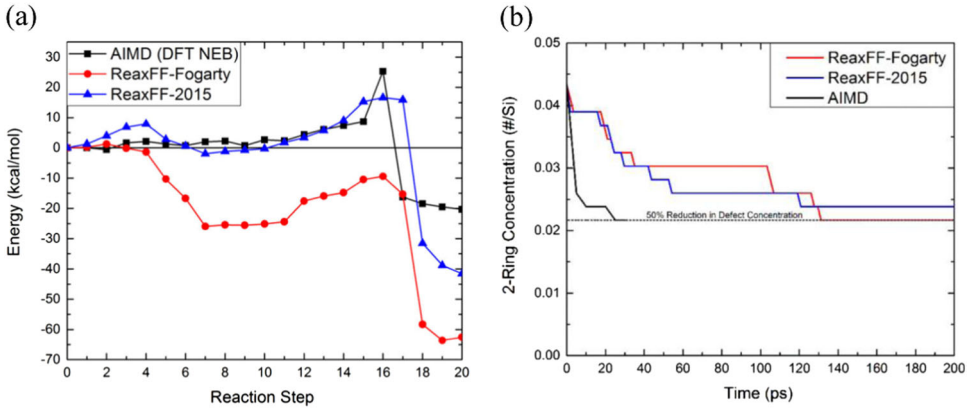

Fig. 8 **a** Comparison of reaction energy vs. reaction coordinates for ab initio and classical molecular dynamics with two versions of the ReaxFF forcefield. **b** Concentration of two-membered ring defects as a function of simulation time (**a, b** reproduced with permission from ref. 99 Copyright 2016 American Chemical Society)

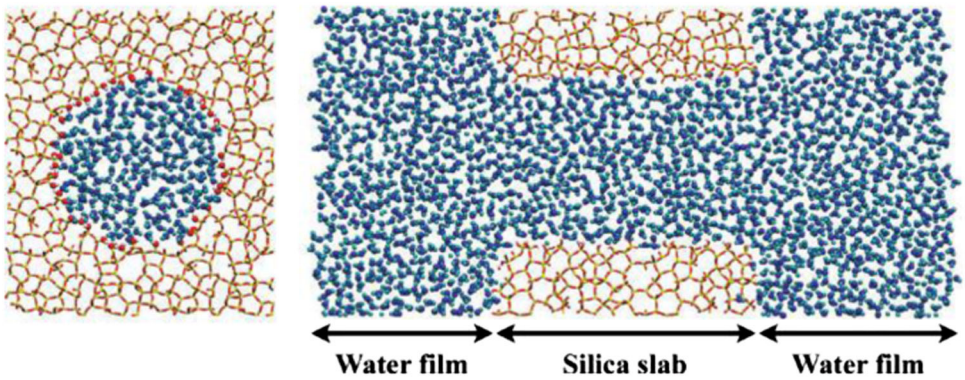

Fig. 9 MD simulations of water in cylinder pores of silica glass. Cross section views along the pore and perpendicular to the pore. The silica pore diameter is 4 nm. (reproduced with permission from ref. 70 Copyright 2012 American Chemical Society)

water.[68] Structured water experiences localized layering as well as the development of hydrogen bond networks and sharp decreases in the water self-diffusivity.[69,70] Figure 9 shows the cross section views of MD simulations of water in cylinder pores in silica from MD simulations. The structure and properties of water depend on the pore diameter with nanoconfinement in pores smaller than 1 nm. For pores with larger diameters (2 to 4 nm), water in the center of the pore behaves like bulk water. The simulation results show that the first monolayer water on silica surface is immobile while the rest of the water freely diffuses. The formation of structured water and limited atomic movement through water–silica systems impacts silica reactivity. It has been suggested that structured or nano-confined water inside the silica gel can influence water and ion transport during dissolution. With narrow pore structures, silica gel can limit the water diffusion and thus controls the speed of dissolution. Further investigation of the effect of nanonconfiment in more complex structures would identify if this effect could be scaled up to allow for passivation of surface layers due to limited water kinetics.

Aspects of water and silica interdiffusion have also been investigated, including details of hydronium ion formation in water as an intermediate step in fast proton transport.[71] Due to the ability to disassociate the water molecule, penetration of the water into the glass up to 8 Å away from the interface has been observed using multiple classical MD potentials.[58,72] This indicates the importance of a dissociative potential to allow for the possibility of water molecules breaking and recombining either inside or outside the silica structure. On the opposite end, the diffusion of silica monomers into water has also been investigated, to provide insight into whether nucleation of silica on the surface may cause reorganization of silica–water interface. Simulation of α-quartz indicates that the surface attracts the SiO_4H_4 with little change in the surface structure after reattachment of the tetrahedron resulting in a more stable quartz surface.[67] Attraction of the silica monomer to the surface may account for the growth of the protective layer and the low concentration of silica far from the interface.

Hydrated porous gel structures have also been investigated in the cement community where structured water molecules distributed in calcium silicate hydrate (C-S-H) determine the mechanical behavior. For example, Hou et al.[73] studied the C-S-H gels with different water contents and their mechanical behaviors using the CSHFF potential. It was found that the increase of water content transforms C-S-H gel into a layered structure. Hou et al.[74] also studied the water confinement in nanoporous C-S-H gel using the ReaxFF potential. It was found that the calcium silicate skeleton significantly influence the adsorption, reactivity, hydrogen-bond network and diffusivity of water molecules. Colliding of water molecules with the calcium silicate backbone was found to weaken the stability of the gel. Despite different chemistry and applications, the porous gel structure in C-S-H and confined water behavior and reactivity show similarity to the gel layer formed during glass dissolution. Plenty of experimental data is available to validate these models and some understanding can be borrowed in the glass corrosion field.

Overall classical MD simulations have provided detailed atomic level information on mechanisms and processes in glass dissolution, but further investigations of combined effects, has been limited. Additionally, the accessible time scale of MD is determined by the time step that is required to be small enough

to ensure accuracy of integration of equation of state. This limits most practical simulation scale to nano to micro-seconds. To extend the simulation time other methods need to be used.

Monte Carlo simulations of glass dissolution

Monte Carlo (MC) is a stochastic method that is commonly used to obtain numerical solutions of complex processes where analytical solutions are difficult to calculate. Application of MC methods to glass dissolution involve solving coupled hydrolysis/dissolution and condensation reactions.[3,75] MC simulations which include a time component are term kinetic MC (KMC). KMC evolves the system from state to state based on reaction rates and can enable simulations of infrequent events and process longer time scales compared to MD simulations.[76,77]

Aertsens and coworkers pioneered KMC simulations of glass dissolution of alkali silicate glasses,[75,78,79] where the glass structures were approximated by diamond lattices due to the topological similarity between the lattice and the network structures in silica. Two types of lattice sites, one easily dissolving and one slowly dissolving component represented by silicon and sodium, respectively, were randomly distributed on the lattice sites. When modifier concentration was high, the dissolution was found to be stoichiometric and there was no gel layer formation. With increased glass former concentration the dissolution became non-stoichiometric and a stable surface layer formed.[79] In additional MC simulations of glass dissolution, it was found that a protective gel layer formed due to silica adsorption or precipitation from the solution. The dissolution rate from MC simulations was found to obey the first order rate law, in agreement with the experimental data.[78]

Devreux et al.[80] further developed the MC methodology and applied it to study the dissolution of sodium borosilicate glasses.[81] Simulations were performed on a diamond lattice with silicon and boron atoms randomly put on the vertices and their proportion consistent to the glass composition, while sodium atoms were put into the interstitial sites near silicon or boron. Silica dissolution is described by three rate constants corresponding to silica with one, two, or three bridging oxygen. The dissolution-condensation equilibrium is schematically expressed as,

$$solid - Q_n + nH_2O \leftrightarrow Solid - (OH)_n + Q_o(n = 1 - 3) \quad (2)$$

where the Q_n denotes silicon atoms with n siloxane bonds (or n bridging oxygen) and Q_0 is silicic acid ($Si(OH)_4$). And the dissolution to condensation rate constant ratio w_n/w_c is expressed as

$$\frac{w_n}{w_c} = \exp\left[-\frac{\Delta H_n}{K_B T}\right] \quad (3)$$

where $\Delta H_n$is the reaction enthalpy, which can be derived from QM calculations or fitted to reproduce experimental data, and K_B is Boltzmann constant and T is the temperature.[82] The MC simulations were performed in two phases: the dissolution and the condensation phase,[82,83] while more complex algorithms were adopted in more recent MC simulations.[84] In the dissolution phase, the surface grids were scanned and the soluble species such as sodium and boron were dissolved unconditionally while the silicon Q_n species were dissolved based on the probability w_n. The dissolved species were replaced with water. In the condensation phase, silicon atoms were deposited at random positions according to the rate of $w_c \times c_{Si}$, where c_{Si} was the silicon concentration. This process generated porous silica at the water–glass interface due to removal of soluble species such as boron and sodium, the removal of isolated silicon species, and the adsorption or redeposition of silicon.[82] The model was able to reproduce the experimental thickness of dissolution alteration layer for samples with different surface area to volume ratios. Figure 10 shows the gel layer formation and morphology

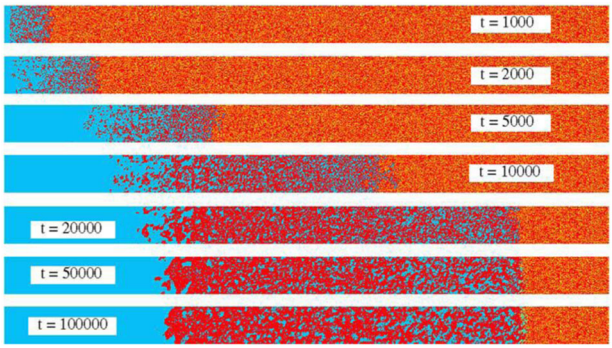

Fig. 10 Evolution of the gel layer morphology during dissolution of borosilicate glasses from MC simulations. Silicon: red pixels, boron: yellow, sodium: not shown, water: blue (reprinted from ref. 82 Copyright 2004, with permission from Elsevier)

evolution as a function of dissolution time from MC simulations of dissolution of a sodium borosilicate glass.[85] It shows that the gel layer is free of boron and sodium and consists of silica with silicon density similar to the bulk glass. Also, the gel structure appears to be inhomogeneous with higher porosity at the gel/glass interface than the gel/water interface.

An important aspect that has been overlooked or treated too simply in early MC simulations of glass dissolution is the transport of dissolved silicon species through the altered layers. Kerisit et al.[84] systematically studied three diffusion models in MC simulations of sodium borosilicate glasses and evaluated the simulation results by comparing with experiments. The three diffusion models include the instantaneous homogenization model which represents the limiting case of much faster diffusion of silicon species as compared to the rates of hydrolysis and condensation, the model with linear silicon concentration across the altered layer, which has been used earlier by Ledieu et al.[86] and the model coupling of hydrolysis and condensation reaction with the 1-dimensional diffusion model by solving the Fick's second law using a finite different method. Due the incorporation of diffusion, a more complex six steps MC algorithm were used: dissolution evaluation and execution, glass connectivity evaluation, diffusion, condensation, liquid connectivity evaluation, and the coordination evaluation.[84] The results show that the instantaneous homogenization and linear diffusion model are appropriate for glasses that dissolves rapidly, for example, sodium borosilicate glasses with low silica content and those with low zirconia concentrations. But for the less dissolvable glasses with higher silica content such as SON68, the assumption of linear diffusion became problematic as silica concentration in the altered layer is not linear, but changes significantly with time and decreases in magnitude with respect to the bulk solution. This highlights the importance of explicit treatment of diffusion of dissolved species in the altered layer in MC algorithms for glass dissolution simulations.[84]

Using similar approaches, Ledieu et al.[87] studied the effect of alumina and zirconia in the dissolution of borosilicate glasses using MC simulations. Two competing processes were found to control the glass dissolution rate: dissolution of soluble components such as B and Na and restructuring of the altered layer due to hydrolysis/condensation reversible reactions. It was also shown that the formation of surface hydrated layer is responsible for slowing dissolution. The replacement of silica with less soluble oxides such as zirconia led to an initial increase of the leached layer thickness, hence a decreased dissolution rate, while further substitution at high zirconia content decreased the leached layer thickness and thus a greater boron release, in agreement with experimental results.[87] This was explained by the fact that these

insoluble oxides impeded the formation of the surface silica layer that controls the dissolution.[87]

Cailleteau et al. also found that the slowdown of the dissolution rate of less durable silicate glasses over time was due to pore closure near the outer surface of the alteration by combining MC simulations with experimental investigations.[88] This kind of morphology transformation provides interpretation of dissolution rate slowdown in some glasses that is different from the theory that accounted for decreasing dissolution rates was to saturation of silica content in the solution, showing that MC can provide insights to complicated processes of dissolution that requires access to long time scales.[88] MC simulations were able to show the formation of the dense polymerized outer layer during borosilicate glass dissolution, nevertheless none of these simulations were able to reproduce the formation of the porous silica gel structure on the top of the dense outer layer, which has been observed experimentally.[84] Fully dense outer layer that prevented diffusion contradicts with experimental observations that there exists a residual dissolution rate in borosilicate glasses, hence further development of MC algorithm to enable the formation of thick gel layer on the top of the dense silica layer is needed.[84] Most of the MC simulations uses regular diamond or cubic lattices with glass network structures mapped on the lattices and modifier cations putting into the interstitial sites. Realistic glass structure models of multicomponent borosilicate glasses can be generated from MD simulations with recently developed potentials.[45,48,49] Another development of MC simulations is thus to incorporate the structure models from MD in MC simulations instead using the ideal lattices.[76,84]

Kerisit et al.[89,90] have further developed the MC simulation methodology for glass dissolutions to take into consideration glass structure features such as NBO and corrosion conditions such as dynamic flow-through experiments.[3] In simulations of flow-through corrosion of borosilicate glasses, it was found that at high flow rate conditions, thick alteration layer was formed and glass dissolves congruently. At low flow rates, highly incongruent dissolution was observed with formation of a permanent protective layer similar to static dissolution conditions. This protective layer, however, can be disrupted or prevented at even slow flow rate that led to intermediate resumption of glass corrosion. Kerisit et al. also studied the effect of glass composition such as the addition of alumina to borosilicate glasses on glass corrosion at static conditions.[90] The role of alumina was found to be complicated. Alumina decreases corrosion due to stronger Al–O–Si linkage than Si–O–Si linkages. On the other hand, alumina has opposite effect on the protective layer formation that controls the residual rate of glass dissolution. Alumina slows down the hydrolysis-condensation reaction of silica hence delays the formation of the protective gel layer but it strengthens the glass network and increases it lifetime, which facilitates the formation of the protective layer. As a result, the extent of dissolution (represented by boron leaching thickness) shows a maximum with alumina concentration in zirconia containing boroaluminosilicate glasses, in agreement with experiments.[90] These results show that MC can provide mechanistic understanding of glass dissolution and glass-water interfacial reactions. It can also be used to study the effects of glass composition and testing conditions thus glass dissolution behaviors.

Current challenges and opportunities

During glass dissolution, several different interfacial layers are formed between the pristine glass and the bulk solution. The atomic and microstructure of these interfacial layers are responsible for controlling the residual rate. Multiple competing mechanisms may occur and increase complexity of the analysis.[12] The structure and properties of the interfacial gel layers are thus critical to identifying the residual rate of glass dissolution.[12]

Computational tools provide the opportunity to investigate the silica gel alteration layers and isolate specific reactions in order to identify which of the competing mechanisms dominates the dissolution process. Currently, ab initio and classical MD simulations have investigated the hydrolysis phase of dissolution but condensation or polymerization of silicic acid to form the gel and protective layer could not be studied due to the long simulation times necessary for the reaction kinetics. Traditionally, MC methods have been used to investigate this regime, though with increasing computing power and the development of reactive potentials, these processes might be able to be studied with MD as well.

Nuclear waste glasses are complicated multicomponent oxides, and much of the dissolution phenomenon varies with composition. For example, inter diffusion occurs between the network modifiers in the glass with the aqueous environment, and changing stability of network formers is credited with the formation of the silica rich gel layers. Thus far, the majority of the investigation of glass dissolution using classical MD and ab initio methods has focused on the analysis of simpler water–silica systems, selected due to the availability of potentials and the wide interest in silicates. The limited information available on multicomponent amorphous oxides is a detriment to the understanding of glass dissolution, when competing mechanisms require simulation of mobile species in the glass. As the field of glass dissolution continues to mature, focus will need to shift on the role of second and tertiary components. In the use of ab initio or DFT methods careful selection of structures due to the small simulation sizes will be necessary, as well as targeted studies to investigate specific aspects of dissolution, such as structural stability of surface features. With classical MD methods the primary challenge is the development of potentials, which are robust enough to handle the chemistry of the complex multicomponent oxides combined with water reactivity.[44,49] While several potentials are currently in development, further detailed validation will be required before the investigation of nuclear waste dissolution.

Most of the MC simulations used ideal diamond or cubic lattices to simplify the simulations and to allow access to larger systems and longer time scales. These lattices are too simplified to represent the complexity of the structure of multicomponent glasses.[75,76] Medium range ring structures, composition dependent coordination change, or the clustering of modifier ions[91] can be important in the dissolution of glasses. The major challenges facing current MC or KMC simulations of glass dissolution is how to include more realistic glass structure information and still keep the computational cost manageable. Thus, applying realistic glass structure models from MD simulations of multicomponent nuclear waste glasses in MC simulations would be a future direction of MC simulations. It has been proposed that other simulation methods such as neural network and genetic algorithm can be used to tackle the challenges of complex glass structures in these simulation processes.[75]

The reaction energy barriers or reaction rate used in MC simulations were usually predetermined in two ways: either from minimum energy path and transition state search based on QM calculations or from fitting the rate constants to reproduce experimental data. When realistic glass structure is used in the MC simulations, it might be possible calculate the reaction rates on the fly during the simulations due to many more possibilities of combination of reactants states in the glass environments during the dissolution process. In this way, the reaction rates can be determined by using effective transition state algorithms such as the dimer method[92,93] according to the local environments during dissolution reactions. This will provide most accurate reaction energies or reaction rates to move MC simulations that will generate most accurate simulations but the challenge is how to keep the computational cost manageable.[76]

Table 1. Reaction energy barrier for silica–water cluster calculations through ab initio simulation

Geometry	Energy (eV)	Intermediate defect	Ref.
Two-membered ring (2-Ring) defects	1.08–1.27	Si^5	14
	0.71–1.11	Si^5	15
	1.1	Si^5	22
	0.3	Protonated bridging oxygen	
	0.9	Si^5	21
	1.17	Si^5	94
	1.09	Si^5	66
Unstrained Si–O–Si	1.24	Protonated bridging oxygen	19
	1.65–1.52	Si^5	95
	1.68	Si^5	85
	0.86–1.24	Si^5	96, 97

With ever increasing computing powers and new development of simulation algorithms, these issues and challenges can be addressed and realistic modeling of the long time dissolution behavior of glasses can be achieved.

SUMMARY

Atomistic computer simulation methods ranging from first principles calculations, ab initio molecular dynamics simulations (AIMD), classical molecular dynamics (MD) simulations and kinetic Monte Carlo (KMC) simulations and their applications to understand glass/water interaction and glass dissolution are reviewed in this paper. It is shown that these simulations provide mechanistic understanding of the strongly coupled ion-exchange, hydrolysis, hydration and associated interfacial processes and transport behaviors during glass dissolution. These simulations also provide insights to the bulk and surface structures of multicomponent glasses, water/glass reaction energetics, porous gel layer formation and water diffusion in confined pores, as well as microstructure evolution due to hydrolysis and condensation of the network structures, which will help to understand the mechanism behind key processes such as the residual rate of glass dissolution. The challenges of the simulations including the development of fully reactive potentials for multicomponent glass–water systems and KMC simulations based on realistic glass structures are discussed. With further development along these and other directions, together with ever increasing computing power and availability of accurate experimental characterizations to validate simulation results, it is conceivable atomistic simulations will play an even more important role in the understanding of long-term glass dissolution behaviors Table 1.

ACKNOWLEDGEMENTS

J.D. acknowledges support of the Center for Performance and Design of Nuclear Waste Forms and Containers, an Energy Frontier Research Center funded by the U.S. Department of Energy, Office of Science, Basic Energy Sciences under Award # DE-SC0016584. J.M.R. acknowledges support of the U.S. Department of Energy Nuclear Energy University Program (NEUP, Project #13-5494) in conjunction with Sandia National Laboratories. Sandia National Laboratories is a multi-mission laboratory managed and operated by National Technology and Engineering Solutions of Sandia, LLC., a wholly owned subsidiary of Honeywell International, Inc., for the U.S. Department of Energy's National Nuclear Security Administration under contract DE-NA0003525.

AUTHOR CONTRIBUTIONS

J.D. designed the outline of the article. J.M.R. wrote section "First-principles-based simulations of glass–water interactions", J.D. wrote section "Monte Carlo simulations of glass dissolution". Both J.D. and J.M.R. wrote the remaining portions of the manuscript.

ADDITIONAL INFORMATION

Competing interests: The authors declare that they have no competing financial interests.

Publisher's note: Springer Nature remains neutral with regard to jurisdictional claims in published maps and institutional affiliations.

REFERENCES

1. Gin, S. et al. An international initiative on long-term behavior of high-level nuclear waste glass. *Mater. Today* **16**, 243–248 (2013).
2. Vienna, J. D., Ryan, J. V., Gin, S. & Inagaki, Y. Current understanding and remaining challenges in modeling long-term degradation of borosilicate nuclear waste glasses. *Int. J. Appl. Glass Sci.* **4**, 283–294 (2013).
3. Pierce, E. M., Frugier, P., Criscenti, L. J., Kwon, K. D. & Kerisit, S. N. Modeling interfacial glass-water reactions: recent advances and current limitations. *Int. J. Appl. Glass Sci.* **5**, 421–435 (2014).
4. Rebiscoul, D., Frugier, P., Gin, S. & Ayral, A. Protective properties and dissolution ability of the gel formed during nuclear glass alteration. *J. Nucl. Mater.* **342**, 26–34 (2005).
5. Rebiscoul, D. et al. Morphological evolution of alteration layers formed during nuclear glass alteration: new evidence of a gel as a diffusive barrier. *J. Nucl. Mater.* **326**, 9–18 (2004).
6. Gin, S. et al. Origin and consequences of silicate glass passivation by surface layers. *Nat. Commun.* **6**, 1–8 (2015).
7. Geisler, T. et al. Aqueous corrosion of borosilicate glass under acidic conditions: a new corrosion mechanism. *J. Non-Cryst. Solids* **356**, 1458–1465 (2010).
8. Gin, S., Ryan, J. V., Schreiber, D. K., Neeway, J. & Cabié, M. Contribution of atom-probe tomography to a better understanding of glass alteration mechanisms: application to a nuclear glass specimen altered 25 years in a granitic environment. *Chem. Geol.* **349**, 99–109 (2013).
9. Gin, S. et al. Atom-probe tomography, TEM and ToF-SIMS study of borosilicate glass alteration rim: a multiscale approach to investigating rate-limiting mechanisms. *Geochim. Cosmochim. Acta* **202**, 57–76 (2016).
10. Grambow, B. A general rate equation for nuclear waste glass corrosion. *Mater. Res. Soc. Symp. Proc.* **44**, 15–27 (1984).
11. Grambow, B. & Müller, R. First-order dissolution rate law and the role of surface layers in glass performance assessment. *J. Nucl. Mater.* **298**, 112–124 (2001).
12. Frugier, P. et al. SON68 nuclear glass dissolution kinetics: current state of knowledge and basis of the new GRAAL model. *J. Nucl. Mater.* **380**, 8–21 (2008).
13. Gin, S. et al. Nuclear glass durability: new insight into alteration layer properties. *J. Phys. Chem. C* **115**, 18696–18706 (2011).
14. Rimola, A. & Ugliengo, P. A quantum mechanical study of the reactivity of $(SiO)_2$-defective silica surfaces. *J. Chem. Phys.* **128**, 204702 (2008).
15. Walsh, T. R., Wilson, M. & Sutton, A. P. Hydrolysis of the amorphous silica surface. II. Calculation of activation barriers and mechanisms. *J. Chem. Phys.* **113**, 9191–9201 (2000).
16. Du, M. -H., Kolchin, A. & Cheng, H. -P. Water–silica surface interactions: a combined quantum-classical molecular dynamic study of energetics and reaction pathways. *J. Chem. Phys.* **119**, 6418–6422 (2003).
17. Jensen, F. *Introduction to Computational Chemistry*. New York (John Wiley & Sons, 2013).
18. Zapol, P., He, H., Kwon, K. D. & Criscenti, L. J. First-principles study of hydrolysis reaction barriers in a sodium borosilicate glass. *Int. J. Appl. Glass Sci.* **4**, 395–407 (2013).
19. Criscenti, L. J., Kubicki, J. D. & Brantley, S. L. Silicate glass and mineral dissolution: calculated reaction paths and activation energies for hydrolysis of a Q_3 Si by H_3O^+ using ab initio methods. *J. Phys. Chem. A.* **110**, 198–206 (2006).
20. Gin, S. Open scientific questions about nuclear glass corrosion. *Proc. Mat. Sci.* **7**, 163–171 (2014).
21. Mischler, C., Horbach, J., Kob, W. & Binder, K. Water adsorption on amorphous silica surfaces: a Car-Parrinello simulation study. *J. Phys.-Condens. Mat.* **17**, 4005–4013 (2005).
22. Masini, P. & Bernasconi, M. Ab initio simulations of hydroxylation and dehydroxylation reactions at surfaces: amorphous silica and brucite. *J. Phys.-Condens. Mat.* **14**, 4133–4144 (2002).

23. Rimsza, J. & Du, J. Ab initio molecular dynamics simulations of the hydroxylation of nanoporous silica. *J. Am. Ceram. Soc.* **98**, 3748–3757 (2015).
24. Kagan, M., Lockwood, G. K. & Garofalini, S. H. Reactive simulations of the activation barrier to dissolution of amorphous silica in water. *Phys. Chem. Chem. Phys.* **16**, 9294–9301 (2014).
25. Wolff-Boenisch, D., Gislason, S. R., Oelkers, E. H. & Putnis, C. V. The dissolution rates of natural glasses as a function of their composition at pH 4 and 10.6, and temperatures from 25 to 74 C. *Geochim. Cosmochim. Acta* **68**, 4843–4858 (2004).
26. Dove, P. M., Han, N., Wallace, A. F. & De Yoreo, J. J. Kinetics of amorphous silica dissolution and the paradox of the silica polymorphs. *Proc. Natl Acad. Sci. USA* **105**, 9903–9908 (2008).
27. Icenhower, J. P. & Dove, P. M. The dissolution kinetics of amorphous silica into sodium chloride solutions: effects of temperature and ionic strength. *Geochim. Cosmochim. Acta* **64**, 4193–4203 (2000).
28. Bird, G., Boon, J. & Stone, T. Silica transport during steam injection into oil sands: 1. Dissolution and precipitation kinetics of quartz: New results and review of existing data. *Chem. Geol.* **54**, 69–80 (1986).
29. Rimstidt, J. D. Quartz solubility at low temperatures. *Geochim. Cosmochim. Acta* **61**, 2553–2558 (1997).
30. Kazi, H., Rimsza, J., Du, J. & Kelber, J. Ar ions and oxygen plasma interactions of amine terminated organosilicate glass: a combined experimental and ab initio simulations study. *J. Vac. Sci. Technol. A.* **32**, 051301 (2014).
31. Xiao, Y. & Lasaga, A. C. Ab initio quantum mechanical studies of the kinetics and mechanisms of silicate dissolution: $H^+(H_3O^+)$ catalysis. *Geochim. Cosmochim. Acta* **58**, 5379–5400 (1994).
32. Lasaga, A. C. & Gibbs, G. Quantum mechanical potential surfaces and calculations on minerals and molecular clusters. *Phys. Chem. Miner.* **16**, 29–41 (1988).
33. Kubicki, J., Blake, G. & Apitz, S. Ab initio calculations on aluminosilicate Q3 species: Implications for atomic structures of mineral surfaces and dissolution mechanisms of feldspars. *Am. Mineral.* **81**, 789–799 (1996).
34. Kubicki, J. & Sykes, D. Molecular orbital calculations on the vibrational spectra of Q_3 T-(OH) species and the hydrolysis of a three-membered aluminosilicate ring. *Geochim. Cosmochim. Acta* **59**, 4791–4797 (1995).
35. Bouyer, F., Geneste, G., Ispas, S., Kob, W. & Ganster, P. Water solubility in calcium aluminosilicate glasses investigated by first principles techniques. *J. Solid State Chem.* **183**, 2786–2796 (2010).
36. Geneste, G., Bouyer, F. & Gin, S. Hydrogen–sodium interdiffusion in borosilicate glasses investigated from first principles. *J. Non-Cryst. Solids* **352**, 3147–3152 (2006).
37. Lee, S. K., Musgrave, C. B., Zhao, P. & Stebbins, J. F. Topological disorder and reactivity of borosilicate glasses: quantum chemical calculations and ^{17}O and ^{11}B NMR study. *J. Phys. Chem. B.* **105**, 12583–12595 (2001).
38. Tossell, J. & Saghi-Szabo, G. Aluminosilicate and borosilicate single 4-rings: Effects of counterions and water on structure, stability, and spectra. *Geochim. Cosmochim. Acta* **61**, 1171–1179 (1997).
39. Tilocca, A. & Cormack, A. N. Modeling the water– bioglass interface by ab initio molecular dynamics simulations. *ACS Appl. Mater. Inter.* **1**, 1324–1333 (2009).
40. Van Beest, B., Kramer, G. J. & Van Santen, R. Force fields for silicas and aluminophosphates based on ab initio calculations. *Phys. Rev. Lett.* **64**, 1955–1958 (1990).
41. Sanders, M., Leslie, M. & Catlow, C. Interatomic potentials for SiO_2. *J. Chem. Soc. Chem. Comm.* **19,** 1271–1273 (1984).
42. Zirl, D. M. & Garofalini, S. H. Structure of sodium aluminosilicate glasses. *J. Am. Ceram. Soc.* **73**, 2848–2856 (1990).
43. Balasubramanian, S. & Rao, K. Molecular dynamics Investigation of structure and transport in the K_2O-$2SiO_2$ system using a partial charge based model potential. *J. Phys. Chem.* **98**, 10871–10880 (1994).
44. Massobrio, C., Du, J., Bernasconi, M. & Salmon, P. S. *Molecular Dynamics Simulations of Disordered Materials*. (Springer, 2015).
45. Xiang, Y., Du, J., Smedskjaer, M. M. & Mauro, J. C. Structure and properties of sodium aluminosilicate glasses from molecular dynamics simulations. *J. Chem. Phys.* **139**, 044507 (2013).
46. Pedone, A., Malavasi, G., Menziani, M. C., Cormack, A. N. & Segre, U. A new self-consistent empirical interatomic potential model for oxides, silicates, and silica-based glasses. *J. Phys. Chem. B.* **110**, 11780–11795 (2006).
47. Tilocca, A., de Leeuw, N. H. & Cormack, A. N. Shell-model molecular dynamics calculations of modified silicate glasses. *Phys. Rev. B* **73**, 104209 (2006).
48. Kieu, L. -H., Delaye, J. -M., Cormier, L. & Stolz, C. Development of empirical potentials for sodium borosilicate glass systems. *J. Non-Cryst. Solids* **357**, 3313–3321 (2011).
49. Deng, L. & Du, J. Development of effective empirical potentials for molecular dynamics simulations of the structures and properties of boroaluminosilicate glasses. *J. Non-Cryst. Solids* **453**, 177–194 (2016).
50. Dell, W., Bray, P. J. & Xiao, S. ^{11}B NMR studies and structural modeling of Na_2O·B_2O_3·SiO_2 glasses of high soda content. *J. Non-Cryst. Solids* **58**, 1–16 (1983).
51. Ren, M., Deng, L. & Du, J. Surface structures of sodium borosilicate glasses from molecular dynamics simulations. *J. Am. Ceram. Soc.*. https://doi.org/10.1111/jace.14654 (2017).
52. Feuston, B. & Garofalini, S. Oligomerization in silica sols. *J. Phys. Chem.* **94**, 5351–5356 (1990).
53. Mahadevan, T. & Garofalini, S. Dissociative water potential for molecular dynamics simulations. *J. Phys. Chem. B.* **111**, 8919–8927 (2007).
54. Hassanali, A. A. & Singer, S. J. Model for the water-amorphous silica interface: the undissociated surface. *J. Phys. Chem. B.* **111**, 11181–11193 (2007).
55. Lopes, P. E., Murashov, V., Tazi, M., Demchuk, E. & MacKerell, A. D. Development of an empirical force field for silica. Application to the quartz-water interface. *J. Phys. Chem. B.* **110**, 2782–2792 (2006).
56. Du, J. & Cormack, A. N. Molecular dynamics simulation of the structure and hydroxylation of silica glass surfaces. *J. Am. Ceram. Soc.* **88**, 2532–2539 (2005).
57. Van Duin, A. C. et al. ReaxFFSiO reactive force field for silicon and silicon oxide systems. *J. Phys. Chem. A.* **107**, 3803–3811 (2003).
58. Fogarty, J. C., Aktulga, H. M., Grama, A. Y., Van Duin, A. C. & Pandit, S. A. A reactive molecular dynamics simulation of the silica-water interface. *J. Phys. Chem.* **132**, 174704 (2010).
59. Yeon, J. & van Duin, A. C. ReaxFF molecular dynamics simulations of hydroxylation kinetics for amorphous and nano-silica structure, and its relations with atomic strain energy. *J. Phys. Chem. C* **120**, 305–317 (2015).
60. Rimsza, J. M., Yeon, J., van Duin, A. C. & Du, J. Water Interactions with nanoporous silica: comparison of ReaxFF and *ab initio* based molecular dynamics simulations. *J. Phys. Chem. C* **120**, 24803–24816 (2016).
61. Rimsza, J. & Du, J. Interfacial structure and evolution of the water–silica gel system by reactive force-field-based molecular dynamics simulations. *J. Phys. Chem. C* https://doi.org/10.1021/acs.jpcc.7b02734 (2017).
62. Garofalini, S. H. Molecular dynamics computer simulations of silica surface structure and adsorption of water molecules. *J. Non-Cryst. Solids* **120**, 1–12 (1990).
63. Garofalini, S. H. & Martin, G. Molecular simulations of the polymerization of silicic acid molecules and network formation. *J. Phys. Chem.* **98**, 1311–1316 (1994).
64. Leed, E. A. & Pantano, C. G. Computer modeling of water adsorption on silica and silicate glass fracture surfaces. *J. Non-Cryst. Solids* **325**, 48–60 (2003).
65. Lockwood, G. K. & Garofalini, S. H. Bridging oxygen as a site for proton adsorption on the vitreous silica surface. *J. Chem. Phys.* **131**, 074703 (2009).
66. Rimsza, J., Van Duin, A. C. & Du, J. Comparison of ReaxFF and ab initio molecular dynamics for water-nanoporous silica interactions. *J. Phys. Chem. C.* **120**, 24803–24816 (2016).
67. Du, Z. & de Leeuw, N. H. Molecular dynamics simulations of hydration, dissolution and nucleation processes at the α-quartz (0001) surface in liquid water. *Dalton. Trans*., **22,** 2623-2634 (2006).
68. Zangi, R. Water confined to a slab geometry: a review of recent computer simulation studies. *J. Phys.-Condens. Mat*. **16**, S5371–S5388 (2004).
69. Bonnaud, P., Coasne, B. & Pellenq, R. J. Molecular simulation of water confined in nanoporous silica. *J. Phys.-Condens. Mat*. **22**, 1–15 (2010).
70. Bourg, I. C. & Steefel, C. I. Molecular dynamics simulations of water structure and diffusion in silica nanopores. *J. Phys. Chem. C* **116**, 11556–11564 (2012).
71. Lockwood, G. K. & Garofalini, S. H. Lifetimes of excess protons in water using a dissociative water potential. *J. Phys. Chem. B.* **117**, 4089–4097 (2013).
72. Mahadevan, T. & Garofalini, S. Dissociative chemisorption of water onto silica surfaces and formation of hydronium ions. *J. Phys. Chem. C* **112**, 1507–1515 (2008).
73. Hou, D., Ma, H., Zhu, Y. & Li, Z. Calcium silicate hydrate from dry to saturated state: structure, dynamics and mechanical properties. *Acta Mater.* **67**, 81–94 (2014).
74. Hou, D., Zhao, T., Ma, H. & Li, Z. Reactive molecular simulation on water confined in the nanopores of the calcium silicate hydrate gel: structure, reactivity, and mechanical properties. *J. Phys. Chem. C* **119**, 1346–1358 (2015).
75. Aertsens, M. & Ghaleb, D. New techniques for modelling glass dissolution. *J. Nucl. Mater.* **298**, 37–46 (2001).
76. Mauro, J. C. & Du, J. Achieving long time scale simulations of glass-forming systems. *Comput. Theor. Chem.* **987**, 122–133 (2012).
77. Mei, D., Du, J. & Neurock, M. First-principles-based kinetic Monte Carlo simulation of nitric oxide reduction over platinum nanoparticles under lean-burn conditions. *Ind. Eng. Chem. Res.* **49**, 10364–10373 (2010).
78. Aertsens, M. The BRAG and GM2003 models for glass dissolution. *Mater. Res. Soc. Symp. Proc.* **985**, 0985-NN02-07 (2007).
79. Aertsens, M. & Van Iseghem, P. Modeling glass dissolution with a monte carlo technique. *Mater. Res. Soc. Symp. Proc.* **412**, 271–278 (1996).
80. Devreux, F., Barboux, P., Filoche, M. & Sapoval, B. A simplified model for glass dissolution in water. *J. Mater. Sci.* **36**, 1331–1341 (2001).

81. Cailleteau, C., Weigel, C., Ledieu, A., Barboux, P. & Devreux, F. On the effect of glass composition in the dissolution of glasses by water. *J. Non-Cryst. Solids* **354**, 117–123 (2008).
82. Devreux, F., Ledieu, A., Barboux, P. & Minet, Y. Leaching of borosilicate glasses. II. model and monte-carlo simulations. *J. Non-Cryst. Solids* **343**, 13–25 (2004).
83. Lobanova, M., Maurer, L., Barboux, P., Devreux, F. & Minet, Y. Monte carlo modelling of glass dissoltuion: comparison with experiments *mater. Res. Soc. Symp. Proc.* **663**, 237–245 (2001).
84. Kerisit, S., Pierce, E. M. & Ryan, J. V. Monte Carlo simulations of coupled diffusion and surface reactions during the aqueous corrosion of borosilicate glasses. *J. Non-Cryst. Solids* **408**, 142–149 (2015).
85. Wallace, A. F., Gibbs, G. & Dove, P. M. Influence of ion-associated water on the hydrolysis of Si–O bonded interactions. *J. Phys. Chem. A.* **114**, 2534–2542 (2010).
86. Ledieu, A., Devreux, F. & Barboux, P. Monte Carlo simulations of borosilicate glass corrosion: predictions for morphology and kinetics. *J. Non-Cryst. Solids* **345**, 715–719 (2004).
87. Ledieu, A., Devreux, F., Barboux, P. & Minet, Y. Contribution of Monte Carlo modeling to understanding the alteration of nuclear glasses by water. *Nucl. Sci. Eng.* **153**, 285–300 (2006).
88. Cailleteau, C. et al. Insight into silicate-glass corrosion mechanisms. *Nat. Mater.* **7**, 978–983 (2008).
89. Kerisit, S. & Pierce, E. M. Monte Carlo simulations of the dissolution of borosilicate glasses in near-equilibrium conditions. *J. Non-Cryst. Solids* **358**, 1324–1332 (2012).
90. Kerisit, S., Ryan, J. V. & Pierce, E. M. Monte Carlo simulations of the corrosion of aluminoborosilicate glasses. *J. Non-Cryst. Solids* **378**, 273–281 (2013).
91. Du, J. & Cormack, A. The medium range structure of sodium silicate glasses: a molecular dynamics simulation. *J. Non-Cryst. Solids* **349**, 66–79 (2004).
92. Henkelman, G. & Jónsson, H. Long time scale kinetic Monte Carlo simulations without lattice approximation and predefined event table. *J. Chem. Phys.* **115**, 9657–9666 (2001).
93. Xu, L. & Henkelman, G. Adaptive kinetic Monte Carlo for first-principles accelerated dynamics. *J. Chem. Phys.* **129**, 114104 (2008).
94. Zhi, L. -l, Zhao, G. -f, Guo, L. -j & Jing, Q. Structural, electronic, and vibrational properties of water molecules adsorbed on silica clusters. *Phys. Rev. B* **77**, 235435 (2008).
95. Nangia, S. & Garrison, B. J. Reaction rates and dissolution mechanisms of quartz as a function of pH. *J. Phys. Chem. A.* **112**, 2027–2033 (2008).
96. Pelmenschikov, A., Leszczynski, J. & Pettersson, L. G. Mechanism of dissolution of neutral silica surfaces: Including effect of self-healing. *J. Phys. Chem. A.* **105**, 9528–9532 (2001).
97. Pelmenschikov, A., Strandh, H., Pettersson, L. G. & Leszczynski, J. Lattice resistance to hydrolysis of Si-O-Si bonds of silicate minerals: Ab initio calculations of a single water attack onto the (001) and (111) β-cristobalite surfaces. *J. Phys. Chem. B.* **104**, 5779–5783 (2000).
98. Rimsza, J., Deng, L. & Du, J. Molecular dynamics simulations of nanoporous silica and organosilicate glasses using reactive force field (ReaxFF). *J. Non-Crystal. Solids* **431**, 103–111 (2016).
99. Morrow, C. P., Nangia, S. & Garrison, B. J. Ab initio investigation of dissolution mechanisms in aluminosilicate minerals. *J. Phys. Chem. A.* **113**, 1343–1352 (2009).

Submitted to Nature Partner Journal Materials Degradations

Nanoporous Silica Gel Structures and Evolution from Reactive Force Field Based Molecular Dynamics Simulations

*J.M. Rimsza, Jincheng Du**

Department of Materials Science and Engineering, University of North Texas, Denton, Texas USA

Abstract

Nanoporous silica-rich gels that form on silicate glasses during dissolution alter the silica-water interfacial behaviors and the overall reactivity of the glasses. Understanding the structures and properties of these gels is critical in elucidating the corrosion mechanisms of multicomponent silicate glasses and the long term residual dissolution rate. Structure models of nanoporous silica gels with random nanoporosity were generated by two methods: one mimics the proposed experimental mechanisms for gel formation by removing the dissolvable species of an International Simplified Glass (ISG) nuclear waste glass structure model, creating a remnant silica gel; and the second type of gel structures were created mimicking the hydrogarnet defect formation process by randomly removing silicon from amorphous silica followed by hydroxylation and hydration. These two types of gel structures were carefully characterized and compared. The results show that the remnant silica gels exhibit higher intermediate range order, which is inherited from the initial segregation of boron and modifier cations consistent to the modified random network (MRN) model of glasses, but with more isolated and closed pores. This contrasts with the more fragmented silica network structures (and more connected pore microstructures) created in the defect formation process. This microstructure difference resulted in nanoconfinement of water in the pores of the remnant silica gel model while the more randomly connected pore structures from the direct model exhibit much higher water diffusivity. These results shed light on the porous silica gel structures formed during silicate dissolution and suggest that, in addition to removal of the dissolvable species, dissolution of the silica network is

required to connect the isolated pores through which water diffuses to the reaction front of pristine glass and allowing for further corrosion.

1. Introduction

Silica gels are hydrated nanoporous silica systems commonly found in the fields of biomaterials, including silicate based bioactive glasses [1, 2], carbon sequestration [3, 4], liquid chromatography [5, 6] and catalysis [7, 8]. Silica gels also form during dissolution and consist of several alteration layers, including a hydrated glass and a crystalline layer[9]. Experimental elemental profiles have shown that the alteration layer is deficient in soluble species, including sodium, boron, and calcium but rich in silicon [9]. The silica-rich gel region undergoes constant restructuring, posing challenges to experimental characterization due to the complex amorphous structure and high level of hydration [10, 11]. Silica gels may passivate the surface by limiting the diffusion of water molecules to reactive interfaces, resulting in limited silicon diffusion into the surrounding environment [9]. Alternatively, densification of the gel due to collapse of silica structure or silica condensation from solution may form a barrier to further dissolution [12-15]. Experimental investigations have attempted to identify the origin of the silica gels and connect its structure to the dissolution rate [10]. Originally, silica gels were theorized to form from the precipitation of silica from an oversaturated solution [16], but studies using isotopically tagged samples indicated that only 1:600 silicon atoms in the gel structure had been deposited through condensation [10]. Therefore, the silica gel is not a precipitate but instead the reorganization of the remnant glass structure after removal of the soluble species [10, 17-19].

Additionally, the gel is nanoporous, and the small pore size may limit diffusion by slowing movement of water molecules through the silica gel by formation of frozen or structured water [10]. Structured water has been identified both experimentally [20-25] and computationally [26-29] and is caused by the formation of hydrogen bond networks at the water-silica interface which slows internal diffusion [30]. Previous investigations of structured water focused on the interface between water and flat silica surfaces or in large single pores, without considering the role of the gel structure [26, 31, 32]. The complexities of the silica gel layer and the resulting effect on water diffusion and dissolution rates makes understanding the structure of silica gels a grand challenge in the field of glass corrosion.

Computational methods provide atomistic insight into the properties of silica gels through the development of atomistic models which allow for structural and kinetic analysis of the system. Direct development of silica gel models is relatively rare, and instead nanoporous silica structures are created and hydrated to form gels. Nanoporous silica models are typically created by removing blocks of atoms from silica, creating highly ordered pore structures which do not represent the complexities of experimental systems [33-35]. Alternatively, nanoporous silica models formed through processes that mimic sol-gel [36, 37] or chemical vapor deposition (CVD)[38] methods have been created by classical molecular dynamics (MD) or Monte Carlo simulations. Experiments indicate that gels form during nuclear waste glasses dissolution inherit features of the original silicate network structures after the release of the dissolvable species (Na, B, or Ca) and are followed by relaxation and repolymerization of the silica network[10], unique from sol-gel or CVD derived porous silica structures and gels. Computational models of silica gels form from an initial multicomponent glass composition are rare in literature, possibly due to the complexity of the multicomponent borosilicate glass system, but these structures will allow for detailed description of the structure and properties of dissolution based silica gels. Recent development of empirical potentials allow for simulations of these boroaluminosilicate glasses [39].

Such models require reactive and dissociative water potentials to simulate water-silica interfaces. Early work by Garafolini et al. introduced a reactive water-silica potential for investigations of hydrated silica systems and interfaces[40]. However, the rigid ion three bodied potential does not distinguish oxygen species in the system, limiting the accuracy of the forcefield. Further development of reactive forcefields included parametrization to established water-silica reaction mechanisms which can limit spontaneous water-silica interactions[41]. More recently, a set of bond order based charge transfer potential in the framework of Reactive Force Field (ReaxFF) has been developed and used to study water-silica interfaces[42]. ReaxFF was originally developed by van Duin, Goddard, and coworkers and then reparametrized by Yeon and van Duin to improve the description of water-silica systems [43-45]. ReaxFF describes bond breakage and formation in the water-silica systems due to the calculation of bonding states based on interatomic distances[45]. The bond order based potential revaluates bonding environments at each MD step, allowing for smooth transitions from bonded to unbonded systems. In addition to accurately reproducing complex structural features, the ReaxFF potential has also been used to

simulate dynamic properties, such as diffusion [42]. The use of the ReaxFF force field in this work allows for simulation of the dynamic heterogeneous nanoporous silica gel structures.

In this work, atomistic silica gels models are formed from two different protocols, one to mimic multicomponent glass dissolution, to provide a unique avenue to understand how the initial structure of a glass can impact the resulting silica gel, and the other from hydrogarnet defect formation from bulk amorphous silica. Hydrogarnet defect is formed by substituting $4H^+$ with Si^{4+} and is the most prevalent structural defect of water uptake in quartz, the stable crystalline form of SiO_2, under equilibrium conditions, as evidenced from both experimental and theoretical studies [46, 47]. This represents one of the first atomistic classical MD models which accounts for remnant silica structures in the development of silica-rich gels, and is critical to the development of silica gel models to understand dissolution processes.

2. Methods

2.1 Protocol for silica gel formation

The first method of silica gel formation mimics hydrogarnet defect formation by removing individual silicon from dense silica, since silica dissolves through successive removal of SiO_4 tetrahedral [48, 49]. Similar methods were used in silica models of molecular sieves, but did not consider the development of surface silanols (Si-OH) or hydration [50]. A dense silica model was selected for the base structure (Fig.1.a). To create the 3000 atom model system the parallel MD simulation package DL_POLY was used, with cubic periodic boundary conditions [51]. A partial charge pair wise potential with a long-range columbic interaction and a short range interaction in the Buckingham form was used, which has been previously applied to silicate glass simulations by Du and Cormack [52, 53]. A randomized initial configuration containing 1000 Si atoms and 2000 O atoms was heated to 4000K and then cooled to 300K at a rate of -5K/ps to form a dense silica structure. All other simulations, after the creation of the silica, used the ReaxFF forcefield (Section 2.2).

As hydrogarnet defect formation (DSG) is the most prevalent form of water update in silica (quartz) under equilibrium conditions[46], nanoporous silica gel structures were also created by introducing hydrogarnet defect in dense amorphous silica structure generated from MD simulations. In this process, silicon atoms were randomly removed forming non-bridging oxygens (NBOs) which were then terminated with hydrogen to create silanol groups. Of the

1000 silicon atoms present either 20%, 40%, or 60% were removed to control the connectivity, with the resulting nanoporous silica containing 400 silicon (DSG-400), 600 silicon (DSG-600), or 800 silicon (DSG-800). For hydration a box of water molecules with a density of 1 g/cm^3 was overlaid on the nanoporous silica and water molecules within 1Å of original system or outside the simulation cell were removed, forming a hydrated silica gel. Coordinates for the DSG silica gel structures are included in Supporting Information.

In the second method the silica remnant of a multicomponent glass structure is used as the base of the silica gel, since dissolution forms interfacial layers by the removal of soluble species [10]. Here a simplified international simple glass composition (sISG) was used containing boron, aluminum, silicon, sodium, and low concentrations of CaoO and ZrO_2 (1.7 mole%), incorporated into the Na_2O and SiO_2 components respectively (Table 1). The simulation of the international simple glass (ISG) [54] composition is not possible with currently available forcefields (including ReaxFF), necessitating the simplification of the composition (Table 1). The selected Deng-Du forcefield [39] has not been parameterized for water-surface interactions, and is therefore only applied in the generation of the initial multicomponent models.

sISG glass models (Fig.2.a) consisting of ~3000 atoms were created from a melt and quench procedure followed by removal of sodium, boron, and aluminum species [9, 55]. During sodium, boron, and aluminum removal NBO defects were formed and then hydrogen terminated to form silanol groups. Extra free oxygen generated during the removal of network modifiers were removed. The nanoporous silica was hydrated by overlaying a box of water molecules on the system and removing overlapping atoms, forming a silica gel (Fig.1.b). Coordinates for the RSG silica gel structures are included in Supporting Information.

Table 1: International simple glass (ISG) composition and the simplified ISG composition used as the initial conditions for creation of the remnant silica gel (RSG) systems [54].

	Composition (mole %)						Al/B Ratio	Density (g/cm^3)
	SiO_2	B_2O_3	Na_2O	Al_2O_3	CaO	ZrO_2		
ISG	60.2	16.0	12.6	3.8	5.7	1.7	0.24	2.50*
sISG	61.8	16.0	18.4	3.8	0.0	0.0	0.24	2.49

*Archimedes method [56]

2.2 Reactive force field (ReaxFF) based MD simulations

Classical MD simulations were performed using the dissociative water-silica potential ReaxFF, developed by van Duin, Goddard, and coworkers and parametrized by Yeon and van

Duin [43-45]. ReaxFF accurately simulates bond breakage and formation in water-silica systems due to the identification of bonding states based on interatomic distances[45]. The number of bonds is revaluated between frames, allowing for smooth transitions from bonded to unbonded systems. All of the parameters used to calculate the system energy decrease smoothly with distance, avoiding sudden step-wise changes in energy [43, 45]. Here, ReaxFF was implemented in the open source code LAMMPS, a classical MD code distributed by Sandia National Laboratories [57]. After the DSG and RSG systems were created, classical MD simulations using the ReaxFF forcefield were performed for 100ps using a 0.25 fs time step to allow for structural relaxation. The temperature (T) was controlled at 300K through a Nosé-Hoover thermostat with a damping time of one hundred time steps. The number (N) of atoms and the simulation volume (V) was also controlled through a canonical (NVT) ensemble.

2.3 Analysis methods

Bond distance and angle data were collected from 25,000 snapshots of the silica gel from the last 50ps of the NVT simulations. Bond angle distribution (BAD) and pair distribution functions (PDF) include variations from the amorphous structure and thermal vibrations, and are reported with the peak location and the the full-width-half-max (FWHM) values. PDF or BAD peak values were normalized due to the changing number of water molecules in the system. Oxygen atoms in the silica and water were separated for analysis by coordination using a 2.25Å cut-off. Geometric parameters were also used to identify hydrogen bonds (H-bonds) by using O_w-O_s (oxygen in water and in a silanol group respectively) distance of less than 3.2Å and O_s-H_s (hydrogen in a silanol group) distances of less than 2.6Å. This method is consistent with the interatomic distances used for identification of H-bonds by several previous authors [58, 59].

Diffusion coefficients were calculated from the atomic positions in a 50ps trajectory recorded every 2fs. The translational diffusion is calculated, which considers only atomic movement through the x-y plane, rather than diffusion of the water molecules in all three dimensions. The mean squared displacement (MSD) was calculated from Eq. 1 with $x_i(0)$ as the position of particle "i" at time equal to 0, $x_i(t)$ as the position of the same particle at time equal to t, and n as the total number of atoms in the system [60]:

$$MSD = \frac{1}{n}\langle\sum_{i=1}^{n}|x_i(0) - x_i(t)|^2\rangle \quad (1)$$

The Einstein diffusion equation (Eq. 2) was used for calculation of the diffusion coefficient [60]:

$$D = \frac{1}{6}\lim_{t\to\infty}\frac{d}{dt}\langle|x_i(0) - x_i(t)|\rangle \quad (2)$$

All analysis of the silica gel was performed in triplicate with values reported as the standard error (SE) unless otherwise noted. SE is calculated using Eq. 3, with SD as the standard deviation and n as the number of observations/iterations.

$$SE = \frac{SD}{\sqrt{n}} \quad (3)$$

3. Results and Discussion

3.1 Short-range structure

Silica gels are hydrated nanoporous silica composed of interconnected SiO_4 tetrahedron surrounded by water, with silicon concentration varying between 40%-80% in the DSG systems. In comparison the RSG structure is composed of ~60% silicon, with all other network modifiers (boron and aluminum) removed (Table 2). Here, the short range features of the silica gel models are discussed to highlight differences in water structuring between the two model systems. The composition of the nanoporous silica backbone is consistent between the two methods of gel development (Table 3). The extended Si-O-H bond angle of ~124° compared to experiment is a feature of the ReaxFF forcefield [61]. A ~4° variation in the Si-O-Si bond angle also occurs, but is within the range of values reported experimentally [62-64]. Some Si-O-Si bond angle variation may be due to the intermediate range structure [65, 66], discussed elsewhere in the manuscript.

Table 2: System size, composition and density for de-polymerized silica gel (DSG) and remnant silica gel (RSG) structures

Structure	DSG-400	DSG-600	DSG-800	RSG
Density (g/cm^3)	1.25±0.00	1.57±0.00	1.91±0.00	1.62±0.01
Remaining Si (%)	40.0	60.0	80.0	60.9
Total Si (atoms)	400	600	800	618
Si/O Ratio*	0.191±0.000	0.290±0.000	0.384±0.005	0.312±0.006

*****Includes all silicon and oxygen atoms in the system, including oxygen from water molecules

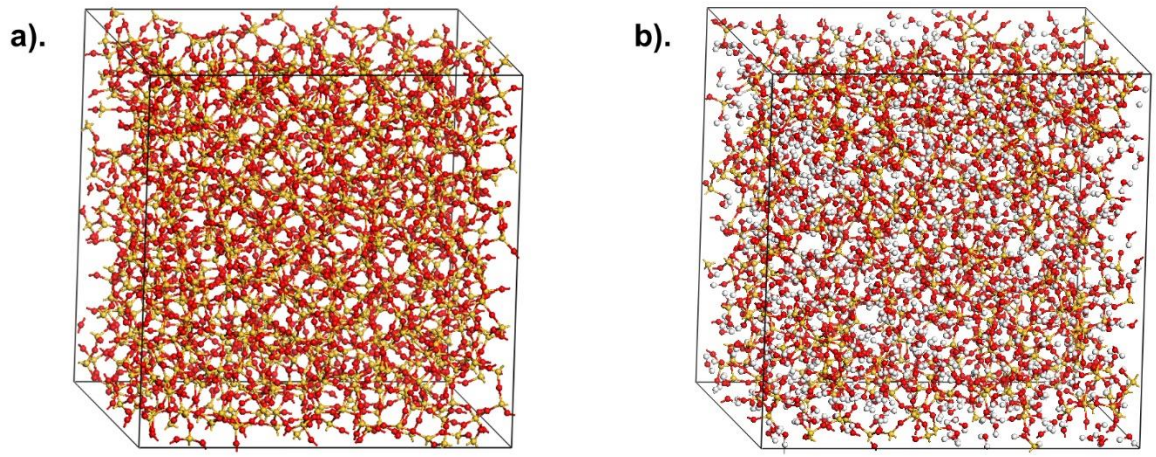

Figure 1: Snapshots of (a) dense silica (b) final DSG-600 structure. Colors: O (red), Si (yellow), H (white)

Table 3: Interatomic distances and bond angles for the silica backbone structure of the de-polymerized silica gel (DSG) and remnant silica gel (RSG) from the peak of the bond angle distribution and pair distribution function with the full-width-half-max in parenthesis.

	Interatomic Distance (Å)			Bond Angle (degree)		
	Si-O	O-O	Si-Si	O-Si-O	Si-O-Si	Si-O-H
DSG-400	1.58 (0.14)	2.59 (0.31)	3.09 (0.16)	109 (17)	155 (29)	124 (11)
DSG-600	1.58 (0.15)	2.60 (0.32)	3.10 (0.17)	109 (18)	156 (28)	124 (11)
DSG-800	1.58 (0.14)	2.58 (0.33)	3.10 (0.18)	108 (18)	154 (29)	124 (11
RSG	1.58 (0.11)	2.59 (0.25)	3.11 (0.13)	109 (14)	158 (25)	124 (11)
SiO_2	1.58 (0.11)	2.55 (0.26)	3.06 (0.14)	108 (16)	152 (22)	-
Expt.	1.61[a]	2.65[b]	3.1[c]	109.4[b]	148[d] 153[b]	118.1[e]

[a]Neutron diffraction [67] [b]Electron diffraction [64] [c]X-ray scattering [68] [d]Nuclear magnetic resonance[66] [e]DFT with 6-31G** Gaussian basis set

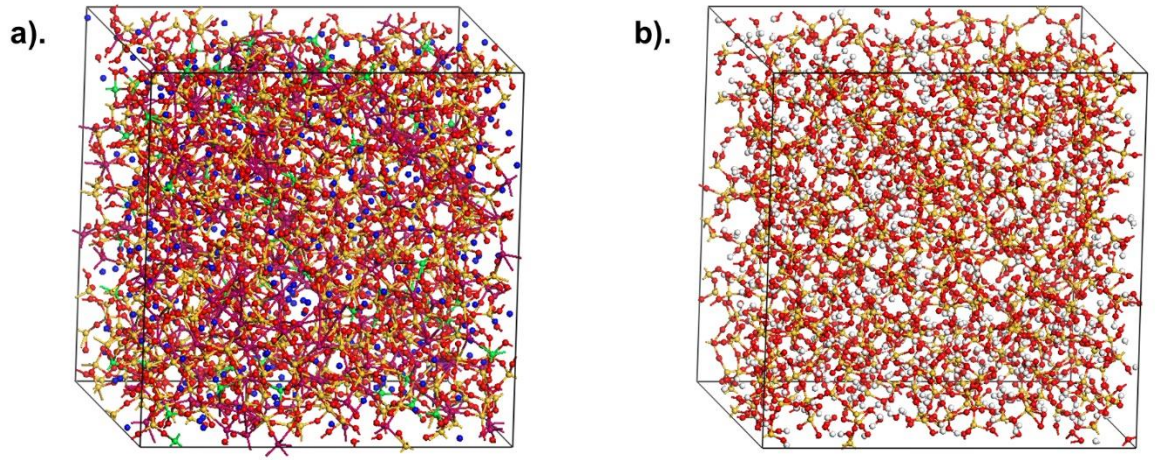

Figure 2: Snapshots of the formation of (a) simplified international simple glass (sISG) and (b) final RSG structure. Colors: O (red), Si (yellow), H (white), Al (green), B (purple), Na (blue)

Structuring of water inside the gel impacts diffusion and reactivity, and has been suggested as a factor in the protective nature of the alteration layers formed during dissolution. In these models the O_w-H_w-O_w bond angles (Fig.3.a) and O_w-O_w interatomic distances (Fig.3.b) exhibit the most variability with the O_w-H_w (0.97Å) and H_w-H_w (1.52Å) interatomic distances and H_w-O_w-H_w bond angles (103º) consistent with experiment. Shorter O_w-O_w bond distances of 2.73±0.02Å are indicative of interfacial structured water which forms within 10Å of a surface identified by proton NMR and neutron diffraction [24, 26, 69-72]. In the DSG systems the O_w-O_w interatomic distances decrease from 2.92Å to 2.78Å with increasing silica concentration, compared to ~2.85Å in bulk water. The contraction of the O_w-O_w PDF for the RSG system is more distinct, with a pre-peak located at ~2.69Å indicating a unique pore structure of the RSG (Fig.3.b). The pre-peak in the RSG system may indicate that the water is either strongly confined, leading to the pre-peak in the O_w-O_w PDF, or in more open diffusive geometries, creating two separate peaks in the PDF. Similar behavior is seen in partially confined water, with slightly contracted O_w-O_w PDF's and a second peak at ~4.0Å for confinement between plates 7.4-8.6Å apart[73]. Further investigation of the complex H-bond networks present in silica gels would be beneficial to understand the role of water confinement in complex geometries.

The O_w-H_w-O_w bond angle is commonly used to identify structured water, with values as low as 139º and as high as 164º depending on the amount of confinement [74, 75]. The O_w-H_w-O_w PDF are all contracted by 4-10% compared to bulk water with the RSG system exhibiting an O_w-H_w-O_w PDF peak value only 7º different than bulk water. Decreasing O_w-H_w-O_w angles have been reported for confined water, for example a ~150 º O_w-H_w-O_w bond angle for water confined between two planes 6.6Å apart [75], providing further evidence for nanoconfined water in complex silica gel systems. No change in the H_w-O_w-H_w bond angle from 104º occurred in any of the simulations, indicating that true hexagonal ice, with a H_w-O_w-H_w bond angle of 109º, is not formed [76, 77]. The structuring of the water in the silica gel effects on the diffusion coefficient of water in the gel and resulting reactivity, which is discussed in subsequent sections.

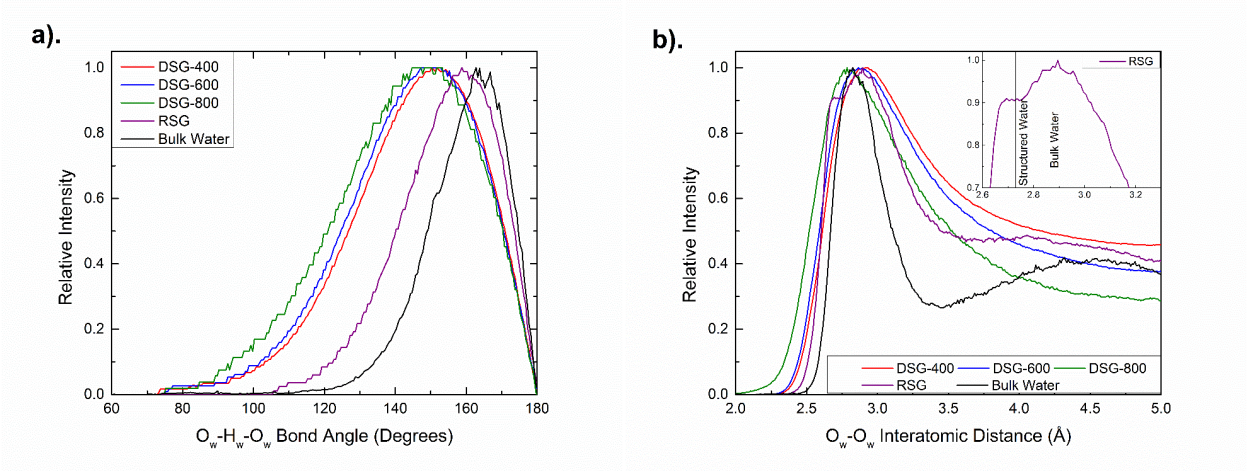

Figure 3: (a) O_w-H_w-O_w bond angle distribution and (b) O_w-O_w pair distribution function (PDF) for silica gel structures [71].

3.2 Connectivity and intermediate range structures

Connectivity of the silica gel alters its stability and reactivity due changing activation energies for Si-O bond breakage due to the number of bridging oxygen bonded to the central silicon atom (Q_n distribution with n as the number of bridging oxygen). In the DSG-800 structure, which has the highest silica concentration, the primary Q_n species is a Q_3 which decreases to Q_2 in the DSG-600 and Q_1 in the DSG-400 structure (Fig.4.a). The RSG structure has a broader peak in the Q_n distribution at ~36% for the Q_2 and Q_3 species (Fig.4.b). The similarity in the Q_2 and Q_3 concentration is partially due to the silica remnant of the sISG model, which contains 36.7% Q_2 species and 34.0% Q_3 species (Fig.4.b). The higher Q_3 concentration results in an increased connectivity of 2.40±0.01 compared to 2.24±0.02 for the DSG-600 system with comparable silica concentration. Previous computational investigations have indicated that the Q_2 and Q_3 species in silica are more stable than the Q_1 and Q_4 species [48, 78], and the higher Q_2 and Q_3 concentrations in the RSG models suggest that the structure would be more stable than comparable DSG systems. An increased concentration of Q_3 species develops in the sISG model, and consequently the RSG structure due to the initial Na^+ concentration which modifies the network through the formation of Q_3 species[9]. Stable concentrations of Q_2 and Q_3 have been reported in experimental silica gels due to retaining Ca^{2+} or Na^+ ions in the glass [9, 79]. With additional extended simulations (100+ ns) we hypothesize a complete transition from Q_3 species to Q_4 or Q_2 [9, 79]. Therefore, the silica gels inherit part of the silica connectivity from the multicomponent glasses structures from which the structures are developed.

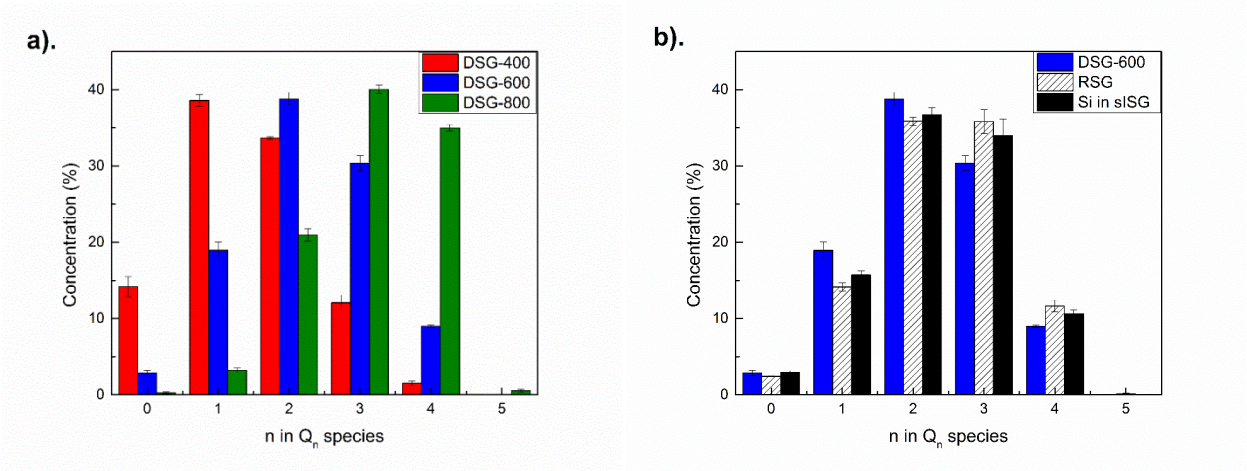

Figure 4: Q_n distribution of (a) de-polymerized silica gel (DSG) and (b) remnant silica gel (RSG) systems and silica component of the simplified international simple glass (sISG) structure.

Intermediate range structures of glasses are analyzed by the ring size distribution, identified by the number of silicon in a ring, with dense silica composed primarily of seven-membered rings [63]. Peak shifts from seven-membered to six- and five-membered rings have been previously identified in nanoporous silica, and continues here (Fig.5.a) [37]. The silica ring concentration in the sISG model used as the basis of the RSG identifies that features of the original structure persist into the RSG system (Fig. 5.b). In both the RSG and the sISG system five-membered rings exhibit the highest concentration, compared to a six-membered ring peak in the DSG-600 system with similar silica concentration. In Fig.5.b the ring size distribution of the silicon atoms in the sISG model indicates a strong five-membered ring peak. Computational silica gel models developed using sol-gel methods identified five-membered rings as an intermediate step in the formation of an interconnected silica network [80, 81], suggesting condensation of the silicon species in the RSG, which is not present in the DSG system. Overall, the RSG system inherits some of the intermediate range order from the multicomponent glass structure, creating a unique structure when compared with DSG systems.

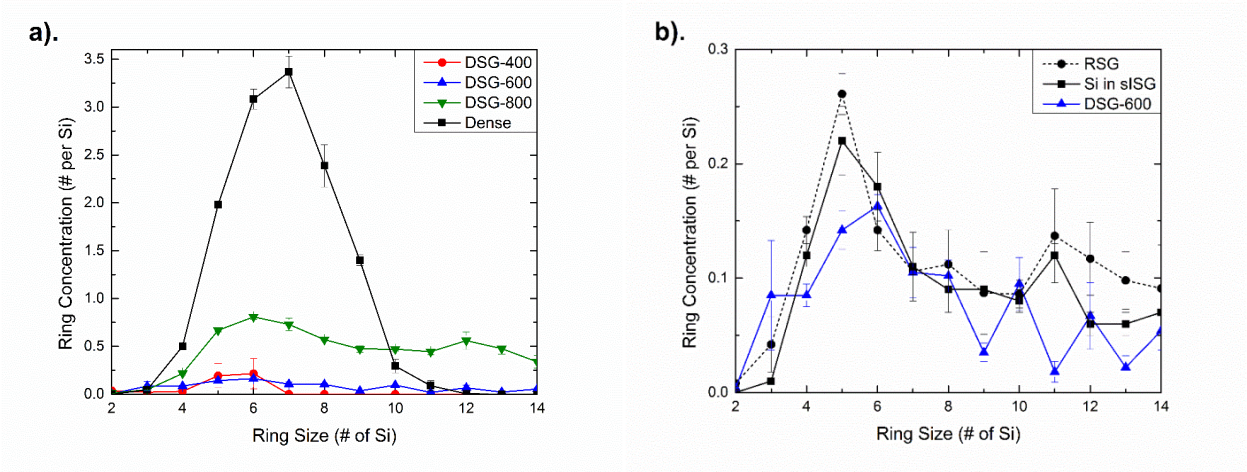

Figure 5: Ring size distribution of (a) de-polymerized silica gel (DSG) and (b) remnant silica gel (RSG) structures and the silica component of simplified international simple glass (sISG) system.

Pore size distributions were also calculated to identify structural differences in the gel between the DSG and RSG systems. The distribution of pore diameters (Fig.6) inside the system is calculated using the method by Bhattacharya and Gubbins [82]. The DSG-400 model with the lowest concentration of silicon has the broadest distribution of pore sizes with the highest concentration of ~4Å pores. The DSG-600 and RSG systems, which contain the same number of silicon (Table 1) exhibit significantly different pore structures, with the RSG systems having a peak pore size of 3.6Å in diameter. In comparison, the DSG-600 system has a much broader distribution of pore sizes indicating that the defect formation process creates more connected pores and a more fragmented silica network. This microstructural differences indicates that the pore structure develops differently in systems which begin with either a dense silica gel or a multicomponent oxide. Overall, the intermediate range order of silica gel systems formed from the multicomponent glass structure and depolymerized process are distinct. Future attempts to create realistic silica gel structures should consider the structure of the original multicomponent glass composition.

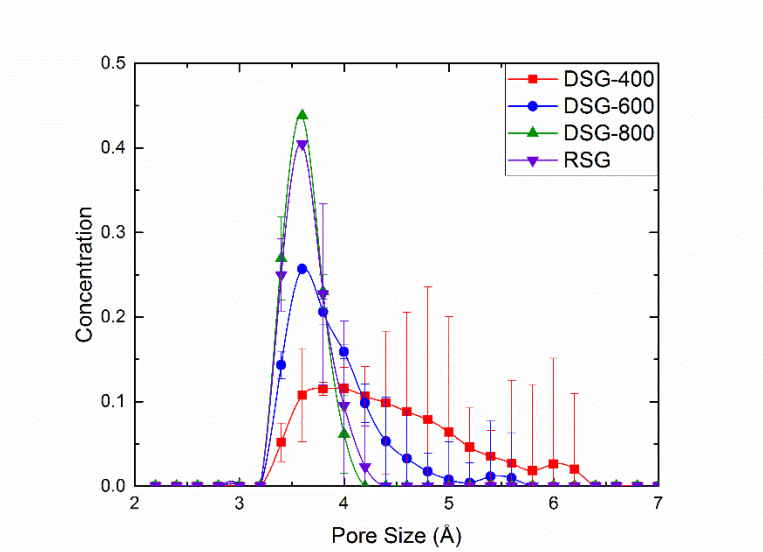

Figure 6: Pore size distribution in silica gel structures. Error bars are the standard deviation of three different gel structures.

3.3 Diffusion inside silica gels

Diffusion coefficients of water in the RSG system exhibit typical nanoconfined behavior, with hydrogen diffusion (D_H) rates below bulk water (Table 4). Limited diffusivity maybe due to structure of confined water, forming H-bond networks adjacent to the surface [83], as suggested by earlier PDF analysis. Due to the complex porosity in the RSG systems most water molecules fall into this interfacial region, resulting in low diffusion coefficients. In Fig.7.a and Fig.8.a visualization of the water diffusion pathways demonstrate that in the RSG systems the water molecules are trapped inside the pore structure and limited diffusion occurs. It is expected that, after further dissolution of the regions between the confined pores, the pores in the RSG system will become connected. In the DSG systems increasing fragmentation results in D_H values from $6.29 \cdot 10^{-5}$ cm^2/s in DSG-400 to $0.39 \cdot 10^{-5}$ cm^2/s in the DSG-800 models. D_H values in the DSG-400 system are on the order of bulk water diffusion, indicating the rapid diffusion of water throughout the system. Increased diffusion can be connected with the diffusion of silica, the Q_0 concentration and the hydrogen-bond network inside the porous structure.

The highly fragmented nanoporous silica structures (DSG-400) may be developing a water-silica suspension, rather than a stable nanoporous gel through which the water diffuses, leading to high water diffusion coefficients. In these models not only are D_H values elevated in the DSG-400 system, but so are the D_{Si} values, which are between $1.0 \cdot 10^{-5}$ cm^2/s to $2.0 \cdot 10^{-8}$ cm^2/s, higher

than the diffusion coefficient of silicon in silica of 10^{-15} cm^2 (800K) [84]. SiO_4H_4 molecules diffuse at a rate of $2.2 \cdot 10^{-5}$ cm^2/s, comparable to the diffusion of silica in the DSG-400 system (Fig.9.a) [85-88]. Additional theoretical investigations identify increased diffusion of silica dimer and trimers as well, in comparison to fully connected network silicon [85]. Here, D_{Si} increases with Q_0 concentration (Fig.9.b) approaching the experimental rate for dissolved silica in water in the DSG-400 system [88]. In a stable silica system with water diffusing through the pores a high D_H/D_{Si} value is expected, and in the DSG-800 model the ratio is ~195 (Table 4) indicating the stability of the silica backbone. In the DSG-400 structure the D_H/DSi is 6.2 suggesting that this low-density gel is comparable to a silica-water suspension, with increased water diffusion occurring due to changes in the viscosity and intermolecular forces [89].

A second compounding factor is the stability of the H-bond network inside the gel [90]. Silanols are predicted to have a H-bond concentration of ~2, with one bond from adsorbed water and the other from adjacent silanols [91]. Calculation of H-bonds contributed by adsorbed water indicates a decreasing concentration from 0.50±0.02 H-bond/silanol in the DSG-400 system to 0.20±0.02 H-bond/silanol in the DSG-800 system (Table 4) indicating an incomplete H-bond network. The RSG system exhibits similarly low concentrations of H-bonds at 0.20±0.02 H-bonds/silanol, below the DSG-600 system with comparable silicon concentrations. The differences in the characteristics of the H-bonds at low concentrations may have an impact on water diffusion through the system, as high H-bond concentrations facilitate water movement by allowing for water hopping through the structure. Movement of silica fragments would exacerbate this affect as the H-bond network is continually disrupted, resulting in water diffusion to reform the network. Further investigation of the water network within a highly variable and unordered silica structure would provide insight into the effect of H-bond saturation on water diffusion.

Ultimately, the differences in the structure of the silica gel models have an impact on the diffusion coefficients, with the RSG system exhibiting slower diffusion associated with nanoconfinement. Therefore, the underlying framework of the silica in the gel imparted by the original ISG composition creates a more interconnected structure than randomly created gels, and lowers the diffusion coefficient. The DSG-600 and RSG systems, with comparable silicon concentrations, exhibit significant differences in the diffusive properties, indicating that the structure will be critical in forming an accurate silica gel model which accounts for changing

diffusion. Future investigations of silica gels formed on the surface of multicomponent glasses will need to consider the role of the original glass composition when creating realistic structure models, due to the impact on the diffusional properties.

Table 4: Diffusion coefficients of hydrogen (D_H) and oxygen (D_O) in the water molecules as well as the silicon (D_{Si}) in the de-polymerized silica gel (DSG) and remnant silica gel (RSG).

	DSG-400	DSG-600	DSG-800	RSG	Water
D_{Si} (10^{-5} cm^2/s)	1.01±0.07	0.07±0.02	0.002±0.002	0.019±0.01	-
D_H (10^{-5} cm^2/s)	6.29±0.26	2.11±0.31	0.39±0.31	0.66±0.29	2.94±0.39
D_H/D_{Si}	6.2	30.1	195.0	34.7	-
Pore Size (Å)	4.0±1.7	3.6±0.8	3.6±0.6	3.6±0.6	-
Hydrogen Bonds (per Si-OH)	0.50±0.02	0.34±0.01	0.22±0.01	0.20±0.02	-

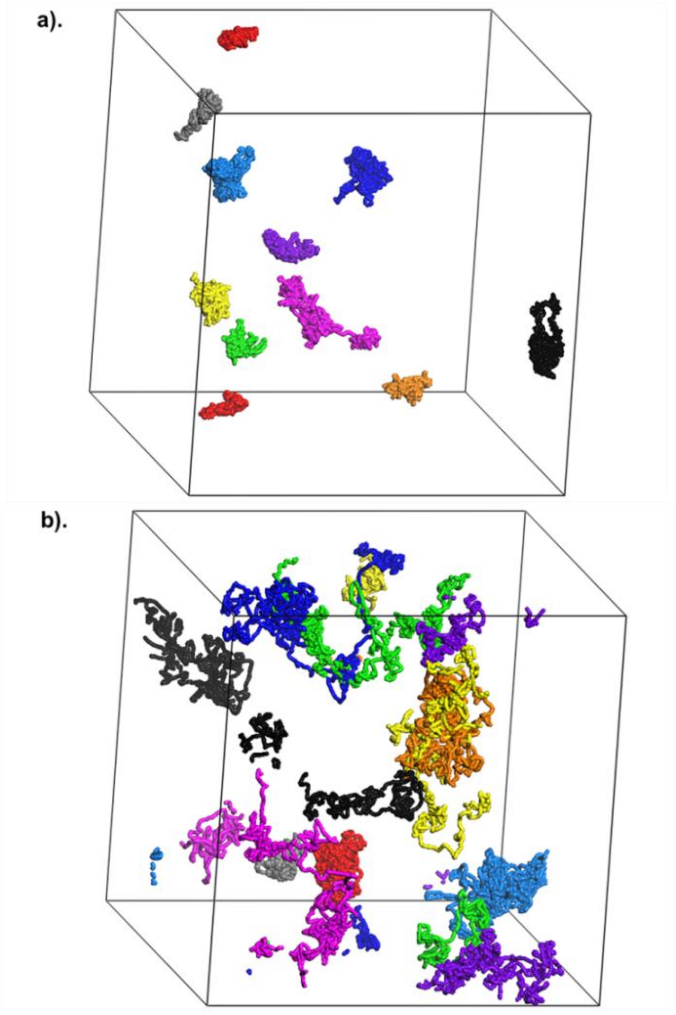

Figure 7: Diffusion pathways of water molecules in the 50ps of simulation time at 300K inside (a) remnant silica gel (RSG) and (b) de-polymerized silica gel (DSG-600) systems. Different colors represent different water molecules.

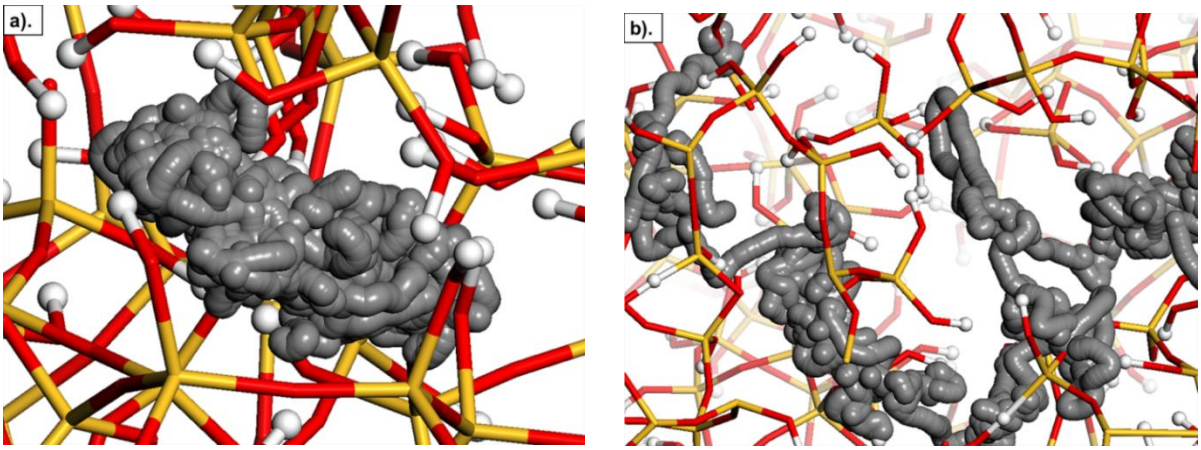

Figure 8: Snapshots of water diffusion pathways in (a) remnant silica gel (RSG) and (b) the de-polymerized silica gel (DSG-600) system. Colors: Si (yellow) O (red) H (white), diffusion pathway (gray)

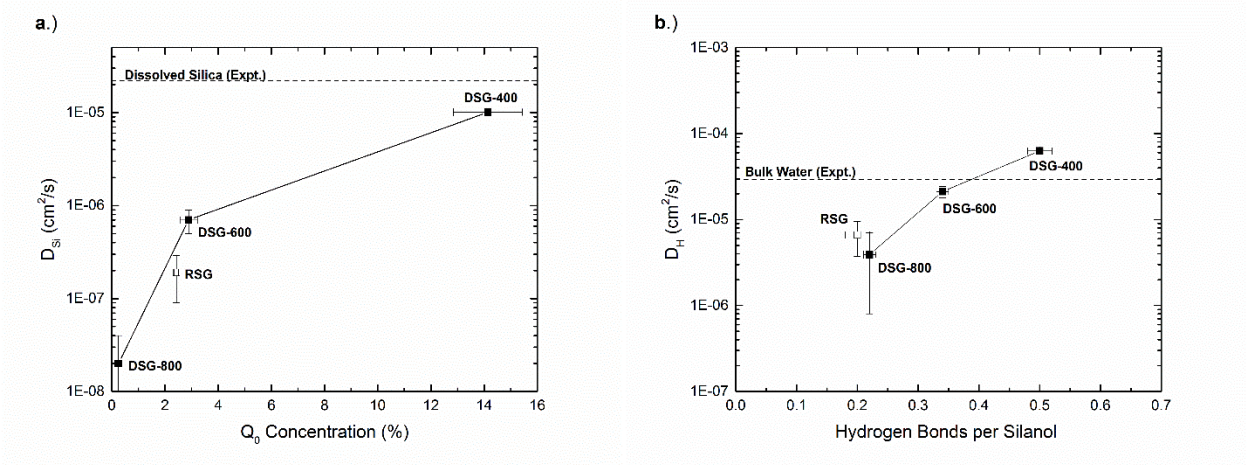

Figure 9: (a) Silicon diffusion coefficient (D_{Si}) in silica gel structures with Q_0 concentration and (b) hydrogen diffusion (D_H) in water molecules with average hydrogen bond per silanol.

4. Conclusions

Silica gel models which mimic the interfacial layers formed during the dissolution of silicates in aqueous solutions were created using Reactive Force Field based molecular dynamics. Two different models were created, one is the silica remnant of a sodium boroaluminosilicate glass (RSG) and the other one is the fragmented dense silica structure which mimics hydrogarnet defect formation by the random removal of silicon (DSG). The RSG systems exhibit higher concentrations of Q_3 species and five-membered rings due to the silica network structure in the original multicomponent glass. In contrast the DSG models with comparable silica concentration exhibits lower connectivity and a more fragmented silica gel

with less intermediate range structure. The remnant gel structures also have small pore sizes and exhibited narrower pore size distributions. Water diffusion coefficients in RSG are significantly lower than in the DSG systems, possibly due to nanoconfinement of water molecules within the porous silica structure with closed and isolated pores. In the DSG models the high fragmentation of the silica structure resulted in structures with more open and connected pores, resulting in increased water diffusion. These results suggest that additional steps of silica backbone dissolution is required to create more connected pores and make water diffusion in the remnant structure possible to reach the reaction front of pristine glasses. Due to the differences in the connectivity and intermediate range structure and their effect on the diffusivity of the system, microstructure of pore morphology is critical for the gel structure development in future understanding the dissolution behaviors especially the residual rates of glass dissolution.

Corresponding Author
*E-mail: du@unt.edu

Notes
The authors declare no competing financial interest.

Supporting Information
Supporting information includes the coordinates for the DSG and RSG silica gel systems.

Acknowledgements

This work is supported by the Department of Energy Nuclear Energy University Project under Project No. 13-5494 and the Center for Performance and Design of Nuclear Waste Forms and Containers, an Energy Frontier Research Center funded by the U.S. DOE, Office of Science, Basic Energy Sciences under Award # DESC0016584, for supporting subsequent data analysis and preparation of this manuscript. J.M. Rimsza acknowledges that this material is based on work supported by the National Science Foundation Graduate Research Fellowship Program under Grant No. DGE-114248. Computational resources are provided by the University of North Texas high performance computing cluster.

Graphical Abstract

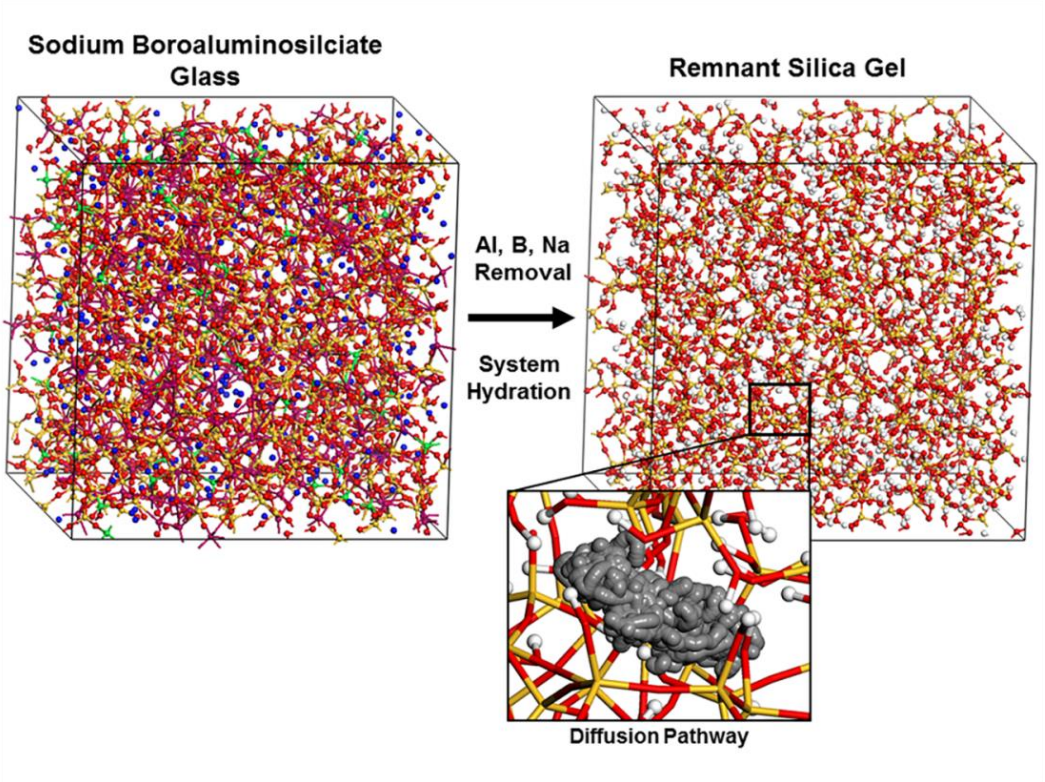

References

(1) Li, P.; Ohtsuki, C.; Kokubo, T.; Nakanishi, K.; Soga, N.; Nakamura, T.; Yamamuro, T. Apatite Formation Induced by Silica Gel in a Simulated Body Fluid. *J Am Ceram Soc* **1992**, *75*, 2094-2097.

(2) Cho, S.; Nakanishi, K.; Kokubo, T.; Soga, N.; Ohtsuki, C.; Nakamura, T.; Kitsugi, T.; Yamamuro, T. Dependence of Apatite Formation on Silica Gel on its Structure: Effect of Heat Treatment. *J Am Ceram Soc* **1995**, *78*, 1769-1774.

(3) Adeyemo, A.; Kumar, R.; Linga, P.; Ripmeester, J.; Englezos, P. Capture of Carbon Dioxide from Flue Or Fuel Gas Mixtures by Clathrate Crystallization in a Silica Gel Column. *Int. J. Greenhouse Gas Control* **2010**, *4*, 478-485.

(4) Leal, O.; Bolívar, C.; Ovalles, C.; García, J. J.; Espidel, Y. Reversible Adsorption of Carbon Dioxide on Amine Surface-Bonded Silica Gel. *Inorg. Chim. Acta* **1995**, *240*, 183-189.

(5) Siouffi, A. Silica Gel-Based Monoliths Prepared by the Sol–gel Method: Facts and Figures. *J. Chromatogr. A* **2003**, *1000*, 801-818.

(6) Nakanishi, K.; Minakuchi, H.; Soga, N.; Tanaka, N. Double Pore Silica Gel Monolith Applied to Liquid Chromatography. *J. Sol Gel Sci. Technol.* **1997**, *8*, 547-552.

(7) Riego, J. M.; Sedin, Z.; Zaldívar, J.; Marziano, N. C.; Tortato, C. Sulfuric Acid on Silica-Gel: An Inexpensive Catalyst for Aromatic Nitration. *Tetrahedron Lett.* **1996**, *37*, 513-516.

(8) Shi, F.; Zhang, Q.; Li, D.; Deng, Y. Silica-Gel-Confined Ionic Liquids: A New Attempt for the Development of Supported Nanoliquid Catalysis. *Chem. Eur. J.* **2005**, *11*, 5279-5288.

(9) Gin, S.; Guittonneau, C.; Godon, N.; Neff, D.; Rebiscoul, D.; Cabié, M.; Mostefaoui, S. Nuclear Glass Durability: New Insight into Alteration Layer Properties. *J. Phys. Chem. C* **2011**, *115*, 18696-18706.

(10) Gin, S.; Jollivet, P.; Fournier, M.; Angeli, F.; Frugier, P.; Charpentier, T. Origin and Consequences of Silicate Glass Passivation by Surface Layers. *Nat. Comm.* **2015**, *6*.

(11) Geisler, T.; Nagel, T.; Kilburn, M. R.; Janssen, A.; Icenhower, J. P.; Fonseca, R. O.; Grange, M.; Nemchin, A. A. The Mechanism of Borosilicate Glass Corrosion Revisited. *Geochim. Cosmochim. Acta* **2015**, *158*, 112-129.

(12) Cailleteau, C.; Angeli, F.; Devreux, F.; Gin, S.; Jestin, J.; Jollivet, P.; Spalla, O. Insight into Silicate-Glass Corrosion Mechanisms. *Nat. Mat.* **2008**, *7*, 978-983.

(13) Cailleteau, C.; Weigel, C.; Ledieu, A.; Barboux, P.; Devreux, F. On the Effect of Glass Composition in the Dissolution of Glasses by Water. *J. Non Cryst. Solids* **2008**, *354*, 117-123.

(14) Jollivet, P.; Angeli, F.; Cailleteau, C.; Devreux, F.; Frugier, P.; Gin, S. Investigation of Gel Porosity Clogging during Glass Leaching. *J. Non Cryst. Solids* **2008**, *354*, 4952-4958.

(15) Rebiscoul, D.; Van der Lee, A.; Rieutord, F.; Né, F.; Spalla, O.; El-Mansouri, A.; Frugier, P.; Ayral, A.; Gin, S. Morphological Evolution of Alteration Layers Formed during Nuclear Glass Alteration: New Evidence of a Gel as a Diffusive Barrier. *J. Nucl. Mater.* **2004**, *326*, 9-18.

(16) Munier, I.; Crovisier, J.; Grambow, B.; Fritz, B.; Clément, A. Modelling the Alteration Gel Composition of Simplified Borosilicate Glasses by Precipitation of an Ideal Solid Solution in Equilibrium with the Leachant. *J. Nucl. Mater.* **2004**, *324*, 97-115.

(17) Brinker, C.; Kirkpatrick, R.; Tallant, D.; Bunker, B.; Montez, B. NMR Confirmation of Strained "defects" in Amorphous Silica. *J. Non Cryst. Solids* **1988**, *99*, 418-428.

(18) Casey, W. H.; Westrich, H. R.; Banfield, J. F.; Ferruzzi, G.; Arnold, G. W. Leaching and Reconstruction at the Surfaces of Dissolving Chain-Silicate Minerals. *Nature* **1993**, *366*, 253-256.

(19) Angeli, F.; Charpentier, T.; Gin, S.; Petit, J. 17 O 3Q-MAS NMR Characterization of a Sodium Aluminoborosilicate Glass and its Alteration Gel. *Chem. Phys. Lett.* **2001**, *341*, 23-28.

(20) Gupta, P. K.; Meuwly, M. Dynamics and Vibrational Spectroscopy of Water at Hydroxylated Silica Surfaces. *Faraday Discuss.* **2013**, *167*, 329-346.

(21) Gouze, B.; Cambedouzou, J.; Parrès-Maynadié, S.; Rébiscoul, D. How Hexagonal Mesoporous Silica Evolves in Water on Short and Long Term: Role of Pore Size and Silica Wall Porosity. *Microporous Mesoporous Mater.* **2014**, *183*, 168-176.

(22) Takamuku, T.; Yamagami, M.; Wakita, H.; Masuda, Y.; Yamaguchi, T. Thermal Property, Structure, and Dynamics of Supercooled Water in Porous Silica by Calorimetry, Neutron Scattering, and NMR Relaxation. *J. Phys. Chem. B* **1997**, *101*, 5730-5739.

(23) Li, I.; Bandara, J.; Shultz, M. J. Time Evolution Studies of the H2O/Quartz Interface using Sum Frequency Generation, Atomic Force Microscopy, and Molecular Dynamics. *Langmuir* **2004**, *20*, 10474-10480.

(24) Pajzderska, A.; Bilski, P.; Wąsicki, J. Phase Diagram of Water Confined in MCM-41 Up to 700 MPa. *J. Chem. Phys.* **2015**, *142*, 084505.

(25) Rosenstihl, M.; Kämpf, K.; Klameth, F.; Sattig, M.; Vogel, M. Dynamics of Interfacial Water. *J. Non Cryst. Solids* **2015**, *407*, 449-458.

(26) Bonnaud, P.; Coasne, B.; Pellenq, R. J. Molecular Simulation of Water Confined in Nanoporous Silica. *J. Phys.: Condens. Matter* **2010**, *22*, 284110.

(27) Hou, D.; Zhao, T.; Ma, H.; Li, Z. Reactive Molecular Simulation on Water Confined in the Nanopores of the Calcium Silicate Hydrate Gel: Structure, Reactivity, and Mechanical Properties. *J. Phys. Chem. C* **2015**, *119*, 1346-1358.

(28) Harrach, M. F.; Klameth, F.; Drossel, B.; Vogel, M. Effect of the Hydroaffinity and Topology of Pore Walls on the Structure and Dynamics of Confined Water. *J. Chem. Phys.* **2015**, *142*, 034703.

(29) Diallo, S. O. Pore-Size Dependence and Characteristics of Water Diffusion in Slitlike Micropores. *Phys. Rev. E* **2015**, *92*, 012312.

(30) Sendner, C.; Horinek, D.; Bocquet, L.; Netz, R. R. Interfacial Water at Hydrophobic and Hydrophilic Surfaces: Slip, Viscosity, and Diffusion. *Langmuir* **2009**, *25*, 10768-10781.

(31) Adeagbo, W. A.; Doltsinis, N. L.; Klevakina, K.; Renner, J. Transport Processes at α-Quartz–Water Interfaces: Insights from First-Principles Molecular Dynamics Simulations. *ChemPhysChem* **2008**, *9*, 994-1002.

(32) Sulpizi, M.; Gaigeot, M.; Sprik, M. The Silica–Water Interface: How the Silanols Determine the Surface Acidity and Modulate the Water Properties. *J. Chem. Theory Comp.* **2012**, *8*, 1037-1047.

(33) Roberts, A. P.; Garboczi, E. J. Elastic Properties of Model Porous Ceramics. *J Am Ceram Soc* **2000**, *83*, 3041-3048.

(34) Coquil, T.; Fang, J.; Pilon, L. Molecular Dynamics Study of the Thermal Conductivity of Amorphous Nanoporous Silica. *Int. J. Heat Mass Transfer* **2011**, *54*, 4540-4548.

(35) Miyoshi, H.; Hata, N.; Kikkawa, T. Theoretical Investigation into Effects of Pore Size and Pore Position Distributions on Dielectric Constant and Elastic Modulus of Two-Dimensional Periodic Porous Silica Films. *Jpn. Appl. Phys.* **2005**, *44*, 1166.

(36) Beckers, J.; De Leeuw, S. Molecular Dynamics Simulation of Nanoporous Silica. *J. Non Cryst. Solids* **2000**, *261*, 87-100.

(37) Rimsza, J.; Du, J. Structural and Mechanical Properties of Nanoporous Silica. *J Am Ceram Soc* **2014**, *97*, 772-781.

(38) Burlakov, V.; Briggs, G.; Sutton, A.; Tsukahara, Y. Monte Carlo Simulation of Growth of Porous SiO X by Vapor Deposition. *Phys. Rev. Lett.* **2001**, *86*, 3052.

(39) Deng, L.; Du, J. Development of Effective Empirical Potentials for Molecular Dynamics Simulations of the Structures and Properties of Boroaluminosilicate Glasses. *J. Non Cryst. Solids* **2016**, *453*, 177-194.

(40) Feuston, B.; Garofalini, S. Empirical Three-body Potential for Vitreous Silica. *J. Chem. Phys.* **1988**, *89*, 5818.

(41) Levine, S.; Garofalini, S. H. A Structural Analysis of the Vitreous Silica Surface Via a Molecular Dynamics Computer Simulation. *J. Chem. Phys.* **1987**, *86*, 2997.

(42) Fogarty, J. C.; Aktulga, H. M.; Grama, A. Y.; Van Duin, A. C.; Pandit, S. A. A Reactive Molecular Dynamics Simulation of the Silica-Water Interface. *J. Chem. Phys.* **2010**, *132*, 174704.

(43) Yeon, J.; van Duin, A. C. ReaxFF Molecular Dynamics Simulations of Hydroxylation Kinetics for Amorphous and Nano-Silica Structure, and its Relations with Atomic Strain Energy. *J. Phys. Chem. C* **2015**, .

(44) Van Duin, A. C.; Dasgupta, S.; Lorant, F.; Goddard, W. A. ReaxFF: A Reactive Force Field for Hydrocarbons. *J. Phys. Chem. A* **2001**, *105*, 9396-9409.

(45) Van Duin, A. C.; Strachan, A.; Stewman, S.; Zhang, Q.; Xu, X.; Goddard, W. A. ReaxFFSiO Reactive Force Field for Silicon and Silicon Oxide Systems. *J. Phys. Chem. A* **2003**, *107*, 3803-3811.

(46) McConnell, J.; Lin, J.; Heine, V. The Solubility of [4H] Si Defects in A-Quartz and their Role in the Formation of Molecular Water and Related Weakening on Heating. *Phys. Chem. Mater.* **1995**, *22*, 357-366.

(47) Lin, J.; Payne, M.; Heine, V.; McConnell, J. Ab Initio Calculations on (OH) 4 Defects in A-Quartz. *Phys. Chem. Miner.* **1994**, *21*, 150-155.

(48) Kagan, M.; Lockwood, G. K.; Garofalini, S. H. Reactive Simulations of the Activation Barrier to Dissolution of Amorphous Silica in Water. *Phys. Chem. Chem. Phys.* **2014**, *16*, 9294-9301.

(49) Frugier, P.; Gin, S.; Minet, Y.; Chave, T.; Bonin, B.; Godon, N.; Lartigue, J.; Jollivet, P.; Ayral, A.; De Windt, L. SON68 Nuclear Glass Dissolution Kinetics: Current State of Knowledge and Basis of the New GRAAL Model. *J. Nucl. Mater.* **2008**, *380*, 8-21.

(50) McDermott, T. C.; Akter, T.; MacElroy, J. M. D.; Mooney, D. A.; McCann, M. T. P.; Dowling, D. P. Diffusion within Ultrathin, Dense Nanoporous Silica Films. *Langmuir* **2011**, *28*, 506-516.

(51) Forester, T.; Smith, W. The DL_POLY_2 Reference Manual. *Daresbury Laboratory, Daresbury* **2000**, .

(52) Du, J.; Cormack, A. N. Molecular Dynamics Simulation of the Structure and Hydroxylation of Silica Glass Surfaces. *J Am Ceram Soc* **2005**, *88*, 2532-2539.

(53) Du, J. Molecular Dynamics Simulations of the Structure and Properties of Low Silica Yttrium Aluminosilicate Glasses. *J Am Ceram Soc* **2009**, *92*, 87-95.

(54) Gin, S.; Abdelouas, A.; Criscenti, L. J.; Ebert, W. L.; Ferrand, K.; Geisler, T.; Harrison, M. T.; Inagaki, Y.; Mitsui, S.; Mueller, K. T. An International Initiative on Long-Term Behavior of High-Level Nuclear Waste Glass. *Mat. Today* **2013**, *16*, 243-248.

(55) Gin, S. Open Scientific Questions about Nuclear Glass Corrosion. *Procedia Mat. Sci.* **2014**, *7*, 163-171.

(56) Guerette, M.; Huang, L. In-Situ Raman and Brillouin Light Scattering Study of the International Simple Glass in Response to Temperature and Pressure. *J. Non Cryst. Solids* **2015**, *411*, 101-105.

(57) Plimpton, S. Fast Parallel Algorithms for Short-Range Molecular Dynamics, *J. Comp. Phys.*, 117, 1-19 (1995).

(58) Shirono, K.; Daiguji, H. Molecular Simulation of the Phase Behavior of Water Confined in Silica Nanopores. *J. Phys. Chem. C* **2007**, *111*, 7938-7946.

(59) Gordillo, M.; Martı, J. Hydrogen Bond Structure of Liquid Water Confined in Nanotubes. *Chem. Phys. Lett.* **2000**, *329*, 341-345.

(60) Chen, C.; Du, J. Lithium Ion Diffusion Mechanism in Lithium Lanthanum Titanate Solid-State Electrolytes from Atomistic Simulations. *J Am Ceram Soc* **2015**, *98*, 534-542.

(61) Rimsza, J. M., Yeon, J. van Duin A.C.T. and Du, J. "Water Interactions with Nanoporous Silica: Comparison of ReaxFF and Ab Initio Based Molecular Dynamics Simulations." *J. Phys. Chem. C* **2016** 120.43 24803-24816.

(62) Campbell, T.; Kalia, R. K.; Nakano, A.; Shimojo, F.; Tsuruta, K.; Vashishta, P.; Ogata, S. Structural Correlations and Mechanical Behavior in Nanophase Silica Glasses. *Phys. Rev. Lett.* **1999**, *82*, 4018-4021.

(63) Yuan, X.; Cormack, A. Efficient Algorithm for Primitive Ring Statistics in Topological Networks. *Comp. Mater. Sci.* **2002**, *24*, 343-360.

(64) Mozzi, R.; Warren, B. The Structure of Vitreous Silica. *J. Appl. Crystallogr.* **1969**, *2*, 164-172.

(65) Rimsza, J.; Deng, L.; Du, J. Molecular Dynamics Simulations of Nanoporous Organosilicate Glasses using Reactive Force Field (ReaxFF). *J. Non Cryst. Solids* **2015**, .

(66) Charpentier, T.; Kroll, P.; Mauri, F. First-Principles Nuclear Magnetic Resonance Structural Analysis of Vitreous Silica. *J. Phys. Chem. C* **2009**, *113*, 7917-7929.

(67) Wright, A. C. Diffraction Studies of Glass Structure. *J. Non Cryst. Solids* **1990**, *123*, 129-148.

(68) Graetsch, H.; Mosset, A.; Gies, H. XRD and 29 Si MAS-NMR Study on some Non-Crystalline Silica Minerals. *J. Non Cryst. Solids* **1990**, *119*, 173-180.

(69) Kinney, D. R.; Chuang, I. S.; Maciel, G. E. Water and the Silica Surface as Studied by Variable-Temperature High-Resolution Proton NMR. *J. Am. Chem. Soc.* **1993**, *115*, 6786-6794.

(70) Gallo, P.; Rovere, M.; Spohr, E. Glass Transition and Layering Effects in Confined Water: A Computer Simulation Study. *J. Chem. Phys.* **2000**, *113*, 11324-11335.

(71) Koga, K.; Zeng, X. C.; Tanaka, H. Freezing of Confined Water: A Bilayer Ice Phase in Hydrophobic Nanopores. *Phys. Rev. Lett.* **1997**, *79*, 5262.

(72) Stillinger, F. H. Water Revisited. *Science* **1980**, *209*, 451-457.

(73) Zangi, R. Water Confined to a Slab Geometry: A Review of Recent Computer Simulation Studies. *J. Phys.:Condens.* **2004**, *16*, S5371.

(74) Zangi, R. Water Confined to a Slab Geometry: A Review of Recent Computer Simulation Studies. *J. Phys.: Condens. Matter* **2004**, *16*, S5371.

(75) Zangi, R.; Mark, A. E. Bilayer Ice and Alternate Liquid Phases of Confined Water. *J. Chem. Phys.* **2003**, *119*, 1694-1700.

(76) Chaplin, M. A Proposal for the Structuring of Water. *Biophys. Chem.* **2000**, *83*, 211-221.

(77) Kuhs, W.; Lehmann, M. The Structure of the Ice Ih by Neutron Diffraction. *J. Phys. Chem.* **1983**, *87*, 4312-4313.

(78) Criscenti, L. J.; Kubicki, J. D.; Brantley, S. L. Silicate Glass and Mineral Dissolution: Calculated Reaction Paths and Activation Energies for Hydrolysis of a Q3 Si by H3O using Ab Initio Methods. *J. Phys. Chem. A* **2006**, *110*, 198-206.

(79) Robinet, L.; Coupry, C.; Eremin, K.; Hall, C. Raman Investigation of the Structural Changes during Alteration of Historic Glasses by Organic Pollutants. *J. Raman Spectrosc.* **2006**, *37*, 1278-1286.

(80) Rao, N. Z.; Gelb, L. D. Molecular Dynamics Simulations of the Polymerization of Aqueous Silicic Acid and Analysis of the Effects of Concentration on Silica Polymorph Distributions, Growth Mechanisms, and Reaction Kinetics. *J. Phys. Chem. B* **2004**, *108*, 12418-12428.

(81) Garofalini, S. H.; Martin, G. Molecular Simulations of the Polymerization of Silicic Acid Molecules and Network Formation. *J. Phys. Chem.* **1994**, *98*, 1311-1316.

(82) Bhattacharya, S.; Gubbins, K. E. Fast Method for Computing Pore Size Distributions of Model Materials. *Langmuir* **2006**, *22*, 7726-7731.

(83) Faux, D.; Cachia, S.; McDonald, P.; Bhatt, J.; Howlett, N.; Churakov, S. Model for the Interpretation of Nuclear Magnetic Resonance Relaxometry of Hydrated Porous Silicate Materials. *Phys. Rev. E* **2015**, *91*, 032311.

(84) Schaeffer, H. A. Oxygen and Silicon Diffusion-Controlled Processes in Vitreous Silica. *J. Non Cryst. Solids* **1980**, *38*, 545-550.

(85) Doltsinis, N.; Burchard, M.; Maresch, W.; Boese, A.; Fockenberg, T. Ab Initio Molecular Dynamics Study of Dissolved SiO 2 in Supercritical Water. *J. Theor. Comp. Chem.* **2007**, *6*, 49-62.

(86) Zotov, N.; Keppler, H. Silica Speciation in Aqueous Fluids at High Pressures and High Temperatures. *Chem. Geol.* **2002**, *184*, 71-82.

(87) Zotov, N.; Keppler, H. Letters. in-Situ Raman Spectra of Dissolved Silica Species in Aqueous Fluids to 900° C and 14 Kbar. *Am. Mineral.* **2000**, *85*, 600-603.

(88) Applin, K. R. The Diffusion of Dissolved Silica in Dilute Aqueous Solution. *Geochim. Cosmochim. Acta* **1987**, *51*, 2147-2151.

(89) Foss, D. R.; Brady, J. F. Structure, Diffusion and Rheology of Brownian Suspensions by Stokesian Dynamics Simulation. *J. Fluid Mech.* **2000**, *407*, 167-200.

(90) Han, S.; Kumar, P.; Stanley, H. E. Absence of a Diffusion Anomaly of Water in the Direction Perpendicular to Hydrophobic Nanoconfining Walls. *Phys. Rev. E* **2008**, *77*, 030201.

(91) Lee, S. H.; Rossky, P. J. A Comparison of the Structure and Dynamics of Liquid Water at Hydrophobic and Hydrophilic Surfaces—a Molecular Dynamics Simulation Study. *J. Chem. Phys.* **1994**, *100*, 3334-3345.

THE JOURNAL OF PHYSICAL CHEMISTRY C

Article

pubs.acs.org/JPCC

Interfacial Structure and Evolution of the Water−Silica Gel System by Reactive Force-Field-Based Molecular Dynamics Simulations

J. M. Rimsza[†] and Jincheng Du*

Department of Materials Science and Engineering, University of North Texas, Denton, Texas 76203, United States

Supporting Information

ABSTRACT: Nanoporous silica gel structures and associated interfaces formed on the surface of silicate and borosilicate glasses play an important role in understanding the dissolution mechanisms of these glasses. Interfacial models that consist of bulk silica, nanoporous hydrated silica gel, and bulk water were constructed and their evolution was studied to understand the water−glass reaction fronts using the Reactive Force Field (ReaxFF)-based molecular dynamics simulations. The short- and medium-range structures of the gel and the interfaces as well as water diffusion and silica dissolution behaviors were studied in detail. It was found that the gel region exhibited an increase in Si−O network connectivity with time, consistent with recent NMR results, due to cross-linking of siloxane bonds in the gel and the dissolution of less connected [SiO_4] groups into the water region. Higher network connectivity of the silica gel can regulate transport of ions and plays the role of passivation. Dissolved silica clusters in water experienced an initial sharp increase and then reached equilibrium concentration at longer time. The development of realistic multiphase nanoporous silica gel interfacial models provides insights into understanding glass-dissolution mechanisms, especially the residual dissolution rate and long-term corrosion behaviors of multicomponent borosilicate glasses.

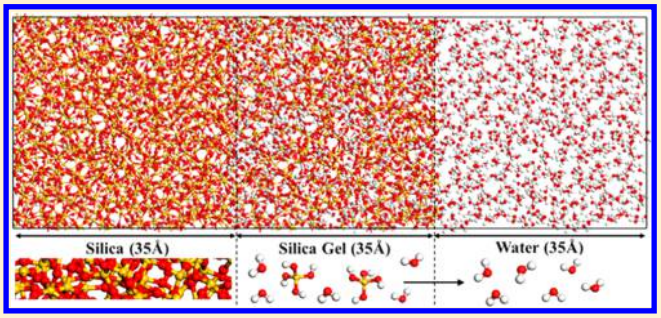

1. INTRODUCTION

Together with other clean energy sources, nuclear power is a key component to solve global environmental and energy challenges. A cornerstone of nuclear energy is the safe disposal of high-level nuclear waste from spent fuels. Borosilicate glasses are accepted as one of the best host materials for the immobilization of nuclear waste through vitrification. Therefore, it is critical to accurately predict and assess the release of radionuclides from these glasses when stored in geological repositories. The corrosion process and long-term chemical durability of the borosilicate glasses is determined by a series of coupled chemical processes of water−glass interactions that lead to the development of a stable gel layer, which controls the residual dissolution rate.[1] These glasses are envisioned to be encapsulated in steel canisters and eventually stored in stable geological underground sites. During storage the eventual contact and interaction of the glass with the groundwater after penetration of the barriers determines the release rate of radioactive elements to the life cycle. It is thus critical to understand the long-term dissolution behaviors of these glasses in aqueous environments. Despite many outstanding experimental investigations in this area,[1−7] one of the key questions is the dissolution front and primary reaction layers that control the residual dissolution rate. This paper sheds light on these complex water−glass interfacial structures and evolution from sophisticated atomistic computer simulations using reactive force-field-based molecular dynamics (MD) simulations.

Silicate and borosilicate glass dissolution occurs in a series of stages. In the first stage a hydroxylated silicate layer depleted in network modifiers forms due to ion exchange between cations in the glass and protons from solution.[1] Next, silica-rich alteration layers form after the removal of soluble species from the surface region and breaking of strained Si−O−Si linkages.[2−5] The alteration layer is in temporary equilibrium with solution, forming a residual dissolution rate, which dominates the lifetime of the glass. The complex structure of the gel layer, including small pore sizes, variable composition, and surface reactions, is credited to limiting rapid dissolution.[5−8] Structural analysis and characterization of the interfacial layers is complicated by the reactivity of the gel and the hydrated amorphous microstructure. Computational methods provide insight into the glass dissolution process by modeling the silica−water interactions with atomic level accuracy. High-resolution simulations can identify reactions that control Si−O bond breakage and local reorganization of the silica structure.

Previous computational investigations of the water−silica interface have identified several processes that alter silica dissolution. For example, slow water diffusion adjacent to the water−silica interface and within the alteration layer will affect kinetics of dissolution reactions.[9−12] Low diffusion coefficients

Received: March 22, 2017
Revised: May 3, 2017
Published: May 4, 2017

DOI: 10.1021/acs.jpcc.7b02734
J. Phys. Chem. C XXXX, XXX, XXX−XXX

limit the ability of water molecules to travel to reactive interfaces during dissolution and may be a factor in alteration layer passivation. Solubility and polymerization have also be investigated, including the stability of dissolved silica structures and changing silica solubility limits with temperature and pressure.[13−16] Previous computational investigations of silica dissolution reactions have focused on atomically flat surfaces and well-ordered pore structures, which lend themselves to analysis. For instance, hydroxylation and dissolution of flat silica surfaces in water have been extensively studied using both ab initio and classical MD methods.[17−22] Alternatively, features of silica−water interactions on larger length scales and complex silica gel structures which develop during dissolution are more difficult to simulate and analyze and therefore are rarely investigated.

More realistic silica dissolution models will provide insight into long-term changes in the surface structure due to the dissolution processes. Structural models that mimic the multiphase glass dissolution products are rare in literature because realistic models of all of the components and the ability to model complex water−silica reactions are required. To our knowledge, this work is the first classical MD model that investigates silica dissolution using not just a water−silica interface but also an interfacial silica gel region. Inclusion of the silica gel region allows for investigation of the alteration layers effect on the dissolution of silicate glasses and will be critical in understanding silica−water reactions in the presence of complex interfaces and hydrated microstructures. The structure of the interfaces, the silica-rich gel, and dissolved silica are analyzed through the use of such an interfacial model. In this manuscript, a three-component model consisting of dense silica, silica gel, and bulk water regions is created, and the effect of these regions on the structure of the silica and gel layers is examined as the system evolves. This allows for the investigation of complex water−glass interfacial structures from robust atomistic classical MD simulations.

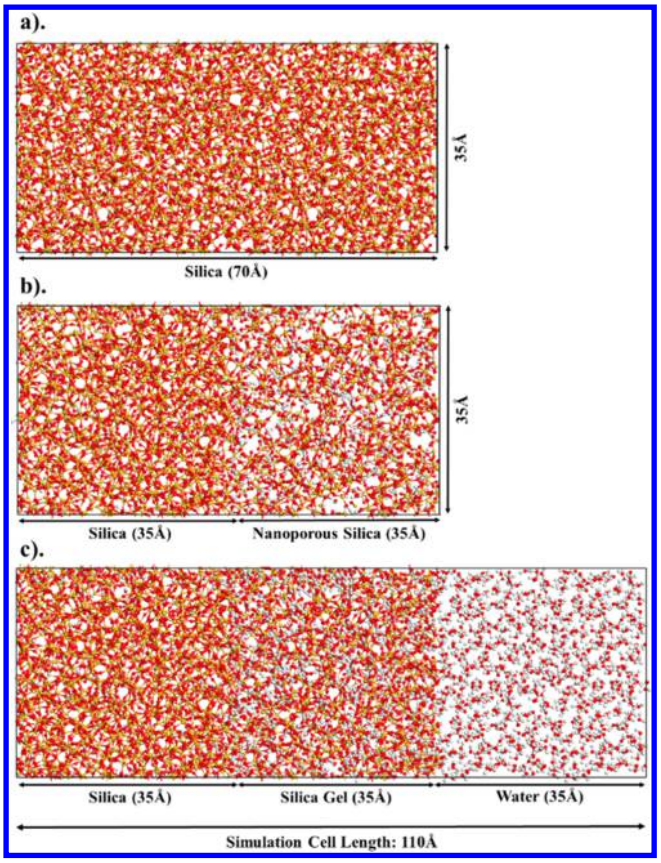

Figure 1. Schematic outline of the generation of the SGW model systems beginning with formation of (a) dense silica, followed by (b) a hydroxylated nanoporous silica in contact with dense silica, and finishing with (c) the complete model (silica on the left, hydrated silica gel in the middle, and bulk water on the right) Colors: oxygen (red), silicon (yellow), and hydrogen (white).

2. COMPUTATIONAL METHODS

2.1. Generation of the Silica−Gel−Water Interface Model. The silica−gel−water (SGW) model contained three sections, silica with a density of 2.2 g/cm^3, a gel structure with a density of ∼1.6 g/cm^3, and bulk water with a density of 1 g/cm^3. To create the SGW model, a 3000 atom silica structure was created from a melt-and-quench procedure using the classical MD simulations with partial charge potentials.[18] Next, a dense 6000 atom silica system was formed from repeating the initial silica structure in the z dimension. This resulted in a 3000 atom dense silica region and a second 3000 atom silica block, which was the basis of the silica gel (Figure 1a). To form the gel structure, silicon atoms in the second silica block were randomly removed while the dangling oxygen atoms were terminated with hydrogen to from silanol groups, mimicking the formation process of hydrogarnet defects.[23] Various percentage of silicon were removed, resulting in silica gel with different porosities. For the interface study, we chose the gel structure with 40% of silicon removed because the simplified international simple glass (ISG) composition proposed to standardize nuclear waste glass dissolution contains 40% soluble network modifiers.[24] The resulting gel structure thus contained 60% of the original silica tetrahedrons with ∼40% porosity and randomly connected pores. A snapshot of the resulting structure is shown in Figure 1b. One of the major advantages of this procedure is that it creates a continuous interface between dense silica region and the nanoporous silica region without artificial interfaces. The gel structure is formed by hydroxylation of the dangling bonds on the internal surfaces of the nanoporous silica structure and then filled with water molecules. A vacuum region 35 Å thick was then added adjacent to the nanoporous silica regions that were filled with bulk water (Figure 1c). This process creates two interfaces: one water/bulk silica interface and one water/gel interface. The final model had a simulation size of 35 Å × 35 Å × 105 Å and contained ∼12 000 atoms. A schematic of the development of the SGW model is included in Figure 1a−c.

Classical MD simulation of the model was performed using the Reactive Force Field (ReaxFF). Dynamic simulations were performed at 300, 500, 700, or 900 K under microcanonical ensemble with a Nosé−Hoover thermostat for 1 ns using a 0.25 fs time step (total 4 × 10^6 steps) at each temperature. Higher temperatures were implemented to allow for faster structural evolution because siloxane bond breakage has an energy barrier ranging from 0.6 to 1 eV,[25] and limited bond breakage and formation occur in realistic simulation times at low temperatures. High temperature also promotes faster evolution of the gel and formation of more advanced structures, thus enabling access to gel structures that are difficult to simulate at low temperatures. Simulations ran at 300 K are termed "SGW-1" to represent the structure that has undergone the lowest annealing and is expected to exhibit the least structural rearrangement.

DOI: 10.1021/acs.jpcc.7b02734
J. Phys. Chem. C XXXX, XXX, XXX−XXX

The remaining systems, SGW-2, SGW-3, and SGW-4, were equilibrated at 500, 700, and 900 K respectively.

Temperature-accelerated dynamics has been used for evaluation of surface diffusion, studies of crystal growth, and the simulation of proteins and included temperatures as high as 1100K.[26−28] In temperature-accelerated dynamics, individual reactions are screened to identify and remove specific high-temperature reactions because thermal energy alters the ratio of high- and low-barrier reactions.[26] Following the 1 ns simulation at elevated temperatures, 100 ps of NVT relaxation at 300 K was performed to cool the systems and remove unstable high-temperature structures. The structural analysis of the systems is based on configurations from this final step.

2.2. Reactive Force Field (ReaxFF). The classical MD simulations in this work were performed using the dissociative water−silica potential ReaxFF, developed by van Duin, Goddard, and coworkers.[29] The water/silica ReaxFF potential was used to study the interface of silica and water by Fogarty et al.[17] This ReaxFF potential was recently reparametrized by Yeon and van Duin to improve the description of energetics of water/silica reactions.[29−31] Rimsza et al. compared the 2015 and the 2010 ReaxFF parameters to simulate water/nanoporous silica reactions with data ab initio MD simulations and confirmed the improvement of the new parametrization.[32] The new water/silica parametrization[30] was used in this study. The ReaxFF force-field parameters are included in the Supporting Information.

ReaxFF allows for both bond breakage and formation by evaluating bond order through calculation of interatomic distances. Bond orders are revaluated at every time step and allow for atoms to transition from one bonding state to another. The force field consists of several partial energy terms (eq 1) that decrease smoothly with distance to avoid stepwise changes in system energy.[29,30]

$$E_{\text{total}} = E_{\text{bond}} + E_{\text{over}} + E_{\text{under}} + E_{\text{LP}} + E_{\text{val}} + E_{\text{pen}} + E_{\text{tors}} + E_{\text{conj}} + E_{\text{VDW}} + E_{\text{Coul}} \quad (1)$$

A description of the partial energies and functional forms is included in ref 29. ReaxFF has been implemented to identify the role of humidity on surface structures,[33] the formation of silica nanocages,[34] the structure of hydrated calcium silicates,[10] and water confined in silicates.[35] In this work, ReaxFF is implemented in the open-source code LAMMPS, a classical MD code distributed by Sandia National Laboratories.[36]

3. RESULTS AND DISCUSSION

3.1. Evolution of the Silica, Gel, and Water Interfacial Structures. After developing of the SGWs models, the structure was analyzed to identify changes in the silica−gel and gel−water interfaces. During the course of the simulation, growth and shrinkage of different regions occurred as atoms diffuse through interfaces. Regions were separated by dividing the simulation cell into 2 Å sections along the z axis and calculating the density of SiO_4 tetrahedron. Silica had a SiO_2 density greater than 2 g/cm^3, 90% of the density of experimental silica (2.2 g/cm^3). The silica gel region had a density greater than 1.0 g/cm^3, 10% less than half the density of silica. Water regions of the SGW model had silica densities of <0.2 g/cm^3. The cutoff values correspond to naturally occurring breaks in the z-density profile of the silica species between regions (Figure 2).

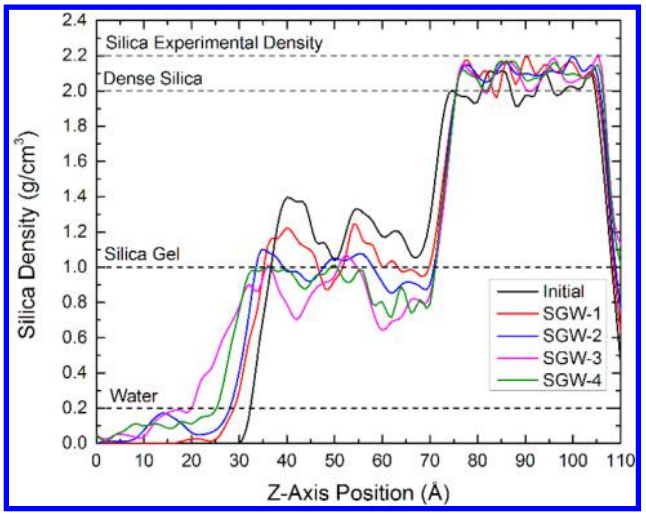

Figure 2. Z-density profile of silica density in SGW models.

The interfaces remain distinct, even for the SGW-4 structure, which experiences the most structural evolution. The silica region is consistently stable with a width of 30 Å and a silica density of 2.10 ± 0.06 g/cm^3. The majority of the structural rearrangement occurs between the gel and water regions with the advancement of the gel−water interface into the water region. The initial gel−water interface thickness is 4 Å and expands to 12 Å in the SGW-3 model, after which slight contraction results in a 10 Å thick interface in the SGW-4 model. With higher temperature evolution of the system, increased Si−O bond breakage and structural rearrangement can occur (discussed in Section 3.2), along with diffusion of water molecules into and out of the gel through the gel−water interface. This may allow for expansion or contraction of the gel region, depending on silica species migration into the water region. Snapshots of the interface included as Figure 3 demonstrate the growth of the gel−water interface into the water region as well as the development of dissolved silica species.

Evolution of the gel region as the model progress is confirmed by the changing pore-size distribution (Figure 4). Pore-size distributions were calculated using the method by Bhattacharya and Gubbins[37] using a probe molecule size of 1 Å. Initially a small narrow pore size distribution is present due to the random removal of silicon forming extremely localized defects, which combine to form larger pores and voids in the structure. As the model progresses the pore-size distribution broadens, with pores as large as 6 Å forming, indicating rearrangement of the gel structure. Model SGW-3, which exhibits the greatest growth in the silica gel region, has the broadest distribution, suggesting that it has undergone the most restructuring. Further discussion of the changing microstructure of the gel is discussed in subsequent sections.

While the SGW model consists of relatively small length scales of the different regions, experimental evidence has identified alteration gel thickness at comparable widths. For example, composition profiles of the 28-component French nuclear waste glasses SON68[38] leeched in a potassium- and silicon-rich solution develop gel layers ∼10 Å thick after 2 weeks and ∼50 Å thick after 3 months.[39] While the systems investigated here are composed of only pure silica and the development of a silica-rich gel layer on the surface of multicomponent oxides is controlled by the composition of the

DOI: 10.1021/acs.jpcc.7b02734
J. Phys. Chem. C XXXX, XXX, XXX−XXX

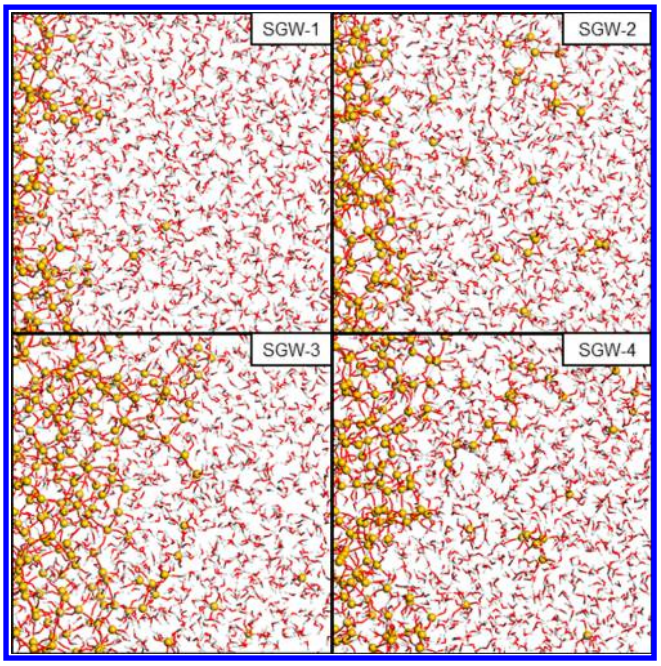

Figure 3. Snapshots of evolving gel−water interface and dissolved silica in the water region for the SGW model structures. Colors: oxygen (red), silicon (yellow), and hydrogen (white).

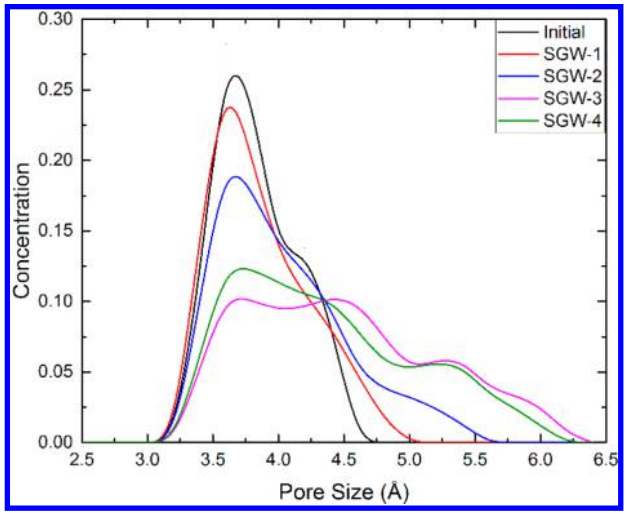

Figure 4. Pore-size distribution of the silica gel region of the SGW models.

glass and solution,[1] the thickness of the gel region used here is consistent with typical nuclear waste glass compositions after 1 to 2 months of dissolution.[39] Further investigations of glass dissolution can increase the width of the silica gel region to approximate glasses, which have undergone more extensive dissolution. Overall, the water−gel interface is more unstable than the gel−silica interface, and understanding the silica dissolution process will require a more in-depth analysis of gel−water interfaces.

3.2. Structure Characterization of the Silica, Gel, And Water Interfaces. Intermediate range features of the silica gel structure identify reorganization of the silica network as the SGW model evolves. For example, the Q_n species, which identify the number of oxygen "n" that are bonded to silicon, have been used to describe the process of silica dissolution. Silica removal from a corrosive interface results in the formation of a SiO_4H_4 molecule or a hydroxylated Q_0 species through a series of sequential steps. Initially, a SiO_4 tetradron is fully coordinated and individual Si−O bonds break one by one, forming a Q_3, then a Q_2, a Q_1, and finally a Q_0 species ($Q_4 \rightarrow Q_3 \rightarrow Q_2 \rightarrow Q_1 \rightarrow Q_0$).[14,15,25] The connectivity (C) can also be calculated and describes the average number of bridging oxygen associated with a silicon atom.

$$C = \sum_{n=0}^{5} n \cdot C_{Q_n} \tag{2}$$

Fully coordinated dense silica is composed entirely of silicon bonded to four bridging oxygen and has a connectivity of four.

In the silica region of the SGW model the Q_n distribution remains relatively constant (Figure 5a). The connectivity

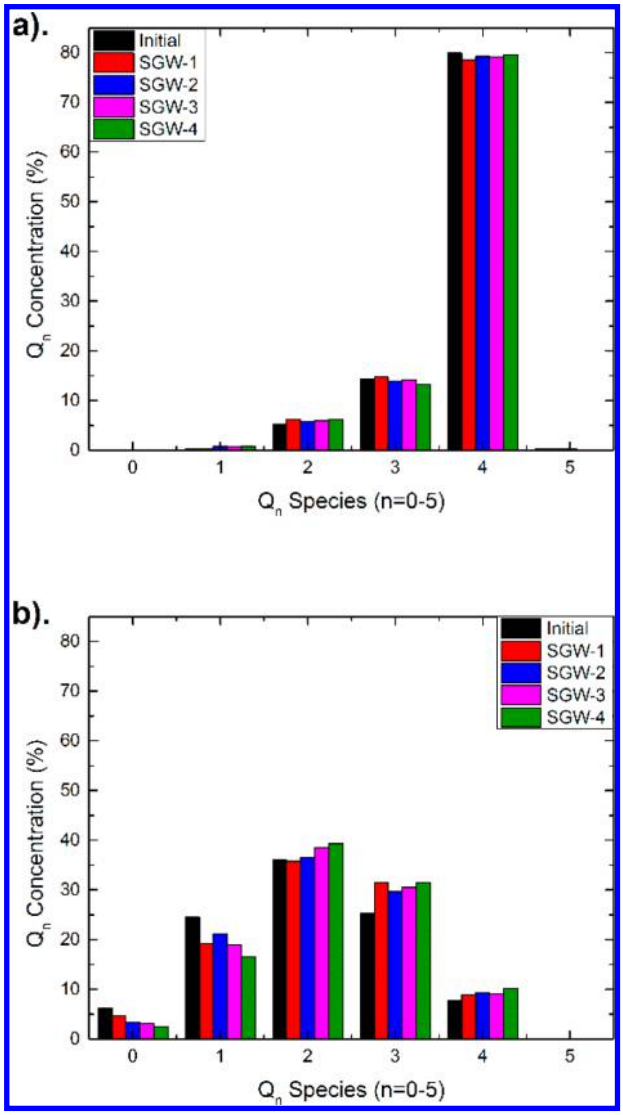

Figure 5. Q_n distribution of the (a) silica and (b) gel regions of the SGW models.

decreases by ∼0.03 from the initial model to the SGW-4 model, which occurs primarily along the interfaces with the conversion of Q_4 and Q_3 to lower Q_n species. The gel region of the SGW model exhibits significantly more structural rearrangement (Figure 5b), with an increase in the connectivity of 0.26 between the initial and SGW-4 structures, a 12% increase.

DOI: 10.1021/acs.jpcc.7b02734
J. Phys. Chem. C XXXX, XXX, XXX−XXX

Table 1. Q_n Distribution and Connectivity (C) in the Silica and Gel Regions of the SGW Models

	silica						gel					
	Q_1	Q_2	Q_3	Q_4	Q_5	C	Q_0	Q_1	Q_2	Q_3	Q_4	C
initial	0.33	5.21	14.33	79.91	0.22	3.74	6.27	24.56	36.06	25.26	7.84	2.04
SGW-1	0.35	6.18	14.69	78.56	0.23	3.72	4.61	19.16	35.74	31.56	8.93	2.21
SGW-2	0.82	5.83	13.87	79.25	0.23	3.72	3.32	21.15	36.56	29.61	9.37	2.21
SGW-3	0.71	5.92	14.20	79.17	0.00	3.72	3.11	18.97	38.41	30.48	9.02	2.23
SGW-4	0.83	6.24	13.29	76.53	0.00	3.72	2.44	16.59	39.27	31.51	10.20	2.30

Examination of individual Q_n distributions identified decreases in Q_0 and Q_1 concentrations due to diffusion of silica monomers into the adjacent water region. Previous computational studies have identified changing activation energies for siloxane bond breakage based on the Q_n species of the silicon atoms.[25,40] Results indicated that the $Q_1 \rightarrow Q_0$ conversion has the lowest activation energy of the coordination structures.[33] This accounts for the decrease in the Q_1 and Q_0 species relative to other silicon in the gel structure. Comparatively the $Q_4 \rightarrow Q_3$ or $Q_3 \rightarrow Q_2$ transitions are reported as having the highest activation energies, indicating retention in the gel structure.[25,40] The increase in the Q_2, Q_3, and Q_4 species reflects this trend. Because of the increase in the connectivity, a more perfect silica backbone structure is developed, which may also be responsible for the formation of a dense silica surface layer. Additionally, the removal of lower coordination structure such as Q_1−Q_0 species may allow for the fully coordinated silicon to condense into crystalline phases. Therefore, the SGW model developed here is consistent with previous classical MD and density functional theory (DFT) reports for stability of Q_n species during silica dissolution.

Experimentally, nuclear magnetic resonance (NMR) has been used to characterize the alteration layers of nuclear waste glasses by identifying the ^{29}Si chemical shift associated with varying coordination environments. Decreasing ^{29}Si chemical shifts are associated with lower Q_n species and have been well established in binary glasses, where the addition of network modifiers results in a clear shift of the ^{29}Si NMR peak.[41] Nuclear waste glasses are modified with highly soluble species, with silicon concentrations of ∼60%.[24] With the inclusion of network modifiers such as calcium or sodium, Q_1 and Q_2 species are stabilized by the charge-compensating mechanisms of the cations.[6] Once those species have dissolved the system is restructured, forming higher concentrations of Q_3 and Q_4 species.[6] Q_n distributions were investigated experimentally in French SON68 nuclear waste glass, a 28-component highly modified sodium borosilicate.[38] SON68 contains ∼46 wt % SiO_2, 5 wt % Al_2O_3, 14 wt % B_2O_3, and 10 wt % Na_2O with the balance composed of additional trace elements.[38] In SON68 glass the Q_n distribution in silica gels was evaluated by NMR and after 7 days concentrations of Q_2 and Q_3 increased and Q_4 species increased after 21 days.[42] Because of the high number of components in SON68 compared with the pure silica systems studied here some inconsistencies between the results are expected. While the simulations performed here are on a much shorter time scale than the reported experimental results, both methods demonstrate an increase in the connectivity of the silica gel. By removing the silicon tetrahedron the remaining silanol groups condense and reform the siloxane bonds, increasing the connectivity.

The SGW models demonstrate increased connectivity, as seen in experiments, and are consistent with differences in Q_n stability identified from both classical MD and DFT simulations (Table 1). Inclusions of additional species in the gel and bulk regions as available force fields develop will allow for targeted investigations of different compositions on the structure of the interfacial gel layer.

Beyond the Q_n distribution, the intermediate range structure of the silica and gel regions is identified through the ring-size distribution. Silica tetrahedral are organized into rings, separated by the number of silicon atoms included in the ring structure, with a six-member ring containing six silicon atoms and six bridging oxygen atoms. Amorphous silica contains primarily six-membered rings, as do crystalline silicate polymorphs such as α and β quartz.[43] The silica region of the SGW model exhibits a clear and consistent peak between six- and seven-membered rings (Figure 6a), which does not change as the system evolves. A few small adjustments, such as decreases in six-membered ring concentrations, are offset by increases in eight-membered ring concentrations and indicate that some restructuring occurs at the interfaces.

The gel region exhibits significant restructuring in the ring size distribution as the SGW models evolves. The clearest features are increases in five-, six-, and seven-membered rings, which indicates reformation of the dense silica, because pure silica has a peak concentration of six-membered rings.[44,45] In the less evolved models (SGW-1, SGW-2, and SGW-3) this affect is less severe, but in the SGW-4 model increases in six- and seven-membered rings indicate a significant formation of ring sizes found in dense silica. Raman spectroscopy of the oglomerization of silica gels noted the initial development of three- and four-membered rings as silica suspensions form a siloxane backbone, followed by the development of a Boson peak in the spectra, characteristic of a glassy material.[46,47] Therefore, as the structure of the gel evolves it is expected that the structure will tend toward developing an amorphous structure (Figure 6b). The development of the silica gel in the SGW model mimics this process, with an intermediate range order that evolves over the course of the simulation to become more consistent with dense silica.

Changes in the short-range structural features, including Si−O bond distances and Si−O−Si bond angles, are limited, suggesting that the silica maintains the structure of the SiO_4 tetrahedral. More information on the short-range structure, including pair distribution functions and bond-angle distributions, is available in the Supporting Information.

3.3. Water Diffusion in the Silica, Gel, and Water Interfacial Regions. A critical factor in evaluating silica dissolution is the effect of the interface and the gel structure on water diffusion. To calculate diffusion coefficients, the mean-squared displacement (MSD) from the last 50 ps of the final 300 K 100 ps equilibrium run is used to remove temperature affects between the different structures. The MSD was calculated from eq 3, with $x_j(0)$ as the position of particle 'j' at time 0, $x_j(t)$ as the position of particle 'j' at time t, and n as the number of atoms in the system.[48]

DOI: 10.1021/acs.jpcc.7b02734
J. Phys. Chem. C XXXX, XXX, XXX−XXX

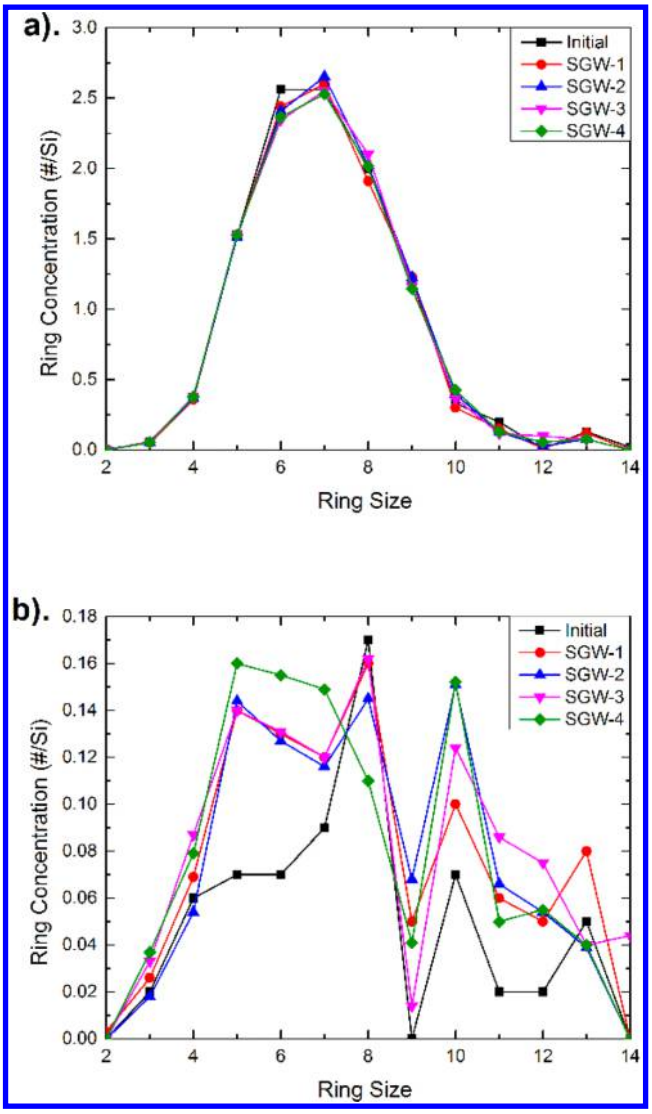

Figure 6. Ring-size distribution for the (a) silica and (b) gel regions of the SGW models and the initial structure.

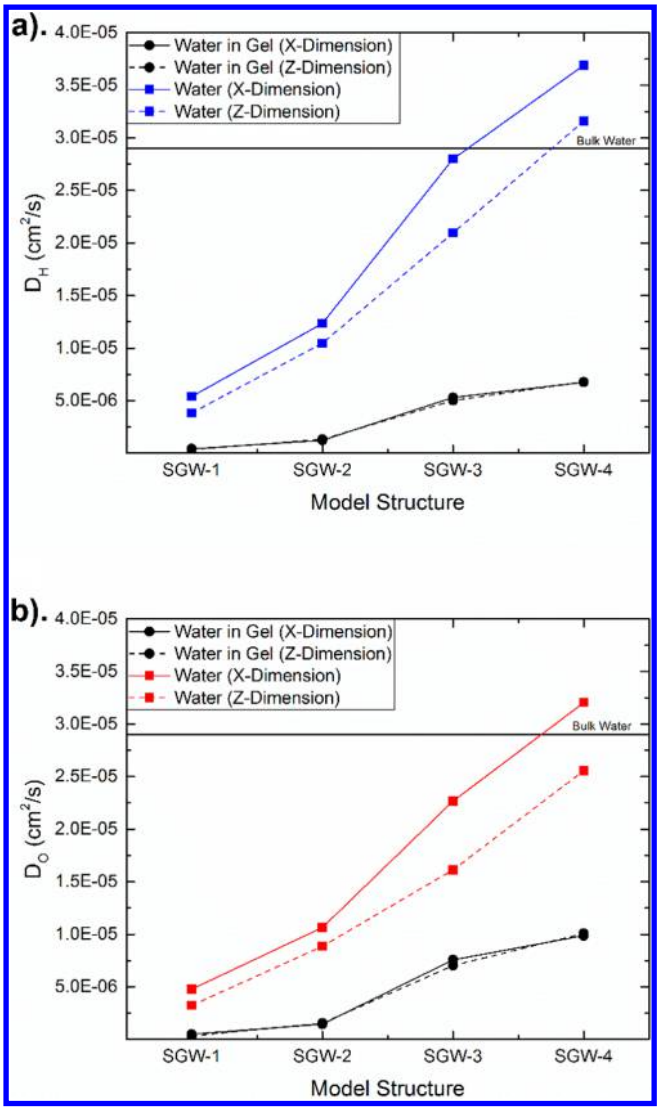

Figure 7. Translational water diffusion, separated by (a) hydrogen and (b) oxygen atoms in the gel and water regions of the SGW model in the x and z dimensions and bulk water.

$$\mathrm{MSD} = \frac{1}{n}\left\langle \sum_{j=1}^{n} |x_j(0) - x_j(t)|^2 \right\rangle \tag{3}$$

The diffusion coefficient was calculated from the MSD using the Einstein diffusion (eq 4)[48]

$$D = \frac{1}{6}\lim_{t\to\infty} \frac{\mathrm{d}}{\mathrm{d}t}\langle |x_j(0) - x_j(t)| \rangle \tag{4}$$

Atomic species were separated into three regions, silica, gel, and water regions. The translational diffusion coefficients were calculated by isolating the diffusion in the x and z dimensions.

As the models evolve, water diffusion (D_H) increases in both the water and gel regions in both the x dimension and z dimension (Figure 7). Increasing D_H values in the gel region are due to the decreasing silica concentration (Figure 2 and Table 2), which allows for less confinement of water within the gel region due to a more open structure. Additionally, decreasing concentrations of Q_0 and Q_1 species may open channels within the system and form larger voids and free space, which allow for water diffusion. Despite the increases in D_H values in the gel as the structure evolves, the diffusion is still sharply limited when compared with D_H in the water region, so that the gel decreases the ability of the water to reach the silica–gel interface. D_H in the x dimension and z dimensions are not significantly different in the gel region, indicating that no opening of the structure is preferred in one dimension over the other and that water is equally confined within the system.

In the water region the D_H values are initially below what has been previously reported for bulk water, at 5×10^{-6} cm^2/s compared with 2.9×10^{-5} cm^2/s.[17] The lower D_H values are accounted for by some bounding effects that occur at the silica–water and gel–water interface, which slow diffusion due to the formation of hydrogen bonds.[49] Low D_H value are more distinct in the z dimension, as water runs into the water–gel and silica–gel interfaces and cannot diffuse farther. In comparison the x-dimension D_H values are consistently higher than those in the z dimension because less restricted movement of the water molecules are allowed parallel to the interface. As the models evolve, D_H values in the water region continue to increase (Figure 7a,b). This is contrary to the hypothesis that dissolved silica monomers would slow water movement by trapping water molecules between silica fragments. Previous investigations of silica gel system, which mimic the gel used in

DOI: 10.1021/acs.jpcc.7b02734
J. Phys. Chem. C XXXX, XXX, XXX−XXX

Table 2. Silica Concentration in Either the Water Region (g/L) and in the Gel, Silica, and Interface Regions (g/cm^3)[a]

	water region: all Si	water region: monomers	water−gel interface	gel region	gel−silica interface	silica region
units	(g/L)	(g/L)	(g/cm^3)	(g/cm^3)	(g/cm^3)	(g/cm^3)
initial	0.00 ± 0.00	0.00 ± 0.00	0.34 ± 0.14	1.21 ± 0.03	1.65 ± 0.17	2.02 ± 0.03
SGW-1	5.19 ± 3.48	2.59 ± 1.32	0.70 ± 0.15	1.06 ± 0.03	1.54 ± 0.20	2.04 ± 0.06
SGW-2	25.93 ± 6.75	7.78 ± 2.17	0.73 ± 0.13	0.98 ± 0.02	1.67 ± 0.20	2.05 ± 0.05
SGW-3	34.58 ± 9.86	9.15 ± 3.56	0.74 ± 0.07	0.84 ± 0.03	1.63 ± 0.22	2.05 ± 0.04
SGW-4	29.77 ± 7.16	9.60 ± 2.79	0.75 ± 0.11	0.89 ± 0.02	1.66 ± 0.20	2.05 ± 0.05

[a]Variation is the standard error.

this model, have noted increased water diffusion in silica−gel suspensions, which contain highly fragmented hydrated silica structures. In these systems the relatively high diffusion coefficients of silica monomers are hypothesized to create a water−silica suspension, with both water molecules and silica fragments diffusing. This results in a disruptive unstable system due to the breakage and reformation of hydrogen-bond networks in the water.

Here the average hydrogen bonds per water molecule were calculated to indicate the strength of the hydrogen-bond network in the water region. Hydrogen bonds were calculated from geometric parameters using a donor−acceptor distance of <3.9 Å and a hydrogen−acceptor distance of <3.2 Å. These parameters have been implemented in previous investigations of hydrogen bonding in water and are reported to provide the upper limit of the number of hydrogen bonds per water molecule.[50] Hydrogen bonding between water and silanol groups used a donor−acceptor distance of <3.2 Å and a hydrogen−acceptor distance of <2.6 Å. These parameters are consistent with calculation of water−silanol hydrogen bonds by previous authors.[49,51] Average hydrogen bonds per water molecule decreased from a 3.46 bonds/mol for the SGW-1 system to 3.26 bonds/mol in the SGW-4 system (3.34 bonds/mol and 3.28 bonds/mol for SGW-2 and SGW-3 models, respectively). Previous authors[52,53] have theorized that the number and strength of hydrogen bonds between water molecules controls the diffusion because a hydrogen bond needs to be broken to allow two molecules to diffuse away from each other. Additionally, hydrogen-bond concentration around water molecules increases as the molecule moves away from an interface, which has also been attributed to slowing water diffusion during nanoconfinement.[54] Therefore, decreasing hydrogen bonds per water molecule seen in the model structures here result in increases in water diffusion in the SGW-4 model compared with the SGW-1 model. A detailed investigation of the strength, structure, and concentrations of the hydrogen-bond network in the silica gel and adjacent to the interface is of interest but is left to future investigations.

In addition to the hydrogen-bond network, jumping and tumbling mechanisms are both suggested as methods of increasing water diffusion in silica−water suspensions.[55,56] The high water diffusion occurs between both the hydrogen (Figure 7a) and oxygen atoms (Figure 7b) in the water, suggesting that the entire water molecule is diffusing, not just hydrogen atoms jumping in-between water molecules. The high diffusion indicates the development of a highly reactive zone adjacent to the gel−water interface, which will have a significant effect on the development of dissolved silica species.

3.4. Silica Dissolution. Silica dissolution is identified by loss of silica from the bulk material and increasing silica concentration in the aqueous solution. Experimentally, silica concentration in water is measured in dilute conditions due to the large volume of water in which glass powders or coupons are submerged.[57] Additionally, time frames for dissolution experiments vary on the order of hours, days, months, or years.[5] Because of computational limitations, the existence of a single silicon atom in the water region results in silica concentrations beyond what would occur in experimental systems, where the silicon concentrations are measured far from the interface. Even so, analysis of the silica concentration provides insight into silica dissolution at the gel−water interface.

The experimental solubility limit of amorphous silica in water at 300 K is ∼1500 ppm (1.5 g/L).[58] During the dissolution of multicomponent glass the silicon concentrations in water are lower at ∼600−700 ppm (0.6 to 0.7 g/L) for sodium borosilicate glasses and even lower for the SONG68 composition (50−120 ppm or 0.05 to 0.12 g/L).[59,60] In this work, dissolved silica concentrations are ∼7 g/L for the SGW-1 model and increase to ∼42g/L for SGW-4 model (Table 2). The dissolved silica concentration is one to 2 orders of magnitude higher than experimental results measured far from the interface. The initial rapid increase in silica concentration (in the SGW-1 model) followed by a leveling off between 40 and 50 g/L indicates the development of an equilibrium condition. The high concentration is due to the limited size of the water region that does not allow for further diffusion of silica away from the interface. Despite the high local concentration, similarly high concentrations of ions have been measured next to surfaces during pitting and crevice corrosion.[61]

Another interesting feature of the dissolved silica in the SGW model is the formation of monomeric silica (SiO_4H_4), silica dimers, or longer silica chains. Primarily monomeric forms of dissolved silica have been identified experimentally by Raman spectroscopy at temperatures below 900 K.[14,15] Monomeric silica is also the primary dissolved silica species identified during the dissolution of multicomponent glasses.[5] Computational analysis of the stability of silica species in water in cluster calculations has indicated that monomers, dimers, and trimers are energetically favorable under certain conditions.[62−64] The polymerization reactions responsible for the condensation of silica from an oversaturated solution identified that the silica progresses from monomers, to dimer, to linear trimers and then to more complex ring structures.[63] Because deposition of silica from solution onto gel surfaces has been suggested as a mechanisms for silica gel formation, the existence of more complex silica species, particularly close to the interface, is of interest.[5]

The identification of the structure of dissolved silica in the SGW model is complicated by the diffuse water−gel interface. Therefore, only silica species that are greater than 3 Å away from the interface are considered to have successfully transitioned from the interface to the bulk water region. Silica concentration was calculated by averaging the density of

DOI: 10.1021/acs.jpcc.7b02734
J. Phys. Chem. C XXXX, XXX, XXX−XXX

dissolved silica in 2 Å segments of the water region and reported with the standard error (SE). SE is calculated using eq 5, with SD as the standard deviation and n as the number of observations/iterations.

$$\mathrm{SE} = \frac{SD}{\sqrt{n}} \tag{5}$$

Throughout the SGW models a number of silica species form, including monomers, dimers, trimers, as well as longer silica chains. Monomers (Q_0) are the majority of the dissolved species with similarly high concentrations of Q_1 species (Figure 8a), which most commonly form as silica dimers or as the end

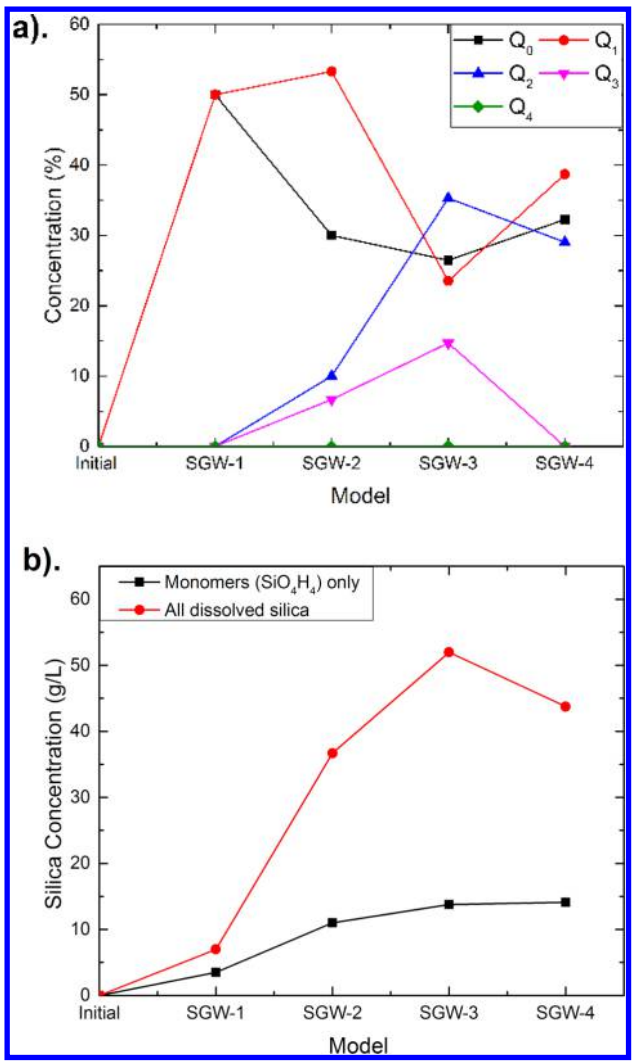

Figure 8. (a) Q_n speciation of dissolved silica in the water region of the SGW models and (b) distribution of dissolved silica molecules by the number of silicon atoms in a cluster. Error bars are the standard error.

silicon in linear chain molecules. Overall, 80%+ of the silica clusters in the water region are either monomers or dimers, with the balance being composed of longer chain structures. The higher temperature of the 1 ns simulation for the SGW-2, SGW-3, and SGW-4 simulations may also allow for diffusion of larger chunks of silica into the water region, which can then break into monomers during the 300 K equilibration run. Additionally, the concentration of large polymerized silica clusters may be the result of the small model size, which develops oversaturation conditions that stabilize silica chains. Additionally, some of the silica appears to dissolve and diffuse into the water region in larger clusters or chunks, with weaker Q_1 and Q_2 linkages breaking, allowing for higher coordination of the dissolved silica. At 300 K the silica chains are unstable and either repolymerize on the silica surface or break up to form smaller clusters or monomers, which diffuse through the solution faster than large molecules.[63]

If only the monomeric silica is considered, because experimentally all of the stable silica in water is reported to be SiO_4H_4, then the concentration of silica increases from 2.59 g/L in SWG-1 to 9.60 g/L in SGW-4 and plateaus, suggesting saturation conditions. This is in contrast with much higher concentration of dissolved silica when larger clusters are considered (Figure 8b). Despite the high silica concentration levels, the trend is consistent with experiment, an initial high development of dissolved silica species, followed by a tapering off of silica concentration once a saturation condition is reached. The stabilizing of dissolved monomer concentration suggests that the model is approaching equilibrium, with a balance between dissolving and repolymerizing silica species occurring at the gel−water interface. Further analysis of the structure for more evolved SGW models will need to be performed to confirm this assertion.

Silica enrichment of the water−gel interface also develops, with the amount of silica doubling from 0.34 (SGW-1) to 0.74 g/cm^3 (SGW-4), compared with a similar decrease in the silica concentration in the gel, transitioning from 1.21 g/cm^3 in the initial structure to 0.84 g/cm^3 in the SWG-4 model. Comparatively, the silica concentration in the gel−silica interface and the silica region remained constant at ∼1.6 and ∼2.05 g/cm^3 in the equilibration steps. Therefore, the majority of the movement of silica is transferring from the gel to the water region, with almost no silicon transferring from the silica to the gel region. Overall, the water−gel interfacial region and the gel are responsible for the development of silica saturation conditions, and further restructuring of the surface, including repolymerization of silica onto the gel, may occur once the system reaches equilibrium conditions.

4. CONCLUSIONS

MD simulations with the bond-order-based Reactive Force Field (ReaxFF) potential were used to create three-component glass dissolution interface models consisting of bulk silica, silica gel, and water regions, with naturally formed water−gel and gel−silica interfaces. The SGW models were allowed to evolve at 300, 500, 700, and 900 K for 3 million steps (∼1 ns) to simulate the progression of the gel layer. These models of the dissolution gel structure provided atomic level insights into the gel, the interfacial structure, and their evolutions. The results indicate that there is a gradual growth of the gel region into the water, resulting in dissolution of silica into the water from the gel, while the dense silica remains intact at these temperatures and time ranges.

The medium range network structure of the gel was analyzed in terms of Q_n and ring-size distributions. The most defective sites in the gel, such as Q_1 and Q_2 species, were dissolved, resulting in an enrichment of the Q_3 and Q_4 species and an increase in network connectivity of the gel region. The trend toward highly connected silica network suggests the tendency of the gel structure to form ordered and stable phases rather than the initial highly fragmented network structure.[59] Similar trends were observed in the ring-size distribution, with the

DOI: 10.1021/acs.jpcc.7b02734
J. Phys. Chem. C XXXX, XXX, XXX−XXX

formation of five-, six-, and seven-membered ring as the gel evolves, which are more consistent with silica with a peak in the ring size distribution at six-membered rings.[45]

It was observed that the silica concentration in the water regions (solution) increased due to both individual silica monomers and small silica clusters breaking from the gel surface and diffusing into the water. Of the dissolved species, the majority (50%+) are monomers, and their concentrations increase to >70% for more evolved systems. Silica monomer concentrations vary from 3 to 10 g/L, 3−8 times the experimental values for pure silica dissolution of ∼1.5 g/L.[48] The relatively low volume of water and short distance between the dissolved silica and the gel−water interface increased the silica concentration in the water region while experimental results measure silica concentration far from the interface. The silica concentration rapidly increases before stabilizing at ∼10 g/L, suggesting that the model has reached a saturation condition for silica in aqueous solutions.

The silica gel structure and associated interfaces generated in this work provide atomic-level structural details and dynamic properties of the porous silica gel structures. It showed that gel structure evolution led to increased silicon−oxygen network connectivity of the silica gel, suggesting that the formation of a highly connected network region that can regulate the diffusion of reactive species and products thus controls the dissolution rate. These models shed light on the key steps of glass dissolution, especially the residual rate behaviors of silicate glasses. With the recent development of force fields that simulate reactions between water and multicomponent oxides, interfacial models that account for the complex gel layers formed during dissolution can be investigated in detail to provide mechanistic insight into the effect of composition on dissolution.

■ ASSOCIATED CONTENT

Supporting Information

The Supporting Information is available free of charge on the ACS Publications website at DOI: 10.1021/acs.jpcc.7b02734.

Short-range structural data (interatomic distances and angles) of the silica, gel, and water regions as well as the ReaxFF force field used in this work. (PDF)

■ AUTHOR INFORMATION

Corresponding Author

*E-mail: Jincheng.du@unt.edu. Tel: (940) 369-8184.

ORCID

Jincheng Du: 0000-0003-4805-7498

Present Address

[+]J.M.R.: Geochemistry Department, Sandia National Laboratories, Albuquerque, NM 87185.

Notes

The authors declare no competing financial interest.

■ ACKNOWLEDGMENTS

This work was supported by the Department of Energy Nuclear Energy University Project under Project No. 13-5494. J.M.R. acknowledges that this material is based on work supported by the National Science Foundation Graduate Research Fellowship Program under Grant No. DGE-114248. Computational resources are provided by the University of North Texas high performance computing cluster.

■ REFERENCES

(1) Gin, S. Open Scientific Questions About Nuclear Glass Corrosion. *Procedia Mater. Sci.* **2014**, *7*, 163−171.

(2) Brinker, C.; Kirkpatrick, R.; Tallant, D.; Bunker, B.; Montez, B. Nmr Confirmation of Strained "Defects" in Amorphous Silica. *J. Non-Cryst. Solids* **1988**, *99*, 418−428.

(3) Casey, W. H.; Westrich, H. R.; Banfield, J. F.; Ferruzzi, G.; Arnold, G. W. Leaching and Reconstruction at the Surfaces of Dissolving. *Nature* **1993**, *366*, 253.

(4) Angeli, F.; Charpentier, T.; Gin, S.; Petit, J. 17 O 3q-MAS NMR Characterization of a Sodium Aluminoborosilicate Glass and its Alteration Gel. *Chem. Phys. Lett.* **2001**, *341*, 23−28.

(5) Gin, S.; Jollivet, P.; Fournier, M.; Angeli, F.; Frugier, P.; Charpentier, T. Origin and Consequences of Silicate Glass Passivation by Surface Layers. *Nat. Commun.* **2015**, *6*, 6360.

(6) Gin, S.; Guittonneau, C.; Godon, N.; Neff, D.; Rebiscoul, D.; Cabié, M.; Mostefaoui, S. Nuclear Glass Durability: New Insight into Alteration Layer Properties. *J. Phys. Chem. C* **2011**, *115*, 18696−18706.

(7) Geisler, T.; Nagel, T.; Kilburn, M. R.; Janssen, A.; Icenhower, J. P.; Fonseca, R. O.; Grange, M.; Nemchin, A. A. The Mechanism of Borosilicate Glass Corrosion Revisited. *Geochim. Cosmochim. Acta* **2015**, *158*, 112−129.

(8) Geisler, T.; Janssen, A.; Scheiter, D.; Stephan, T.; Berndt, J.; Putnis, A. Aqueous Corrosion of Borosilicate Glass under Acidic Conditions: A New Corrosion Mechanism. *J. Non-Cryst. Solids* **2010**, *356*, 1458−1465.

(9) Bonnaud, P.; Coasne, B.; Pellenq, R. J. Molecular Simulation of Water Confined in Nanoporous Silica. *J. Phys.: Condens. Matter* **2010**, *22*, 284110.

(10) Hou, D.; Zhao, T.; Ma, H.; Li, Z. Reactive Molecular Simulation on Water Confined in the Nanopores of the Calcium Silicate Hydrate Gel: Structure, Reactivity, and Mechanical Properties. *J. Phys. Chem. C* **2015**, *119*, 1346−1358.

(11) Harrach, M. F.; Klameth, F.; Drossel, B.; Vogel, M. Effect of the Hydroaffinity and Topology of Pore Walls on the Structure and Dynamics of Confined Water. *J. Chem. Phys.* **2015**, *142*, 034703.

(12) Diallo, S. Pore-Size Dependence and Characteristics of Water Diffusion in Slitlike Micropores. *Phys. Rev. E* **2015**, *92*, 012312.

(13) Garofalini, S. H.; Martin, G. Molecular Simulations of the Polymerization of Silicic Acid Molecules and Network Formation. *J. Phys. Chem.* **1994**, *98*, 1311−1316.

(14) Zotov, N.; Keppler, H. Silica Speciation in Aqueous Fluids at High Pressures and High Temperatures. *Chem. Geol.* **2002**, *184*, 71−82.

(15) Zotov, N.; Keppler, H. Letters. In-Situ Raman Spectra of Dissolved Silica Species in Aqueous Fluids to 900° C and 14 Kbar. *Am. Mineral.* **2000**, *85*, 600−603.

(16) Martin, G. E.; Garofalini, S. H. Sol-Gel Polymerization: Analysis of Molecular Mechanisms and the Effect of Hydrogen. *J. Non-Cryst. Solids* **1994**, *171*, 68−79.

(17) Fogarty, J. C.; Aktulga, H. M.; Grama, A. Y.; Van Duin, A. C.; Pandit, S. A. A Reactive Molecular Dynamics Simulation of the Silica-Water Interface. *J. Chem. Phys.* **2010**, *132*, 174704.

(18) Du, J.; Cormack, A. N. Molecular Dynamics Simulation of the Structure and Hydroxylation of Silica Glass Surfaces. *J. Am. Ceram. Soc.* **2005**, *88*, 2532−2539.

(19) Mahadevan, T.; Garofalini, S. Dissociative Chemisorption of Water onto Silica Surfaces and Formation of Hydronium Ions. *J. Phys. Chem. C* **2008**, *112*, 1507−1515.

(20) Masini, P.; Bernasconi, M. Ab Initio Simulations of Hydroxylation and Dehydroxylation Reactions at Surfaces: Amorphous Silica and Brucite. *J. Phys.: Condens. Matter* **2002**, *14*, 4133.

(21) Ceresoli, D.; Bernasconi, M.; Iarlori, S.; Parrinello, M.; Tosatti, E. Two-Membered Silicon Rings on the Dehydroxylated Surface of Silica. *Phys. Rev. Lett.* **2000**, *84*, 3887.

(22) Sulpizi, M.; Gaigeot, M.-P.; Sprik, M. The Silica−Water Interface: How the Silanols Determine the Surface Acidity and Modulate the Water Properties. *J. Chem. Theory Comput.* **2012**, *8*, 1037−1047.

DOI: 10.1021/acs.jpcc.7b02734
J. Phys. Chem. C XXXX, XXX, XXX−XXX

(23) Stenina, N. G. Water-Related Defects in Quartz. *Bull. Geosci.* **2004**, *79*, 251−268.
(24) Gin, S.; Abdelouas, A.; Criscenti, L. J.; Ebert, W. L.; Ferrand, K.; Geisler, T.; Harrison, M. T.; Inagaki, Y.; Mitsui, S.; Mueller, K. T.; et al. An International Initiative on Long-Term Behavior of High-Level Nuclear Waste Glass. *Mater. Today* **2013**, *16*, 243−248.
(25) Kagan, M.; Lockwood, G. K.; Garofalini, S. H. Reactive Simulations of the Activation Barrier to Dissolution of Amorphous Silica in Water. *Phys. Chem. Chem. Phys.* **2014**, *16*, 9294−9301.
(26) So/rensen, M. R.; Voter, A. F. Temperature-Accelerated Dynamics for Simulation of Infrequent Events. *J. Chem. Phys.* **2000**, *112*, 9599−9606.
(27) Abrams, C. F.; Vanden-Eijnden, E. Large-Scale Conformational Sampling of Proteins Using Temperature-Accelerated Molecular Dynamics. *Proc. Natl. Acad. Sci. U. S. A.* **2010**, *107*, 4961−4966.
(28) Montalenti, F.; Sørensen, M.; Voter, A. Closing the Gap between Experiment and Theory: Crystal Growth by Temperature Accelerated Dynamics. *Phys. Rev. Lett.* **2001**, *87*, 126101.
(29) van Duin, A. C.; Strachan, A.; Stewman, S.; Zhang, Q.; Xu, X.; Goddard, W. A. ReaxffSiO Reactive Force Field for Silicon and Silicon Oxide Systems. *J. Phys. Chem. A* **2003**, *107*, 3803−3811.
(30) Yeon, J.; van Duin, A. C. Reaxff Molecular Dynamics Simulations of Hydroxylation Kinetics for Amorphous and Nano-Silica Structure, and its Relations with Atomic Strain Energy. *J. Phys. Chem. C* **2016**, *120*, 305−317.
(31) Van Duin, A. C.; Dasgupta, S.; Lorant, F.; Goddard, W. A. Reaxff: A Reactive Force Field for Hydrocarbons. *J. Phys. Chem. A* **2001**, *105*, 9396−9409.
(32) Rimsza, J. M.; Yeon, J.; van Duin, A. C. T.; Du, J. Water-nanoporous silica interactions: comparison of ReaxFF and ab initio based molecular dynamics simulations. *J. Phys. Chem. C* **2016**, *120*, 24803−24816.
(33) Leroch, S.; Wendland, M. Simulation of Forces between Humid Amorphous Silica Surfaces: A Comparison of Empirical Atomistic Force Fields. *J. Phys. Chem. C* **2012**, *116*, 26247−26261.
(34) Ning, N.; Calvo, F.; Van Duin, A.; Wales, D.; Vach, H. Spontaneous Self-Assembly of Silica Nanocages into Inorganic Framework Materials. *J. Phys. Chem. C* **2009**, *113*, 518−523.
(35) Pitman, M. C.; Van Duin, A. C. Dynamics of Confined Reactive Water in Smectite Clay−Zeolite Composites. *J. Am. Chem. Soc.* **2012**, *134*, 3042−3053.
(36) Plimpton, S. Fast Parallel Algorithms for Short-Range Molecular Dynamics. *J. Comput. Phys.* **1995**, *117*, 1−19.
(37) Bhattacharya, S.; Gubbins, K. E. Fast Method for Computing Pore Size Distributions of Model Materials. *Langmuir* **2006**, *22*, 7726−7731.
(38) Frugier, P.; Gin, S.; Minet, Y.; Chave, T.; Bonin, B.; Godon, N.; Lartigue, J.-E.; Jollivet, P.; Ayral, A.; De Windt, L.; et al. SON68 Nuclear Glass Dissolution Kinetics: Current State of Knowledge and Basis of the New Graal Model. *J. Nucl. Mater.* **2008**, *380*, 8−21.
(39) Valle, N.; Verney-Carron, A.; Sterpenich, J.; Libourel, G.; Deloule, E.; Jollivet, P. Elemental and Isotopic (29 Si and 18 O) Tracing of Glass Alteration Mechanisms. *Geochim. Cosmochim. Acta* **2010**, *74*, 3412−3431.
(40) Criscenti, L. J.; Kubicki, J. D.; Brantley, S. L. Silicate Glass and Mineral Dissolution: Calculated Reaction Paths and Activation Energies for Hydrolysis of a Q_3 Si by H_3O^+ Using Ab Initio Methods. *J. Phys. Chem. A* **2006**, *110*, 198−206.
(41) Maekawa, H.; Maekawa, T.; Kawamura, K.; Yokokawa, T. The Structural Groups of Alkali Silicate Glasses Determined from ^{29}Si MAS-NMR. *J. Non-Cryst. Solids* **1991**, *127*, 53−64.
(42) Gouze, B.; Cambedouzou, J.; Parres-Maynadie, S.; Rébiscoul, D. How Hexagonal Mesoporous Silica Evolves in Water on Short and Long Term: Role of Pore Size and Silica Wall Porosity. *Microporous Mesoporous Mater.* **2014**, *183*, 168−176.
(43) Sharma, S. K.; Mammone, J. F.; Nicol, M. F. Raman Investigation of Ring Configurations in Vitreous Silica. *Nature* **1981**, *292*, 140−141.
(44) Yuan, X.; Cormack, A. Efficient Algorithm for Primitive Ring Statistics in Topological Networks. *Comput. Mater. Sci.* **2002**, *24*, 343−360.
(45) Rimsza, J.; Du, J. Structural and Mechanical Properties of Nanoporous Silica. *J. Am. Ceram. Soc.* **2014**, *97*, 772−781.
(46) Nedelec, J.; Hench, L. Ab Initio Molecular Orbital Calculations on Silica Rings. *J. Non-Cryst. Solids* **1999**, *255*, 163−170.
(47) McIntosh, C.; Toulouse, J.; Tick, P. The Boson Peak in Alkali Silicate Glasses. *J. Non-Cryst. Solids* **1997**, *222*, 335−341.
(48) Chen, C.; Du, J. Lithium Ion Diffusion Mechanism in Lithium Lanthanum Titanate Solid-State Electrolytes from Atomistic Simulations. *J. Am. Ceram. Soc.* **2015**, *98*, 534−542.
(49) Shirono, K.; Daiguji, H. Molecular Simulation of the Phase Behavior of Water Confined in Silica Nanopores. *J. Phys. Chem. C* **2007**, *111*, 7938−7946.
(50) Torshin, I. Y.; Weber, I. T.; Harrison, R. W. Geometric Criteria of Hydrogen Bonds in Proteins and Identification Ofbifurcated'hydrogen Bonds. *Protein Eng., Des. Sel.* **2002**, *15*, 359−363.
(51) Gordillo, M.; Martı, J. Hydrogen Bond Structure of Liquid Water Confined in Nanotubes. *Chem. Phys. Lett.* **2000**, *329*, 341−345.
(52) Luzar, A.; Chandler, D. Hydrogen-Bond Kinetics in Liquid Water. *Nature* **1996**, *379*, 55.
(53) Luzar, A.; Chandler, D. Effect of Environment on Hydrogen Bond Dynamics in Liquid Water. *Phys. Rev. Lett.* **1996**, *76*, 928.
(54) Hou, D.; Li, Z. Molecular Dynamics Study of Water and Ions Transport in Nano-Pore of Layered Structure: A Case Study of Tobermorite. *Microporous Mesoporous Mater.* **2014**, *195*, 9−20.
(55) Laage, D.; Hynes, J. T. A Molecular Jump Mechanism of Water Reorientation. *Science* **2006**, *311*, 832−835.
(56) Benesi, A. J.; Grutzeck, M. W.; O'Hare, B.; Phair, J. W. Room Temperature Solid Surface Water with Tetrahedral Jumps of 2h Nuclei Detected in $2H_2O$-Hydrated Porous Silicates. *J. Phys. Chem. B* **2004**, *108*, 17783−17790.
(57) Fournier, M.; Ull, A.; Nicoleau, E.; Inagaki, Y.; Odorico, M.; Frugier, P.; Gin, S. Glass Dissolution Rate Measurement and Calculation Revisited. *J. Nucl. Mater.* **2016**, *476*, 140−154.
(58) Gunnarsson, I.; Arnórsson, S. Amorphous Silica Solubility and the Thermodynamic Properties of H_4SiO_4 in the Range of 0 to 350 C at P Sat. *Geochim. Cosmochim. Acta* **2000**, *64*, 2295−2307.
(59) Guittonneau, C.; Gin, S.; Godon, N.; Mestre, J.; Dugne, O.; Allegri, P. A 25-Year Laboratory Experiment on French SON68 Nuclear Glass Leached in a Granitic Environment−First Investigations. *J. Nucl. Mater.* **2011**, *408*, 73−89.
(60) Ferrand, K.; Abdelouas, A.; Grambow, B. Water Diffusion in the Simulated French Nuclear Waste Glass Son 68 Contacting Silica Rich Solutions: Experimental and Modeling. *J. Nucl. Mater.* **2006**, *355*, 54−67.
(61) Wolfe, R. C.; Weil, K. G.; Shaw, B. A.; Pickering, H. W. Measurement of Ph Gradients in the Crevice Corrosion of Iron Using a Palladium Hydride Microelectrode. *J. Electrochem. Soc.* **2005**, *152*, B82−B88.
(62) Tossell, J. Theoretical Study on the Dimerization of $Si(OH)_4$ in Aqueous Solution and Its Dependence on Temperature and Dielectric Constant. *Geochim. Cosmochim. Acta* **2005**, *69*, 283−291.
(63) Doltsinis, N.; Burchard, M.; Maresch, W.; Boese, A.; Fockenberg, T. Ab Initio Molecular Dynamics Study of Dissolved SiO_2 in Supercritical Water. *J. Theor. Comput. Chem.* **2007**, *6*, 49−62.
(64) Rimsza, J.; Du, J. *ab initio* Molecular Dynamics Simulations of the Hydroxylation of Nanoporous Silica. *J. Am. Ceram. Soc.* **2015**, *98*, 3748−3757.

DOI: 10.1021/acs.jpcc.7b02734
J. Phys. Chem. C XXXX, XXX, XXX−XXX

Journal of Non-Crystalline Solids 452 (2016) 161–168

Contents lists available at ScienceDirect

Journal of Non-Crystalline Solids

journal homepage: www.elsevier.com/locate/jnoncrysol

Influence of low concentration V and Co oxide doping on the dissolution behaviors of simplified nuclear waste glasses

Xiaonan Lu [a], James J. Neeway [b], Joseph V. Ryan [b], Jincheng Du [a,*]

[a] Department of Materials Science and Engineering, University of North Texas, Denton, TX 76203, United States
[b] Pacific Northwest National Laboratory, Richland, WA 99354, United States

ARTICLE INFO

Article history:
Received 5 July 2016
Received in revised form 12 August 2016
Accepted 20 August 2016
Available online xxxx

Keywords:
Boroaluminosilicate glass
Nuclear waste glass
Chemical durability
Characterization
Transition metal oxide

ABSTRACT

Transition metal oxides are commonly present in nuclear waste and they can alter the structure, property and especially dissolution behaviors of the glasses used for waste immobilization. In this paper, we investigated vanadium and cobalt oxide induced structural and properties changes, especially the dissolution behavior, of International Simple Glass (ISG), a simulant nuclear waste glass system. Static chemical durability tests were performed at 90 °C with a pH value of 7 and a surface-area-to-solution-volume of 200 m^{-1} for 112 days on three glasses: ISG, ISG doped with 0.5 mol% Co_2O_3, and ISG doped with 2.0 mol% V_2O_5. Inductively Coupled Plasma-Mass Spectrometry (ICP-MS) was used to analyze the dissolved ion concentrations. It was found that doping with vanadium and cobalt oxide, even at the low doping concentration, significantly reduced the extent of the ISG glass dissolution. Differential Scanning Calorimetry (DSC) analysis showed that vanadium oxide doping reduced the glass transition temperature (T_g) while cobalt oxide did not significantly change the T_g of ISG. X-ray diffraction (XRD), Raman spectrometry and scanning electron microscopy (SEM) were used to analyze the glass samples before and after corrosion to understand the phase and microstructure changes. These results show that transition metal oxide can have a profound effect on the physical properties and dissolution behaviors of nuclear waste glasses.

1. Introduction

Vitrification is a mature process and space saving technology for nuclear waste disposal. Additionally, the amorphous nature of glass makes it relatively insensitive to the effects of radiation and allows the incorporation of a wide range of elements [1,2]. To ensure the long-term stability of the waste glass the chemical durability as a function of several variables must be understood.

Numerous factors are known to alter the chemical durability of glass [3–7]. These factors include glass composition [4], leachant composition [8,9], temperature [10–12], glass surface-area-to-solution-volume ratio (*S/V*) [6,13], pH [4,12,14,15], waste loading [16,17], and the effect of radiation doses [18,19]. Phenomenological analysis findings commonly divide glass alteration into three stages: initial diffusion/hydration, residual rate and rate resumption, based on the leaching rate change as a function of time [20]. Following the first stage, an amorphous, depleted, and hydrated layer, often referred to as a gel layer, is formed at the surface of glass [21,22]. The most acceptable mechanisms responsible for the five stages are ion exchange, water molecules attacking bridging oxygen bonds, chemical affinity of initial glass or passivating effect of the alteration layer, reactive diffusion between water or glass elements through the gel layer, and precipitation of secondary phases [23]. Recent findings also support a new mechanism represented by the stoichiometric dissolution of the glass and reprecipitation of an amorphous silica phase on the surface called interfacial dissolution-reprecipitation [24–26]. There is not yet a universally applicable mechanism and the exact one depends on glass compositions and alteration conditions.

Borosilicate glasses have demonstrated the ability to immobilize radioactive nuclides due to their stability, and relatively easy and inexpensive fabrication process [27]. International Simple Glass (ISG) is a simplified model composition for corrosion study of HLW glass. ISG was developed by researchers from six nations (the USA, France, the UK, Japan, Belgium and Germany) in a collaborative effort to study nuclear waste glass dissolution/corrosion mechanisms [12,20]. The idea is that with a standard composition, and, in a collaborative environment, the results from different groups are more comparable and detailed mechanism of glass dissolution can be elucidated in an expedited way.

To date, several studies have been performed with ISG and here we summarize the findings from a few of those. Inagaki et al. [12] have investigated the initial dissolution rate of ISG under dynamic leaching conditions with a variety of pH (3 — 10) and temperatures (25–90 °C). Static chemical durability tests on ISG were also studied by Fournier et al. [14] at high pH and temperature to accurately measure the time and rate of resumption of alteration. Gin et al. [15] investigated the corrosion behavior of ISG under alkaline condition, which leads to an extremely high

* Corresponding author.
E-mail address: Jincheng.du@unt.edu (J. Du).

http://dx.doi.org/10.1016/j.jnoncrysol.2016.08.026
0022-3093/

solubility of silicon and rapid dissolution. Reiser et al. [9] have started investigating the alteration of ISG in an iron-rich environment, which is present in the container that will hold the waste glass. Chemical durability of ISG containing rare-earth oxides (10 and 15 mol%) was studied by Mohd Fadzil et al. [17], which revealed a relatively good ability of ISG for immobilizing rare earth oxide waste. Other properties, such as topography, surface chemical composition, as well as thermal and mechanical properties of ISG have recently been studied [17,28–30].

Transition metal (TM) oxides have been found to strongly influence the structural and physical properties including the chemical durability of oxide glasses. For example, it is known that incorporation of a high valence cation, such as zirconium or hafnium, even at low concentrations, into oxide glasses can significantly improve the chemical durability, which is explained by its high cation field strength [2,31–36]. Fe^{3+} and Zn^{2+} ions were also found to improve the mechanical and chemical durability of oxide glasses due to their structural role as glass formers [37]. The presence of ZnO in borosilicate glass was found to significantly decrease the initial dissolution rate but increase the residual rate [6]. TiO_2 is less effective in terms of decreasing the initial dissolution rate of soda-lime borosilicate glass as compared to ZrO_2, but a drop of the rate can be observed when 4 mol% TiO_2 is added into the base glass in comparison with a smaller amount of TiO_2 added [31]. On the contrary, adding MoO_3 (0.5, 1.0, 2.0, and 4.0 mol%) into alkali borosilicate glasses causes phase segregation that leads to a decrease of chemical durability [38].

Although a number of chemical durability studies and the effect of glass composition on representative nuclear waste glasses have been performed, the effect of weakly soluble oxides in glasses, such as TM oxides, on the leaching behavior of glasses and their influence on gel layer formation and properties are still poorly understood. Our understanding of the effects of glass composition and structure on the chemical durability is still incomplete, as each kinetic regime of glass dissolution has a specific composition dependency, for instance, Zn in borosilicate glass has different effects on initial and residual rate [6], and synergistic effects of each glass component in the glass system exist [39]. The purpose of this work is to study the effect of TM oxide addition, especially at low concentration doping, on the thermal properties and dissolution behaviors of ISG-based glasses. More systematic studies of wider doping concentration ranges are being studied and will be reported separately.

ISG was used as the base glass composition due to the availability of the wide range of dissolution data under different conditions as a result of studies from the international community. To avoid the interaction effect, only one type of TM oxide was introduced in each sample. Co_2O_3 and V_2O_5 were chosen in order to study the effects of physical properties and chemical durability upon addition of these dopants. Cobalt and vanadium were chosen to be representative of group V and group VIII transition metals, respectively. In addition, V_2O_5 has been shown to improve sulfur solubility in borosilicate glasses, which is essential for immobilization of sulfate containing HLW [40,41]; therefore, understanding the effects of adding this oxide is beneficial. We have recently studied the influence of TM doping on optical absorption in ISG in order to understand their effect on the performance of laser assisted local electrode atom probe (LEAP) [42].

The rest of the paper is arranged as follows. The experimental details of glass synthesis, characterization such as thermal analysis, diffraction and scanning electron microscopy, and glass dissolution testing procedure and data analysis methods are then introduced. This is followed by results of the effect of Co_2O_3 or V_2O_5 doping on the dissolution, and thermal properties of ISG. Finally the discussion of the current results and conclusion is presented.

2. Experiment details and data analysis methods

2.1. Glass synthesis procedures

The glass samples were prepared by a two-step melting process to ensure homogeneity. Firstly, around of 500 g of ISG glass with composition shown in Table 1 was melted in a Pt—Rh crucible. The batch of the reagent grade raw transition metal oxide chemicals was mixed in an agate mill and then melted in the platinum crucible at 1275 °C for an hour in an electrical furnace. The melts were poured onto a stainless steel plate to cool to room temperature in air. After cooling, the glass sample was crushed into powders in a tungsten mill. In the second step, 50 g ISG powders were mixed with 0.5 mol% Co_2O_3 (ISG + Co) and 2.0 mol% V_2O_5 (ISG + V), respectively, and the mixtures were re-melted at 1350 °C for one hour. The melt was cast into a preheated stainless steel mold. The prepared glass samples were then annealed at T_g (around 550 °C) for 6 h and cooled down to room temperature at a rate of 60 °C/h. The ISG + V glass showed a light green color and the ISG + Co glass showed a blue-purple color. The color of both glass samples was homogeneous suggesting homogeneity of the glasses.

Ingots of standard ISG (provided by MO-SCI Corporation), ISG + V and ISG + Co were crushed and sieved to particle sizes of 63 μm–125 μm. Four coupons (about 5 mm × 5 mm) of each sample were polished to 0.04 μm. The powder samples and coupons were washed in both deionized (DI) water and then ethanol three times ultrasonically for 3 min. The washed powder and coupon samples were dried in an oven at 90 °C overnight before being used in the chemical durability tests.

2.2. Physical property characterization

Differential scanning calorimetry (DSC) was carried out on a NETZSCH STA 499 F3 in an argon environment with a gas flow of 60 mL/min, a heating rate of 5 °C/min, with a powdered glass sample (particle size between 63 μm to 125 μm) weighing between 23 mg and 25 mg in an Al_2O_3 pan.

Environmental scanning electron microscopy (ESEM) was conducted on an FEI Quanta ESEM with a spot size of 3.0 or 3.5 μm and electron energy of 15 kV to 30 kV to observe surface tomography of altered bulk samples after Au coating. Energy dispersive spectroscopy (EDS) was performed on an EDAX (TSL) EDS/EBSD system configured with the ESEM.

Glass powders before and after chemical durability tests were characterized with high resolution X-ray diffraction (XRD) on a Rigaku Ultima III with a scanning speed of 2°/min and a step of 0.05°/point.

Almega XR Raman spectrometer (Thermo Electron) was used for characterization of glass powders before and after chemical durability tests with an excitation wavelength of 532 nm and a spectral resolution of 2 cm^{-1}.

2.3. Chemical durability tests

Static chemical durability tests were performed at 90 ± 1 °C in a compact air forced convection oven (MTI Corporation) for 112 days with a glass surface-area-to-solution-volume (S/V) ratio of 200 m^{-1}. The geometric surface area of glass sample was estimated from an equation provided in McGrail et al. [43].

$$S_{GEO} = \frac{3}{\rho r} \tag{1}$$

where S_{GEO} is the specific surface area in m^2/g, r is the average radius of the particle (m), and ρ is the particle density (g/m^3). In this case, particle density used for calculation is 2.497 g/cm^3, calculated by the method

Table 1
Chemical composition of ISG.

Oxide	Al_2O_3	B_2O_3	CaO	Na_2O	SiO_2	ZrO_2
mol%	3.84%	15.97%	5.73%	12.65%	60.20%	1.62%
wt.%	6.10%	17.30%	5.00%	12.20%	56.30%	3.10%

developed by Fluegel [44]. The average radius of the particle is 47 μm. Therefore, the estimated geometric surface area of the glass powder is 0.0256 m^2/g. In addition, the density of standard ISG was measured using specific gravity of solids method with density bottles (10 mL and 25 mL) at room temperature. Four measurements were carried on standard ISG powders with a particle size between 63 μm to 125 μm, and a mass of about 1 g for the 10 mL density bottle and about 5 g for the 25 mL density bottle. Bubbles in the glass powders and deionized water were removed ultrasonically for at least 30 min until there was no visible bubble movement. It yielded a density of 2.523 ± 0.043 g/cm^3, when the density of distilled water used for calculation was 0.997 g/cm^3.

A buffer solution with a pH value of 7 was prepared using 0.2 mol/L of tris (hydroxymethyl) aminomethane (TRIS) buffer solution in 0.1 mol/L HNO_3 solution similar to a study by Rajmohan et al. [4]. There was no stirring during the whole chemical durability tests. A blank buffer solution was added as a reference to show whether elements leached from the PFA standard jar (Savillex Corporation) to confirm that the cleaning process was thorough.

5 mL solution aliquots were obtained at 1 day, 7 days, 14 days, 28 days, 56 days and 112 days (±0.5 h). Measurements of pH were performed using room temperature solutions on a bench-top pH/mV meter (Sper Scientific) with an accuracy of ±0.02 pH. The aliquots were filtered to 10,000 Da (0.45 μm) with syringe filters, then acidified with 5 mL of 0.5 mol/L HNO_3 to prevent the formation of colloids. Corroded coupon samples were obtained at 7 days, 56 days and 112 days, and cleaned in ethanol and air-dried. At the end of the corrosion test, powder samples were obtained and washed in ethanol, then dried at 90 °C overnight.

Solution analysis was carried out by a Varian 820 inductively coupled plasma-mass spectrometry (ICP-MS) with an uncertainty of ~3%. Solution samples were prepared by diluting the original solution samples by a factor of 100 with 2% (0.16 mol/L) HNO_3. Mixed standard solutions for calibration curves of ICP-MS were prepared in 2% HNO_3 at 100, 250, 500, 750, 1000 μg/L for silicon, sodium, calcium, aluminum and boron, and 10, 25, 50, 75, 100 μg/L for zirconium, vanadium and cobalt.

The silicon concentration in the solutions could not be determined accurately in this experiment because the R^2 value of silicon standard curve was less than 0.99. This situation might be caused by hydrolyzation of Si in the standard solutions. Additionally, Shabani et al. [45] have investigated the polyatomic species derived from silicon sample solution in the plasma, such as SiO, and SiOH, which may be another reason for the failure of Si concentration analysis.

2.4. Dissolution data analysis

ICP-MS results were used to calculate the normalized mass loss (NL, g/m^2) from the following equation,

$$NL_i = \frac{C_i}{X_i \frac{S}{V}} \tag{2}$$

where C_i is the concentration (g/m^3) of element i in solution, S/V is the glass surface-area-to-solution-volume ration (m^{-1}) and X_i is the mass fraction of element i in the glass. The decreasing volume of solution due to sampling was taken into account when calculating the NL.

Altered glass percentage, altered glass equivalent thickness and retention factor were also calculated according to the study by Rajmohan et al. [4].

The altered glass percentage (AG_B%) calculation is

$$AG_B\% = \frac{m^{leached}_{boron}}{m^0_{boron}} = \frac{m^{leached}_{boron}}{m^0_{glass}\cdot\chi_B} = \frac{C^t_B\cdot V^t + \sum_{i=1}^{t-1} C^i_B\cdot V^i_{sv}}{m^0_{glass}\cdot\chi_B} \tag{3}$$

where C^i_B is the boron concentration (g/m^3) at time i in solution, C^t_B is the boron concentration (g/m^3) at time t in solution, V^t is the solution volume (m^3) remaining in the reactor at time t, V^t_{sv} is the solution volume (m^3) sampled at the time t, m^0_{glass} is the initial mass of glass powder (g) and χ_B is the boron mass fraction in the glass (g/g).

Altered glass equivalent thickness $Eq(i)$ is obtained from the altered glass percentage AG_i%

$$Eq(i) = \left(1-(1-AG_i\%)^{\frac{1}{3}}\right)R_0 \tag{4}$$

where

$$R_0 = \frac{3}{\rho S_p} \tag{5}$$

where ρ is glass density (g/m^3). It is assumed that glass grains are perfect spheres and have the same specific surface area, S_p (m^2/g).

The retention factor (RF) for element i in the glass alteration products can be calculated using

$$RF_i = 1-\frac{Eq(i)}{Eq(B)} \tag{6}$$

3. Results

3.1. Effects of Co_2O_3 or V_2O_5 on transition temperature of ISG

DSC curves of standard ISG, ISG + Co, and ISG + V are shown in Fig. 1. The glass transition temperatures (T_g) were determined by intersecting tangents from the DSC curves with visual selection as shown in Fig. 1. Estimated errors of reported T_g are ±3 °C, according to a study by Guerette [29], where visual selection was also used when determining T_g. Moreover, T_g of ISG in the study by Guerette et al. is 575 ± 3 °C measured by differential thermal analysis in N_2 environment with a heating rate of 10 °C/min [29]. The T_g of ISG + Co is 6 °C higher than the un-doped ISG, while V_2O_5 reduces the T_g of ISG by 19 °C.

3.2. Effects of Co_2O_3 or V_2O_5 doping on ISG glass dissolution behaviors

The pH data obtained for the duration of the chemical durability experiments for the blank sample, standard ISG, ISG + V, and ISG + Co are shown in Fig. 2. The pH values of the buffer solutions from standard ISG and ISG + Co were close to the blank sample throughout the entire test, while ISG + V had lower pH values compared to the blank sample beginning at day 28. The difference became larger with extended time and the pH in the ISG + V test was 0.2 pH units lower than the other tests. The reason why V_2O_5 leads to a decrease of pH value might be the reaction of vanadate with either hydroxyl and amino functions of TRIS and forming V(V) complexes [46].

Comparisons of NLs of Al, B, Ca, Na, Zr, Co, and V in ISG, ISG + V and ISG + Co versus time are shown Fig. 3. B and Na had almost identical leaching behavior, except that B had about 10% higher NLs throughout the entire test. The release of B and Na started to decrease after about 14 days, where NLs of B and Na decreased by about 50% with V or Co oxides doping. Ca had similar NLs among the three glass samples through the test. Al values plateaued around 28 days for standard ISG and ISG + Co and 14 days for ISG + V. Standard ISG sample had the highest NL of Al among three samples, while ISG + V had the lowest. NLs of Zr in standard ISG and ISG + Co did not change significantly throughout the entire test, while Zr in ISG + V had about a six times higher NL than ISG and ISG + Co. In terms of dopants in ISG, NL of Co was about eight times higher than V in ISG after 60 days corrosion.

Retention factors of Na, Ca, Al, and Zr in ISG, ISG + V and ISG + Co at 112 days are shown in Table 2. Al and Zr were the elements mostly

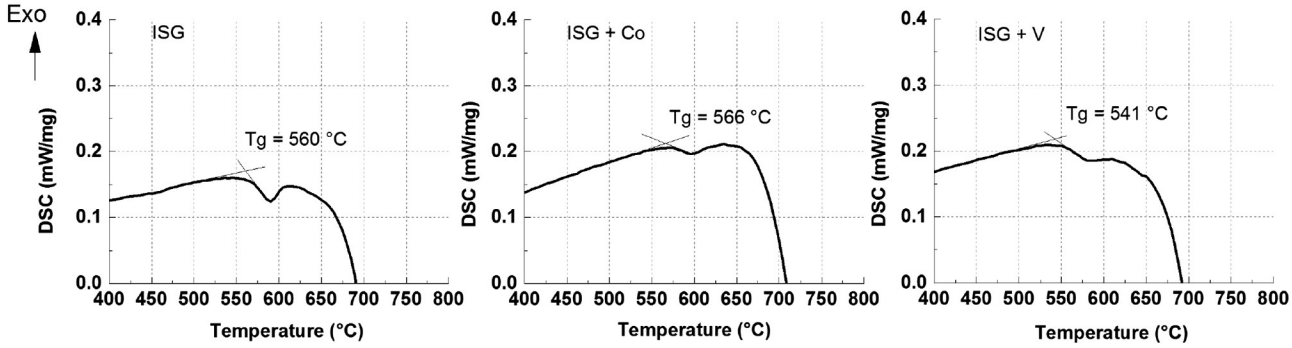

Fig. 1. DSC curves of ISG (left), ISG + Co (middle), and ISG + V (right) between 400 °C and 800 °C with a heating rate of 5 °C/min.

retained in the gel layer. Even though Si was not detected accurately from the ICP-MS analysis, it is well known that Si should also be retained in the gel layer. The amount of retained Na in the gel layer decreased by about 42% with addition of V_2O_5 or Co_2O_3 in comparison with un-doped ISG. The amount of Ca retained decreased by ~22% for Co_2O_3 and ~38% for V_2O_5 in comparison with un-doped ISG.

XRD patterns of standard ISG and 112 days corroded ISG powders are presented in Fig. 4. Due to the large amount of amorphous phase, there was no identification of crystalline phases after 112 days corrosion. XRD patterns of ISG + V and ISG + Co before and after corrosion are the same with un-doped ISG, which are not included in this paper for conciseness. However, in the study by Rajmohan et al. [4], where different conditions were used, XRD patterns of altered borosilicate glass surfaces are able to give some indications for the formation of calcium silicate hydrates after 150 days of alteration, even though clear identification is not possible due to the large amount of amorphous materials in the samples.

Raman spectroscopy was used to identify whether secondary phases were formed on the corroded glass surface. Raman spectra of standard ISG, ISG + Co, and ISG + V powder samples before and after 112 days corrosion are shown in Fig. 5. Peaks at 500 cm^{-1}, 630 cm^{-1}, 1000 cm^{-1} and 1450 cm^{-1} are contributed by Si-O-Si bending band, breathing mode of borosilicate rings, Q^n bands and the vibration band of the BO_3 group, respectively [16,29,47,48]. No secondary phases could be identified after 112 days of corrosion under the experimental conditions used for the three samples. Lower intensities of Raman peaks of ISG + Co samples may be due to the absorption of the 532 nm laser wavelength (532 nm). The UV–Vis spectrum of ISG + Co can be found in another study of ours [42]. An interesting finding is that the peak around 1000 cm^{-1} shifted to lower wavelengths as a result of adding V_2O_5 in ISG, which suggested depolymerization according to peak assignments of ISG from a study by Abdelouas et al. [49] This finding is consistent with the decrease of transition temperature induced by adding V_2O_5 in ISG, where lower the connectivity of glass structure would reduce the glass transition temperature. Similar Raman results can be found in a study by Molières et al. [16] where pristine and altered lanthanum-enriched borosilicate glasses were successfully characterized by Raman spectroscopy. Q^n bands shifted to lower wavenumbers with increasing lanthanum content in their study, while Si-O-Si shifted to higher wavenumbers. Raman spectra of the altered glass without lanthanum indicated complete polymerization of the silicate network, and the Q^n bands were better defined for the samples containing lanthanum [16].

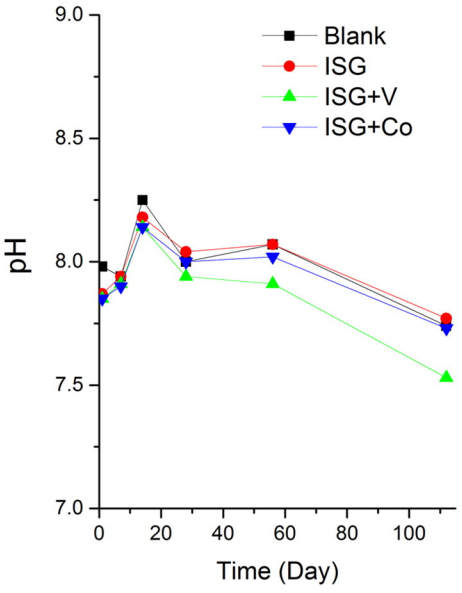

Fig. 2. pH values as a function of time for the blank sample, standard ISG, ISG + V, and ISG + Co. pH values were measured at room temperature.

3.3. Surface analyses

SEM images of standard ISG and ISG corroded for 7 days, 56 days and 112 days are shown in Fig. 6. Standard ISG started showing cracking after 7 days of corrosion and this phenomenon became more severe after 56 days. Cracks formed on the gel layer may be due to surface tension generated from evaporation of water in the gel layer during the air-drying process. This could be avoided by using the critical drying method to get around the surface tension induced damage during evaporation [50]. Possible precipitates were observed on the surface of the ISG sample corroded for 112 days. However, no secondary phase was detected with XRD and Raman spectroscopy study of the corroded samples. This can be due to the small volume of the secondary phase formed on the surface. SEM images of ISG + V and ISG + Co before and after corrosion are not presented in the paper, since they were almost the same as the images of standard ISG.

EDS analysis of cations in un-doped ISG and 112 days corroded ISG was performed, as presented in Table 3. Boron was not detected with the EDS analysis. The results show that the corroded glass surface has a decrease of Na and an increase of Si while Al remains as a similar fraction as compared to pristine ISG. This suggests that the corroded glass is covered by an alteration layer that is rich in silica. Although EDS analysis could not give accurate compositional changes of the gel layer due to its large interaction volume, the trend of increasing silicon and decreasing sodium content is evident here, which is also supported by solution analysis. EDS analysis was used to study corroded nuclear waste glass samples by Weaver et al. [30] and a decrease of sodium content of the altered layer as compared to the bulk was observed.

4. Discussion

The ICP-MS analysis results of the dissolution studies indicate that B and Na have almost identical leaching behaviors. V_2O_5 or Co_2O_3 at the

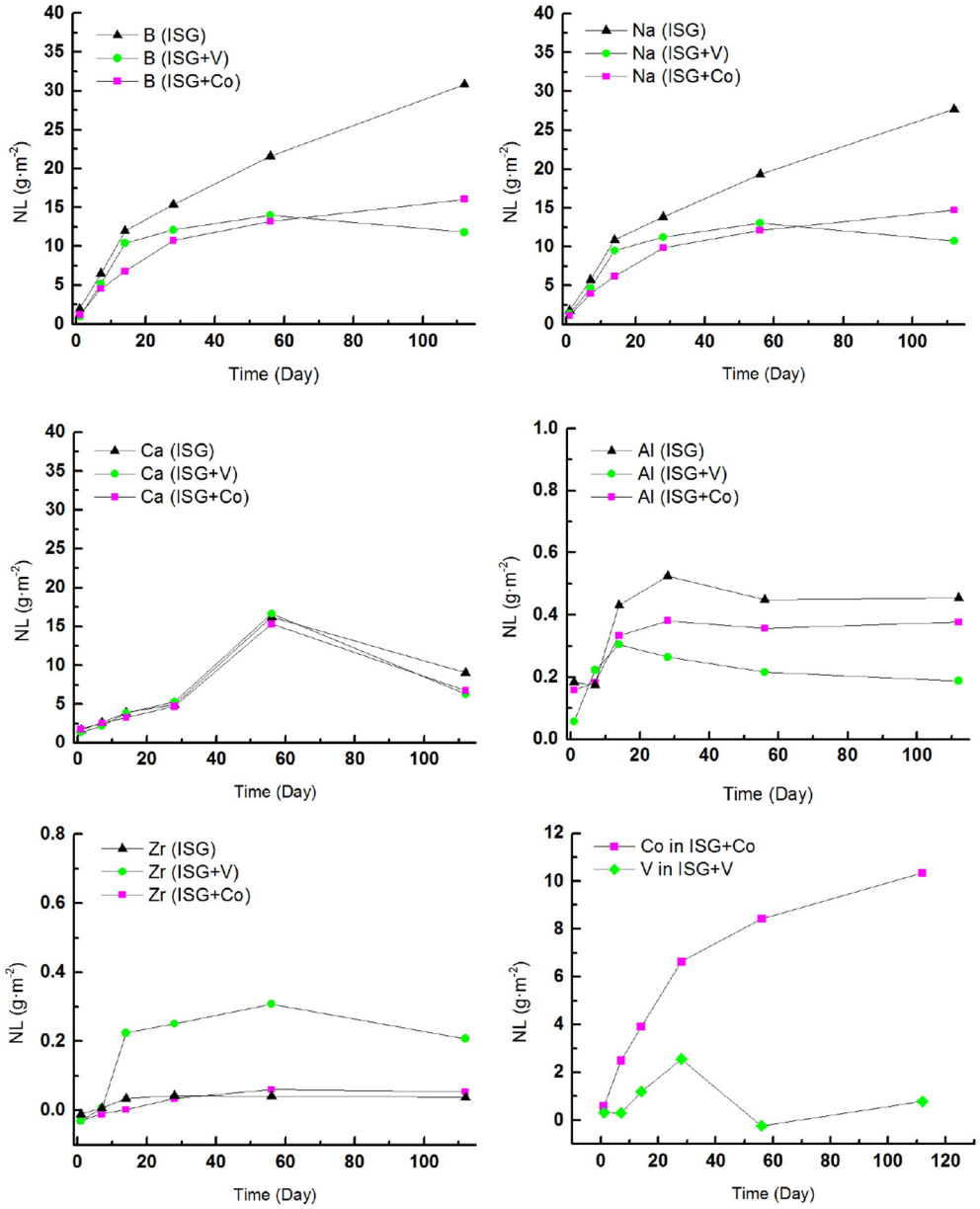

Fig. 3. Comparison of normalized mass losses versus time for B, Na, Ca, Al, Zr, Co, and V in ISG, ISG + V and ISG + Co.

doping level below 2 mol% was found to significantly reduce the dissolution rate as reflected in the large decrease of NL for B and Na. Ca in the three studied glasses showed similar NL values during the chemical durability tests. A decrease in NL of Ca was observed after 56 days, which might be due to the precipitation of secondary phases (such as calcium silicate hydrates). Even though both Al and Zr had relatively low NLs (less than 0.6 g/m^2) as compared to other elements, ISG + V had the lowest NL of Al and the highest NL of Zr. As for the NL of dopants in ISG, NL of V was less than Co even though the doping concentration is higher for V.

Table 2
Retention factors of Na, Ca, Al and Zr in ISG, ISG + V and ISG + Co at 112 days.

	Retention factor			
Sample	Na	Ca	Al	Zr
ISG	0.172	0.791	0.990	0.999
ISG + V	0.099	0.490	0.985	0.984
ISG + Co	0.099	0.611	0.980	0.997

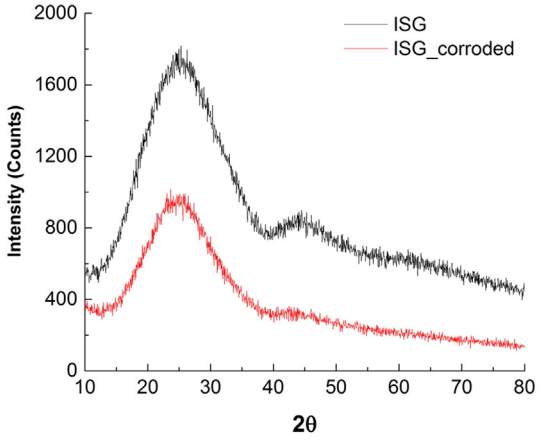

Fig. 4. XRD patterns of standard ISG and 112 days corroded ISG powder samples.

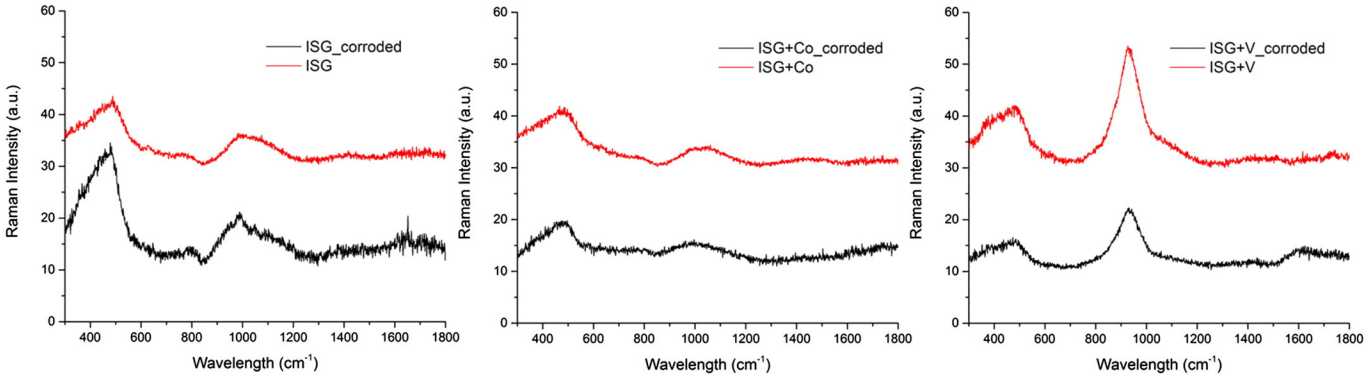

Fig. 5. Raman spectra of standard ISG (left), ISG + Co (middle), ISG + V (right) powder samples before and after 112 days' corrosion test.

The retention factor calculated from the dissolution data indicated that Al and Zr were the elements most retained in the gel, consistent with a study by Rajmohan et al. [4]. Even though Si was not able to be determined, it is well known that Si should also be retained in the gel. Some Ca^{2+} ions are retained in the gel layer and play the role of charge compensators for Al and Zr in the studied glasses; otherwise, as observed in dissolution of calcium-free glasses, Na would be partially retained in the alteration layer as a charge compensator which would result in different dissolution behavior of B and Na [4]. V_2O_5 or Co_2O_3 doping reduced the amount of Ca retained in the gel layer, with the larger reduction for V_2O_5 doping. This result suggests that some V or Co ions are retained in the amorphous gel layer to compensate the charge of Al in the network instead of Ca, where higher change state and doping concentration of V ions compared with Co ions might be the reasons that larger reduction of Ca retained in the gel layer for V_2O_5 doping. Further systematic studies of concentration effect of the two oxides are required.

According to our previous study of UV-spectra of V_2O_5 or Co_2O_3 doped ISG [42], where ISG + V has an absorption cutoff at 400 nm and ISG + Co has an absorption peak at 450–700 nm, as well as a cutoff at 300 nm, and other studies on the charge state and local environment of V or Co in borosilicate glasses with optical absorption [51,52], X-ray absorption [40,53], NMR [41], tetrahedral V^{5+} and octahedral Co^{2+} would be assumed to be the most dominant species in ISG structure.

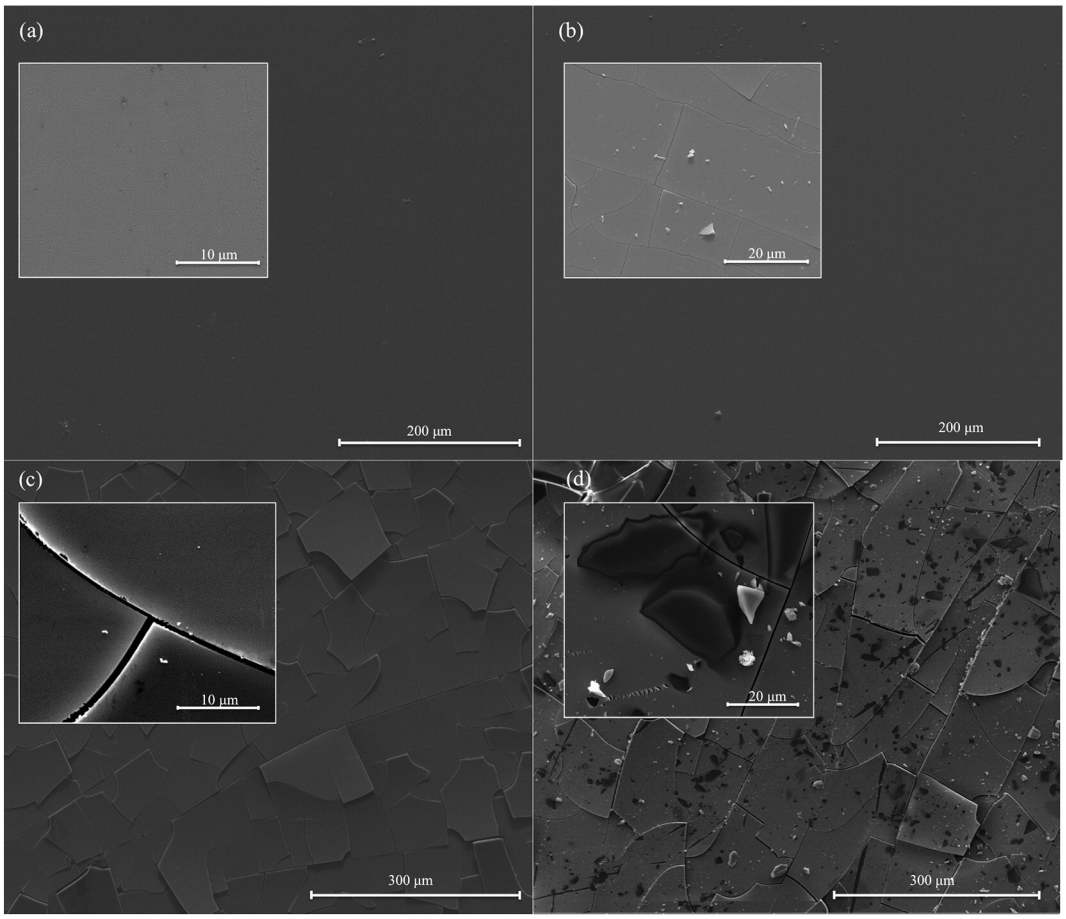

Fig. 6. SEM images of standard ISG (a), 7 days (b), 56 days (c) and 112 days (d) corroded ISG.

Table 3
Gross compositional analysis of cations in standard ISG and 112 days corroded ISG with EDS.

Element (at.%)	Standard ISG	112 days corroded ISG
Na	6.7	1.9
Al	5.0	6.1
Si	76.3	84.8
Ca	12.1	7.2

Future investigations are needed on structural roles and local environment of cations in ISG. Under the circumstances, according to field strength of the interstitial cations,

$$\varepsilon = \frac{Z_c}{(r_c + r_o)^2} = \frac{Z_c}{a^2}$$

where Z_c is the valence of the cation, and a is the ion-oxygen bond distance, which equals to the sum of ionic radius of cation r_c and the ionic radius of oxygen ion r_o [54]. Tetrahedral V^{5+} has a larger field strength due to a higher charge state and a smaller Shannon ionic radius (0.355 Å) as compared with octahedral Co^{2+} (0.65 Å for low spin and 0.745 Å for high spin) [55]. This may be one of the reasons that ISG + V had the highest chemical durability among all three glasses. Due to its high field strength, vanadium and cobalt ions are expected to be located in the modifier and non-bridging oxygen (NBO) rich regions based on the modified random network theory. They will increase the bonding strength of modifier rich region thus increasing the chemical durability as we observed. Molecular dynamics based computer simulations of Eu_2O_3 doped silica and sodium silicate glass showed that Eu^{3+} ions indeed enter the modifier-rich regions in modified glasses and have higher coordination numbers and more symmetric local environments as compared to in pure silica [56,57]. However, at much higher doping concentrations of TM oxide, their effect on chemical durability might change. For example, it was found by Douglas et al. [58] in vanadium oxide (0.1 to 2.0 mol%) doped soda lime silicate glasses that low doping increases T_g and density of the glass and surface tension of the melt. At doping concentrations higher than 1.5 mol%, vanadium oxide leads to a rapid decrease in these properties [58]. This was explained by the changing structural role of vanadium with concentration. At low concentration, vanadium ions enter the alkali-rich regions and strengthen the glass structure, while at high concentrations, vanadium ions (V^{5+}) become fourfold coordinated, replace Si^{4+} to enter and weaken the glass network [58]. Hence the effect of TM oxide on the dissolution behavior and physical properties can be more complicated due to similar effects of changing structure roles of TM ions in the glasses.

DSC thermal analysis showed that the T_g of ISG + Co is essentially the same as that of ISG within experimental error (±3 °C). On the other hand, ISG + V had a noticeable decrease of T_g. Siligardi et al. [59] have studied small amount (0.1, 0.5, 1.0 mol%) of vanadium oxide induced changes in CaO-ZrO_2-SiO_2 glasses. It was also found that V_2O_5 doping leads to a decrease of T_g, consistent with our findings. However, it was found in that work that V_2O_5 doping leads to a decrease of chemical durability of the base glass. This might be due to the presence of ZrO_2, which is known to significantly increase the corrosion resistant of oxide glasses [2,31–36].

5. Conclusions

Static chemical durability tests of ISG + Co, ISG + V and standard ISG samples were performed and the dissolution behaviors up to 112 days were studied using ICP-MS. The results show that doping with vanadium and cobalt oxide, even at low doping levels, significantly reduce the extent of dissolution, which was clearly shown by the reduction of the normalized mass losses of Na and B as compared to un-doped ISG. Interestingly, the dissolution product concentration analyses suggested that addition of transition metal oxide, especially V_2O_5 in ISG, significantly reduce the retention factor of Ca in the amorphous gel layer. The effects of TM oxide doping on thermal properties were also studied using DSC analyses and it was found that vanadium oxide doping reduces the T_g of ISG while Co_2O_3 doping did not significantly change the T_g of standard ISG. The results suggest that further studies of concentration effect of the two oxides, as well as other TM oxides and rare earth oxides, on ISG dissolution behaviors are necessary for a complete understanding of the doping effect. These works are underway and will be presented in future publications.

Acknowledgment

We gratefully acknowledge the financial support by DOE Nuclear Energy University Program (NEUP, project #13-5494). Glass melting was performed in the Glass Development Laboratory (GDL) at Pacific Northwest National Laboratory (PNNL). PNNL is operated by Battelle for the U.S. DOE under Contract DE-AC05-76RL01830. ESEM/EDS, XRD and Raman experiments were conducted at the Center for Advanced Research and Technology (CART) at the University of North Texas (UNT). We would like to acknowledge the support of Dr. Guido F. Verbeck and his group members, especially Emma Gorishek, for the assistance of ICP-MS analyses in the Laboratory of Imaging Mass Spectrometry at UNT. We would also like to acknowledge the support of the staffs of GDL of PNNL and UNT CART. Lastly, we want to thank Benjamin Parruzot (PNNL) and three anonymous reviewers for both their insightful comments and helpful suggestions.

References

[1] W. Lutze, R.C. Ewing, Radioactive Waste Forms for the Future, North-Holland, 1988.
[2] I.L. Pegg, Turning nuclear waste into glass, Phys. Today 68 (2015) 33–39.
[3] S. Ribet, I.S. Muller, I.L. Pegg, S. Gin, P. Frugier, Compositional effects on the long-term durability of nuclear waste glasses: a statistical approach, MRS Online Proc. Libr. 824 (2004).
[4] N. Rajmohan, P. Frugier, S. Gin, Composition effects on synthetic glass alteration mechanisms: part 1. Experiments, Chem. Geol. (2010) 106–119.
[5] S. Gin, X. Beaudoux, F. Angéli, C. Jégou, N. Godon, Effect of composition on the short-term and long-term dissolution rates of ten borosilicate glasses of increasing complexity from 3 to 30 oxides, J. Non-Cryst. Solids 358 (2012) 2559–2570.
[6] S. Gin, P. Frugier, P. Jollivet, F. Bruguier, E. Curti, New insight into the residual rate of borosilicate glasses: effect of S/*V* and glass composition, Int. J. Appl. Glas. Sci. 4 (2013) 371–382.
[7] I.W. Donald, Waste Immobilization in Glass and Ceramic Based Hosts: Radioactive, Toxic and Hazardous Wastes, 2010.
[8] T. Geisler, A. Janssen, D. Scheiter, T. Stephan, J. Berndt, A. Putnis, Aqueous corrosion of borosilicate glass under acidic conditions: a new corrosion mechanism, J. Non-Cryst. Solids 356 (2010) 1458–1465.
[9] J. Reiser, L. Neill, J. Weaver, B. Parruzot, C. Musa, J. Neeway, J. Ryan, N. Qafoku, S. Gin, N.A. Wall, Glass corrosion in the presence of iron-bearing materials and potential corrosion suppressors, MRS Online Proc. Libr. 1744 (2015) 139–144.
[10] J. Neeway, A. Abdelouas, B. Grambow, S. Schumacher, C. Martin, M. Kogawa, S. Utsunomiya, S. Gin, P. Frugier, Vapor hydration of SON68 glass from 90 °C to 200 °C: a kinetic study and corrosion products investigation, J. Non-Cryst. Solids 358 (2012) 2894–2905.
[11] B. Parruzot, P. Jollivet, D. Rébiscoul, S. Gin, Long-term alteration of basaltic glass: mechanisms and rates, Geochim. Cosmochim. Acta 154 (2015) 28–48.
[12] Y. Inagaki, T. Kikunaga, K. Idemitsu, T. Arima, Initial dissolution rate of the international simple glass as a function of pH and temperature measured using microchannel flow-through test method, Int. J. Appl. Glas. Sci. 4 (2013) 317–327.
[13] C. Jégou, S. Gin, F. Larché, Alteration kinetics of a simplified nuclear glass in an aqueous medium: effects of solution chemistry and of protective gel properties on diminishing the alteration rate, J. Nucl. Mater. 280 (2000) 216–229.
[14] M. Fournier, P. Frugier, S. Gin, Resumption of alteration at high temperature and pH: rates measurements and comparison with initial rates, Prog. Mater. Sci. 7 (2014) 202–208.
[15] S. Gin, P. Jollivet, M. Fournier, C. Berthon, Z. Wang, A. Mitroshkov, Z. Zhu, J.V. Ryan, The fate of silicon during glass corrosion under alkaline conditions: a mechanistic and kinetic study with the international simple glass, Geochim. Cosmochim. Acta 151 (2015) 68–85.
[16] E. Molières, F. Angeli, P. Jollivet, S. Gin, T. Charpentier, O. Majérus, P. Barboux, D. de Ligny, O. Spalla, Chemical durability of lanthanum-enriched borosilicate glass, Int. J. Appl. Glas. Sci. 4 (2013) 383–394.
[17] S. Mohd Fadzil, P. Hrma, M.J. Schweiger, B.J. Riley, Liquidus temperature and chemical durability of selected glasses to immobilize rare earth oxides waste, J. Nucl. Mater. 465 (2015) 657–663.

[18] M. Tribet, S. Rolland, S. Peuget, V. Broudic, M. Magnin, T. Wiss, C. Jégou, Irradiation impact on the leaching behavior of HLW glasses, Prog. Mater. Sci. 7 (2014) 209–215.
[19] R.C. Ewing, W.J. Weber, F.W. Clinard Jr., Radiation effects in nuclear waste forms for high-level radioactive waste, Prog. Nucl. Energy 29 (1995) 63–127.
[20] S. Gin, A. Abdelouas, L.J. Criscenti, W.L. Ebert, K. Ferrand, T. Geisler, M.T. Harrison, Y. Inagaki, S. Mitsui, K.T. Mueller, J.C. Marra, C.G. Pantano, E.M. Pierce, J.V. Ryan, J.M. Schofield, C.I. Steefel, J.D. Vienna, An international initiative on long-term behavior of high-level nuclear waste glass, Mater. Today 16 (2013) 243–248.
[21] C. Cailleteau, F. Angeli, F. Devreux, S. Gin, J. Jestin, P. Jollivet, O. Spalla, Insight into silicate-glass corrosion mechanisms, Nat. Mater. 7 (2008) 978–983.
[22] C. Cailleteau, F. Devreux, O. Spalla, F. Angeli, S. Gin, Why do certain glasses with a high dissolution rate undergo a low degree of corrosion? J. Phys. Chem. C 115 (2011) 5846–5855.
[23] P. Frugier, S. Gin, Y. Minet, T. Chave, B. Bonin, N. Godon, J.E. Lartigue, P. Jollivet, A. Ayral, L. De Windt, G. Santarini, SON68 nuclear glass dissolution kinetics: current state of knowledge and basis of the new GRAAL model, J. Nucl. Mater. 380 (2008) 8–21.
[24] R. Hellmann, S. Cotte, E. Cadel, S. Malladi, L.S. Karlsson, S. Lozano-Perez, M. Cabie, A. Seyeux, Nanometre-scale evidence for interfacial dissolution-reprecipitation control of silicate glass corrosion, Nat. Mater. 14 (2015) 307–311.
[25] S. Gin, P. Jollivet, M. Fournier, F. Angeli, P. Frugier, T. Charpentier, Origin and consequences of silicate glass passivation by surface layers, Nat. Commun. 6 (2015) 6360.
[26] S. Gin, J.V. Ryan, D.K. Schreiber, J. Neeway, M. Cabié, Contribution of atom-probe tomography to a better understanding of glass alteration mechanisms: application to a nuclear glass specimen altered 25 years in a granitic environment, Chem. Geol. 349–350 (2013) 99–109.
[27] W.J. Weber, R.C. Ewing, C.R.A. Catlow, T. Diaz de la Rubia, L.W. Hobbs, C. Kinoshita, H. Matzke, A.T. Motta, M. Nastasi, E.K.H. Salje, S.J. Zinkle, Radiation effects in crystalline ceramics for the immobilization of high-level nuclear waste and plutonium, 13 (1998) 1434.
[28] Y. Gong, A.W. Wren, N.P. Mellott, Quantitative morphological and compositional evaluation of laboratory prepared aluminoborosilicate glass surfaces, Appl. Surf. Sci. 324 (2015) 594–604.
[29] M. Guerette, L. Huang, In-situ Raman and Brillouin light scattering study of the international simple glass in response to temperature and pressure, J. Non-Cryst. Solids 411 (2015) 101–105.
[30] J.L. Weaver, J. Reiser, O.K. Neill, J.S. McCloy, N.A. Wall, A sampling method for semi-quantitative and quantitative electron microprobe analysis of glass surfaces, MRS Online Proc. Libr. 1744 (2015) 101–106.
[31] B. Bergeron, L. Galoisy, P. Jollivet, F. Angeli, T. Charpentier, G. Calas, S. Gin, First investigations of the influence of IVB elements (Ti, Zr, and Hf) on the chemical durability of soda-lime borosilicate glasses, J. Non-Cryst. Solids 356 (2010) 2315–2322.
[32] F. Angeli, T. Charpentier, M. Gaillard, P. Jollivet, Influence of zirconium on the structure of pristine and leached soda-lime borosilicate glasses: towards a quantitative approach by 17O MQMAS NMR, J. Non-Cryst. Solids 354 (2008) 3713–3722.
[33] G. Ferlat, L. Cormier, M.H. Thibault, L. Galoisy, G. Calas, J.M. Delaye, D. Ghaleb, Evidence for symmetric cationic sites in zirconium-bearing oxide glasses, Phys. Rev. B 73 (2006).
[34] L. Galoisy, E. Pélegrin, M. Arrio, P. Ildefonse, G. Calas, D. Ghaleb, C. Fillet, F. Pacaud, Evidence for 6-coordinated zirconium in inactive nuclear waste glasses, J. Am. Ceram. Soc. 82 (1999) 2219–2224.
[35] E. Pèlegrin, G. Calas, P. Ildefonse, P. Jollivet, L. Galoisy, Structural evolution of glass surface during alteration: application to nuclear waste glasses, J. Non-Cryst. Solids 356 (2010) 2497–2508.
[36] J. Hopf, S.N. Kerisit, F. Angeli, T. Charpentier, J.P. Icenhower, B.P. McGrail, C.F. Windisch, S.D. Burton, E.M. Pierce, Glass–water interaction: effect of high-valence cations on glass structure and chemical durability, Geochim. Cosmochim. Acta 181 (2016) 54–71.
[37] G. Calas, L. Cormier, L. Galoisy, P. Jollivet, Structure–property relationships in multicomponent oxide glasses, C. R. Chim. 5 (2002) 831–843.
[38] Y. Kawamoto, K. Clemens, M. Tomozawa, Effects of MoO_3, on phase separation of Na_2O-B_2O_3-SiO_2 glasses, J. Am. Ceram. Soc. 64 (1981) 292–296.
[39] S. Gin, Open scientific questions about nuclear glass corrosion, Prog. Mater. Sci. 7 (2014) 163–171.
[40] D.A. McKeown, I.S. Muller, K.S. Matlack, I.L. Pegg, X-ray absorption studies of vanadium valence and local environment in borosilicate waste glasses using vanadium sulfide, silicate, and oxide standards, J. Non-Cryst. Solids 298 (2002) 160–175.
[41] P. Sengupta, K.K. Dey, R. Halder, T.G. Ajithkumar, G. Abraham, R.K. Mishra, C.P. Kaushik, G.K. Dey, Vanadium in borosilicate glass, J. Am. Ceram. Soc. 98 (2015) 88–96.
[42] X. Lu, D.K. Schreiber, J. Neeway, J.V. Ryan, J. Du, Effects of optical dopants and laser wavelength on atom probe tomography analyses of borosilicate glasses, (in preparation).
[43] B.P. McGrail, W.L. Ebert, A.J. Bakel, D.K. Peeler, Measurement of kinetic rate law parameters on a Na-Ca-Al borosilicate glass for low-activity waste, J. Nucl. Mater. 249 (1997) 175–189.
[44] A. Fluegel, Global model for calculating room-temperature glass density from the composition, J. Am. Ceram. Soc. 90 (2007) 2622–2625.
[45] M.B. Shabani, Y. Shiina, F.G. Kirscht, Y. Shimanuki, Recent advanced applications of AAS and ICP-MS in the semiconductor industry, Mater. Sci. Eng. B 102 (2003) 238–246.
[46] A.S. Tracey, M.J. Gresser, Vanadium (V) oxyanions: interactions of vanadate with 1,1,1-tris (hydroxymethyl)ethane and with the buffer tris(hydroxymethyl) aminomethane, Inorg. Chem. 27 (1988) 1269–1275.
[47] D. Manara, A. Grandjean, D.R. Neuville, Advances in understanding the structure of borosilicate glasses: a Raman spectroscopy study, Am. Mineral. 94 (2009) 777–784.
[48] A.A. Osipov, L.M. Osipova, V.E. Eremyashev, Structure of alkali borosilicate glasses and melts according to Raman spectroscopy data, Glas. Phys. Chem. 39 (2013) 105–112.
[49] A. Abdelouas, Y. El Mendili, A. Aït Chaou, G. Karakurt, C. Hartnack, J. Bardeau, T. Saito, H. Matsuzaki, A preliminary investigation of the ISG glass vapor hydration, Int. J. Appl. Glas. Sci. 4 (2013) 307–316.
[50] R. Pandithage, Brief Introduction to Critical Point Drying, 2012.
[51] W.D. Johnston, Optical spectra of the various valence state of vanadium in $Na_2O{\bullet}2SiO_2$ glass, J. Am. Ceram. Soc. 48 (1965) 608–611.
[52] C. Nelson, W.B. White, Transition metal ions in silicate melts. IV. Cobalt in sodium silicate and related glasses, J. Mater. Res. 1 (1986) 130–138.
[53] H. Wen, P.A. Tanner, Optical properties of 3d transition metal ion-doped sodium borosilicate glass, J. Alloys Compd. 625 (2015) 328–335.
[54] X.H. Zhang, Y.L. Yue, H.T. Wu, Effects of cation field strength on structure and properties of boroaluminosilicate glasses, Mater. Res. Innov. 17 (2013) 212–217.
[55] R.D. Shannon, Revised effective ionic radii and systematic studies of interatomic distances in halides and chalcogenides, Acta Crystallogr. Sect. A: Cryst. Phys., Diffr., Theor. Gen. Crystallogr. 32 (1976) 751–767.
[56] J. Du, L. Kokou, Europium environment and clustering in europium doped silica and sodium silicate glasses, J. Non-Cryst. Solids 357 (2011) 2235–2240.
[57] L. Kokou, J. Du, Rare earth ion clustering behavior in europium doped silicate glasses: simulation size and glass structure effect, J. Non-Cryst. Solids 358 (2012) 3408–3417.
[58] D.R. Wing, A.G. Clare, L.E. Jones, The Effects of Vanadium Additions on the Surface Tension of Soda Lime Silicate Melts, Anonymous Advances in Fusion and Processing of Glass III, John Wiley & Sons, Inc. 2006, pp. 135–152.
[59] C. Siligardi, A.M. Ferrari, C. Leonelli, S. Bruni, Vanadium doping in CaO-ZrO2-SiO2 glasses, Phys. Chem. Glasses 43 (2002) 97–101.

Received: 7 February 2017 | Accepted: 11 May 2017

DOI: 10.1111/jace.14987

ORIGINAL ARTICLE

Journal of the American Ceramic Society

Effects of optical dopants and laser wavelength on atom probe tomography analyses of borosilicate glasses

Xiaonan Lu[1] | **Daniel K. Schreiber**[2] | **James J. Neeway**[2] | **Joseph V. Ryan**[2] | **Jincheng Du**[1]

[1]Department of Materials Science and Engineering, University of North Texas, Denton, Texas

[2]Pacific Northwest National Laboratory, Richland, Washington

Correspondence
Jincheng Du, Department of Materials Science and Engineering, University of North Texas, Denton, TX.
Email: du@unt.edu

Funding information
Nuclear Energy University Programs, U.S. Department of Energy (DOE), Grant/Award Number: #13-5494; EFRC: Center for Performance and Design of Nuclear Waste Forms and Containers, U.S. Department of Energy, Office of Science, Basic Energy Sciences, Grant/Award Number: #DESC0016584.

Abstract

Atom probe tomography (APT) is a novel analytical microscopy method that provides three dimensional elemental mapping with sub-nanometer spatial resolution and has only recently been applied to insulating glass and ceramic samples. In this paper, we have studied the influence of the optical absorption in glass samples on APT characterization by introducing different transition metal optical dopants to a model borosilicate nuclear waste glass. A systematic comparison is presented of the glass optical properties and the resulting APT data quality in terms of compositional accuracy and the mass spectra quality for two APT systems: one with a green laser (532 nm, LEAP 3000X HR) and one with a UV laser (355 nm, LEAP 4000X HR). These data were also compared to the study of a more complex borosilicate glass (SON68). The results show that the analysis data quality, particularly the compositional accuracy and sample yield, was clearly linked to optical absorption when using a green laser, while for the UV laser optical doping aided in improving data yield but did not have a significant effect on compositional accuracy. Comparisons of data between the LEAP systems suggest that the smaller laser spot size of the LEAP 4000X HR played a more critical role for optimum performance than the optical dopants themselves. The smaller spot size resulted in more accurate composition measurements due to a reduced background level independent of the material's optical properties.

KEYWORDS

atom probe tomography, borosilicate glass, microscopy, nuclear waste glasses, optical properties, rare earth oxide, transition metal oxide

1 | INTRODUCTION

Atom probe tomography (APT) is a novel microscopy analysis technique that is capable to provide three dimensional composition distributions at sub-nanometer resolution.[1,2] The recent introduction of modern laser pulsing systems[3-5] has expanded materials systems that can be studied by APT from primarily metals[6,7] to semiconductors,[8] inorganic glasses,[9-12] and ceramics materials.[13-16] There exist rich microstructure evolutions in glass materials in the nanometer scale, such as phase separation and nucleation behaviors, where APT can provide direct local compositional information that is challenging to obtain using standard microscopy methods such as scanning electron microscopy (SEM) and transmission electron microscopy (TEM). Borosilicate glasses, for example, have wide industrial and technological applications, and are the accepted form to immobilize high-level nuclear wastes.[17] APT has been

applied to study the corrosion layer microstructure of samples undergone long-term dissolutions and provide insights on the dissolution mechanism.[9,10]

A schematic illustration of a local electrode atom probe (LEAP) system, the most common commercial APT system, is shown in Figure 1. By applying a high DC voltage and either laser or voltage pulses onto a very sharp (~100 nm diameter) needle-shaped specimen, atoms from the specimen apex are field evaporated in a controllable manner. A position-sensitive single-ion detector collects both chemical (time of flight mass spectrometry) and spatial information for each ion, enabling reconstruction of a 3D elemental map of the specimen with optimally sub-nanometer spatial resolution.[18] There is, however, significant uncertainty regarding the laser-tip interaction for these novel materials systems and particularly the correlation between optical properties of the bulk material and its behavior in the high-field environment of field evaporation.[19-21]

Field evaporation of oxides by different laser systems in LEAP analyses has also been studied and compared recently. Santhanagopalan et al.[22] have compared the green wavelength (532 nm) laser-assisted LEAP 3000X Si and UV wavelength (355 nm) laser-assisted LEAP 4000X HR on the analysis of $LiFePO_4$ and results revealed significant amounts of Li deficiency using the green wavelength laser despite nominally similar field evaporation conditions. Many studies have systematically investigated the effects of specimen shapes, laser wavelength, laser power and frequency on field evaporation of oxides in APT.[3,13,14,23,24] Shorter wavelength of laser has been proven to provide better field evaporation for oxides, which leads to a higher mass resolving power and signal-to-noise ratio with fewer premature specimen fractures.

Recently Gin et al.[10] analyzed a nuclear glass specimen altered 25 years in a granitic environment using laser-assisted APT, which provided insights into the glass corrosion processes and mechanisms at shorter length scales than was possible previously. This study was soon thereafter replicated by others in similar glass corrosion environments to propose a dissolution/reprecipitation model of glass alteration.[9] Both studies investigated the interface between hydrated and pristine glass in SON68, a non-radioactive surrogate of the French nuclear waste glass R7T7. The concentration profiles of key elements at the hydration interface from APT showed that boron exhibits an extremely sharp profile located outside of the Li/H inter-diffusion layer, which is contrary to prior theories. Moreover, a comparison of the width of the boron profile within the hydrated glass as measured by APT, energy filtered transmission electron microscopy and high resolution secondary ion mass spectroscopy (NanoSIMS) revealed that APT appeared to be the most accurate and reliable technique to determine concentration profiles at the water/glass interface. Hellmann et al.[9] subsequently investigated SON68 altered at 50°C in deionized water by APT and SIMS and proposed an interfacial dissolution-reprecipitation mechanism, which is not a diffusion-controlled process. Critical to this interpretation is whether or not depletion profiles of Na and Li, measured by both Gin et al.[10,12] and Hellmann et al.[9] using APT, can be considered to be reliable or an artifact of the field evaporation process.

However, the usage of transparent glass samples poses a challenge to laser-assisted APT due to low optical absorption at the laser wavelength of the samples. Without impurities or doping, sodium boroaluminosilicate glasses are transparent in the visible range. Doping with

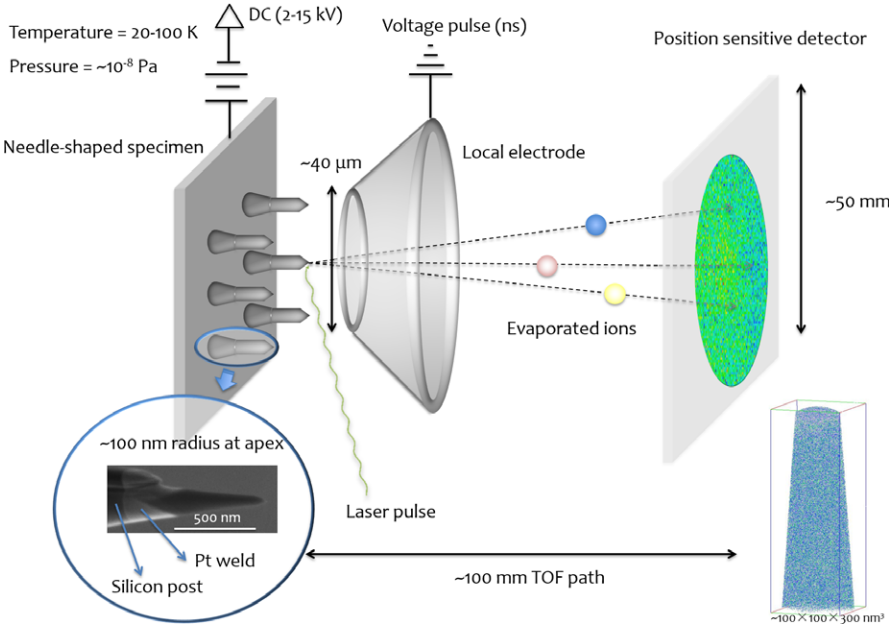

FIGURE 1 Schematic illustration (not to scale) of a local electrode atom probe (LEAP) system (adapted from Kelly et al.[1] and Schreiber et al.[2]) and its application to glass samples [Color figure can be viewed at wileyonlinelibrary.com]

transition metals leads to absorption peaks in visible wavelengths that create color due to electron excitation in the split d electronic energy level of transition metal ions. For free transition metal ions, the 3*d* electronic levels are degenerate; however, for transition metal ions in a crystal or glass, the coordinating anions create an electrical field, called ligand or crystal field, that leads to a small splitting of d electron energy levels (~1-3 eV). The absorption of photons by electronic excitation between the splitting d electron levels results in absorption and color formation in the visible range.[25] The purpose of this paper is to test the effect of selected transition metal and rare earth doping on optical absorption and in term of the detection efficiencies of APT of nuclear waste glass model systems with two generations of APT systems that equip different laser sources. In particular we consider the quantitative accuracy of APT for alkali species (e.g. Li and Na), which are critical to glass corrosion but difficult to quantify reliably.

A simple model glass has recently been developed by a collaborative international working group for studying nuclear waste glass dissolution/corrosion mechanisms. The International Simple Glass (ISG) is a model, non-activated high-level waste aluminoborosilicate glass containing only 6 oxides, in contrast to the approximately 26 components that make up the SON68 that it is based on.[26,27] However, difficulties appeared while analyzing ISG samples. Frequent sample fractures were accompanied by a prevalence of Si^{3+} in the mass spectra, not typically observed in SON68 under similar analysis conditions and suggestive of a higher evaporation field,[28] and a lower than expected Na concentration. In a study by Gin et al.,[12] 20% rate of success was obtained for APT analysis on ISG. Together these suggest that achieving controlled field evaporation of ISG is more challenging than it is for SON68 glass. Bunton et al.[3] presented that pulse energy density, thermal diffusivity of the specimen material, specimen tip radius, specimen taper angle, laser spot size and wavelength are the six interrelated factors that influence instrument performance. In their study, smaller spot size improved the mass resolving power of aluminum but had no effect on the stainless steel, while shorter wavelength improved the mass resolving power of stainless steel but had no effect on the aluminum. There is not enough literature available about influences of laser parameters on the characterization of glass and ceramic materials, let alone vitrified nuclear waste. Also, APT studies on nuclear glasses have generated significant new discussions on corrosion mechanisms that need further validation using simpler material systems that do not necessarily perform as well during field evaporation.

In this paper, the influences of transition metal dopants on glass composition measurements and overall APT data quality and yield are studied systematically using APTs equipped with lasers of different wavelengths and spot sizes.

2 | EXPERIMENTAL DETAILS

2.1 | Glass sample preparation

The nominal batch composition of the ISG is shown in Table 1. A master 500 g batch of ISG was prepared in which the reagent grade chemicals were first mixed in an agate with a grinding machine for 4 minutes to homogenize the mixture. The ISG was lab-batched to control the raw materials and subsequent optical absorption, hence not from the standard ISG produced by MO-SCI Corporation (Rolla, MO).[26] The powder mixture was then placed into a platinum crucible with a lid and melted in an electrical furnace at 1275°C for 1 hour. The melts were then poured onto a stainless steel plate to cool to room temperature. After cooling, the glass was crushed with a vibrational mill using a tungsten mortar and ball for 5 minutes. The first series of doped ISG compositions were then prepared using 50 g of the crushed ISG powder thoroughly mixed with different oxides of transition metals or rare earth elements, each dopant and batch compositions are listed in Table 2. The mixtures were re-melted at 1350°C for 1 h and cast into a preheated stainless steel mold (~2 cm×4 cm×1 cm). The higher temperature used for doped ISG samples was to increase the homogeneity of the glasses, where the colors of the glass samples distributed uniformly at this melting condition. The glass samples were annealed at 550°C for 6 hours and cooled to room temperature at a rate of 60°C/h. The cast, annealed bars, were then mechanically cut and polished for UV-Vis analysis and APT sample preparation. Needle-shaped APT specimens were prepared from V_2O_5-doped ISG (ISG+V), Co_2O_3-doped ISG (ISG+Co) and SON68 samples (composition of SON68 can be found in a study by Neeway et al.[29]) using standard focused ion beam lift-out procedures with a dual-beam scanning electron microscope/focused ion beam system (FEI Helios Nanolab 600 and FEI Quanta 3D-FEG, Hillsboro, OR, USA).[30] Annular milling was performed using 30 kV Ga^+ and final cleanup was performed with 2 kV Ga^+ to minimize ion beam damage to the sample surface. The nominal final tip diameter was approximately 100 nm.

TABLE 1 Batch chemical composition of ISG

Oxide	Al_2O_3	B_2O_3	CaO	Na_2O	SiO_2	ZrO_2
Mol%	3.84%	15.97%	5.73%	12.65%	60.20%	1.62%
Wt%	6.10%	17.30%	5.00%	12.20%	56.30%	3.10%

TABLE 2 Nominal loading of transition metal (TM) and rare earth (RE) element oxide dopants added to ISG

TM Oxide	Cr_2O_3	Fe_2O_3	Co_2O_3	V_2O_5	MnO_2	NiO	CuO	TiO_2
Cation at.%	0.42%	0.40%	0.39%	0.35%	0.37%	0.50%	0.50%	0.50%
Oxide wt%	0.50%	0.50%	0.50%	0.50%	0.50%	0.58%	0.62%	0.62%
RE Oxide	**Er_2O_3**	**Pr_6O_{11}**	**CeO_2**	**Nd_2O_3**	**Eu_2O_3**	**Sm_2O_3**		
Cation at.%	0.50%	0.50%	0.50%	0.50%	0.50%	0.50%		
Oxide wt%	1.49%	1.32%	1.34%	1.31%	1.37%	1.36%		

2.2 | UV-Vis absorption spectra measurement

UV-Vis spectra were collected at room temperature using a Thermo Scientific Evolution 220 (ThermoFisher Scientific, Waltham, MA, USA) for wavelengths between 200 and 800 nm. Samples for UV-Vis analysis were cut and polished down to grade P1200 (about 15 μm) on both sides. The thicknesses of the samples varied from 1 to 10 mm, which were later used for the calculations of extinction coefficients of the samples. Since the lab-batched ISG is transparent and has no absorption in the visible range, the extinction coefficients were normalized relative to the sample thickness.

2.3 | Atom probe tomography methods

APT analyses were performed using two different models of the CAMECA (Gennevillier Cedex, France) LEAP equipped with different laser pulsing systems: a LEAP 3000X HR and a LEAP 4000X HR. The LEAP 3000X HR uses a 532 nm wavelength laser and achieves a nominal spot size at the specimen of about 10 μm diameter (4σ confidence interval), while the LEAP 4000X HR has a 355 nm wavelength laser and in-vacuum optics that achieve a substantially smaller spot size of about 3 μm diameter.[31] These spot size estimates are approximate and therefore calibration experiments were performed for comparing data from the two tools using commercially available pre-sharpened Si microposts that exhibit reproducible tip shapes and absorb both laser wavelengths efficiently. The silicon charge state ratio (Si^{2+}:Si^{1+}) was determined as a function of laser energy at a fixed base temperature of 40 K, a laser pulsing rate of 200 kHz and a detection rate of 0.55% (0.0055 detected ions per pulse) for both tools. Data were collected with both ascending and descending laser energies to obviate any effect of tip radius evolution. The results are plotted in Figure 2. To achieve similar Si field evaporation, the LEAP 3000X HR required approximately a factor of 25 higher laser energy per pulse than the LEAP 4000X HR, in comparison to a factor of 15 difference reported for similar tools previously.[22] An additional

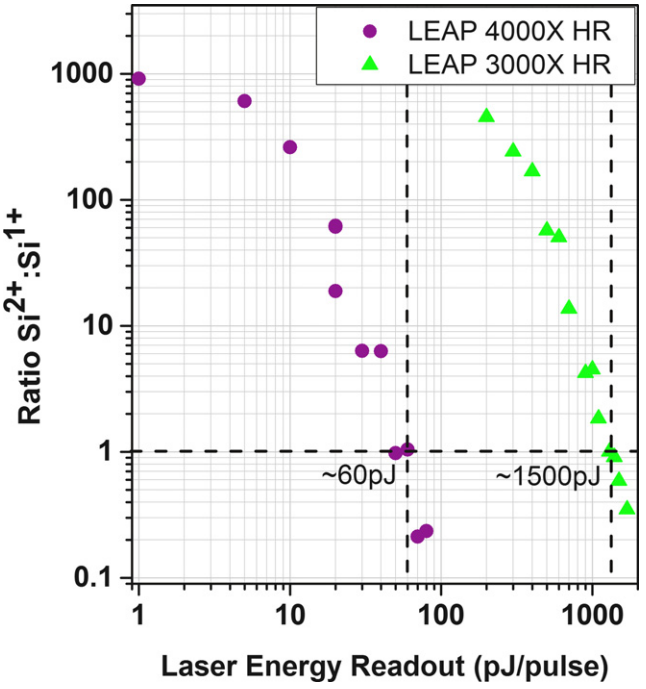

FIGURE 2 Comparison of Si charge state ratio as a function of laser energy readout for the LEAP 3000X HR and the LEAP 4000X HR [Color figure can be viewed at wileyonlinelibrary.com]

comparative analysis of a LEAP 3000X HR and a LEAP 5000X HR, which uses nominally the same laser system as a LEAP 4000X HR, recently showed a similar factor of 12 difference.[32] Note that the calibration is imperfect as it is not possible to separate differences in laser spot size from laser wavelength and other uncontrollable experimental parameters (e.g. tip shape differences), but it does enable a reasonable comparison of experimental parameters between the two tools.

Experimental parameters for APT data collection were selected based on prior experience with altered SON68 glass using the LEAP 4000X HR.[10] From this baseline, APT data of ISG+V, ISG+Co and SON68 were collected with the LEAP 4000X HR at a base temperature of 40 K, a pulsing rate of 200 kHz, a detection rate of 0.25% or 0.3% and laser energies between 120 and 700 pJ/pulse. Based on the calibration experiment above, the running

parameters for the LEAP 3000X HR were selected to be a base temperature of 40 K, a pulse rate of 200 kHz, a detection rate of 0.2% and laser energies between 4 and 10 nJ/pulse (the maximum practical energy for this laser system). Data reconstruction and analyses were performed with the IVAS 3.6.8 software package (CAMECA).

3 | RESULTS

3.1 | Effect of glass composition on UV-Vis adsorption spectra

The measured absorption coefficients of un-doped ISG and SON68 from UV-Vis analysis are plotted in Figure 3. In each panel of the figure, a circle is used to indicate the 355 nm wavelength of the laser in the LEAP 4000X HR and a triangle marks the 523 nm wavelength of the LEAP 3000X HR. By definition, ISG is a simple glass with few additional elements that enable optical absorption. This results in a visibly transparent and colorless glass to the human eye. This is confirmed by UV-Vis characterization that reveals a very sharp drop off in the optical absorption around 300 nm with no sigifnicant absorption within the visible wavelength range. By contrast, SON68 contains several elements that absorb well within the visible spectrum resulting in the glass being visually black in appearance. In the UV-Vis absorption spectrum, this black appearance is reflected by significant absorption across much of the visible light spectrum. In the context of the two laser pulsing systems used in this study, un-doped ISG is not expected to absorb well at either wavelength, while SON68 is expected to absorb the UV wavelength laser (355 nm) well, and only moderately well at the green wavelength laser (532 nm).

The addition of transition metals evokes a wide range of optical properties in the ISG. For example, ISG+Co, ISG+Ni and ISG+Mn have good absorption at ~600, ~450 and ~475 nm, respectively. ISG+Cu has an absorption band at ~750 nm, while ISG+Cr absorbs wavelengths between 350 and 625 nm. The resulting UV-Vis absorption spectra from a wide range of transition metal doped ISG are exhibited in Figure 4. ElBatal et al.[33] have also studied UV-Vis absorption of transition metal doped SiO_2–B_2O_3–Na_2O glasses and the optical density of the borosilicate glasses containing different transition metals. The absorption peak positions for the doped ISG samples are in a good agreement with those from the study by ElBatal et al.,[33] even though there are some noticeable shifts due to the difference in base glass compositions between the two that influences the splitting of the 3*d* electronic level.

The optical properties of ISG can also be altered by incorporating rare earth oxide elements. The resulting UV-Vis absorption spectra from these samples are summarized in Figure 5. Compared to the broad absorption peaks created by the 3*d* transition metals in ISG, the absorption spectra of rare earth doped glasses show more complex and sharper features across much narrower ranges of wavelengths. These well-defined features are consistent with the published spectra in the literature. For example, a study by Nachimutht and Jagannathan[34] on the absorption spectrum of Pr^{3+}-doped $2CaO–3B_2O_3–Al_2O_3$ glass, and spectra of absorption coefficients of Nd^{3+} (3 wt%) glass in a study by Dorosz[35] are in excellent agreement with the measured spectra of rare earth doped ISGs. It is well-known that shielding of $5S^25P^6$ orbitals causes 4*f* electrons to be less influenced by the ligand fields and hence their absorption spectra have sharp features nominally independent of the host environment. Conversely, the electronic levels of *d* electrons of the transition metals are strongly influenced by the local environment and ligand fields.

In the context of improving the optical properties of ISG for characterization by laser-pulsed APT, it is apparent that the broader absorption peaks created by transition metal doping are more advantageous than the extremely sharp features created by rare earth incorporation. Therefore, ISG+V, ISG+Co and SON68 were chosen for laser-assisted APT analyses according to their relevant optical

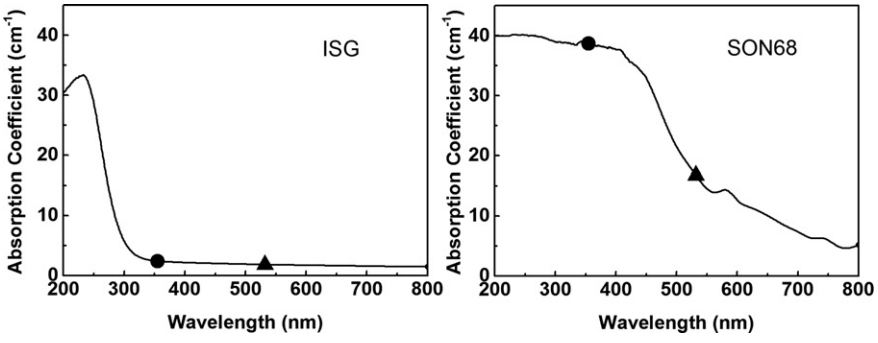

FIGURE 3 Absorption coefficient plots of ISG and SON68. The circle represents the absorption coefficient for UV laser wavelength (355 nm) and the triangle represents the absorption coefficient for green laser wavelength (532 nm)

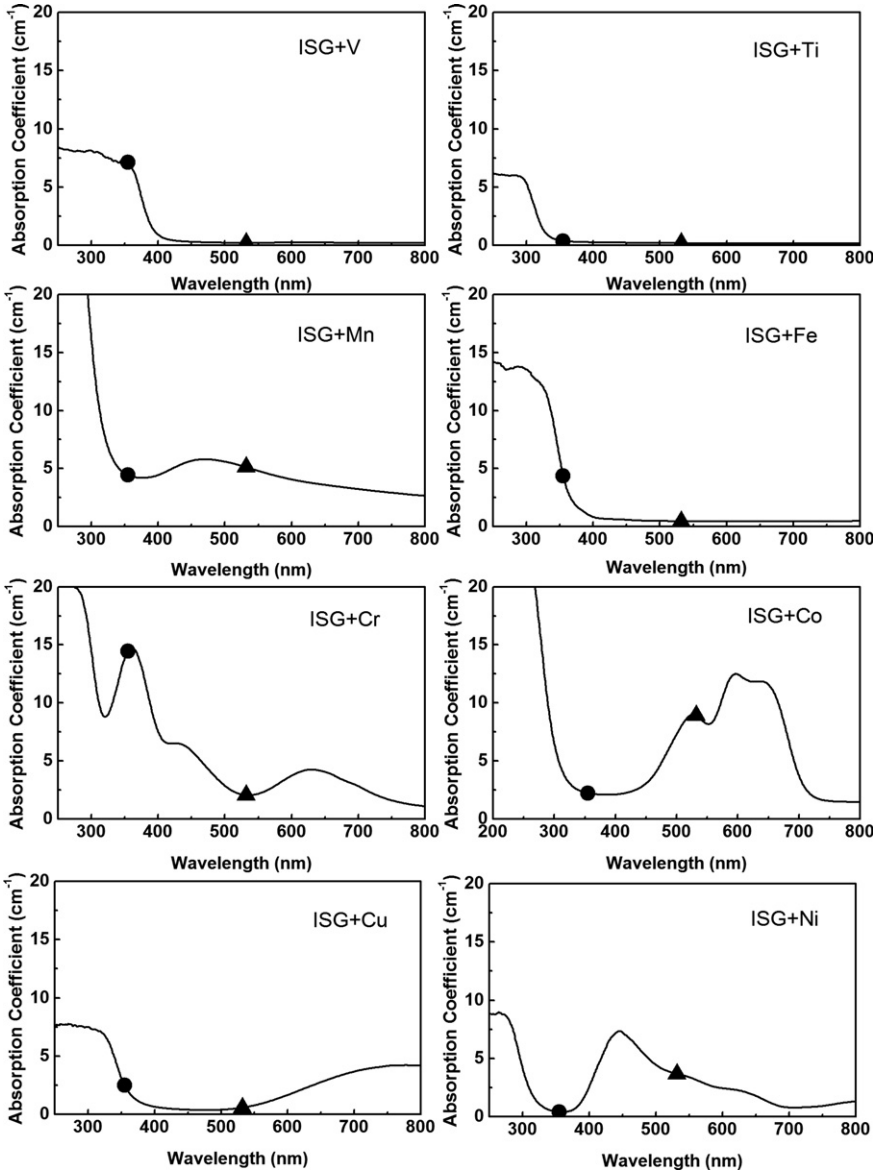

FIGURE 4 Absorption coefficient plots of first series of transition metal elements doped ISGs. The circle represents the absorption coefficient for UV laser wavelength (355 nm) and the triangle represents the absorption coefficient for green laser wavelength (532 nm)

absorption properties. The measured absorption coefficients of ISG+V, ISG+Co and SON68 at the relevant wavelengths of the laser utilized in this study are summarized in Table 3. Un-doped ISG has an absorption cutoff at ~300 nm, suggesting that, neglecting field-induced band bending during APT field evaporation,[20] it is nominally transparent to both the UV and green laser wavelengths. ISG+V has a good absorption coefficient for the UV laser wavelength and is nominally transparent to the green laser wavelength, and conversely ISG+Co has good absorption at green wavelengths and is relatively transparent at the UV laser wavelength. Lastly SON68 glass has a good absorption coefficient at both wavelengths, but is significantly more efficient at the UV wavelength (355 nm) than the green wavelength (532 nm). Comparison of APT data collected from these three samples could therefore provide novel insights into the systematic influence of transition metal doping, optical properties and applied laser wavelength on the overall APT data quality.

3.2 | Effect of glass composition on APT characterization

3.2.1 | Comparison of APT mass spectra

Mass spectra collected using green (λ=532 nm) laser pulsing on the LEAP 3000X HR are presented in Figure 6. A broad and prominent evaporation hump is apparent in all three spectra, indicating significant delayed evaporation of ions at an ill-defined time after the laser pulse. As the

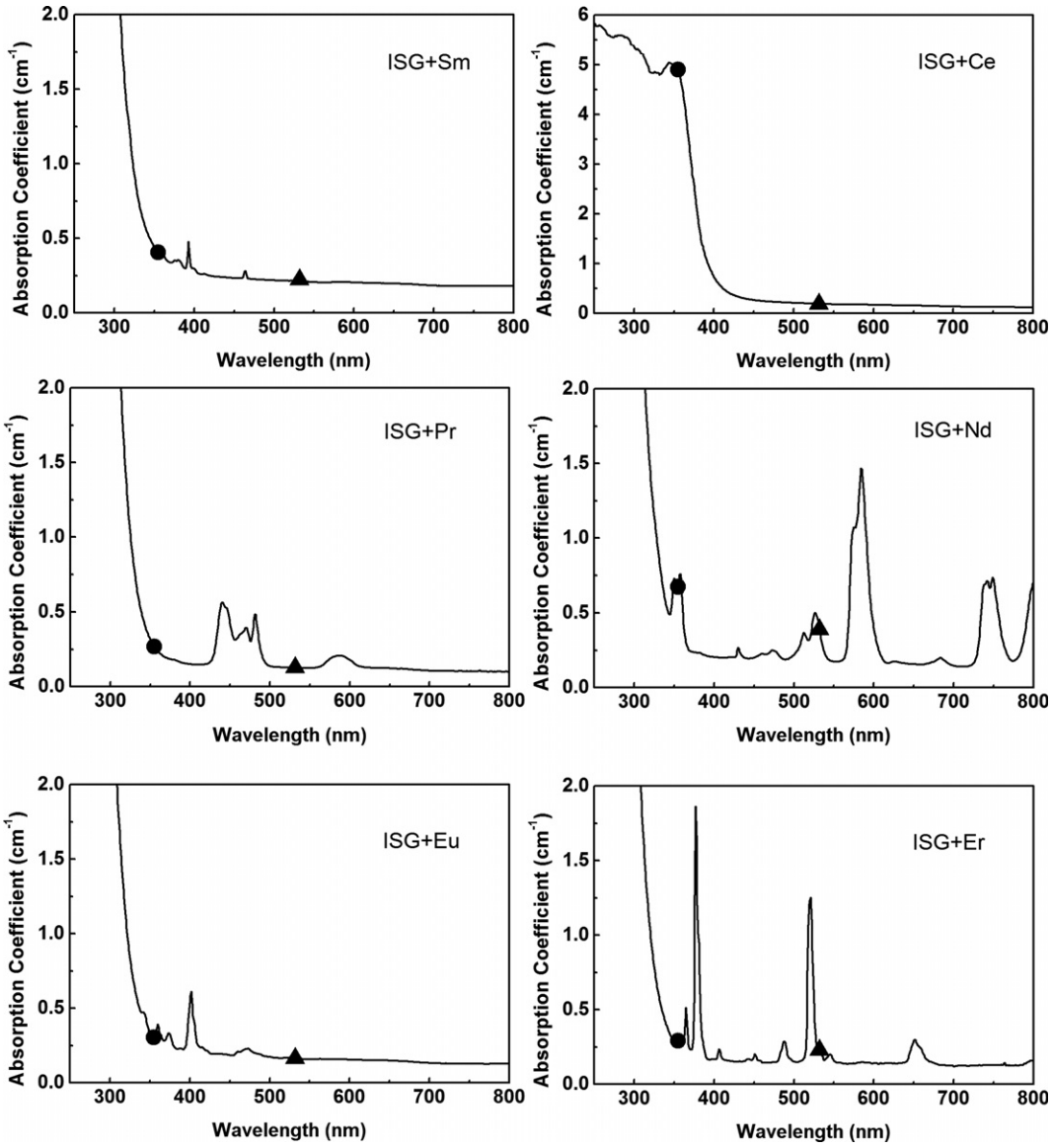

FIGURE 5 Absorption coefficient plots of selected rare earth elements doped ISGs. The circle represents the absorption coefficient for UV laser wavelength (355 nm) and the triangle represents the absorption coefficient for green laser wavelength (532 nm)

absorption efficiency decreases from SON68 to ISG+V the prominence of the broad delayed evaporation peak increases. This suggests that the optical properties of the glass influences the ability of the laser pulse to produce well-defined evaporation peaks when utilizing the LEAP 3000X HR with a green wavelength laser and a relatively large laser spot size.

Mass spectra collected using UV wavelength (λ=355 nm) laser pulsing with the LEAP 4000X HR from SON68, ISG+V and ISG+Co samples are presented in Figure 7. In comparison to the mass-spectra collected with green laser pulsing, none of the mass spectra from UV laser pulsing exhibit a significant delayed evaporation hump, resulting in a much more uniform background across the spectra. All three spectra collected with UV laser pulsing exhibit generally similar peak shapes and background levels, suggesting similar evaporation behavior despite the ISG+Co exhibiting a gap in absorption at 355 nm.

3.2.2 | Comparison of glass compositions from APT measurements

The APT-measured composition of the doped ISG and SON68 glass samples from both LEAP systems are summarized in Tables 4 and 5 along with the expected nominal compositions. In all cases there are significant discrepancies between the measured and anticipated compositions. There is a consistent O deficiency in the APT measured composition for all datasets, except ISG+Co and SON68

TABLE 3 Absorption coefficients of ISG+V, ISG+Co and SON68

Absorption Coefficient (cm^{-1})	532 nm	355 nm
ISG+V	0.21	7.12
ISG+Co	8.92	2.23
SON68	16.74	38.72

measured with green laser pulsing. This is generally anticipated for APT characterization of many oxides, although the exact mechanism resulting in this deficiency is still uncertain.[36] The measured alkali content is also of great interest for glass corrosion behaviors and shows tremendous variability among the measurements. For SON68 glass, where both laser wavelengths are expected to absorb reasonably well, UV laser pulsing results in generally reasonable alkali concentrations while green laser pulsing results in tremendous deficiencies for both Na and Li of ~82% and ~60% relative to their nominal concentration, respectively. Alkali deficiencies also exist in the doped ISG samples for both laser systems, where UV laser pulsing resulted in Na deficiencies of ~67% and ~78% with Co and V dopants, respectively. This alkali deficiency is still worse for green laser pulsing with nearly 100% of the Na going undetected or unidentified in background for the two doped ISGs.

Boron is another critical element to quantify reliably in glass corrosion studies. No systematic trends were observed for B across the samples and laser wavelengths with excess detected (e.g. SON68 for both laser wavelengths and ISG+V with green laser pulsing) while others indicated a small deficit (ISG+Co for both laser wavelengths and ISG+V with UV laser pulsing). Combined this suggests that detection of B is not itself a major problem for APT characterization; however, its quantification has a significant uncertainty. Part of this uncertainty originates from peak overlaps of $^{27}Al^{16}O_x$ with $^{11}B^{16}O_{x+1}$ that are difficult to decompose. From an overall perspective, it appears that

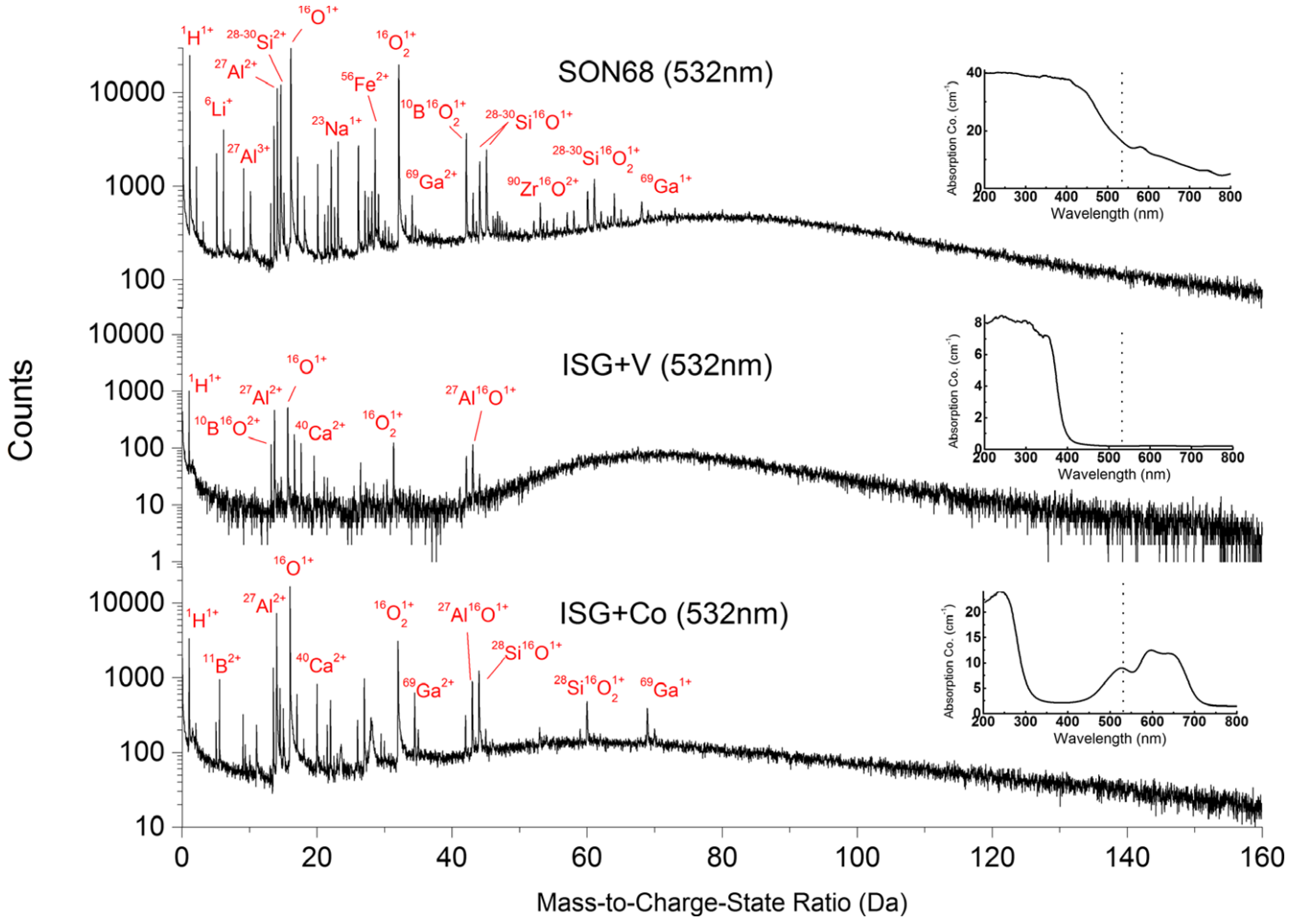

FIGURE 6 APT mass spectra of SON68 and doped ISGs collected using green laser pulsing with a LEAP 3000X HR. Prominent ion peaks are labeled in each mass spectrum. A fully labeled mass spectrum (0 to 80 Da) of SON68 analyzed on LEAP 4000X HR can be found in the appendix. UV-Vis spectra are inset for each material and the vertical dashed line indicates the 532 nm laser wavelength [Color figure can be viewed at wileyonlinelibrary.com]

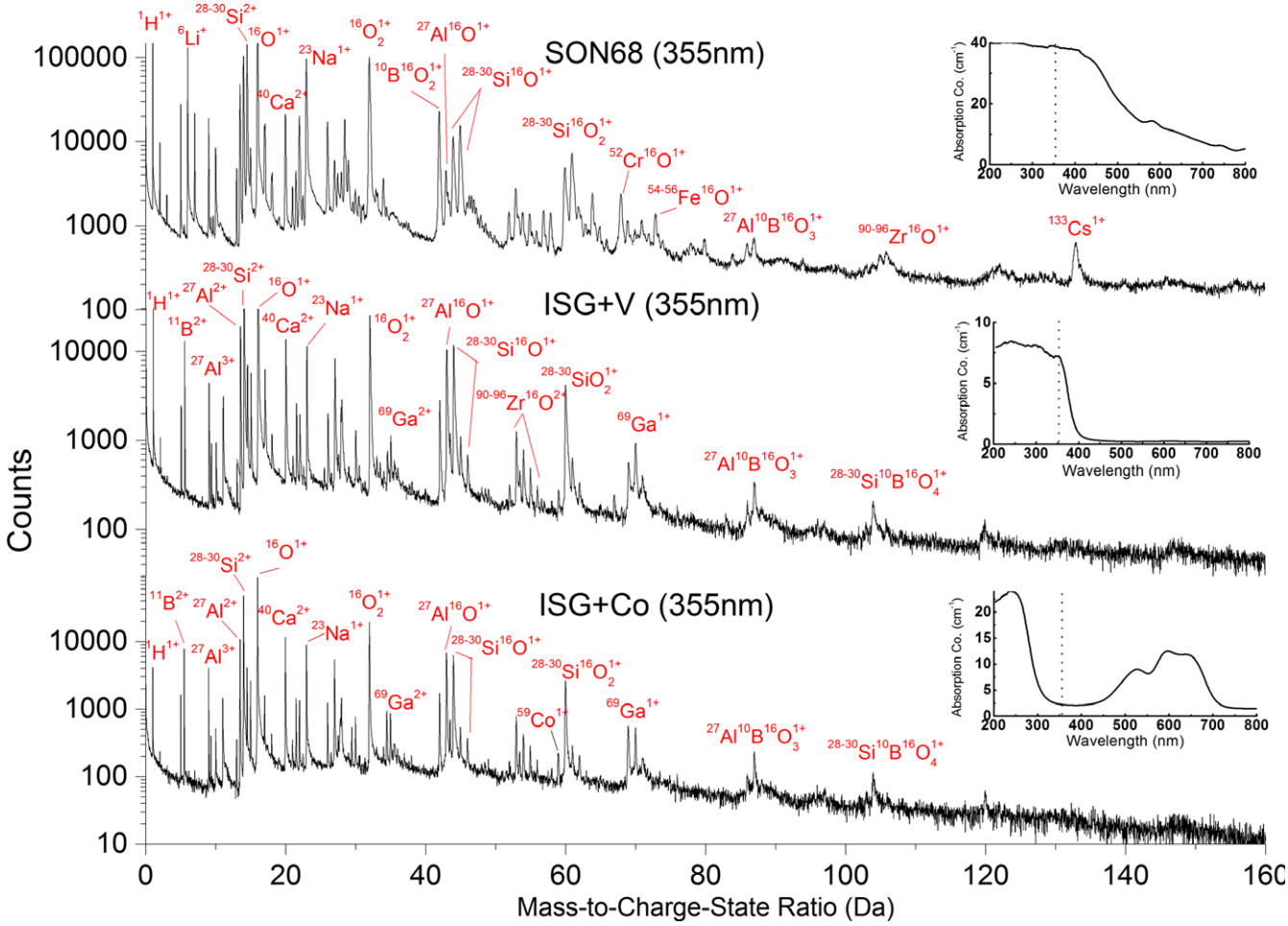

FIGURE 7 APT mass spectra of SON68 and doped ISGs collected using UV laser pulsing with a LEAP 4000X HR. Prominent ion peaks are labeled in each mass spectrum. A fully labeled mass spectrum (0 to 80 Da) of SON68 analyzed on LEAP 4000X HR can be found in the appendix. UV-Vis spectra are inset for each material and the vertical dashed line indicates the 355 nm laser wavelength [Color figure can be viewed at wileyonlinelibrary.com]

UV laser pulsing produced generally reasonable compositions with the exception of the substantial Na deficiency in the ISG samples, while green laser pulsing resulted in much more substantial alkali deficiencies for all samples. Hydrogen is also an element of great interest in glasses and glass corrosion, but there are challenges to quantify its concentration and no effort was made to study H in this work.[37-39]

3.2.3 | Closer inspection of APT mass spectra

Further inspection of the collected mass spectra was performed to better understand the possible origins of the measured compositional deficiencies and identify metrics that can potentially indicate the reliability of each APT measurement. The calculated mass resolving powers ($m/\Delta m$) from the full-width at half maximum (FWHM) of the $^{16}O^{1+}$ peak, a common metric in determining the quality of the mass spectra,[40] are summarized in Table 6. Higher values generally reflect better data quality. For ISG+Co and SON68, the data collected using green laser pulsing yielded a significantly higher mass resolving power than the corresponding data collected using UV laser pulsing. For ISG+V

TABLE 4 Nominal and APT-measured concentrations (at.%) of the key elements (exclude H and Ga) for ISG doped with either Co or V when using UV (λ=355 nm; small laser spot size) or green (λ=532 nm; larger laser spot size) laser pulsing

		ISG+Co		ISG+V	
ISG	Nominal	532 nm	355 nm	532 nm	355 nm
B	9.56%	6.95%	8.19%	22.20%	7.66%
Ca	1.71%	1.26%	3.00%	2.23%	2.46%
O	60.33%	60.86%	57.54%	57.83%	57.68%
Na	7.58%	0.07%	2.46%	0.00%	1.66%
Al	2.30%	2.94%	3.48%	7.56%	3.44%
Si	18.03%	25.54%	23.61%	9.48%	26.14%
Zr	0.49%	1.99%	1.45%	0.00%	0.78%
Other	0.00%	0.39%	0.27%	0.70%	0.18%

TABLE 5 Nominal and APT-measured concentrations (at.%) of the key elements (excluded H and Ga) for SON68 when using either UV (λ=355 nm; small laser spot size) or green (λ=532 nm; larger laser spot size) laser pulsing

Element	Nominal	532 nm	355 nm
B	8.41%	11.14%	10.45%
Ca	1.50%	0.86%	1.55%
O	59.13%	60.09%	55.28%
Na	6.83%	1.19%	7.26%
Al	2.03%	1.58%	2.34%
Si	15.80%	11.30%	13.66%
Li	2.76%	1.09%	4.03%
Other	3.54%	12.75%	5.43%

the data from UV laser pulsing yielded a slightly higher mass resolving power, possibly as a result of the very small dataset produced from green-laser pulsing. When taking into account the overall appearance of the mass spectra it is apparent that the nature of the background in the spectra results in this contradictory quantification. For green laser pulsing, the $^{16}O^{1+}$ peak contains relatively low background as the majority of the background is confined to much higher mass-to-charge-state ratios as a result of the delayed evaporation hump. In contrast, background from UV laser pulsing is much more localized to the peaks themselves, leading to a higher background affecting the mass-resolving power calculation. Therefore, the mass spectra from UV laser pulsing yields a quantitatively worse mass resolving power despite a visually "better" appearance overall and much more accurate compositional measurements.

Considering the misleading nature of this most common metric for data quality, other metrics were pursued to better compare the mass spectra. The most useful of these is the percentage of ions that were successfully identified and ranged, as summarized in Table 7, which shows very clear differences between the data collected using the LEAP 4000X HR and the LEAP 3000X HR. The data collected using UV laser pulsing yielded consistent identification of ~62% (including H and Ga ions) of the spectrum count within the reconstructed field of view for all three samples. Conversely, green laser pulsing resulted in less than 30% of the detected counts in identifiable peaks, with the ISG+V sample having less than 4% identified from its detected events, albeit from a relatively small dataset. Note that background subtraction was not performed for these calculations. These quantifications directly reflect the general visual quality of the mass spectra and also the resulting compositional reliability, particularly when comparing the data between the two laser systems. However, this metric does not reflect the significant alkali deficiency in the data collected by UV laser pulsing for doped ISG (alkali deficient, 62% of ions identified) versus SON68 (not alkali deficient, 62% of ions identified).

Percentage of multihits was also considered as an indicator of data quality. A multihit event is defined as the detector observed more than one detection event during a single pulse interval.[41] To date there are only sparse data that link multihit fractions with compositional errors,[42,43] although multihit fraction is a rarely reported data parameter in general. The percentage of multihit events for the glass samples analyzed here are summarized in Table 8. No clear trend is apparent for alkali loss as a function of multihit fraction, although the multihit fraction is significantly smaller for ISG+V especially with green laser pulsing, which exhibited the largest loss of alkalis among the six measurements. This suggests that atypically small multihit fractions could indicate greater alkali loss. Currently this hypothesis appears inconclusive but it is suggested that future studies consider this parameter.

If the laser energy absorbed is significantly different among these datasets, one might expect the evaporation field to also be significantly different. It is common to use the charge state ratio of specific elements to give some indication of the relative field strength during APT analysis. In the case of oxides, it can be argued that the ion ratio of $^{16}O^{1+}$:$^{16}O_2{}^{1+}$ gives the best indication of the field evaporation condition[44] and this parameter is summarized for the glass samples in Table 9. Significant variability exists among the measurements with one noteworthy trend. For UV laser pulsing, the doped ISG samples exhibit higher ratios, indicative of a higher evaporation field, than the SON68 glass. This correlates with alkali loss in the ISG samples, which could occur via selective evaporation of the more easily ionized alkalis between pulses at the higher standing field. However, there are no consistent trends among the green laser data, or between data collected with green and UV lasers for any one glass.

TABLE 6 The mass resolving power ($m/\Delta m$) of APT data for the full-width at half maximum (FWHM) using the $^{16}O^{1+}$ peak from ISG+Co or ISG+V and SON68 glass

Sample	ISG+Co		ISG+V		SON68	
wavelength	532 nm	355 nm	532 nm	355 nm	532 nm	355 nm
$m/\Delta m$	764	608	428	503	715	218

TABLE 7 Percentage of ranged ions (included H and Ga) from APT data of glass samples using UV or green laser pulsing

	ISG+Co		ISG+V		SON68	
	532 nm	**355 nm**	**532 nm**	**355 nm**	**532 nm**	**355 nm**
Ranged ion count	127 500	620 345	5328	1561 561	488 454	5 865 986
Spectrum count	513 971	999 947	138 575	2 488 866	1 851 159	9 555 426
Percentage ranged	28.7%	62.0%	3.8%	62.7%	26.4%	61.4%

TABLE 8 Percentage of multiple hit ions to total ions detected from reconstructed APT volume during APT field evaporation of glass samples using either green or UV laser pulsing

	ISG+Co		ISG+V		SON68	
	532 nm	**355 nm**	**532 nm**	**355 nm**	**532 nm**	**355 nm**
Multiple hits	219 978	401 833	23 240	608 811	546 032	3 437 675
Total ions	513 965	999 941	138 570	2 488 861	1 851 155	9 555 552
Percentage multihit	42.8%	40.2%	16.8%	24.5%	29.5%	36.0%

TABLE 9 Ratios of $^{16}O^{1+}$:$^{16}O_2{}^{1+}$ ions from APT data collected from glass samples using either green laser or UV laser pulsing.

Corrected	ISG+Co		ISG+V		SON68	
ion count	**532 nm**	**355 nm**	**532 nm**	**355 nm**	**532 nm**	**355 nm**
$^{16}O^{1+}$	25 110	169 142	76	476 714	62 332	1 081 937
$^{16}O_2{}^{1+}$	9229	56 583	94	119 915	51 215	417 704
Ratio	3.68	2.99	0.81	3.98	1.22	2.59

4 | DISCUSSION

The combination of the glass optical properties and laser pulsing system resulted in significant changes in both the appearance of the APT mass spectra and compositional quantification of the various borosilicate glasses used in this study. The smaller spot size and shorter wavelength of the UV laser on the LEAP 4000X HR resulted in improved peak identification and compositional accuracy especially for alkali species for all samples, even though the ISG+Co exhibited better absorption at green laser wavelengths than UV during zero-field UV-Vis absorption analyses. This result is in good agreement with previous attempts to compare alkali quantification on the two LEAP platforms for $LiFePO_4$, in which the green laser-pulsed system exhibited similarly strong Li deficiencies.[22] Generally speaking, the larger spot size and longer wavelength of the LEAP 3000X HR produced a very prominent delayed evaporation hump across all accessible parameter space. This resulted in a relatively small percentage of the detected ions arriving at identifiable peaks as compared to data from the LEAP 4000X HR. This mass spectrum difference correlated with the selective loss of nearly all alkali species in data collected with the LEAP 3000X HR.

The reliability of APT to characterize alkali species and boron in borosilicate glass, both spatially and compositionally, is at the heart of a debate regarding the mechanism of borosilicate glass alteration.[9,10,12] In the work of Gin et al.,[10] a LEAP 4000X HR (λ=355 nm, 50-120 pJ/pulse) was used to demonstrate two distinct compositional profiles in altered SON68 glass: a sharp B dissolution front, and a broader ion exchange layer consisting primarily of H exchange with Li and Na. Subsequently, Hellman et al.[9] produced similar APT data also using SON68 glass on a CAMECA LaWaTAP (λ=340 nm, 10 nJ/pulse) in which they reproduced the sharp B dissolution front but ascribed the Li and Na depletion observed in both studies to an aberration from surface diffusion and migration. Although not mentioned in the Hellman manuscript, the nominal laser spot size of a LaWaTAP has been reported previously to be about 100 μm or larger diameter.[45] Here we focus our discussion on the reliability of the APT data itself and not on the impact of those data on glass alteration mechanisms.

The data presented in the current manuscript clearly demonstrate that the quantification of alkali species depends on both the glass composition (i.e. optical properties) and the laser pulsing system used to initiate field

evaporation. For all three glass compositions used in this study, green laser pulsing with a relatively large spot size produced strong alkali deficiencies that were slightly less prominent in the glass that absorbed most efficiently (SON68). Conversely, UV laser pulsing with a small laser spot size produced near-stoichiometric concentrations of alkali for SON68 and significant Na deficiencies for doped ISG materials. It is also interesting to compare the compositions measured by Hellman et al.[9] on SON68, with ~1 at.% Li and ~1 at.% Na and ~5 at.% B. These concentrations are all much smaller than the expected stoichiometry but fairly close to the concentrations obtained on SON68 using the green laser LEAP 3000X HR, which has a significantly smaller spot size than the LaWaTAP system, although the B concentration is much lower. This is likely due to differences in handling the peak overlaps related to AlO_x and BO_{x+1} and other overlaps, whereas Li and Na have no significant peak convolution issues. Taken together, these analyses suggest that a proper alkali measurement requires both efficient absorption of the laser and also a small spot size. If either of these criteria are not met, significant alkali deficiencies can be expected.

Considering the likelihood of compositional errors in these measurements, it would be advantageous to have features within the APT data that could indicate the quality of the measurement. Visual inspection of the mass spectra obtained using the LEAP 3000X HR, as shown in Figure 6, immediately showed prominent delayed evaporation that could not be assigned to any one element. These spectral features coincided with massive alkali deficiencies and should be considered a possible indicator of significant compositional errors. Conversely, mass spectra obtained using the LEAP 4000X HR for the doped ISG materials did not exhibit any significant features that could be indicative of the corresponding alkali deficiencies in comparison to the spectrum collected from SON68 glass. Indeed the mass resolving power, percentage of identified ions, multi-hit fraction and the ratio of O^{1+}:$O_2{}^{1+}$ show no significant trends among the materials when using the LEAP 4000X HR and therefore cannot be reasonably used to validate the resulting composition measurement.

One of the tangential goals of optical doping of the ISG was to improve its overall yield and viability for APT characterization. In particular, we note from Table 8 that green laser pulsing of ISG+V was particularly prone to premature tip fracture and very small datasets and also exhibited the worst laser absorption. It is interesting to note that Co doping was successful in improving the yield of ISG using UV laser pulsing despite not exhibiting a significant change in UV-Vis absorption at 355 nm. It is speculated that the absorption spectra is significantly altered during the high-field conditions of APT analysis, which have been shown to shift the band structure of most insulators.[21] While the limited set of APT data presented in this study is not definitive, it is suggested that higher levels of doping may be more advantageous and potentially result in overcoming the alkali concentration deficiency observed in the data collected from the ISG. However, doping levels should be chosen carefully as even low concentration of vanadium or cobalt oxide added to ISG has been shown to significantly reduce the dissolution rate in aqueous solutions.[46]

One additional topic of discussion is that the ISG analyzed here is lab-batched. The lab-batched glass is completely colorless in comparison with the light-green color of the standard ISG produced by MO-SCI Corporation (Rolla, MO).[26] Therefore, different APT performances and results between the ISG in this paper and the standard ISG might be observed due to their different UV absorption cut-offs, which should be considered when comparing the current data with future results published using the widely distributed batch of ISG produced by MO-SCI. More studies regarding influences of optical absorptions of materials on its characterization by APT and laser parameters (wavelength, spot size, laser energy, etc.) of LEAP systems are suggested, especially investigations of UV-Vis absorption of materials under high evaporation field or similar conditions with LEAP experiments. Local compositional information from APT can provide insight of the fundamental mechanism of these property changes.

5 | CONCLUSIONS

Transition metal and rare earth ion doped model nuclear waste glasses in the base composition of ISG were prepared and their optical absorption properties were measured and compared with the literature. Based on the optical absorption, three base glass compositions were chosen to perform laser-assisted APT experiments on two LEAP systems with different laser wavelengths and spot sizes. The results provide insights on the influence of the test material's optical properties and the APT laser setup on the successful analysis of glass materials. Several conclusions can be drawn from the study: (i) there is a 25 times laser energy readout difference between LEAP 3000X HR and LEAP 4000X HR due to different laser spot size, laser wavelength and other tool parameters; (ii) shorter laser wavelength and smaller spot size can improve overall evaporation behavior, compositional accuracy, and chemical identification in APT analysis on nuclear waste glasses; and (iii) spot size may have stronger effect than wavelength and a comparison of two lasers of the same spot size would be highly valuable. Finally, the results show that altering the optical absorption by adding small amount of transition metal in ISG could improve the performance in the green laser-assisted APT studies.

ACKNOWLEDGMENTS

We gratefully acknowledge financial support from U.S. Department of Energy (DOE) Nuclear Energy University Program (NEUP, project #13-5494) for supporting the presented experiments and the Center for Performance and Design of Nuclear Waste Forms and Containers, an Energy Frontier Research Center funded by the U.S. DOE, Office of Science, Basic Energy Sciences under Award # DE-SC0016584, for supporting subsequent data analysis and preparation of this manuscript. LEAP 3000X HR APT experiments were conducted at the Center for Advanced Research and Technology (CART) at University of North Texas (UNT). LEAP 4000X HR APT experiments were performed at EMSL, a U.S. DOE Office of Science User Facility sponsored by the office of Biological and Environmental Research and located at Pacific Northwest National Laboratory (PNNL). PNNL is operated by Battelle for the U.S. DOE under Contract DE-AC05-76RL01830. We would also like to acknowledge the support of staffs of Glass Development Laboratory (GDL) and EMSL at PNNL, and UNT CART for the assistance in the experiments.

REFERENCES

1. Kelly TF, Larson DJ. Local electrode atom probes. *Mater Charact*. 2000;44:59-85.
2. Schreiber D, Ryan JV. Atom Probe Tomography of Glasses. In: Affatigato M, ed. *Modern Glass Characterization*. Hoboken, NJ: John Wiley & Sons, Inc.; 2015:1-39.
3. Bunton JH, Olson JD, Lenz DR, Kelly TF. Advances in pulsed-laser atom probe: instrument and specimen design for optimum performance. *Microsc Microanal*. 2007;13:418-427.
4. Gault B, Vurpillot F, Vella A, et al. Design of a femtosecond laser assisted tomographic atom probe. *Rev Sci Instrum*. 2006;77:043705.
5. Cerezo A, Clifton PH, Lozano-Perez S, Panayi P, Sha G, Smith GDW. Overview: recent progress in three-dimensional atom probe instruments and applications. *Microsc Microanal*. 2007;13:408-417.
6. Schreiber DK, Olszta MJ, Bruemmer SM. Directly correlated transmission electron microscopy and atom probe tomography of grain boundary oxidation in a Ni–Al binary alloy exposed to high-temperature water. *Scripta Mater*. 2013;69:509-512.
7. Gwalani B, Alam T, Miller C, et al. Experimental investigation of the ordering pathway in a Ni-33 at.%Cr alloy. *Acta Mater*. 2016;115:372-384.
8. Liu F, Huang L, Davis RF, et al. Composition and interface analysis of InGaN/GaN multiquantum-wells on GaN substrates using atom probe tomography. *J Vacuum Sci Technol B, Nanotechnol Microelectr: Mater, Process, Measurement, Phenomena*. 2014;32:051209.
9. Hellmann R, Cotte S, Cadel E, et al. Nanometre-scale evidence for interfacial dissolution-reprecipitation control of silicate glass corrosion. *Nat Mater*. 2015;14:307-311.
10. Gin S, Ryan JV, Schreiber DK, Neeway J, Cabié M. Contribution of atom-probe tomography to a better understanding of glass alteration mechanisms: application to a nuclear glass specimen altered 25 years in a granitic environment. *Chem Geol*. 2013;349–350:99-109.
11. Greiwe G, Balogh Z, Schmitz G. Atom probe tomography of lithium-doped network glasses. *Ultramicroscopy*. 2014;141:51-55.
12. Gin S, Jollivet P, Barba Rossa G, et al. Atom-probe tomography, TEM and ToF-SIMS study of borosilicate glass alteration rim: a multiscale approach to investigating rate-limiting mechanisms. *Geochim Cosmochim Acta*. 2017;202:57-76.
13. Ohkubo T, Chen YM, Kodzuka M, Li F, Oh-ishi K, Hono K. Laser-assisted atom probe analysis of bulk insulating ceramics. *MRS Online Proc Library*. 2009;1231.
14. Li F, Ohkubo T, Chen YM, Kodzuka M, Hono K. Quantitative atom probe analyses of rare-earth-doped ceria by femtosecond pulsed laser. *Ultramicroscopy*. 2011;111:589-594.
15. Chen YM, Ohkubo T, Hono K. Laser assisted field evaporation of oxides in atom probe analysis. *Ultramicroscopy*. 2011;111:562-566.
16. Bachhav M, Danoix F, Hannoyer B, Bassat JM, Danoix R. Investigation of O-18 enriched hematite (α-Fe_2O_3) by laser assisted atom probe tomography. *Int J Mass Spectrom*. 2013;335:57-60.
17. Donald IW. *Waste Immobilization in Glass and Ceramic Based Hosts: Radioactive, Toxic and Hazardous Wastes*. West Sussex: Wiley-Blackwell; 2010.
18. Gribb AA, Kelly TF. Atom probe analysis. *Adv Mater Processes*. 2004;162:31-34.
19. Karahka M, Kreuzer HJ. Field evaporation of oxides: a theoretical study. *Ultramicroscopy*. 2013;132:54-59.
20. Silaeva EP, Karahka M, Kreuzer HJ. Atom probe tomography and field evaporation of insulators and semiconductors: theoretical issues. *Curr Opin Solid State Mater Sci*. 2013;17:211-216.
21. Silaeva EP, Arnoldi L, Karahka ML, et al. Do dielectric nanostructures turn metallic in high-electric dc fields?. *Nano Lett*. 2014;14:6066-6072.
22. Santhanagopalan D, Schreiber DK, Perea DE, et al. Effects of laser energy and wavelength on the analysis of $LiFePO_4$ using laser assisted atom probe tomography. *Ultramicroscopy*. 2015;148:57-66.
23. Vella A, Mazumder B, Da Costa G, Deconihout B. Field evaporation mechanism of bulk oxides under ultra fast laser illumination. *J Appl Phys*. 2011;110:044321.
24. Bachhav M, Danoix R, Danoix F, Hannoyer B, Ogale S, Vurpillot F. Investigation of wüstite ($Fe_{1-x}O$) by femtosecond laser assisted atom probe tomography. *Ultramicroscopy*. 2011;111:584-588.
25. Shelby JE. *Introduction to Glass Science and Technology*. Cambridge: The Royal Society of Chemistry; 2005.
26. Gin S, Abdelouas A, Criscenti LJ, et al. An international initiative on long-term behavior of high-level nuclear waste glass. *Mater Today*. 2013;16:243-248.
27. Inagaki Y, Kikunaga T, Idemitsu K, Arima T. Initial dissolution rate of the international simple glass as a function of pH and temperature measured using microchannel flow-through test method. *Int J Appl Glass Sci*. 2013;4:317-327.
28. Kingham DR. The post-ionization of field evaporated ions: a theoretical explanation of multiple charge states. *Surf Sci*. 1982;116:273-301.
29. Neeway J, Abdelouas A, Grambow B, et al. Vapor hydration of SON68 glass from 90°C to 200°C: a kinetic study and corrosion products investigation. *J Non Cryst Solids*. 2012;358:2894-2905.

30. Thompson K, Lawrence D, Larson DJ, Olson JD, Kelly TF, Gorman B. In situ site-specific specimen preparation for atom probe tomography. *Ultramicroscopy*. 2007;107:131-139.
31. Larson D, Prosa T, Ulfig R, Geiser B, Kelly T. *Local Electrode Atom Probe Tomography–A User's Guide*. New York, NY: Springer Verlag; 2013.
32. Peng Z, Choi P, Gault B, Raabe D. Evaluation of analysis conditions for laser-pulsed atom probe tomography: example of cemented tungsten carbide. *Microsc Microanal*. 2017;23:1-12.
33. ElBatal FH, Selim MS, Marzouk SY, Azooz MA. UV-vis absorption of the transition metal-doped SiO_2–B_2O_3–Na_2O glasses. *Phys B*. 2007;398:126-134.
34. Nachimuthu P, Jagannathan R. Optical absorption spectral studies of Pr^{3+}, Nd^{3+}, Er^{3+} and Tm^{3+} ions in the CaO-B_2O_3-Al_2O_3 glass system. *Phys Chem Glasses*. 1996;36:194-200.
35. Dorosz D. Rare earth ions doped aluminosilicate and phosphate double clad optical fibres. *Techn Sci*. 2008;56.
36. Gault B, Saxey DW, Ashton MW, et al. Behavior of molecules and molecular ions near a field emitter. *New J Phys*. 2016;18:033031.
37. Larson D, Alvis R, Lawrence D, et al. Analysis of bulk dielectrics with atom probe tomography. *Microsc Microanal*. 2008;14:1254-1255.
38. Marquis EA, Bachhav M, Chen Y, Dong Y, Gordon LM, McFarland A. On the current role of atom probe tomography in materials characterization and materials science. *Curr Opin Solid State Mater Sci*. 2013;17:217-223.
39. Oberdorfer C, Stender P, Reinke C, Schmitz G. Laser-assisted atom probe tomography of oxide materials. *Microsc Microanal*. 2007;13:342-346.
40. Valderrama B, Henderson HB, Gan J, Manuel MV. Influence of instrument conditions on the evaporation behavior of uranium dioxide with UV laser-assisted atom probe tomography. *J Nucl Mater*. 2015;459:37-43.
41. Imago Scientific Instruments. LEAP 3000 HR and 3000X HR System User Manual, Madison, WI: IMAGO Scientific Instruments; 2007.5-27.
42. Williams CA, Marquis EA, Cerezo A, Smith GDW. Nanoscale characterisation of ODS–Eurofer 97 steel: an atom-probe tomography study. *J Nucl Mater*. 2010;400:37-45.
43. Meisenkothen F, Steel EB, Prosa TJ, Henry KT, Prakash Kolli R. Effects of detector dead-time on quantitative analyses involving boron and multi-hit detection events in atom probe tomography. *Ultramicroscopy*. 2015;159:101-111.
44. Schreiber DK, Chiaramonti AN, Gordon LM, Kruska K. Applicability of post-ionization theory to laser-assisted field evaporation of magnetite. *Appl Phys Lett*. 2014;105:244106.
45. Grenier A, Duguay S, Barnes JP, et al. 3D analysis of advanced nano-devices using electron and atom probe tomography. *Ultramicroscopy*. 2014;136:185-192.
46. Lu X, Neeway JJ, Ryan JV, Du J. Influence of low concentration V and Co oxide doping on the dissolution behaviors of simplified nuclear waste glasses. *J Non Cryst. Solids*. 2016;452:161-168.

How to cite this article: Lu X, Schreiber DK, Neeway JJ, Ryan JV, Du J. Effects of optical dopants and laser wavelength on atom probe tomography analyses of borosilicate glasses. *J Am Ceram Soc*. 2017;100:4801–4815. https://doi.org/10.1111/jace.14987

APPENDIX

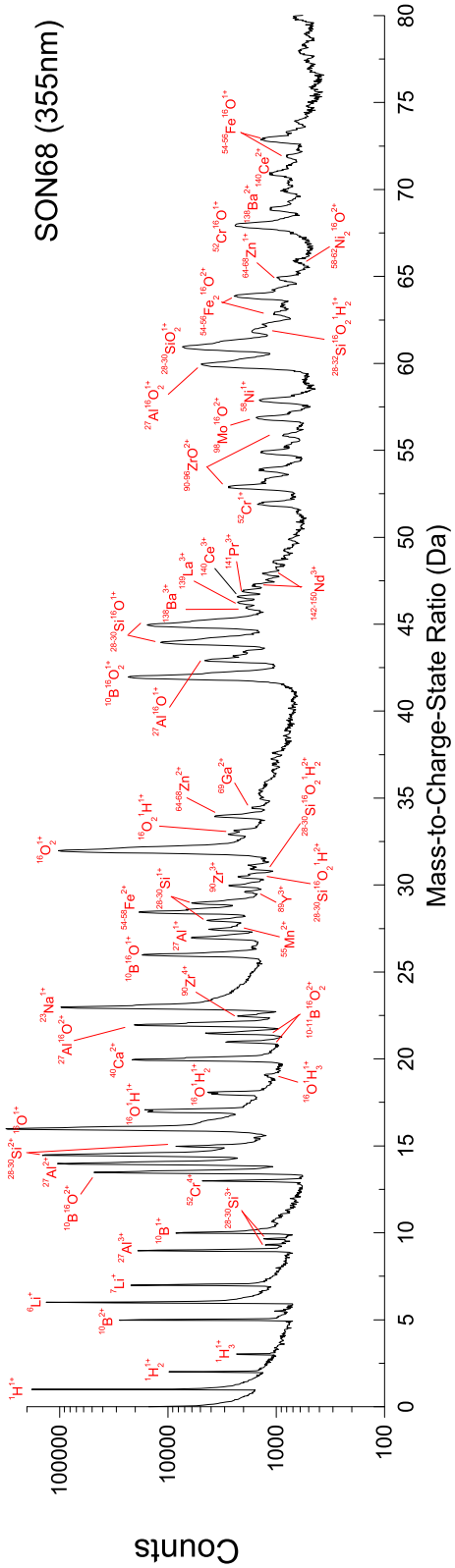

FIGURE A1 Fully arranged mass spectrum (0 to 80 Da) of SON68 analyzed on LEAP 4000X HR [Color figure can be viewed at wileyonlinelibrary.com]